Modelling the Permeation of Mechanically Sensitive Ion Channels in Auditory Hair Cells and its Implications for Preventing Drug-Induced Ototoxicity

Virginia Noëlle Mahieu

Submitted for the degree of Doctor of Philosophy

University of Sussex

July 2020

Declaration

Whilst I have collected all the electrophysiology data presented in this thesis, the code underlying the automated channel permeation modelling was developed in collaboration with Mr. Joshua Porter. Furthermore, some ototoxicity data from other lab members were included for comparison with my modelling results.

The data and photos presented in **figure 3-10** were obtained by Professor Guy Richardson and Ms. Cynthia Smith, and the figures were compiled by Dr. Richard Osgood.

The photo in **figure 4-1** was taken by Professor Guy Richardson. The data in **figure 4-11** (panel A) were obtained by Professor Guy Richardson and Ms. Jodi Parslow, and the graph was created by Dr. Richard Osgood and modified with permission.

Additionally, the images in **figure 6-1** showing a structural model of TMC1 were kindly produced for this thesis by Dr. Angela Ballesteros.

I hereby declare that this thesis has not been submitted, either in whole or in part, to this or any other University for a degree.

_____

Virginia Noëlle Mahieu

Acknowledgements

First, I would like to thank my supervisor, Professor Corné Kros. Since the day I walked into his office for our first meeting about my 3rd year undergraduate project, Corné has encouraged me to follow my intuition and creativity and has unfailingly supported me whenever I needed help. He has also supported by determined efforts to stay active with music while pursuing this PhD (and has even joined in on occasion!), for which I am incredibly grateful.

Thank you also to Professor Guy Richardson who gave me a chance and kicked off my journey in auditory research, and for all his help and advice over the years. Thank you to Emma Kenyon for being incredibly supportive and always ready to help or just chat. Thank you to Andrew Penn for imparting some of his deep physiology and statistics wisdom. Thank you to Marwa Elmasri for teaching me how to patch neurons, then Nerissa Kirkwood and Siân Kitcher for teaching me how record MET currents in hair cells. Thank you to Molly O'Reilly and Terri Desmonds for their emotional support whenever the patching got difficult. Thank you to Richard Osgood for teaching me how to make good figures and making me laugh at lunch. And thank you to Gabby Taylor for being the greatest office buddy.

I want to thank my wonderful family. My mom, Sharon Varney-Mahieu for being my academic role model. I helped you finish your thesis when I was a baby, now you've helped me finish mine–circle complete! Thank you to my dad and stepmom, Pierre-Olivier Mahieu and Jing-Jing Tu for all their support and encouragement. And my little brothers, Jiao-Fu Mahieu and Hong-Wei Mahieu, for being the most adorable boys ever.

I want to give huge thanks to my dear friend Joshua Porter for his patient, steady, and never-ending technical and emotional support throughout this thesis. I went in not knowing a thing about programming and came out with a thesis that is centred around Python, thanks to him. Without him my PhD would have been a completely different (and far less interesting) animal.

I would like to thank my lovely ladies Perrin Givan, Aisling Lyle and Monika Pawlik for being wonderful friends, always there for me through the many ups and downs of the past few years. And finally, I want to thank all of my folkies for the excellent laughs and tunes: Emma Nolan, George Gavin, Jacob Ward, Nick Greenslade, Becky Champion, Jay Chalmers, Suzie Wilcox, James Scott-Solache, James Green, and Mark Russell.

Summary

The experiments presented in this thesis are aimed at better understanding the ion and drug permeation properties of the mechano-electrical transduction (MET) channels of the hair cells responsible for hearing. Aminoglycosides (AGs) are potent antibiotics prescribed worldwide in the treatment of gram-negative infections such as sepsis, neonatal infections, and those associated with cystic fibrosis. AGs permeate into hair cells of the inner ear via the MET channels, which are large, non-selective mechanosensitive cation channels at the tips of the stereocilia. Once inside, AGs cause death of hair cells with varying degrees of severity depending on the drug family member and location of the cell along the length of the cochlea, with basal outer hair cells (OHCs) dying more readily than apical OHCs and inner hair cells (IHCs). By experimentally modelling the interaction between the MET channel and drugs that block it, we can determine electrical properties of the channel and calculate entry rates of the drugs into the cells. I present evidence for a correlation between the toxicity of three AGs (gentamicin, kanamycin and amikacin) and their entry rate through the MET channel in OHCs, with gentamicin being the most readily permeable and amikacin being the least. Furthermore, I have found that all four drugs (including the fluorescently conjugated gentamicin-Texas Red) that I have modelled permeate at a higher rate through individual channels in basal OHCs than those in apical OHCs. I have also probed the roles of calcium, maturation, and driving force in drug permeation, and addressed aspects of the genetics of the channel and how these may relate to our model. Lastly, I present evidence for the existence of volume-regulated anion channels (VRACs) in the membranes of OHCs, which could potentially be an alternative route of entry for ototoxic compounds.

Key abbreviations

ASIC	Acid-sensing ion channel
AG	Aminoglycoside antibiotic
δ_b	Relative distance of the binding site
CDH23	Cadherin 23
ΔE	Difference in energy barriers
DHS	Dihydrostreptomycin
E_1	First energy barrier
E_2	Second energy barrier
E_b	Free energy of the binding site
GTTR	Gentamicin-Texas Red
k_1	Forward rate over the first energy barrier
K_D	Half-blocking concentration
IHC	Inner hair cell
MET	Mechano-electrical transducer
n_H	Hill coefficient
OHC	Outer hair cell
P	Postnatal day
PCDH1	Protocadherin 15
RVD	Regulatory volume decrease
ROI	Region of interest
TMC	Transmembrane channel-like
V_0	Voltage of maximum block (calculated)
V_{max}	Voltage of maximum block (measured)
VRAC	Volume-regulated anion channel

Table of Contents

Table of Figures

Table of Tables

Chapter 1

Introduction

1.1 Hearing

The peripheral auditory system is an extraordinarily complex and finely tuned apparatus capable of detecting signals with impressive fidelity, and it enriches our lives with beautiful sensory detail. Our sense of hearing is essential to communication and to the appreciation of music, both of which are sources of joy for many. Unfortunately, due to its delicate nature hearing loss can easily transpire, and those that experience it often suffer greatly. In fact, hearing loss is frequently comorbid with dementia *(Uhlmann et al., 1989; Lin and Albert, 2014)* indicating an essential role in quality of life. Depending on the cause, hearing loss can be irreversible. Striving for a better understanding of the synergistic ballet of the peripheral auditory system and the mechanisms by which it can be damaged is paramount in the effort to preventing hearing loss and deafness in the population.

1.1.1 Transduction of sound to the inner ear

When something moves (i.e. a car, vocal cords, or the strings on a violin), it generates waves of pressure in the atmosphere around it. These waves propagate outward in all directions, and in the simplest of terms our ears detect them and relay them to the brain. Sound waves can be described in terms of amplitude and frequency, and together these make up a waveform *(Purves et al., 2018)*. The simplest waveform is a pure sine wave, which we often use in the lab as a stimulus when studying the transduction of sound. Sound waves produced in the environment are rarely this simple. Not only do waveforms from different sources add and subtract from each other (constructive and destructive interference), but furthermore, what we think of as individual notes in a scale are in fact made up of many harmonic overtones—multiples of the fundamental tone—characteristic to the instrument that is playing them. These overtones sum together to produce distinctive waveforms, and we can use these waveforms to identify the sources of sounds—for example, a violin versus a human voice as in **figure 1-1**. Waveforms from multiple sources sum to produce a single, continuous and seemingly random waveform. Waveforms can be deconstructed into their composing frequencies by a mathematical process called a Fourier transform. Incredibly, the clever arrangement of our peripheral auditory system allows it to perform this operation mechanically. The auditory nerve (VIIIth cranial nerve) then relays the decomposed signal to the auditory brainstem and cortex for further processing *(Purves et al., 2018)*.

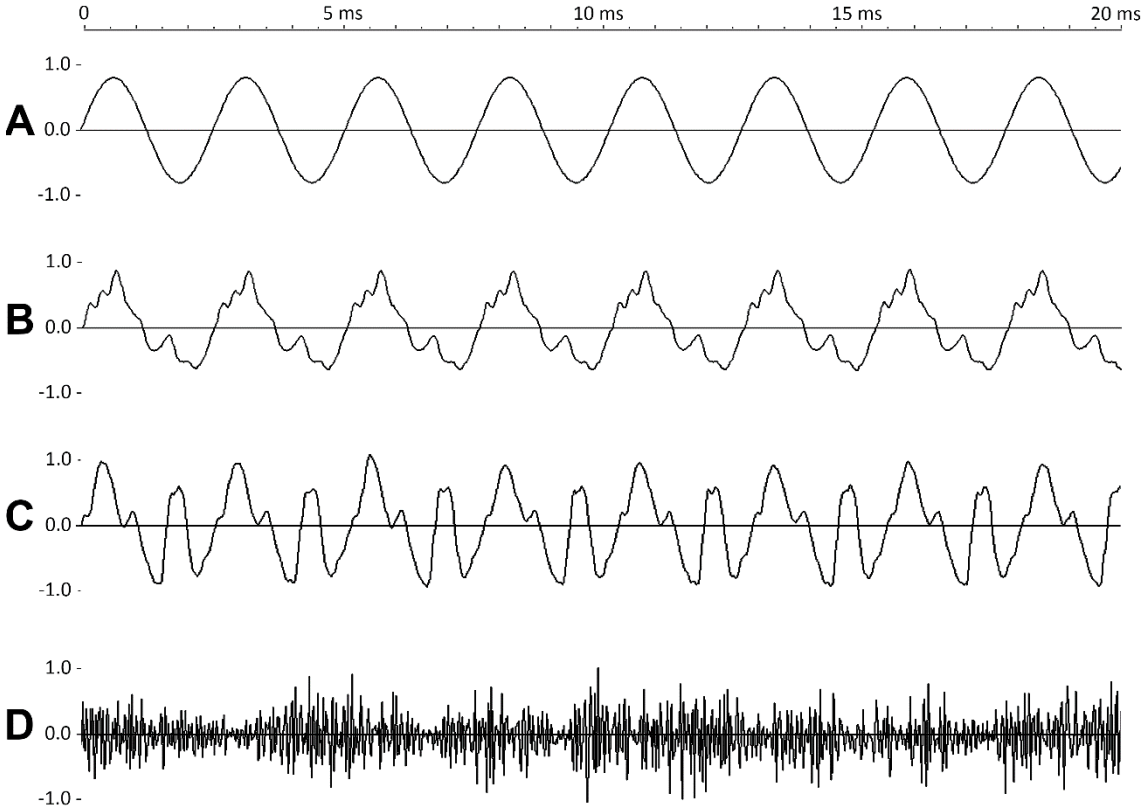

FIGURE 1-1 : The complexity of sound. (A) A pure sine wave of a G_4 (392 Hz). (B) A violin playing a G_4. (C) A human voice singing a G_4. (D) A "random" noise produced by an egg shaker.

As a sound wave arrives at the ear, it is gathered by the pinna and concha—the visible parts of the auditory system which are commonly referred to as the ear. In fact, these are only the very first part of the structure: the outer ear. In humans, the pinna and concha perform an equalisation of the soundscape by passively boosting the sound pressure of frequencies between 2 to 5 kHz about 30- to 100-fold *(Purves et al., 2018)*. The pinna and concha also selectively filter sounds by their angle of arrival, giving a rough indication of the direction of the sound source *(Purves et al., 2018)*. The sound is then funnelled down the ear canal and arrives at the entrance to the middle ear: the ear drum, or tympanic membrane. The ear drum is a thin membrane that collects the vibrations in air pressure and transfers them down the ossicles of the middle ear: the hammer, anvil, and stirrup (malleus, incus and stapes). These are among the smallest bones in the human body, and they transmit vibrations from the relatively large ear drum onto the much smaller entrance to the inner ear, the oval window of the cochlea. This process amplifies the pressure of the signal about 200-fold *(Purves et al., 2018)*. Thus, the middle ear performs the first transformation of the signal in the pathway to hearing: matching the low-impedance vibrations of air pressure to high-impedance vibrations in fluid pressure inside the cochlea *(Purves et al., 2018)*.

Inside the skull resides the inner ear, comprising the utricle and semi-circular canals (responsible for balance and the sensing of movement), and the cochlea. **Figure 1-2** details the components of the peripheral auditory system. The cochlea is a coiled bony shell, and it decomposes sounds by pitch along its length, analogous to a piano inside the head with high pitches sensed at the basal end of the coil and low pitches sensed at the apex (**figure 1-3**). This property is referred to as tonotopy. Along its interior run three fluid-filled compartments: the scala vestibuli, scala tympani, and the scala media (**figure 1-4**). The scala vestibuli and the scala media are separated by Reissner's membrane, and the scala media and scala tympani are separated by the basilar membrane. The scala vestibuli and tympani contain perilymph, while the scala media contains an unusual medium called endolymph which will be further discussed in section 1.1.3. The basilar membrane is key to frequency tuning of the cochlea. It moves in the shape of a traveling wave from the base to the apex of the coil, resonating at specific locations along its length depending on the frequency (or pitch) of the signal. Within the scala media along the top of the basilar membrane, lies the organ of Corti: a collection of highly specialised cells including the stars of sound transduction, the hair cells *(Purves et al., 2018)*.

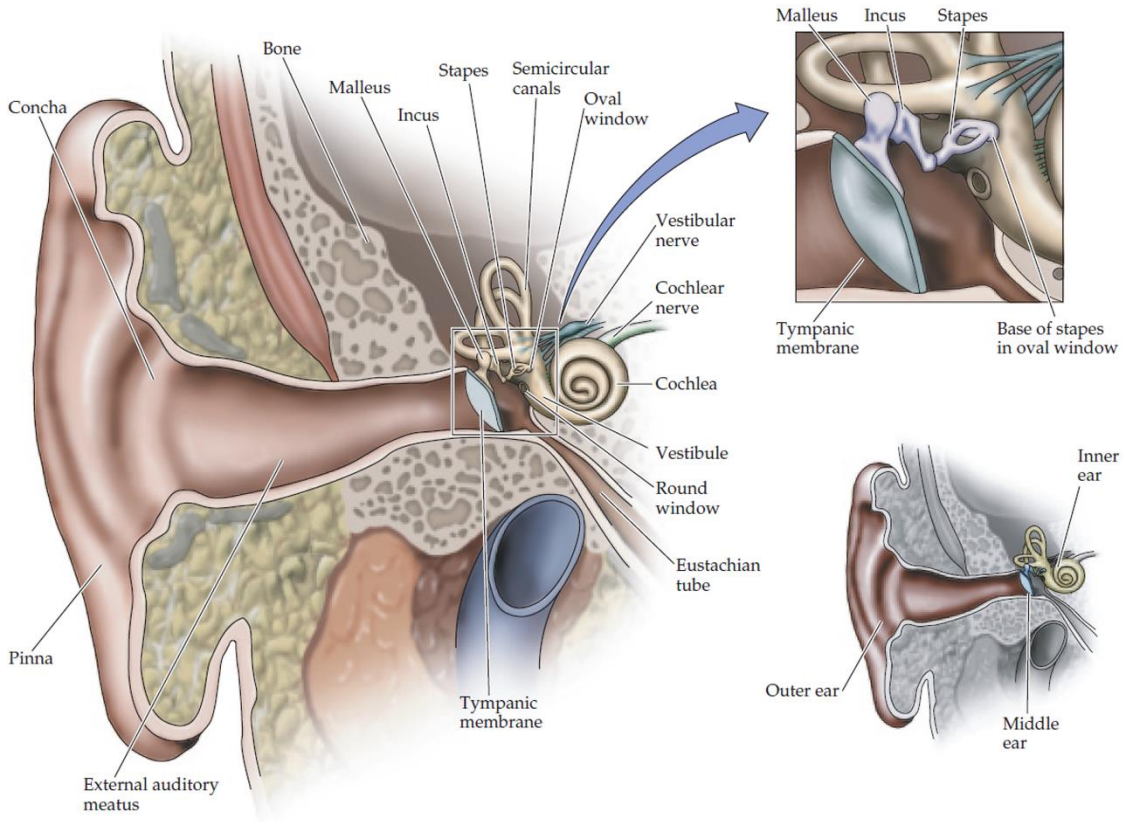

FIGURE 1-2: The human ear. *(Purves et al., 2018)*

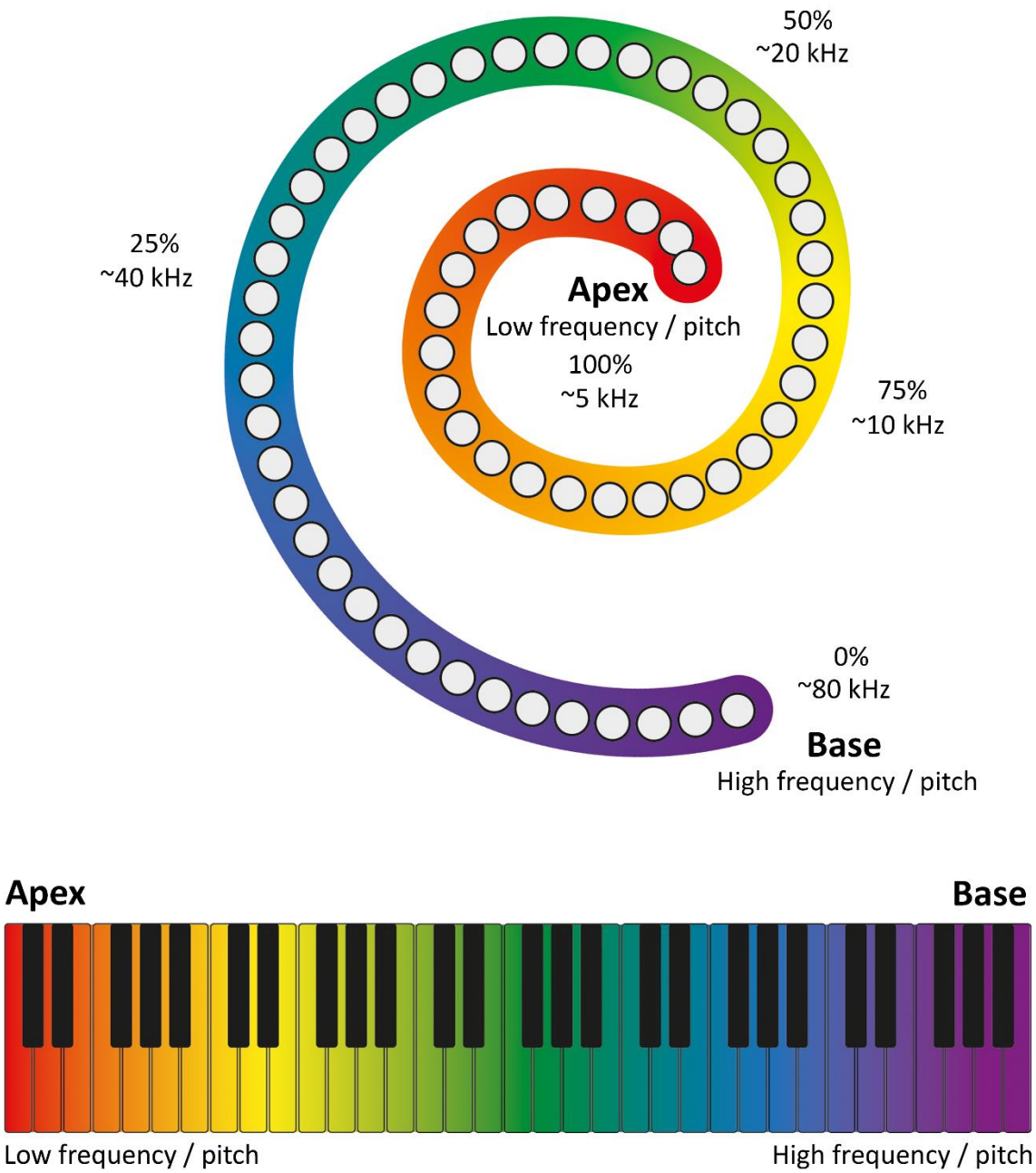

FIGURE 1-3: The piano in the head. The cochlea is tonotopically distributed so that cells in the basal region sense high frequency sounds and cells in the apical region sense low frequency sounds with a smooth gradient in between. Approximate frequencies for a mouse cochlea were calculated using the formula d(%) = 156.5 - 82.5 x log10(*f*) from *Müller et al., 2005*.

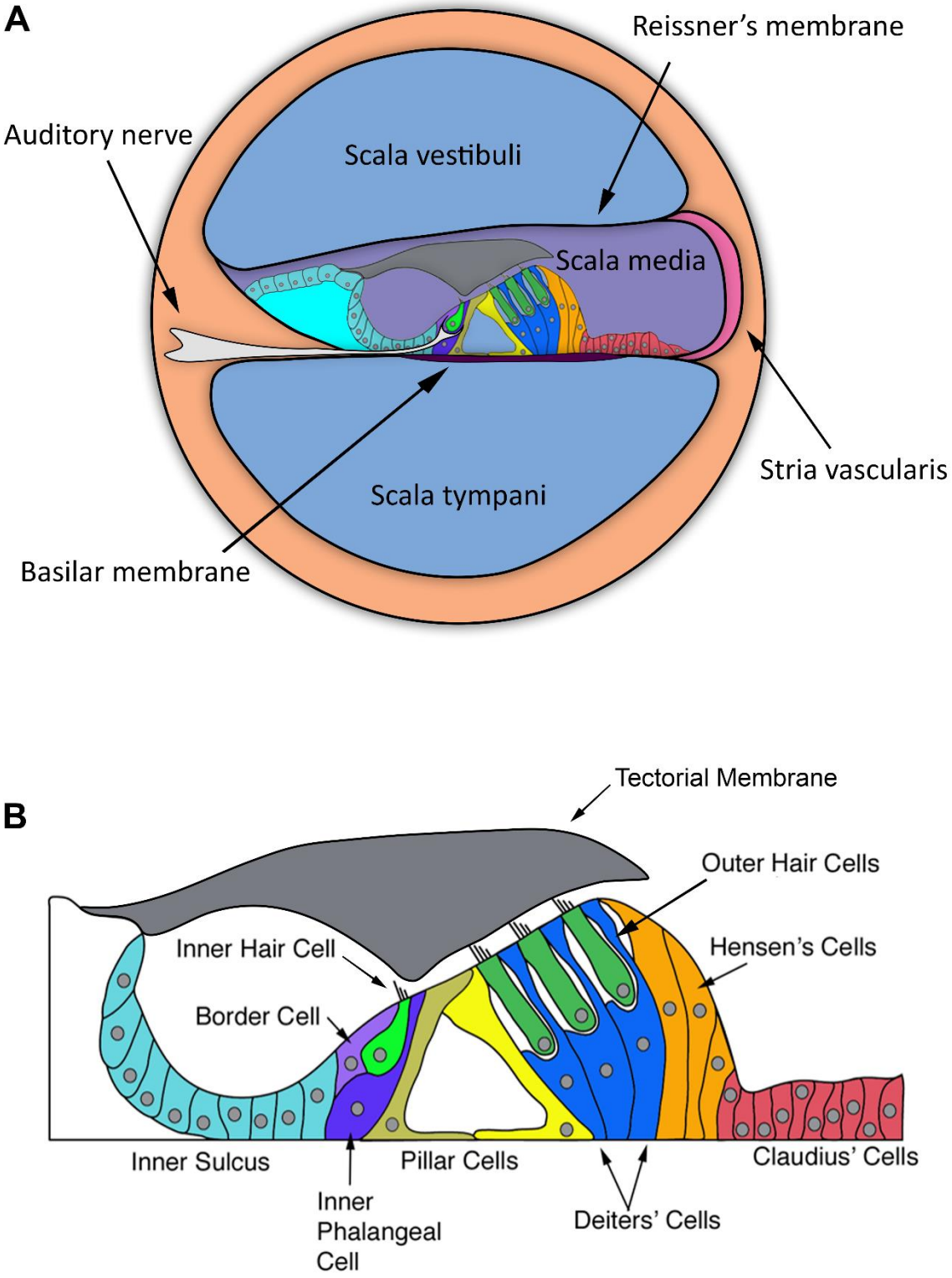

FIGURE 1-4: The cochlea. (A) Cross-section of the chochlea and its compartments. (B) The organ of Corti. Illustration of the organ of Corti in (A) and (B) by Professor Andrew Groves (Baylor College of Medicine), modified with permission.

1.1.2 Sensory hair cells

There are many interesting components of the organ of Corti, problems in any of which can contribute to hearing loss. But few are as complex as the hair cells. Along the length of the organ are four rows of sensory hair cells; three rows of outer hair cells (OHCs) and one row of inner hair cells (IHCs) as illustrated in **figure 1-4**. This thesis will focus on the OHCs of the mouse.

OHCs are long, tubular cells atop which sit a V-shaped bundle of stiff, rod-like stereocilia. These stereocilia are arranged into three rows ranging from shortest to tallest and are linked together at the top by tip links composed of protocadherin-15 (PCDH15) on the lower third and cadherin-23 (CDH23) on the upper two thirds *(Kazmierczak et al., 2007)*. The OHC hair bundles are embedded in the tectorial membrane, while the IHC hair bundles are generally less organised and are probably not directly attached the tectorial membrane *(Engström and Engström, 1978)*. At the top of the shorter stereocilia, the tip links of both OHCs and IHCs are anchored to a large proprietary nonselective cation channel called the mechano-electrical transducer (MET) channel. Deflection of the bundle by a sound wave produces a shearing motion of the stereocilia against the tectorial membrane. This puts tension on the tip links and physically pulls open the MET channels allowing influx of ions (mainly potassium and calcium) carrying electrical current and causes depolarisation of the cell (**figure 1-5**). The process of mechanotransduction will be reviewed in detail in section 1.2.

OHCs respond to sound by contracting with impressive fidelity in time with the signal, amplifying the movement of the basilar membrane *(Ashmore, 2008; Dallos, 2008)*. The change in voltage of the OHCs due to opening of the MET channel causes the membrane to contract much like a Hoberman sphere (**figure 1-5**). This property is known as electromotility and is due to activation of voltage-sensitive prestin embedded in the OHC membranes *(Ashmore, 2008; Dallos, 2008)*, and it can be observed in excised mouse OHCs from about postnatal day 7 (P7) onwards. The amplified movement of the fluid under the tectorial membrane is then sensed by the stationary IHCs, which transmit the signal to the auditory nerve and up to the brain. Both OHCs and IHCs are innervated, though the ratios of each type of innervation are different. While IHCs are innervated by about 95% of the afferent neurons (ascending to the brain), OHCs are only innervated by the remaining 5% *(Purves et al., 2018)*. Additionally, efferent neurons (descending from the brain) innervate the OHCs but their exact function remains unclear. The movement of OHCs produces sound called otoacoustic emissions, so it is thought that efferent innervation may tune this movement to regulate the stiffness of the basilar membrane *(He, 1997; Wersinger and Fuchs, 2011)*. This may have a role in protecting the cochlea from acoustic trauma.

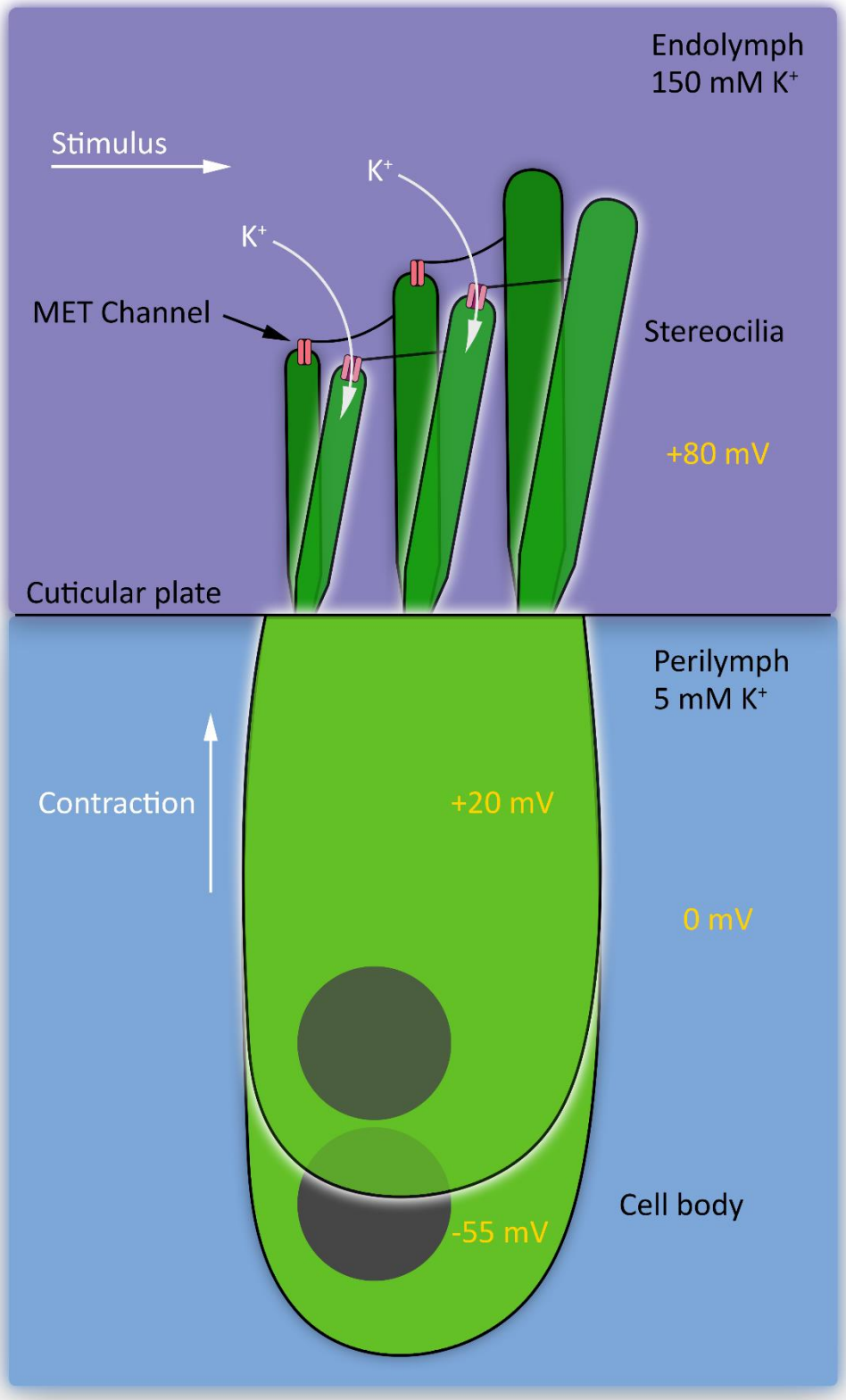

FIGURE 1-5: Outer hair cell form and function. When a stimulus arrives, it deflects the stereocilia towards the tallest row, pulling on the tip links and opening the MET channel. This allows influx of K^+ into the cell, causing depolarisation and contraction of the membrane due to voltage-sensing prestin.

1.1.4 Gradients in the development of hair cells

During development of the inner ear, a complicated sequence of gene expression produces a smooth gradient in the components of the cochlea. Morphogens diffuse away from one end to the other and depending on the threshold of the signal cells will differentiate accordingly. In the mouse, the cochlea originates from sensory progenitor cells of the ectoderm on either side of the hindbrain *(Groves and Fekete, 2012)*. The earliest marker of the developing inner ear is PAX2, which also gives rise to the epidermis *(Groves and Fekete, 2012)*. SOX2 is then expressed in multiple pro-sensory patches which will give rise to the three cristae of the semi-circular canals, the two maculae of the utricle, and the cochlear epithelium *(Bok et al., 2007; Groves et al., 2013)*. The anterior-posterior axis of the inner ear is set up by retinoic acid synthesis on the posterior side and degradation on the anterior side *(Bok et al., 2011)*.

The organ of Corti itself grows out from one point in the pro-sensory domain set up by SOX2. Notch patterning differentiates cell fates between hair cells and supporting cells *(Batts, 2009)*. ATOH1 is the key hair cell specifier, and its expression begins in the basal cells of the mouse cochlea on embryonic day (E) 13.5, progressing towards the apex *(Chen et al., 2002; Groves et al., 2013)*. Apical OHCs then mature about five days later than basal OHCs *(Groves et al., 2013)*. The regulating factor for this wave of maturation is cyclin-dependent kinase inhibitor $P27^{kip1}$: conditional knock-out of $P27^{kip1}$ leads to supernumerary proliferation and survival of hair cells into adulthood *(Walters et al., 2014)*.

As well as a difference in the timing of maturity, apical and basal OHCs have morphological differences in size and function. The smaller size of the basal cells means a smaller membrane capacitance, allowing them to respond to the faster signals of the high frequencies *(Johnson et al., 2011)*. Bundle morphology of OHCs changes in the base and apex, with basal bundles starting out slightly taller than apical but shortening over the first few postnatal days *(Lelli et al., 2009)*. The acquisition of mechanotransduction also occurs in a gradient, with transduction beginning in the base at P0 and progressing through to the apex to full completion by P7 *(Lelli et al., 2009)*. Recent evidence also shows that the tip links of OHCs demonstrate an increased stiffness in basal cells compared to apical *(Tobin et al., 2019)*. Gradients that alter the properties of mechanotransduction along the cochlea are numerous, and even occur at the level of the conductance and genetic composition of the MET channel itself.

1.2 The MET channel and its history

1.2.1 Biokinetics of the mechanotransduction complex in hair cells

The MET channel is characterised by a large single-channel conductance of approximately 100 pS *(Pan et al., 2013, Kim et al., 2013, Beurg et al., 2018, Beurg et al., 2019)* and ultra-fast kinetics of up to 100 kHz *(Doll et al., 2012)*. These properties are essential to the precise and faithful transduction of the extremely fast stimulus that is sound, and the way in which the MET channel achieves this impressive feat will be summarised here.

The driving force for current flow through the MET channel is set up by the endocochlear potential, a large electrochemical gradient in between the scala media and the scala tympani. The endolymph in the scala media contains an unusually high extracellular K^+ concentration in excess of 150 mM, compared to the 5 mM of the perilymph in the scala tympani *(Purves et al., 2018)*. This high K^+ concentration is generated and actively maintained by the stria vascularis, which secretes K^+ into the scala media *(Tasaki and Spyropoulos, 1959; Purves et al., 2018)*. This difference in ionic composition produces an electrical potential difference of approximately +80 mV between the endolymph and the perilymph *(Purves et al., 2018)*. The hair bundle sits in the endolymph, whereas the cell body is bathed in perilymph. As the interior of the cell sits between -40 and -70 mV relative to the perilymph *(Mammano and Ashmore, 1996; Marcotti and Kros, 1999; Johnson et al., 2011)*, this means that there is a gradient of up to +150 mV between the endolymph and the hair cell; an absolutely massive amount of pressure pushing positively charged ions (and other molecules!) into the cell. **Figure 1-5** illustrates the environment of an OHC. The endocochlear potential is stronger in the base than the apex of the cochlea *(Konishi and Mendelsohn, 1970; Guo et al., 2012)*, further tuning the tonotopic function of the hair cells. K^+ is cleared from the cells by ion channels in the basolateral membrane *(Fettiplace, 2017)*.

At its narrowest point, the pore of the channel is commonly thought to measure approximately 12.5 Å, with a mouth width of 17 Å and a total length of 31 Å *(Farris et al., 2004)*. Recent permeation studies suggest that this could in fact be a drastic underestimation and that the pore can fit larger molecules, including the peptide D-JNKi1 of 15 Å *(Desmonds, 2015)*, and even the 3 kDa dextran-Texas Red *(Ballesteros et al., 2018)* of 23 Å (*Choi et al., 2010*). Permeation of fluorescent compounds follows the tonotopic gradient, with basal cells showing stronger labelling than apical cells *(Gale et al., 2001, Lelli et al., 2009; Desmonds, 2015; Ballesteros et al., 2018)*.

Early extracellular recordings localised the MET channel to the tops of the stereocilia *(Hudspeth, 1982)*, and fast confocal imaging confirmed their location at the insertion point of the lower end of the tip links (*Beurg et al., 2009*). The tip links are composed of a handshake between protocadherin 15 (PCDH15) and cadherin 23 (CDH23) (*Kazmierczak et al., 2007; Goodyear et al. 2010; Sotomayor et al., 2012; Bartsch et al., 2018*). CDH23 is bound to a myosin-motor complex on the inside of the taller stereocilia, and PCDH15 contacts the MET channel complex on the top of the shorter stereocilia *(Beurg et al., 2009)*. The interaction between CDH23 and PCDH15 is calcium-dependent and buffering of calcium with BAPTA or EGTA breaks the tip links and abolishes mechanotransduction *(Assad et al., 1991; Zhao et al., 1996)*. During daily life, tip links can act as a pressure valve to protect the hair cell. They can be broken by excessively high stimuli, but amazingly can regenerate over a period of 24 hours *(Zhao et al., 1996; Indzhykulian et al., 2013)*. This may be partly to blame for that unpleasant sensation of tinnitus and mild hearing loss when you go to bed after a loud gig.

The MET channel exhibits two types of adaptation, slow and fast, both of which are dependent on calcium *(Ricci and Fettiplace, 1997; Wu et al., 1999; Ricci, 2002; Corns et al., 2014)*. Fast adaptation happens on the order of a millisecond or faster and is likely due to calcium binding either directly to the channel or to the gating spring, reducing the open probability. Slow adaptation is more complex and is thought to involve calcium diffusion through the stereocilia and affecting the myosin-motor of the tip link attached to the next shortest row. This motor is thought to involve myosin VIIa *(Kros et al., 2002)*, which interacts with CDH23 through calmodulin *(Grati and Kachar, 2011)*. When calcium binds to calmodulin, it releases the interaction and the myosin motor slips down, decreasing the tension in the tip link. It then begins to crawl back up, retensioning the tip link and resetting the operation point of the channel *(Gillespie, 2004; Grati and Kachar, 2011)*.

In the absence of stimulation, the channel has a resting open probability of 0.1 to 0.5 *(Howard and Hudspeth, 1988; Farris et al., 2006; Beurg et al., 2010)* indicating that a proportion of channels are open at rest. This can be observed as a constant membrane current even while blocking basolateral ion channels and can be calculated as a proportion of the maximal MET current that can be elicited. The resting current is abolished when a negative stimulus is applied to the hair bundles—this releases the proportion of tip links that are under tension at rest, closing all the remaining channels. It is thought that there are two or possibly more MET channels per stereocilium *(Beurg et al., 2006; Fettiplace, 2009; Beurg et al., 2018)*, though the implications of this for the joint gating of multiple permeation pathways, while feasible, are still unclear *(Sul and Iwasa, 2010; Corey et al., 2019)*.

To achieve its incredibly quick activation time *(Doll et al. 2012)*, the MET channel must be physically coupled to the tip link. The gating-spring model was first introduced by Corey and Hudspeth in 1983 to account for the observation that activation of MET channels caused a reduction in hair bundle stiffness. But experiments using electron microscopy *(Kachar et al., 2000)* and molecular dynamics simulations *(Sotomayor et al., 2010, Sotomayor et al., 2012, Powers et al. 2017)* have suggested that the tip links themselves are too stiff to be the gating spring, so it is thought there may be another component in the complex that gates the opening of the MET channel. Alternatively, the spring could be the membrane itself, as tent-like deformations around the insertion point of the tip link have been shown *(Powers et al., 2012; Reichenbach and Hudsepth, 2014)*. Either way, differences in adaptation in apex and base *(Ricci, 2002; Ricci et al., 2003)* suggest that the stiffness of the gating spring could be dependent on intracellular Ca^{2+} concentration immediately inside the transduction channel *(Reichenbach and Hudspeth, 2014)* and would require a calcium-sensing domain that could bind to and modulate the permeation properties of the channel. A recent candidate for this function is CIB2 *(Giese et al., 2017)* which will be discussed in section 1.2.3.

1.2.2 The discovery of the MET channel and its pore-forming subunit

Mechanically sensitive electrical activity of the hair bundle was first described by Hudspeth and Corey in a 1977 publication in PNAS, who subsequently did much early work characterising the activity of the MET channel in the bullfrog sacculus *(Corey and Hudspeth, 1979; Corey and Hudspeth, 1983)*. MET currents were first recorded in the mouse by Kros et al. in 1992. Since, the MET channel has generated huge interest and has been the subject of countless publications across the last 3 decades.

Characterising the channel responsible for these fascinating mechanically-sensitive currents has been a challenge to the research community: its study is confounded by the small number of channels per hair cell (~100), and the fact that no large-scale hair cell lines exist as of yet. The molecular composition of the channel is difficult to tease apart because it is likely a complex of several different proteins, and eliminating any single component of the chain can have profound effects on its kinetics and even abolish mechanotransduction. Due to the remote location of the MET channel relative to the cell body, many proteins are thought to be involved in targeting and trafficking of the various MET channel components to the tips of the stereocilia, further complicating the issue. It has also been difficult to find high-affinity ligands specific to the channel that exist for purification, likely because the channel is assembled at the stereocilia tips

(Wu and Muller, 2016). Similarly, it is difficult to image protein localisation at the tips of the stereocilia as they are so small, and there is often a build-up of precursor and trafficking proteins in the cuticular plate at the insertion point of the stereocilia into the apical surface of the cell *(Ugawa et al., 2006, Ugawa et al., 2008)*.

For many years, the identity of the MET channel was the subject of controversial debate. Several candidates have been proposed in the race for the pore-forming subunit, but until recently none have been shown to form ion permeation pathways when expressed in cell membrane. Many reviews have been published on the subject, including a pair of contrasting articles in 2016 as part of the Dual Perspectives series in the Journal of Neuroscience: one by Corey and Holt, and the other by Wu and Müller. Until very recently opinions were split over the identity of the pore-forming subunit, but conclusive evidence was published by Pan et al. in 2018 proving it beyond doubt to be the transmembrane channel-like isoforms 1 and 2 (TMC1 and TMC2). The remaining subunits of the channel remain inconclusive, however. Other proteins that have been closely implicated include LHFPL5, TMIE, CIB2, and ASIC1b (**figure 1-7**). The evidence for these and their possible functions will be reviewed here.

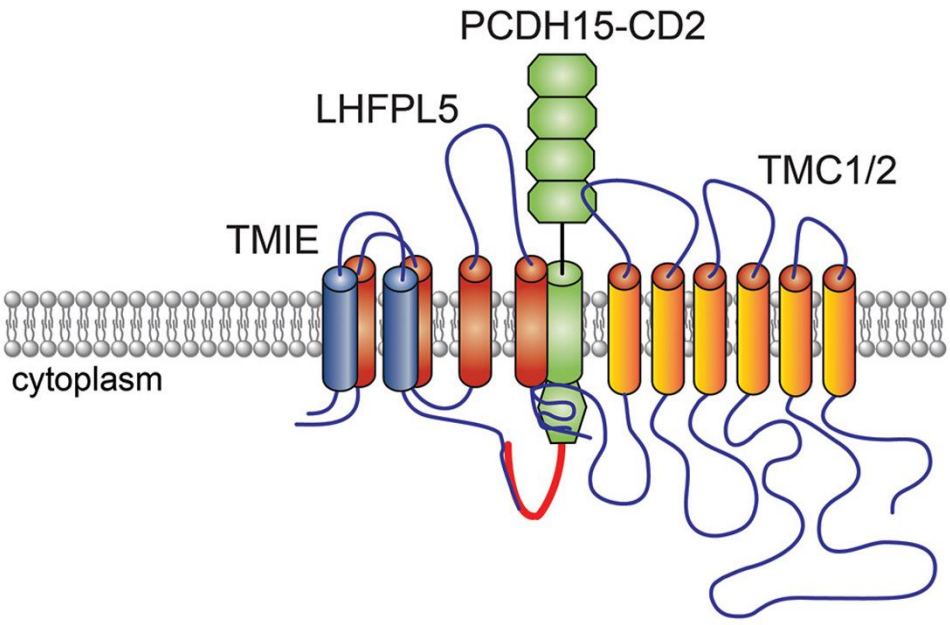

FIGURE 1-7: A proposed structure of the MET channel complex *(Wu and Müller, 2016)***.** Note this excludes the most recent potential additions, CIB2 and ASIC1b.

1.2.3 Potential MET channel complex candidates (the runners-up for the pore)

LHFPL5 (formerly known as TMHS) causes deafness in mice when mutated and is localised near the lower end of the tip links *(Xiong et al., 2012)*. *Lhfpl5*$^{-/-}$ mutants have up to a 90% reduction in mechanotransduction from stepwise deflections of the bundle, and single-channel recordings show that the conductance of the MET channel is impaired *(Xiong et al., 2012)*. However, the MET channel currents are not fully abolished, which almost definitely excludes LHFPL5 from being the pore-forming subunit. LHFPL5 was also shown to regulate the transport of PCDH15 into stereocilia, thereby potentially controlling the efficiency of tip-link formation *(Xiong et al., 2012)*. It was later found that LHFPL5 binds to TMC1 and PCDH15, and that TMC1 is no longer localised to stereocilia in *Lhflp5*$^{-/-}$ mutants *(Beurg et al., 2015)*. Structural similarities have been shown between LHFPL5 and the TARP subunits of AMPA receptors, which regulate both the transport and pore formation of AMPA receptors *(Cais et al., 2014)*. It is possible that LHFPL5 may be performing a similar role in the MET channel complex *(Wu and Müller, 2016)*.

Another protein, the aptly named trans-membrane inner ear protein (TMIE) is also linked to deafness and localised to the tip links *(Gleason et al., 2009, Zhao et al., 2014)*. *Tmie*$^{-/-}$ zebrafish mutants show degeneration of the hair cells and lack a microphonic response to vibration—indicating compromised mechanotransduction *(Gleason et al., 2009)*. In mice, *Tmie*$^{-/-}$ mutants have abnormal mechanotransduction but normal tip link assembly, and acute re-expression of TMIE in early postnatal ages can rescue mechanotransduction, indicating that it is not solely necessary in development *(Zhao et al., 2014)*. Interestingly, TMIE only binds to PCDH15 and not to either TMC1 or TMC2, unlike LHFPL5. In fact, it appears that in the absence of TMIE all other known MET channel proteins are correctly targeted, and yet the channel is non-functional *(Wu and Müller, 2016)*. TMIE could be supporting another as-yet unknown function of the MET channel, or it could potentially bind other channel subunits together.

The MET channel is permeable to calcium and some of its properties—such as adaptation—are modulated by calcium concentrations. It is thought that one or more of the accessory proteins of the MET channel may be involved with calcium sensing. The calcium- and integrin-binding protein 2 (CIB2) was identified as associated with non-syndromic deafness in humans and was recently localised to the tips of the shorter stereocilia *(Michel et al., 2017)*. *Cib2* mutation was associated with mild disruption of hair bundle formation, followed by profound OHC loss by P110 *(Giese et al., 2017)*. This suggests that CIB2 is not essential for the formation of hair bundles but does play an essential role in mechanotransduction. In fact, *Cib2* mutants showed no uptake of FM1-43, a commonly used MET channel-permeable dye *(Gale et al., 2001)*, and whole-cell

patch-clamp recordings in the IHCs showed no MET currents. CIB2 was found to form strong interactions with both TMC1 and TMC2 *(Giese et al., 2017)*. This places CIB2 quite convincingly alongside the MET channel complex, and it is currently suspected that CIB2 may perhaps be a calcium sensor for fast adaptation, or even the elusive gating spring *(Powers et al., 2012; Giese et al., 2017)*.

Finally, the acid-sensing ion channel 1b (ASIC1b) has emerged as a potential candidate for an accessory to the MET channel complex for several reasons: it has been localised to the stereocilia of OHCs *(Ugawa et al., 2006)*; it is likely to be mechanically gated *(Ugawa et al., 2008)*; and it is blocked by amiloride (a high blood pressure medication) in the same manner as the MET channel complex *(Rusch et al., 1994; Ugawa et al., 2008)*. Though ASIC1b is known to form a mechanically sensitive channel *(Ugawa et al., 2008)*, it is unlikely to be the pore-forming subunit of the channel complex because *Asic1b*$^{-/-}$ still elicit a seemingly normal MET current when stimulated. A potential role for ASIC1b in the MET channel complex is that it may have a role in proton sensing similar to its function in other systems. It could be that ASIC1b is involved with adapting the MET channel to changes in extracellular pH during aging *(Ugawa et al., 2008)*.

Each of these candidates is unlikely the be the pore itself, but they are all clearly intimately implicated in the MET channel complex. Their exact contributions to the complex are yet unknown.

1.2.4 TMC1 and TMC2

TMC1 and TMC2 were first identified for their role in hearing loss in a positional cloning study of genes involved in deafness *(Kurima et al., 2002)*. More than 35 mutations in *Tmc1* cause human hearing loss *(Kawashima et al., 2011)*, making it one of the most common deafness genes *(Fettiplace, 2016)*. Interestingly, mutations in *Tmc2* do not cause deafness *(Kurima et al., 2002)*, and the first studies of *Tmc1*$^{-/-}$ early postnatal mouse mutants were unpromising as they exhibited normal MET currents *(Marcotti et al., 2006)*, but it was soon found that these currents were abolished from the second postnatal week onward *(Kawashima et al., 2011)*. Furthermore, it was found that TMC1 and TMC2 are co-expressed from early development and are functionally redundant until TMC2 is downregulated from about P10 (**figure 1-4**), and that *Tmc1*$^{-/-}$/*Tmc2*$^{-/-}$ mutation does in fact completely abolish MET currents *(Kawashima et al., 2011; Pan et al., 2013)*. It was also found that deletion of *Tmc1* and *Tmc2* does not alter either the tip links or the hair bundle morphology *(Kawashima et al., 2011)*. Fluorescently tagged TMC1 and TMC2 were

then successfully localised to the lower end of tip links *(Kurima et al., 2015)*, and it was found that both TMC1 and TMC2 form linkages with PCDH15—the lower component of the tip links *(Maeda et al., 2014, Beurg et al., 2015)*. A single point mutation called *Tmc1*$^{Bth/Bth}$ (the Beethoven mouse mutant) alters the calcium permeability of the MET channel, as well as the response to the aminoglycoside (AG) dihydrostreptomycin (DHS) which is known to bind to the inside of the channel pore *(Corns et al., 2016)*.

One of the major hurdles in concluding the roles of TMC1 and TMC2 in the MET channel permeation pathway was that for a long time attempts to show that either of these proteins could form an ion-conducting pore in a lipid bilayer failed, bar one report *(Chatziegeorgiou et al., 2013)*. Recently however evidence for TMC1 and TMC2 as the pore-forming subunits of the MET channel has been mounting. In 2018, Pan et al. used cysteine mutagenesis carried by AAV2/1 viral vectors expressing 18 variants of mouse TMC1 and showed that several of these sites caused reduction or total abolishment of transduction currents. They further found that for 5 of these, treatment with MTSET (which irreversibly binds to cysteine residues) caused further non-recoverable reduction of the transduction current, indicating that these sites likely line the pore of the channel. Homology modelling of TMC1 with the related TMEM16 proteins revealed a wide anionic cavity near the surface of the protein, indicating a potential cation permeation pathway *(Ballesteros et al., 2018)*. Intriguingly, these two studies also indicate that TMC1 likely assembles as a dimer. Soon after, the same group that created the viral vectors for TMC1 showed that gene therapy in mice with deficiencies in *Tmc1* restored hearing and balance *(Nist-Lund, 2019)*. And finally, a recent study managed to express isolated TMC1 from the green sea turtle and TMC2 from the budgerigar in insect cells and showed that these could elicit ion channel activity *(Jia et al., 2020)*.

1.2.5 Understanding the tonotopic gradient in OHC MET channel kinetics

There are many gradients in the cochlea which influence mechanotransduction. In fact, the MET channel itself varies in several aspects of its kinetics, following the tonotopic axis. Understanding the mechanisms of this gradient is not entirely straightforward and requires some picking apart of the evidence presented by the scientific community over the last few years.

The first evidence for a tonotopic gradient in mechanotransduction of OHCs was the observation that twice as much calcium entered basal cells during depolarisation than apical cells *(Ricci et al., 2000)*. Then, a gradient was found in the rate of adaptation of the MET channel *(Ricci, 2002)*, and it was found to exhibit a gradient in macroscopic, whole-cell conductance, with basal cells

eliciting larger currents than apical cells *(Ricci et al., 2003; Beurg et al., 2006; Lelli et al., 2009; Desmonds, 2015)*. Furthermore, a visible gradient in the passage of large fluorescently tagged molecules has often been reported, for example FM1-43 *(Gale et al., 2001)*, GTTR *(Dai et al., 2005)*, D-JNKi1 *(Desmonds, 2015)*, and dextran-TR *(Ballesteros et al., 2018)*, with basal cells always showing considerably strongly labelling than apical cells. The reason for these observations could easily be interpreted as basal cells having more channels than apical cells. But there are many reports that measures of single-channel activity by breaking tip links with BAPTA show that the gradient in channel conductance persists at the level of individual channels *(Ricci et al., 2003; Beurg et al., 2006; Kim and Fettiplace, 2014; Beurg et al., 2015; Beurg et al., 2018)*.

The question remains of what is setting up these differences. As mentioned, during development there is a gradual change in the expression pattern of TMC1 and TMC2, with TMC2 initially dominating the entire coil, and expression of TMC1 starting from the base and moving up to the apex so the mature MET channel only contains TMC1 (**figure 1-7**) *(Kawashima et al., 2011; Kurima et al, 2015)*. The function of TMC2 in the cochlea is unclear and has been suggested to be an evolutionary remnant *(Corns et al., 2017)*, as its expression persists in vestibular cells which are similar to immature apical cells of the cochlea and likely to be evolutionarily related.

Pan et al. *(2013)* proposed that the variable dynamics of the MET channel in neonatal OHCs may depend on the expression profiles of TMC1 and TMC2 in each cell due to differences in conductance between the two isoforms. But subsequent evidence has emerged than TMC1 itself has a gradient in single-channel conductance, and TMC2 a similar but much smaller gradient *(Kim et al., 2013; Beurg et al., 2018)*. Beurg et al. *(2018)* go so far as to suggest the existence of several variants of TMC1 each with distinctive “levels” of conductances, apparently in multiples of approximately 50 pS. They further propose evidence for multiple TMC1 pores at each MET channel complex (~8 in the apex and ~20 in the base), beyond the TMC1 dimers that have also been recently suggested *(Pan et al., 2018, Ballesteros et al., 2018)*. The molecular correlates of this variation in conductance is uncertain, as are the details of how such multiple TMCs would be cooperatively gated by the tip link *(Sul and Iwasa, 2010)*. There are also suggestions of multiple phosphorylation sites on TMC1 *(Pan et al., 2018)*, implicating the possibility of posttranslational modifications in channel configuration *(Corey et al., 2019)*.

Another interesting avenue is a variation in tip link stiffness and rotation recently reported by Tobin et al. *(2019)*, which could impact gating of the MET channel. However, a difference in tension should cause a difference in resting open probability which is not seen *(Tobin et al.,*

2019). If there were an active gating mechanism in between the tip link and the channel pore this could potentially compensate for differences in tension until the channel is opened. Thus, differences in channel tensioning could be involved in the conductance levels seen by Beurg et al. *(2018)* through distortion of the channel pore. Tobin et al. found no gradient in the tensioning of IHC tip links, which matches the lack of a gradient in IHC single-channel conductance *(Pan et al., 2013; Pan et al., 2018; Beurg et al., 2018; Corey et al., 2019)*.

The current models by which MET channel conductance modulation is achieved are by no means complete. Because this thesis addresses questions of differences in channel kinetics between the apex and base, I will further discuss the models of graded transduction and how my experimental results and my review of recent literature may relate to these in chapter 8.

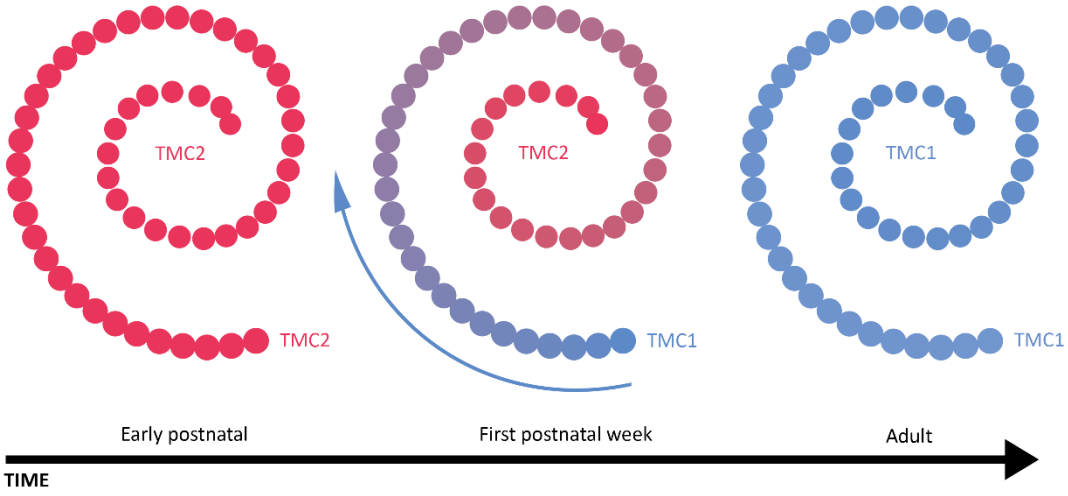

FIGURE 1-7: Expression patterns of TMC1 and TMC2 change in early development.

1.3 Hearing loss and ototoxicity

Due to their incredible complexity, the sensory hair cells of the inner ear can easily be damaged by excessive exposure to noise, through genetic mutation, or by a variety of ototoxic compounds that make their way into the endolymph of the ear. As mammals we only get one set of sensory hair cells in our lifetimes. If they die, this causes permanent hearing loss. As such it is important to protect them and doing so requires an understanding of how they function and how they can be damaged.

1.3.1 General causes of hearing loss

Hearing loss and deafness are complex disorders that can manifest from a wide range of issues within the auditory system. In the brain, hearing loss is usually due to a lesion in the central auditory pathway. Types of central hearing loss includes aphasia, pure word deafness, auditory agnosia, and central presbycusis in which speech discrimination in the elderly is worse than expected given their hearing thresholds *(Willcox and Artz, 2007)*. The existence of this latter condition is debated *(Humes et al., 2012)*. In these conditions, the peripheral auditory apparatus is behaving as normal, but the brain is not processing the signal correctly if at all. The more common cause of hearing loss is peripheral, of which there are two types: conductive and sensorineural. In conductive hearing loss the outer and middle ear do not transmit sound to the inner ear properly, due to for example: damage to the ear drum, fixation of the ossicles, or wax impaction *(Cunningham and Tucci, 2017)*. Fortunately, these conditions can usually be successfully treated to restore hearing.

Sensorineural is the more alarming type of peripheral hearing loss. Sensorineural hearing loss occurs when there is dysfunction within the cochlea. It can arise due to problems with the maintenance of the endocochlear potential by the stria vascularis *(Wangemann, 2006)*, or with damage to the spiral ganglion neurons in the auditory nerve *(Starr and Rance, 2015)*. But it is usually due to loss of sensory hair cells *(Cunningham and Tucci, 2017)*. Unfortunately, mammals cannot regenerate hair cells, so this type of hearing loss is often permanent. Furthermore, loss of hair cells leads to degeneration of the auditory nerve over a period of several months, rendering the use of cochlear implants ineffective if not implemented quickly *(Cunningham and Tucci, 2017)*.

One common cause of hair cell loss is exposure to excessively loud noise, especially for prolonged periods of time—musicians are at high risk of this, as are people who work in construction and airports. Moreover, concerts, movie theatres, loud fitness classes, shooting, and listening to music through headphones can all be sources of damage. A temporary threshold shift refers to short term hearing loss after noise exposure and can be reversed—though it may leave a mark on hair cell synapses *(Kujawa and Liberman, 2009)*—but repeated exposure can make it permanent *(Cunningham and Tucci, 2017)*.

Age-related hearing loss in the elderly population is widespread and is generally due to the accumulation of noise exposure and ototoxic factors within the ear, but it can also be hereditary. Age-related hearing loss commonly begins at higher frequencies and moves down, making speech progressively difficult to understand *(Allen and Eddins, 2010; Cunningham and Tucci, 2017)*. Hereditary genetic mutations that result in hearing loss affect approximately 1 in 1000 new-borns, while adult-onset hearing loss affects between 25 and 55% of the population *(Cunningham and Tucci, 2017)*. Over 100 genes have been identified that result, when mutated, in nonsyndromic hearing loss (i.e. they do not produce any other disorders of the body), with an additional 500 genes implicated in syndromes that include hearing loss *(Cunningham and Tucci, 2017)*.

1.3.2 Aminoglycoside-induced ototoxicity

Another cause of hearing loss is unfortunately by medically prescribed ototoxic drugs. These drugs include the aminoglycoside antibiotics (AGs), and the anti-cancer drug cisplatin. Among the most commonly used AGs are gentamicin, kanamycin, tobramycin, neomycin (only used topically), and amikacin. In the West, AGs are confined to use in life-saving situations, but in developing countries are more commonplace due to their broad spectrum of activity, stability, and rapid bactericidal activity *(Krause et al., 2016; O'Sullivan et al., 2017)*. AGs are prescribed in the treatment of dangerous gram-negative pathogens such as sepsis, neonatal infections, tuberculosis *(Krause et al., 2016)*, endocarditis *(O'Sullivan et al., 2017)* and are often given long-term to cystic fibrosis patients to prevent repeated infections *(Krause et al., 2016; Cunningham and Tucci, 2017)*. Unfortunately, AGs cause some degree of irreversible hearing loss in 20-30% of patients *(Duggal and Sarker, 2007; Schacht et al., 2012)* as well as generally reversible damage to the kidneys (nephrotoxicity) *(Lopez-Novoa et al., 2011)*.

It is difficult to relate the dosage of AGs given to patients and the resulting the concentration in the endolymph of the cochlea that will cause hair cell death. Furthermore, patients have varying

susceptibilities to AG ototoxicity. The closest estimate for the concentration of AG in the endolymph that will cause ototoxicity is approximately 1 μM *(Tran Ba Huy et al., 1981)*. AGs permeate into hair cells primarily via the MET channel due to their polycationic charges *(Marcotti et al., 2005; van Netten and Kros, 2007; Alharazneh et al., 2011; Corns et al., 2016; O'Sullivan et al., 2017)*. Once inside the cell, build-up of AGs causes ototoxicity and cell death mainly through disruption of protein synthesis by binding to the 30s ribosomal subunit *(Davies and Davis, 1968; Cabañas et al., 1978; Tanaka, 1983)* and through inhibition of mitochondrial respiration *(O'Reilly, 2019)*.

In the lab, we use excised mouse cochleae to understand the mechanisms of ototoxicity. Organotypic cochlear cultures can be incubated with AGs to look at their deleterious effects (**figure 1-8**) *(Russell and Richardson, 1987; Kotecha and Richardson, 1994; Alharazneh et al., 2011; Kenyon et al., 2017; O'Reilly et al. 2019; Kitcher et al., 2019; Kros and Steyger, 2019; Osgood, 2020)*. Members of the AG family vary in severity of ototoxicity: cultures incubated with the same concentration of different AGs will have varying levels of hair cell death, with gentamicin being the most toxic *(Kotecha and Richardson, 1994)*. The mechanism for this has thus far been unknown. It has been assumed that these differences were related to intracellular pathways for activating apoptosis. Patients with AG-induced ototoxicity tend to predominantly lose high-frequency hearing *(Al-Malky et al., 2011, Garinis et al., 2017)*. Interestingly, ex vivo organotypic cochlear cultures that are incubated with AGs also display a gradient in OHC toxicity with basal hair cells dying at lower concentrations of drug than apical cells *(Kotecha and Richardson, 1994, Wu et al., 2001, Alharazneh et al., 2011; O'Reilly, 2019; Kitcher, 2019)* following the tonotopic gradient in fluorescent labelling. The reason for this has also thus far been unclear and is generally thought to be related to differences in channel number, size, and metabolic activity of apical and basal cells.

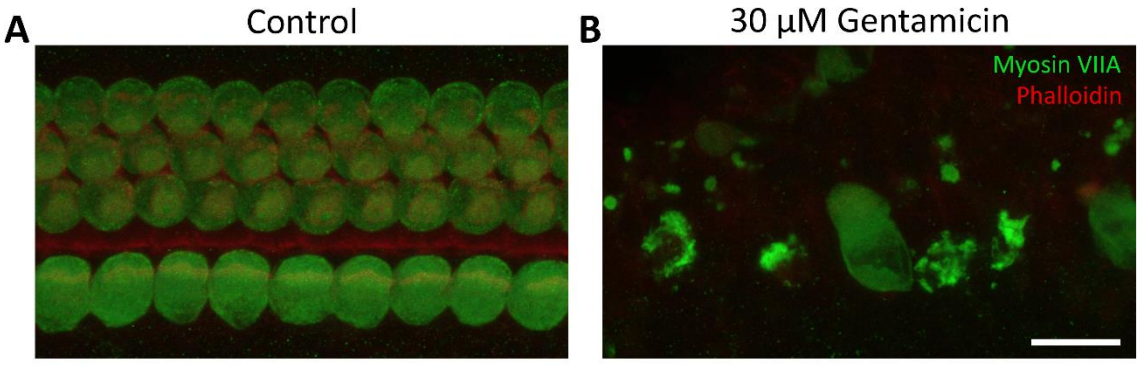

FIGURE 1-8: Gentamicin kills hair cells. The basal turn of an ex vivo organotypic cochlear culture was incubated with 30 μM gentamicin for 48 hours. Scale bar is 10 μm.

1.3.3 Preventing ototoxicity by targeting the MET channel

The large size of the MET channel pore leaves the hair cells vulnerable to molecules that would not normally permeate into other cells. Some compounds have been found to provide protection against gentamicin in culture, though these mainly act through decreasing the formation of reactive oxygen species and generally do not confer protection *in vivo (Kitcher, 2019)*. Perhaps a better strategy towards otoprotection is to prevent the entry of gentamicin into hair cells. A recent focus of the Richardson and Kros labs has been to find otoprotectants that reversibly block the MET channel and stop AGs from entering the cell through this route *(Kirkwood et al., 2017; Kenyon et al., 2017; O'Reilly et al. 2019; Kitcher et al., 2019)*. Ideally, a co-administered compound would temporarily and reversibly block the MET channel with no other deleterious effects, preventing AG entry into the cell and thus protecting the hair cells from death.

Through a screen of over 10,000 compounds for hair cell protection again neomycin in zebrafish (5,000 of which I screened myself during an undergraduate summer project), several compounds have been identified with otoprotective potential that are currently undergoing further testing *in vitro* and *in vivo*. Some of the compounds that our lab has studied have recently been published, including a smaller screen of ion channel modulators *(Kenyon et al., 2017)*, and a paper on two promising otoprotective compounds, d-turbocurarine and berbamine *(Kirkwood et al., 2017)*. Unfortunately, berbamine was found to be highly toxic at higher concentrations (>30 μM), so its value as an otoprotectant *in vivo* may be questionable. Nevertheless, these compounds are a promising proof-of-principle for otoprotection by competing for entry into the OHCs at the level of the MET channel. Further promising compounds include a derivative of carvedilol *(O'Reilly et al. 2019)* and the novel compound ORC-13661 *(Kitcher et al., 2019)*. All the compounds here mentioned have been found to interact with the MET channel, producing reversible block of inward MET channel currents, and thus presumably competing for entry with ototoxic drugs *(Kirkwood et al., 2017; O'Reilly et al., 2019; Kitcher et al., 2019)*.

Finding otoprotectants through this pipeline has thus far produced some viable candidates, but the process is slow and challenging. Furthermore, there are still no FDA-approved otoprotectants, so the search is still on. A deeper understanding of the way in which AGs permeate through the channel could help guide and refine the search, and it could eventually lead to redesign of AGs that are less permeant and therefore less ototoxic.

1.3.4 Modelling the MET channel as a tool to aid in the search for otoprotectants

As drugs permeate through the channel, they leave a signature mark: a reduction in current as they transiently bind to the inside of the pore. This block is usually voltage- and concentration-dependent so that extracellularly applied drugs block the channel at hyperpolarised membrane potentials when the channel is opened by excitatory deflections of the hair bundle. If the drugs are permeant, then block of the channel at most negative potentials is relieved, indicating that the driving force on the molecules overpowers their binding to the channel pore and forces them into the cell. By modelling data from whole-cell patch-clamp electrophysiology, we can measure this signature and determine the permeation properties of the drugs.

We currently employ a two-barrier one-binding site model that describes this entry (**figure 1-9**) *(Marcotti et al., 2005; van Netten and Kros, 2007; Corns et al., 2016; Kirkwood et al., 2017)* based on a model produced by Woodhull in 1973 to describe H^+ permeation through a Na^+ channel in frog nerve cells and more generally adapted for ion channel permeation in Hille, 2001. According to this model, as drugs pass through the channel, they encounter a first energy barrier at the entrance to the channel pore. Upon overcoming this barrier, they bind to an area of negative charge on the inside of the channel pore and block inward current to the cell. Finally, they overcome a second barrier at the exit of the pore and permeate into the cell. The profile of this interaction between a drug and the MET channel can be obtained by fitting the two-barrier one-binding site model to a full complement of fractional block curves measured across a range of voltages.

The Hill coefficient (n_H) describes the degree of cooperativity between the blocker and the pore *(Hille, 2001)*, and can be obtained by fitting dose response curves of drug block with the Hill equation at individual voltages. A neutral Hill coefficient of 1 generally indicates an interaction between a single drug molecule and a single binding site. A Hill coefficient above 1 may indicate cooperativity in which binding of one drug molecule increases the probability of a second or more molecule(s) binding to other sites within the permeation pathway, whereas a Hill coefficient below one may point to negative cooperativity, where binding of one molecule reduces the probability of a another binding to other sites. Examples of each of these types of interactions have been demonstrated between various drugs and the MET channel *(Gale et al., 2001; Marcotti et al., 2005; Desmonds, 2015; Corns et al., 2016)*.

The full permeation characterisation of only one AG, dihydrostreptomycin (DHS), has thus far been published *(Marcotti et al., 2005)*. The half-blocking concentration (K_D) of DHS at a

membrane voltage of -84 mV was found to be 7 µM, and the block was only seen on inward currents *(Marcotti et al., 2005)*. Furthermore, single excitatory force step stimuli at a fixed membrane voltage of -84 mV showed a large inward current followed by rapid decline, and a slow closure upon stepping to the inhibitory direction *(Marcotti et al., 2005)*. The entry rate for DHS into OHCs was calculated at 9000 molecules per second per OHC at therapeutic concentrations *(Marcotti et al., 2005)*. The Hill coefficient for DHS was found to be approximately 1 across the voltages in which it produced block, indicating a single binding site for DHS within the channel pore.

To date only preliminary data have been acquired with regards to the channel-blocking effects of the clinically relevant AG gentamicin and its fluorescent-tagged companion, gentamicin Texas-red (GTTR), or any of the other clinically used ototoxic AGs. Little study has been done on the differences in drug permeation between apical and basal OHCs. It is also unknown what the effects of maturation would be on AG permeation at the level of the channel, and how these might differ from the neonate commonly used to model ototoxicity. Furthermore, the molecular correlates inside the TMC1 permeation pathway for the sites of interaction described by our model are still unknown.

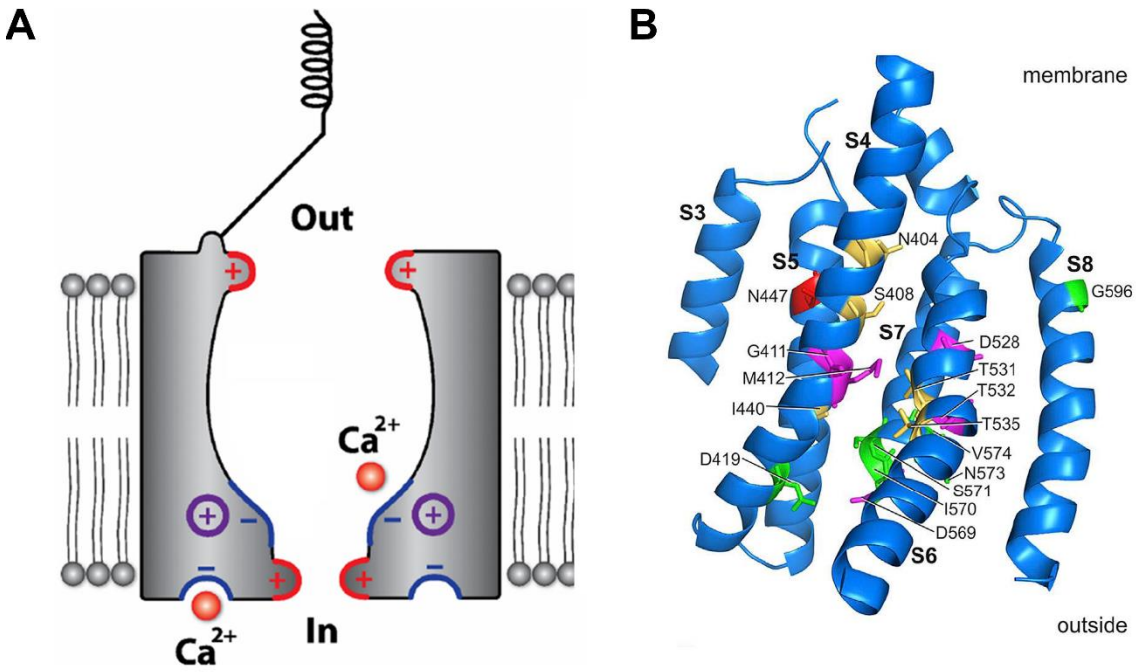

FIGURE 1-9: Modelling the MET channel. (A) Schematic model of the proposed points of bioelectrical interaction within the channel pore based on experimental data (modified with permission from *Corns et al., 2016*). (B) Proposed structural model of TMC1, the pore-forming subunit of the MET channel based on homology modelling with TMEM16 *(Pan et al., 2018)*.

1.4 Thesis aims

The overarching goal of this thesis is to better understand the mechanism by which ototoxic drugs permeate through the very channel that makes the hair cells so special: the MET channel. The permeation of these drugs is fascinating both for understanding the physiology of mechanotransduction, and for understanding what makes these cells vulnerable and how we can help protect them in the fight against hearing loss.

Specifically, I aim to:

- Investigate the permeation properties of several AGs, how these differ from each other and how these are related to their degrees of toxicity in hair cells.
- Investigate the permeation properties of GTTR, how these may differ from native gentamicin and what this could mean for its use as an indicator of gentamicin permeation.
- Investigate tonotopic variation in the permeation of the MET channel by AGs.
- Investigate how maturation and genetic mutation might affect permeation through the MET channel.
- Identify a potential alternative route of entry for ototoxic drugs into hair cells.
- Provide insight into the permeation pathway of the MET channel, and how comparative modelling can help us understand the structure of the MET channel complex.

Chapter 2

Methods

2.1 Acute and cultured tissue preparation

2.1.1 Use of acute and cultured cochleae

Acute or cultured preparations were used depending on the experiment. Acute preparations are generally favoured for electrophysiology as they are simpler in preparation and do not require aseptic technique. There is also a range of ages from which the cochleae can be dissected, offering more days of potential testing and the option to examine changes in the electrophysiology of hair cells over early postnatal days. Cultured preparations are useful for drug screening as they can be incubated with compounds to examine long-term cell toxicity. Cultures were used in the portions of this thesis directly comparable to ototoxicity experiments to keep conditions consistent with those data.

MET currents are typically more stable in cultures, except in *Tecta/Tectb*$^{-/-}$ mutants which have exceptionally large and consistent MET currents even in acute preparations. I believe this is because the process of dissection (particularly the removal of the tectorial membrane) may temporarily damage the tip links, rendering the MET currents recorded from acute preparations generally rarer and smaller. This is especially evident in basal OHCs in which recording from acute preparations is unreliable, so cultures were used for making apical-basal comparisons as this gives time for the tip links to repair *(Zhao et al. 1996, Indzhykulian et al., 2013)*.

2.1.2 Animal husbandry and preparation type

Animals were bred in the University of Sussex Life Science department facility following UK Home Office regulations, and mice of either sex were used. Swiss CD-1 mice were originally obtained from Charles River, and were used for making the cochlear cultures in chapters 3 and 4, parts of chapter 5, and chapter 7. *Asic1b*$^{-/-}$ mice in chapter 6 were obtained from Professor Shinya Ugawa (Nagoya, Japan) and the cochleae were prepared acutely. *Tecta/Tectb*$^{-/-}$ mice in chapter 5 were made in house by Professor Guy Richardson and the cochleae were prepared acutely as well.

2.2.3 Acute cochlear preparation

Acutely isolated cochleae were prepared from postnatal day (P) 2-10 mouse pups depending on the experiment and the strain of mice. The mice were killed by cervical dislocation in accordance with UK Home Office regulations (Schedule 1), and death was confirmed by removal of the head. The heads were bisected, brains removed, and the inner ears excised and transferred whole to a clean dish of ice-cold extracellular medium (made as described in section 2.2.2). From this point the inner ears were kept on ice until just before the start of a recording session, for a maximum of 2 h. When the experiments were ready to begin, the cochleae were dissected by removal of the cartilaginous or bony (depending on age) shell, the modiolus, and stria vascularis, leaving the organ of Corti. The basal turns of the cochleae were cut off to flatten the preparations. The apical turns were transferred with a spoon to the recording chamber and clamped underneath a nylon grid pulled taught over an aluminium ring in order to expose the OHCs of the mid-apex for recording (**figure 2-1**, panel A). Finally, the tectorial membranes were removed with fine forceps to expose the stereocilia.

2.1.4 Cultured cochlear preparation

Organotypic cochlear cultures were prepared from P2 CD-1 mice *(Russell and Richardson, 1987)*. As for acute preparations, the mice were killed by cervical dislocation, and the heads were removed. The heads were surface sterilised by three one-minute washes in 80% ethanol, then bisected and transferred to dishes containing 10 mM HEPES-buffered Hanks' Balanced Salt Solution (ThermoFisher 14025050). The cochleae were dissected as for acute preparations but using aseptic technique under a laminar flow hood and leaving the basal turn and tectorial membrane intact. The organs of Corti were plated onto collagen-coated (Corning 354236) coverslips (ThermoFisher 10256354) and fed with cochlear culture medium (93% DMEM-F12 (Sigma-Aldrich; D8062), 7% fetal bovine serum (Thermo Scientific; HyClone SV30180-03) and 2µg.ml^{-1} ampicillin). The cultures were wax-sealed in glass Maximow dishes and incubated at 37°C, 5% CO_2 for 24-48 hours, allowing time for the tissue to adhere to the collagen and grow outward (**figure 2-1**, panel B).

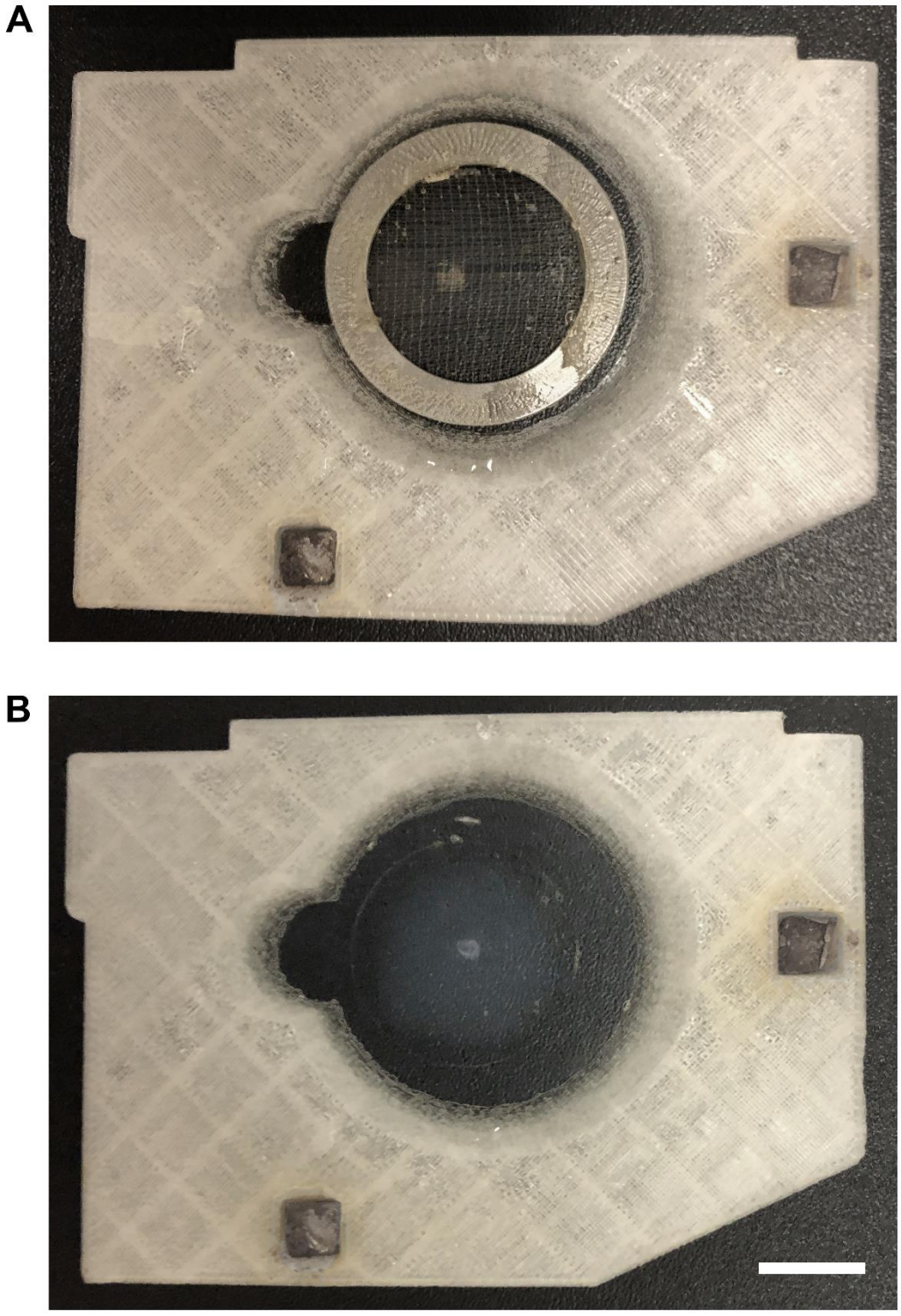

FIGURE 2-1: Acute and cultured cochlear preparations. (A) Acutely dissected cochlea held down by a nylon grid stretched over an aluminium ring. (B) Cultured cochlea adhered to collagen on a 22cm coverslip. Scale bar is 1 cm.

2.2 Electrophysiology

2.2.1 Experimental equipment

I spent the first five months of this PhD building my electrophysiology setup. This gave me a thorough understanding of the wiring and operation of the system, and the opportunity to tailor it specifically to the experiments ahead. A large part of the building process involved 3D printing of custom components (for example, the chamber in **figure 2-1**). I mostly used an Ultimaker 2+ 3D printer and designed objects using Google Sketchup.

The cells were viewed on an upright microscope (Zeiss, Germany) using Nomarski Differential Interference Contrast optics (63X water immersion objective (Leica, UK), plus 15X eyepieces), and monitored with a QICAM Fast 1394 CCD camera (QImaging, BC, Canada) through μManager *(Edelstein et al., 2014)*.

Currents were recorded and amplified by an Axopatch 200b (Axon Instruments, Union City, CA), filtered at 10kHz (except where otherwise noted) using an 8-pole Bessel filter, digitised with a Cambridge Electronic Devices (CED) Power 1401 and sampled at 20kHz (except where otherwise noted) using Signal v6.03 (CED, Cambridge, UK). The CED Power 1401 also sends a signal generated by Signal to a piezo driver, which powers the fluid jet stimulator. The setup is shown in **figure 2-2**, panel A.

The ground signal from the bath was passed through an external calibrator so that cells could be clamped at -80 mV constantly even when not running a protocol from the computer, thus avoiding accidental stress.

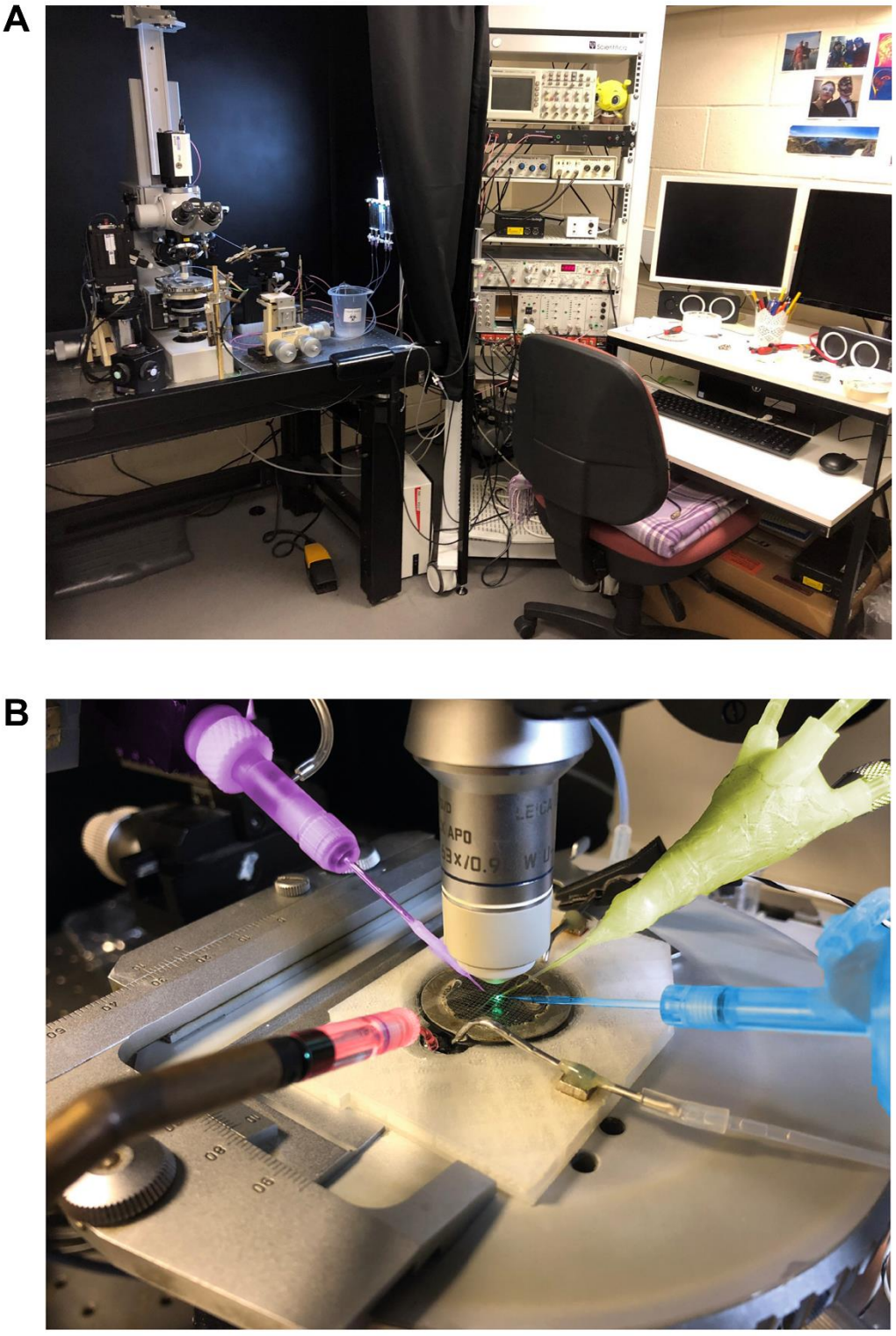

FIGURE 2-2: Electrophysiology setup. (A) Overview of the system. (B) Close-up of the stage. Colourised in red, bath electrode; blue, fluid jet; green, superfusion; purple, patch pipette.

2.2.2 Solutions and patch pipettes

Preparations, either acute or cultured, were placed in the microscope chamber and continually perfused with extracellular solution. This contained (in mM): 135 NaCl, 5.8 KCl, 1.3 $CaCl_2$, 0.9 $MgCl_2$, 0.7 NaH_2PO_4, 5.6 D-glucose, 10 HEPES-NaOH, 2 sodium pyruvate (pH adjusted to 7.5 with 1M NaOH, osmolality ~305 mOsmol kg^{-1}). This solution also contained amino acids and vitamins for Eagle's minimum essential medium, without L-glutamine (Invitrogen).

Additionally, OHCs were superfused with test drugs by a 4-channel gravity-driven manifold leading into a 200 μm nozzle at a ~100° angle to the hair bundles to minimise effect on the stereocilia. This allowed each cell to be tested at up to 3 concentrations of drug, plus control. The control superfusion solution contained (in mM): 145 NaCl, 5.8 KCl, 1.3 $CaCl_2$, 0.9 $MgCl_2$, 0.7 NaH_2PO_4, 5.6 D-glucose, 10 HEPES-NaOH, 2 sodium pyruvate (pH adjusted to 7.48 with 1M NaOH, osmolality ~310 mOsmol kg-1) and into this were diluted stock concentrations of test drugs. This solution was modified where indicated in chapters 5, 6, and 7. AGs were purchased from Sigma-Aldrich and stored at 4°C. Gentamicin-Texas red (GTTR) was obtained from Professor Peter Steyger (Creighton University).

Patch pipettes were pulled from soda glass capillaries (Harvard Apparatus, Edenbridge, UK) using a Narishige PC-10 (London, UK) puller and the shank was coated with surf wax (Mr Zogs SexWax, Carpinteria, CA, USA) to reduce surface capacitance. Patch pipettes had a resistance of about 2.6 MΩ and were filled with an intracellular solution containing (in mM): 137 CsCl, 2.5 $MgCl_2$, 1 EGTA-CsOH, 2.5 Na_2ATP, 10 sodium phosphocreatine, 5 HEPES-CsOH (pH adjusted to 7.3 with CsOH, osmolality ~295 mOsmol kg^{-1}). Caesium-based solution was used to block voltage-gated potassium channels in the basolateral membrane of the OHCs and thus reduce noise and series-resistance errors in MET current recordings. The extracellular and intracellular solutions were estimated to produce a liquid-junction potential of approximately -4 mV which was included in all mentions of cell voltage in this thesis.

The stage configuration is shown in **figure 2-2**, panel B.

2.2.3 Whole cell recording of MET currents

Whole-cell patch clamp recordings were made from third-row OHCs in either the apical (9-12 kHz region) or basal (30-36kHz region) turn of the cochlea. All recordings were performed at room temperature (21-23°C). The supporting cells directly adjacent to the OHCs were removed by suction through a glass micropipette with a 10-12μm tip filled with extracellular solution, exposing the basolateral membrane. If recording from the basal end of a culture and the tectorial membrane was too close to the hair bundles, it was removed by suction with a 15-20 μm pipette.

Patch pipettes was manoeuvred close to the cell with positive pressure so that a small dimple in the cell membrane could be seen. Once positioned, positive pressure was removed, and gentle negative pressure applied until a seal of at least 1 GOhm formed with the cell membrane. At this point, the calibrator was set to hold the cell at -80 mV. Sharp negative pressure was applied to break the cell membrane and gain access to the inside of the cell. Whole-cell capacitance and resistance were compensated for, and series resistance compensation was applied up to 80%.

Hair bundles were mechanically stimulated using a fluid jet driven by a piezoelectric disc *(Kros et al., 1992)* to produce MET channel currents. Stimuli were calibrated at the start and throughout experiments to produce saturating excitation of the MET channel, thereby minimising adaptation. Gentle negative pressure was kept constant in the fluid jet to allow suction of superfused drugs and avoid mixing of solutions. The recording configuration is illustrated in **figure 2-3**.

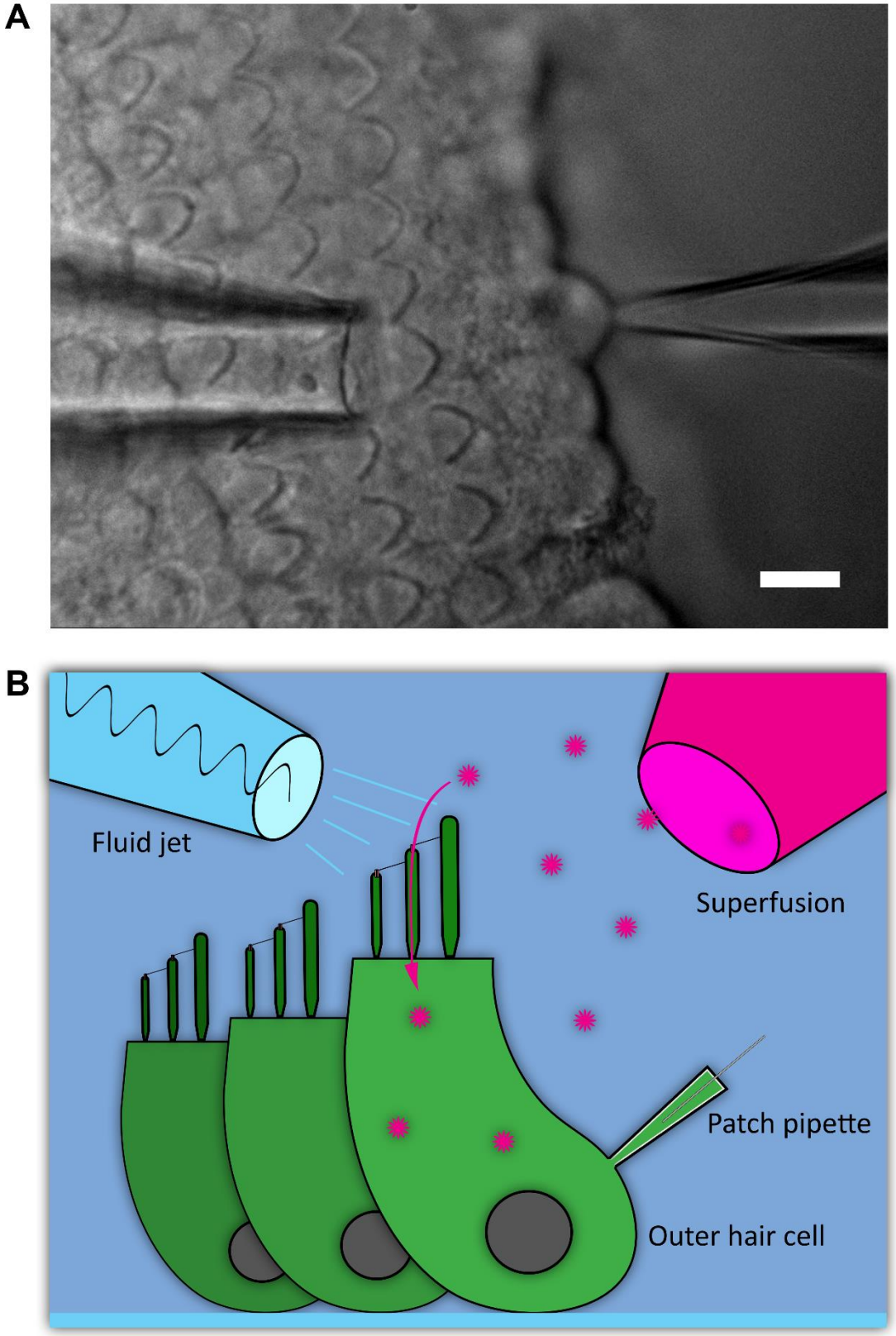

FIGURE 2-3: Whole-cell patch clamping of outer hair cells. (A) View down the microscope, with fluid jet stimulator to the left and patch pipette on a cell to the right. Scale bar is 10 µm (B) Schematic of experimental configuration.

2.3 Recording protocols and primary data analysis

The procedure described here applies to chapters 3, 4, and parts of chapter 5. Specific recording and analysis methods for the remaining experiments are described in those chapters.

The main recording protocol offered a characterisation of the effects of voltage on drug block during a standard sine wave. Sine waves were preferred to ensure saturating stimulation of the MET channel, which is evident as a flattening of the current in the range of maximal bundle deflection (**figure 2-4**). The protocol consisted of a 4-cycle sinewave stimulation at 45 Hz, combined with 14 voltage steps in 20 mV increments ranging from -164 mV to +96 mV (corrected for liquid-junction potential) (**figure 2-4**). Recordings were repeated 2-3 times per condition.

At the end of each experiment, recordings were batch exported from Signal native format .cfs to .txt using a script graciously provided by a CED employee. Primary off-line analysis of the data was done in OriginPro 2019 (OriginLab, Northampton, MA), using custom-written scripts in LabTalk for batch processing. Current-voltage (IV) curves were calculated by determining maximal MET current size at each voltage and subtracting the current during inhibitory stimulation from the current during excitatory stimulation. The maximal current was averaged for each phase of the sine wave, omitting the first. The IV curves for multiple repetitions in the same cell were averaged. Fractional block curves were obtained by dividing the averaged IV curve during superfusion of test drug by the averaged IV curve during superfusion of control solution (**figure 2-5**). The point at -4 mV is omitted due to large errors incurred by dividing small values by one another.

The second main recording protocol was aimed at determining the temporal kinetics of the channel. As previously found, AGs act as open-channel blockers of the MET channel *(Marcotti et al., 2005)*. Upon deflection of the hair bundle, a large inward current first appears that then declines to a steady state. The time course of this decay in current is related to the speed with which the molecules overcome the first energy barrier at the entrance of the channel, as described in section 2.4.1. Time constants were calculated by fitting an exponential decay function to the decay in current at the start of stimulation during excitatory square force steps of the hair bundle:

$$I = I_0 + A\, e^{-(t - t_0)/\tau},$$

(eq. 1)

where I is current, t is time, and τ is the time constant of decay.

Two protocols were used as shown in **figure 2-6**. The basic protocol consisted of holding the cell at the voltage of maximal block for the drug and stimulating with an excitatory force step (**figure 2-6**, panel A). This protocol worked well for gentamicin and GTTR which had a large, relatively slow current decay upon channel opening.

However, because the decay was much faster for kanamycin and amikacin an alternative protocol was used as described in Marcotti et al., 2005. This protocol consisted of a depolarising voltage step to +96 mV which releases the block, followed immediately by a hyperpolarising step to -124 mV for kanamycin, or -144 mV for amikacin, all during excitatory stimulation of the bundle (**figure 2-6**, panel B). This led to block that was purely brought on by voltage of maximal block, and therefore not dependent on the kinetics of the fluid jet. For this protocol, the data were filtered at 20 kHz and sampled at 100 kHz. Capacitive transients at the start and end of the voltage steps as well as linear leak and voltage-dependent membrane currents were removed by subtracting recordings from identical voltage steps in the absence of fluid-jet stimulation. Because they were so fast, time constants for amikacin and kanamycin especially were challenging to obtain and many had to be discarded due to filtering issues.

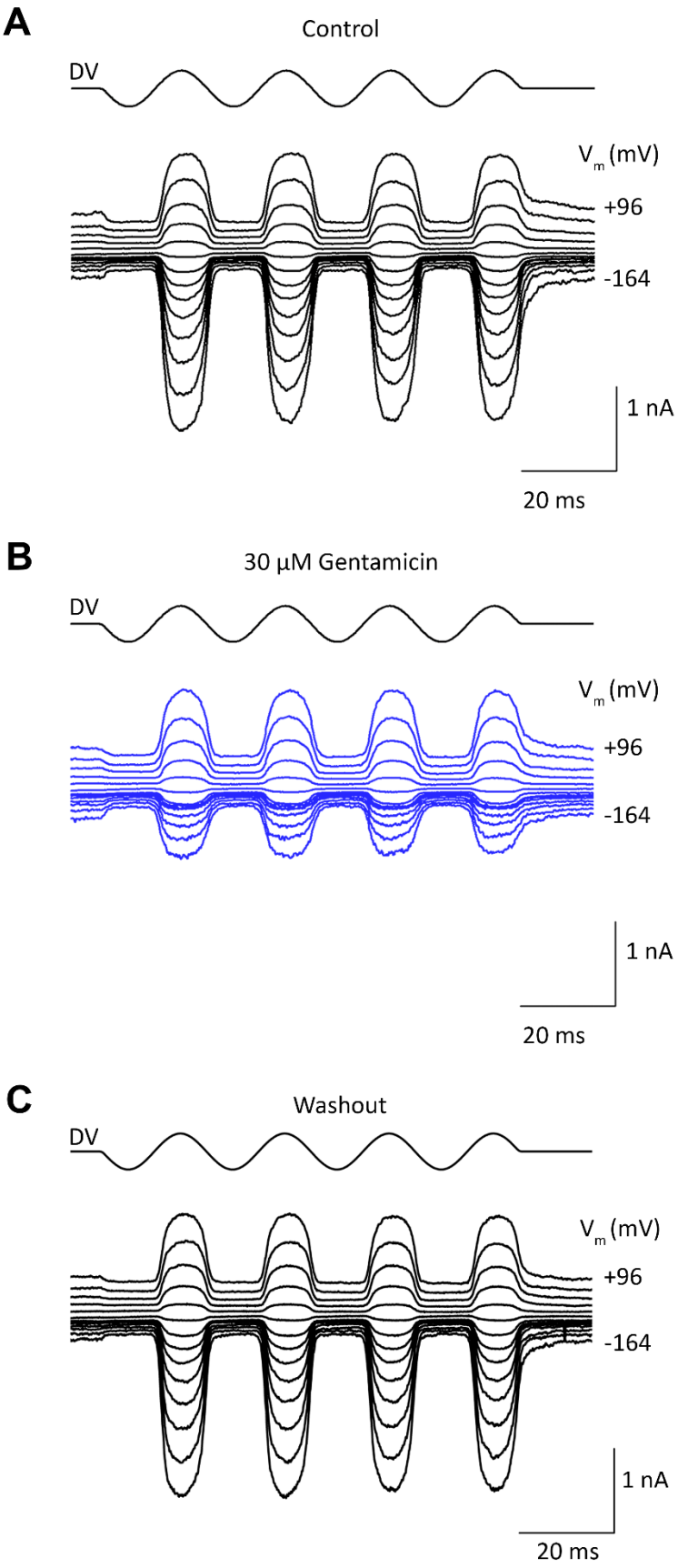

FIGURE 2-4: Standard sine wave MET current recording protocol. Application of gentamicin in (B) causes block of the large inward MET currents. (C) Gentamicin can be rapidly and fully washed out, recovering maximal MET current size.

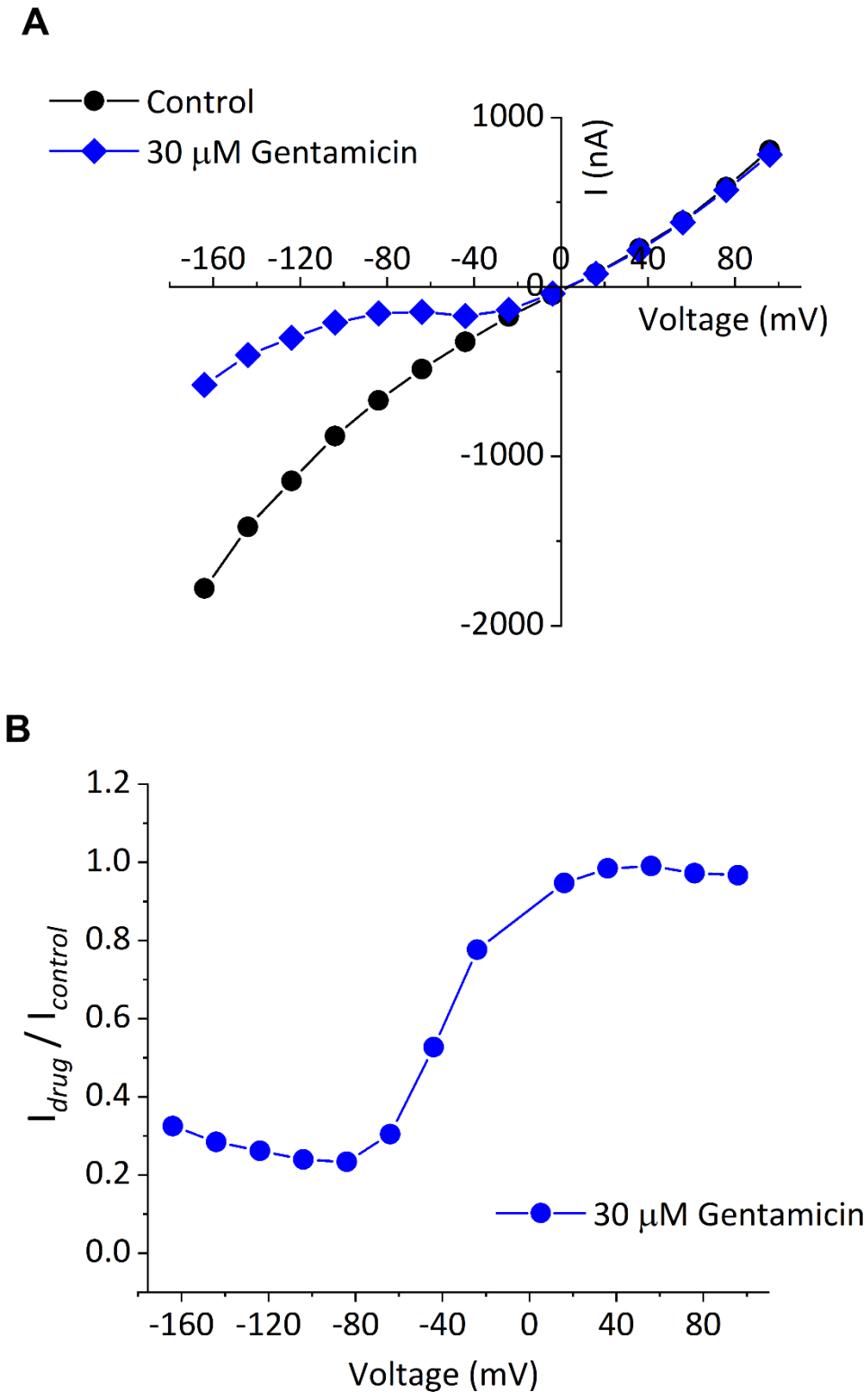

FIGURE 2-5: Example of quantification of MET current block. (A) IV curves obtained by measuring the peak MET current at each voltage in a standard sine wave protocol before and during application of gentamicin as in figure 2-4. (B) Fractional block curve obtained by dividing IV curve during application of gentamicin by control current.

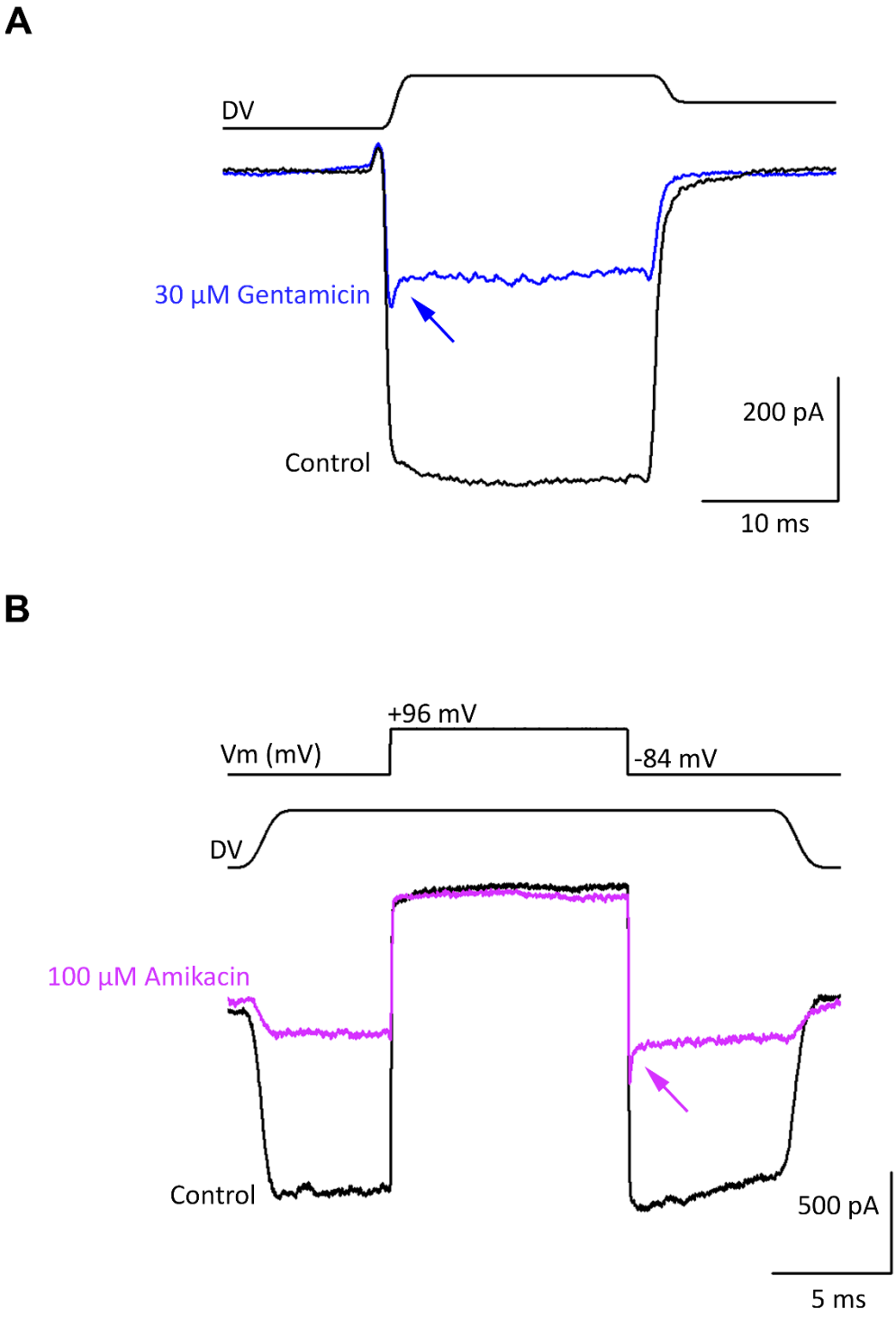

FIGURE 2-6: Time constant recording protocols examples. The arrows indicate the decay in current due to open-channel block by AGs. This portion of the trace is fit with an exponential decay function (eq. 1) to calculate time constants of drug binding (τ). (A) For gentamicin in this example, τ = 0.543 ms, (B) For amikacin in this example, τ = 0.134 ms.

2.4 Channel modelling

2.4.1 Two-barrier one binding-site model of permeation of the MET channel

To model permeation of drugs through the MET channel, we fit a two-barrier one-binding site model to the fractional block and time constant data and extract parameters that describe the biokinetics of the interaction between molecules and the channel pore *(Marcotti et al., 2005; van Netten and Kros, 2007)*. Calculating these parameters requires a complete dataset with a compound tested at multiple concentrations spanning its entire dose response range from no block to full block.

In brief, the model can be described as such:

$$C + B_o \underset{k_{-1}}{\overset{k_1}{\Leftrightarrow}} CB \underset{k_{-2}}{\overset{k_2}{\Leftrightarrow}} C + B_i$$

(eq. 2)

where C is the channel, B is the blocking agent (B_o, outside and B_i, inside). In this model, k_1 and k_2 are the binding constants, and k_{-1} and k_{-2} are the dissociation constants over the first and second energy barriers. This model represents a system in which the blocker overcomes the first energy barrier to bind to the inside of the open channel, transiently binds to the inside of the channel pore, then overcomes a second barrier to permeate into the cell.

Dose response curves were generated at each of the 7 most negative voltage steps of the fractional block curves and were fitted with the Hill equation to calculate the half-blocking concentration (K_D) and Hill coefficient (n_H):

$$\frac{I_{drug}}{I_{control}} = \frac{1}{1 + \left(\frac{D}{K_D}\right)^{n_H}},$$

(eq. 3)

where $I_{control}$ is the control current and D is the concentration of the drug in the extracellular solution.

Fractional block curves were fitted with the two-barrier one-binding site model:

$$\frac{I_{drug}}{I_{control}} = \left(1 + \left(e\left(E_b + \frac{\delta_b * z * V_m}{26}\right)\right)^{-1} * \left(1 + e\left(-\Delta E - \frac{V_m}{26}\right)\right)^{-1} D^{n_H}\right)^{-1},$$

(eq. 4)

where E_b is the free energy of the binding site in the channel pore (expressed in terms of kT: 4.1 x 10^{-21} J), δ_b is the fractional position, from the outside, of the binding site across the electrical field of the membrane, V_m is the membrane potential in mV, 26 is kT/e (the unitary charge) in mV, z is effective valence of the drug D; and ΔE is the difference between the two free energy barriers: the free energy of the barrier E2 on the intracellular side minute the free energy of the barrier E1 on the extracellular side (again in terms of kT).

The inverse of the time constants as a function of drug concentration were fitted with a linear regression line in order to calculate the slope, which in this model equals k_1:

$$\tau^{-1} = k_1[B_o]^{n_H} + k_{-1} + k_2$$

(eq. 5)

Using these parameters, the values that describe the energy profiles and entry rates of drug permeation were calculated as follows:

$$V_0 = -V_s\left(\Delta_E + ln\left(\frac{\delta_b}{1-\delta_b}\right)\right)$$

(eq. 6)

$$V_s = \frac{kT}{zq_e}$$

(eq. 7)

$$K_1 = e^{E_b+\delta_b(V/V_s)}\left(1 + e^{-\Delta E-(V/V_s)}\right)$$

(eq. 8)

$$K_D = [K_1(V)]^{\frac{1}{n_H}}$$

(eq. 9)

$$E_1 = -ln\left(\frac{k_1}{k_0}\right)$$

(eq. 10)

$$E_2 = E_1 + \Delta E$$

(eq. 11)

$$k_{-1} = k_0 e^{-(E_1-E_b)+\delta_b(V/V_s)}$$

(eq. 12)

$$k_{-2} = k_0 e^{-E_2}$$

(eq. 13)

$$k_2 = k_0 e^{-(E_2-E_b)-(1-\delta_b)(V/V_s)}$$

(eq. 14)

$$N_{entry} = \frac{N_{ch} p_0 k_2}{1 + K_1/((D * 10^{-9})^n)}$$

(eq. 15)

where V_0 is the potential of maximum block, z is the valence (apparent charge) of the blocker, q_e is the elementary unit of charge (1.6 x 10^{-21} C), K_D is the voltage-dependent half-blocking concentration, E_1 and E_2 are the first and second energy barriers, k_{-1}, k_2, and k_{-2} are the forward and reverse rate constants over the two energy barriers, and N_E is the entry rate at a given concentration, D (in μM).

2.4.2 Model automation in Python 3.0

I automated the process of modelling the drug permeation of the MET channel in Python 3.0 with the help of Mr. Joshua Porter. This reduced human error when performing calculations across multiple datasets and allowed me flexibility in adjusting fitting parameters and to process datasets consistently and rapidly. The automated model starts by taking file inputs for mean fractional block and for raw time constant data, using the pandas package to load and structure the data by index. At the start is the option to specify initiation and fixing of values for certain parameters of the global fitting later: for example, binding energy and Hill coefficient. This is crucial when swapping between native AGs and GTTR, as they have vastly different fitting parameters. There is also the option to set the fixed parameters to calculate the entry rate through channel in the final stages, such as number of channels per cell, concentration of drug, resting open probability, and temperature.

Curve fitting of the data is done using the scipy function curve_fit *(Virtanen et al., 2020)*. This function performs a least-squares minimisation using the Levenberg-Marquardt algorithm. It takes initiation values and bounds for each fitting parameter. When first running a dataset, these values are estimated from the literature or from previous datasets and then manually adjusted according to the results to produce the best fit. For example, the binding energy for gentamicin was originally estimated to be about -10 kT based off previous results for DHS *(Marcotti et al., 2005)*. This proved very similar to the final result, and further adjustments did not affect the fit. By contrast, the initiation value for the binding energy of kanamycin was adjusted to -5 kT to produce the best fit. Similarly, the parameter bounds are set to encompass the potential fit values by a wide margin.

The first calculation is fitting the dose response curves (eq. 3). The script loops through each voltage in the index of the dataset and fits the Hill equation at each voltage, appending the

values for the half-blocking concentration (K_D) and the Hill coefficient (n_H) each to a list. The script then does a global fit of the two barrier-one binding site model to the entire fractional block dataset with two dependent variables: voltage and concentration (eq. 4). The next calculation is fitting a linear regression through the time constant data (eq. 5). The slope from this fit (k_1) is returned, as this corresponds to the rate over the first energy barrier later in the modelling process.

The final stage is generating the energy profile and entry rates using the fitting results. First, constants are defined such as the Boltzmann constant and the proportionality constant for the first order rate constant. Then, the MET channel permeation model is given 13 parameters (the values of which are either specified constants or from the fits) and returns the following: entry rate, potential of maximum block (V_0), first and second energy barriers (E_1 and E_2), both reverse constants (k_{-1} and k_{-2}), and the time constant over the second energy barrier (k_2) (eq. 6-15). These values are used to plot the energy profiles and entry rate graphs.

Sample scripts and datasets are available in GitHub repository (https://github.com/Xenothy/METchannelpermeationVM). Figures were made using OriginPro 2019 or Matplotlib 3.2.1 and edited in Adobe Photoshop CC 2019. All errors quoted and figure error bars are 95% confidence intervals. The confidence intervals are reported in the text and tables as a point estimate ± the margin of error.

Chapter 3

Comparing the Permeation Properties of Three Clinically Relevant Aminoglycosides through the MET Channel

3.1 Introduction

Gentamicin, kanamycin and amikacin (**figure 3-1**) are used for a wide range of antibacterial treatments, and all three of these AGs can cause hearing loss, tinnitus, and/or vestibular disfunction. AGs do not take up very well in the GI tract and are generally administered systemically or topically *(Kushner et al., 2016)*. It is difficult to determine the dosage of AGs that will lead to hearing loss *(Kushner et al., 2016)*, probably due to variation in how effectively they will enter the endolymphatic space of the inner ear *(Li and Steyger, 2011)*. It is thought that administering AGs in larger doses less frequently may reduce incidence ototoxicity, and this dosing does not detrimentally impact treatment effectivity *(Kushner et al., 2016; Krause et al., 2016)*.

These three members of the AG family also have vastly different levels of toxicity to hair cells *in vitro* when given at the same concentration (**figure 3-10**), as has been previously suggested *(Kotecha and Richardson, 1994)*. The reason for these differences is at present unclear. AGs clearly enter the hair cell primarily through the MET channel as any manipulation that reduces or abolishes mechanotransduction prevents AG ototoxicity *in vitro* (*Gale et al., 2001; Marcotti et al., 2005; Owens et al., 2009; Kawashima et al., 2011; Alharezneh et al. 2011; Kenyon et al., 2017; O'Reilly et al., 2019; Kitcher et al., 2019)*. Entry via endocytosis at the cell membrane is also reported but is thought not to overwhelm the cell as entry is slower than via the MET channels and the drugs are already within compartments for degradation *(Hailey et al., 2017)*. Furthermore, it is widely reported that basal OHCs are more sensitive to AG ototoxicity than apical cells even in culture. I have therefore compared the permeation properties of gentamicin, kanamycin, and amikacin in both apical and basal OHCs to determine whether differences in toxicity may be related to permeation rate through the MET channel.

Gentamicin is given in clinic as a mix of several isoforms and there is indication that some isoforms are more ototoxic than others *(O'Sullivan et al., 2020)*. The gentamicin used in this experiment was a mixture of the 3 major C isoforms, C_1 (45%), C_{1a} (35%), and C_2 (30%) with an approximate molecular weight of 463.6 g/mol. The kanamycin was kanamycin A, which is the most commonly used variant and has a molecular weight of 484.5 g/mol. Amikacin is a derivative of kanamycin A and has a molecular weight of 585.6 g/mol. It is worth noting that the results previously published for dihydrostreptomycin (DHS) by Marcotti et al. in 2005 and in Van Netten & Kros 2007 were obtained under slightly different conditions (i.e. age and strain of mice, location along the coil), and thus may not be directly comparable to the results here. In this present study, the conditions were kept constant for every drug to minimise variability in results.

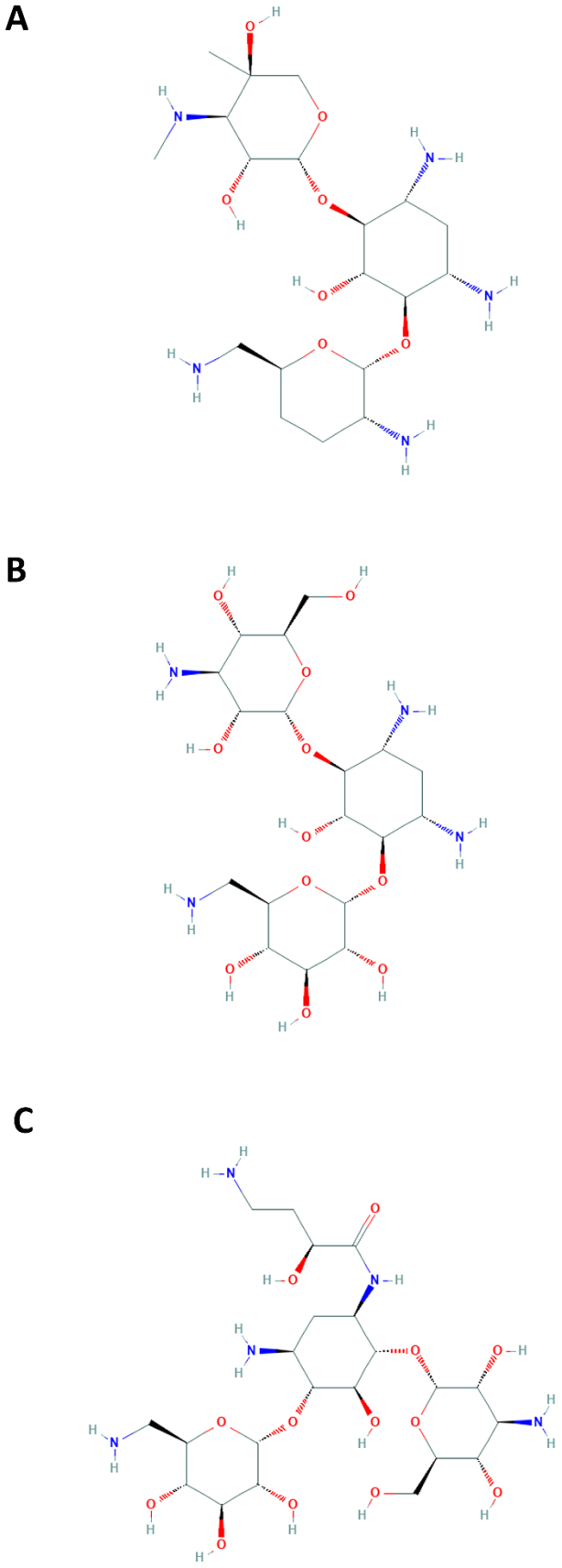

FIGURE 3-1: Molecular structures of three aminoglycosides. (A) gentamicin C1, (B) kanamycin A, and (C) amikacin. Structures from PubChem.

3.2 Results

This chapter includes data recorded from 71 apical OHCs and 72 basal OHCs of P2+1 and P2+2 cultured CD-1 wild type mouse cochleae. The average MET current size at -164 mV was -1.11 ± 0.003 nA in the apex, and -1.56 ± 0.004 nA in the base. The average resting MET current at -164 mV was 5.6% of the maximum in both the apex and base. This is smaller than the usually reported values of 10 to 50% (*Farris et al., 2006; Beurg et al., 2010),* possibly due to the negative pressure kept in the fluid jet which slightly pulls on the hair bundle, slackening the tip links and lowering the open probability. The largest MET current recorded was -2.29 nA in the apex, and -2.44 nA in the base. Average cell capacitance was 5.36 ± 0.01 pF in the apex and 5.03 ± 0.01 pF in the base, and average access resistance was 6.19 ± 0.02 MΩ. Permeation modelling was done at -55 mV and 25°C to match the approximate driving force on cells in experimental conditions. All modelling results are presented for a single open channel, thus with an open probability of 1.

3.2.1 Block of MET current by three aminoglycosides

All three AGs block MET channel currents in a generally similar manner to that reported for DHS by Marcotti et al. in 2005. **Figure 3-2** shows examples of MET currents during control superfusion and during exposure to 30 μM of each AG, recorded as described in sections 2.2.3 and 2.3. The outward currents at depolarising voltages are unaffected, but when the cell is hyperpolarised in the presence of each AG the large inward MET currents are strongly blocked. AGs could be quickly and fully washed out to recover full MET currents, as shown in **figure 2-4**. A comparison of the fractional block curves—calculated as described in section 2.3—at 30 μM of each AG is shown in **figure 3-3**. All fractional block curves at each concentration and for each AG and coil are shown in **figure 3-4**. **Figure 3-5** shows dose response curves at each voltage fitted with the Hill equation as described in section 2.4.1. The results of this fit are shown in **figure 3-6**.

At the most negative membrane potentials a relief in block of the MET current was seen for all three drugs, indicating permeation of the drugs through the channel. The half-blocking concentrations (K_D) varied significantly between drugs but were similar between apex and base. For all drugs, the K_D increased dramatically and became meaningless at potentials above -24 mV as the drugs do not bind to the channel. These results are shown in **Table 3-1**. The Hill coefficient for all three drugs was approximately 1 in both apex and base and was therefore set to 1 in the two-barrier one-binding site model.

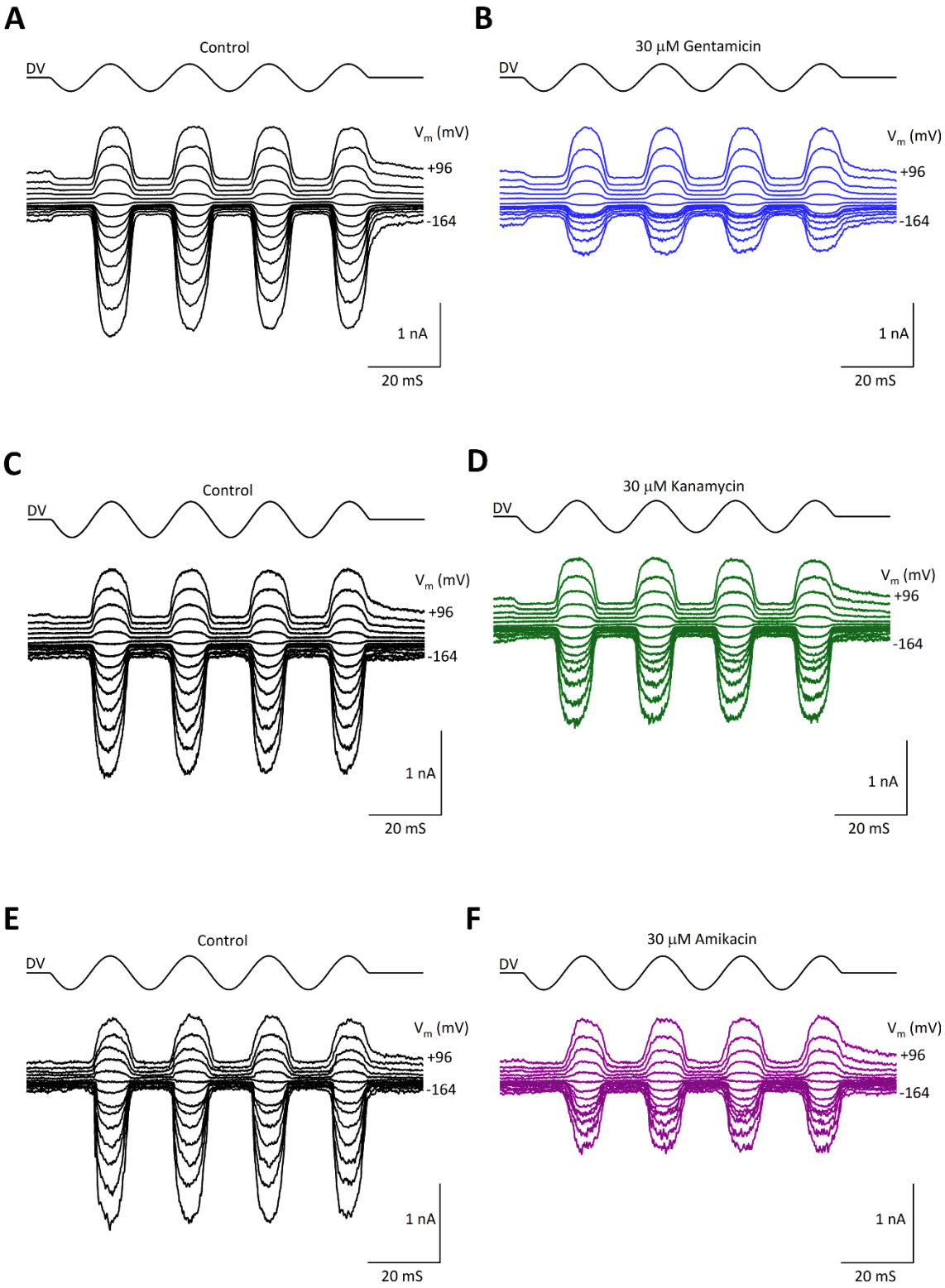

FIGURE 3-2: Examples of MET currents in basal OHCs before and during aminoglycoside superfusion. (A and B) Gentamicin, (C and D) Kanamycin, (E and F) Amikacin.

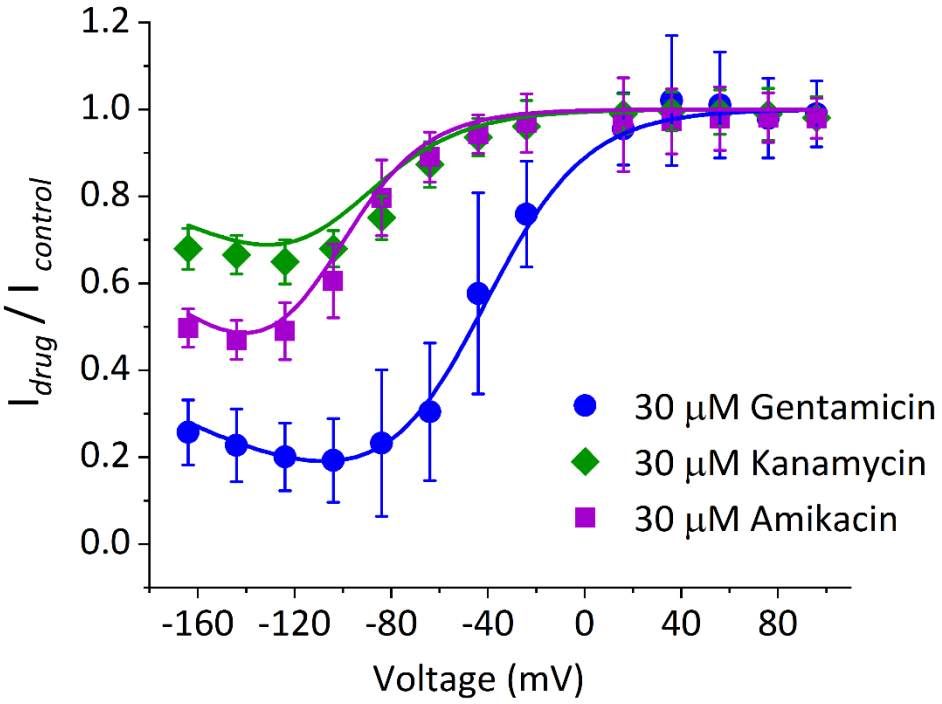

FIGURE 3-3: Comparison of fractional block by 30 µM of three aminoglycosides in basal OHCs. Number of cells per drug: gentamicin, n = 6; kanamycin, n = 9; amikacin, n = 8.

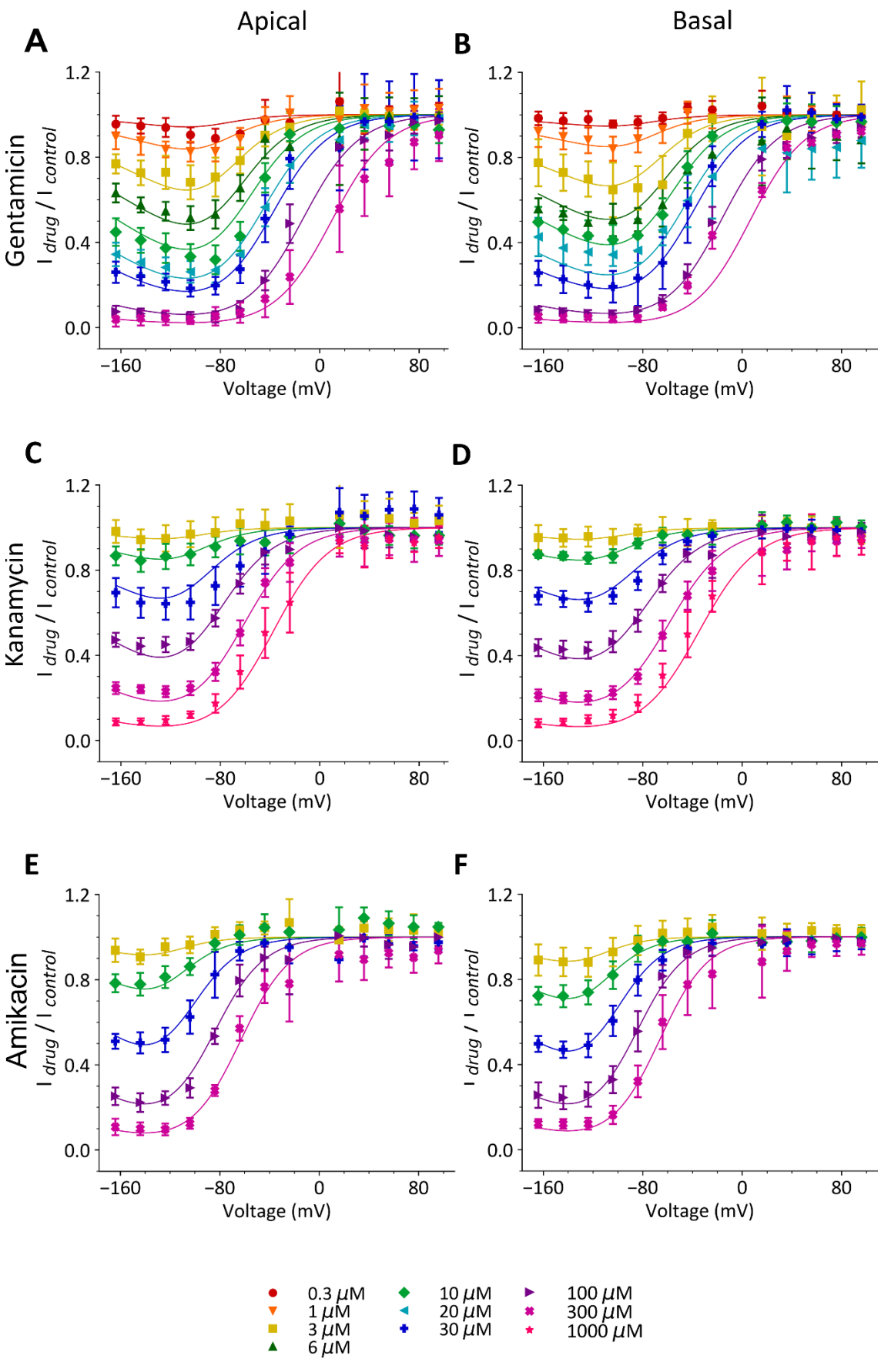
Apical
Basal
A
B
C
D
E
F
Gentamicin
Kanamycin
Amikacin
I drug / I control
Voltage (mV)
1.2
0.8
0.4
0.0
−160
−80
0
80
0.3 μM
1 μM
3 μM
6 μM
10 μM
20 μM
30 μM
100 μM
300 μM
1000 μM

FIGURE 3-4: Fractional block curves for three aminoglycosides in apical and basal OHCs. The number of cells per location at each concentration is: (A) Gentamicin, apical OHCs: 0.3 μM, n = 5; 1 μM, n = 5; 3 μM, n = 6; 6 μM, n = 10; 10 μM, n = 7; 20 μM, n = 6; 30 μM, n = 6; 100 μM, n = 10; 300 μM, n = 5. (B) Gentamicin, basal OHCs: 0.3 μM, n = 4; 1 μM, n = 5; 3 μM, n = 5; 6 μM, n = 8; 10 μM, n = 7; 20 μM, n = 6; 30 μM, n = 6; 100 μM, n = 10; 300 μM, n = 4. (C) Kanamycin, apical OHCs: 3 μM, n = 10; 10 μM, n = 6; 30 μM, n = 9; 100 μM, n = 6; 300 μM, n = 9; 1000 μM, n = 9. (D) Kanamycin, basal OHCs: 3 μM, n = 4; 10 μM, n = 10; 30 μM, n = 9; 100 μM, n = 5; 300 μM, n = 4; 1000 μM, n = 5. (E) Amikacin, apical OHCs: 3 μM, n = 6; 10 μM, n = 7; 30 μM, n = 7; 100 μM, n = 5; 300 μM, n = 5. (F) Amikacin, basal OHCs: 3 μM, n = 8; 10 μM, n = 8; 30 μM, n = 8; 100 μM, n = 5; 300 μM, n = 5.

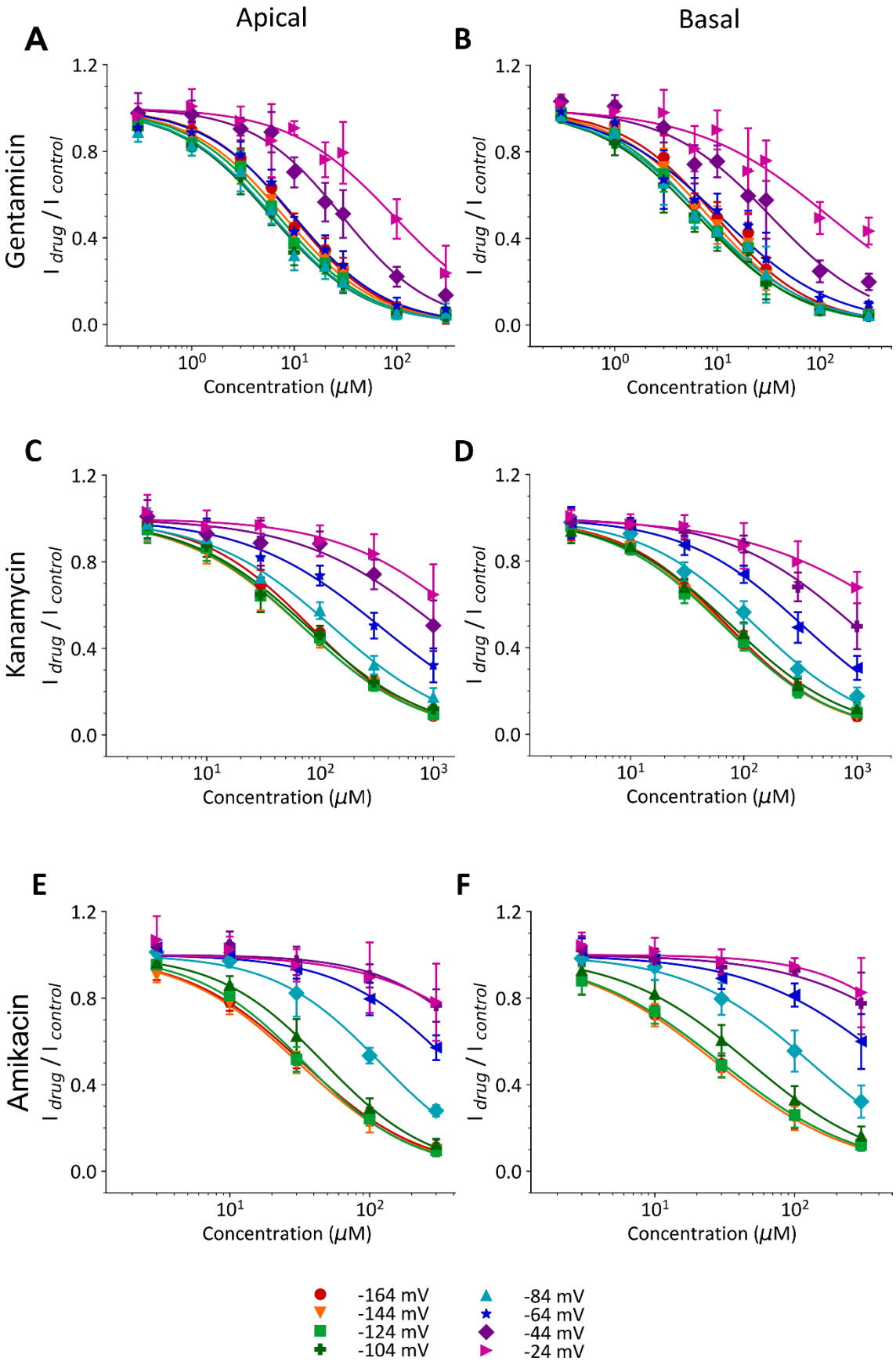

FIGURE 3-5: Dose response curves for three amingolycosides in apical and basal OHCs. Number of cells as in **figure 3-3**.

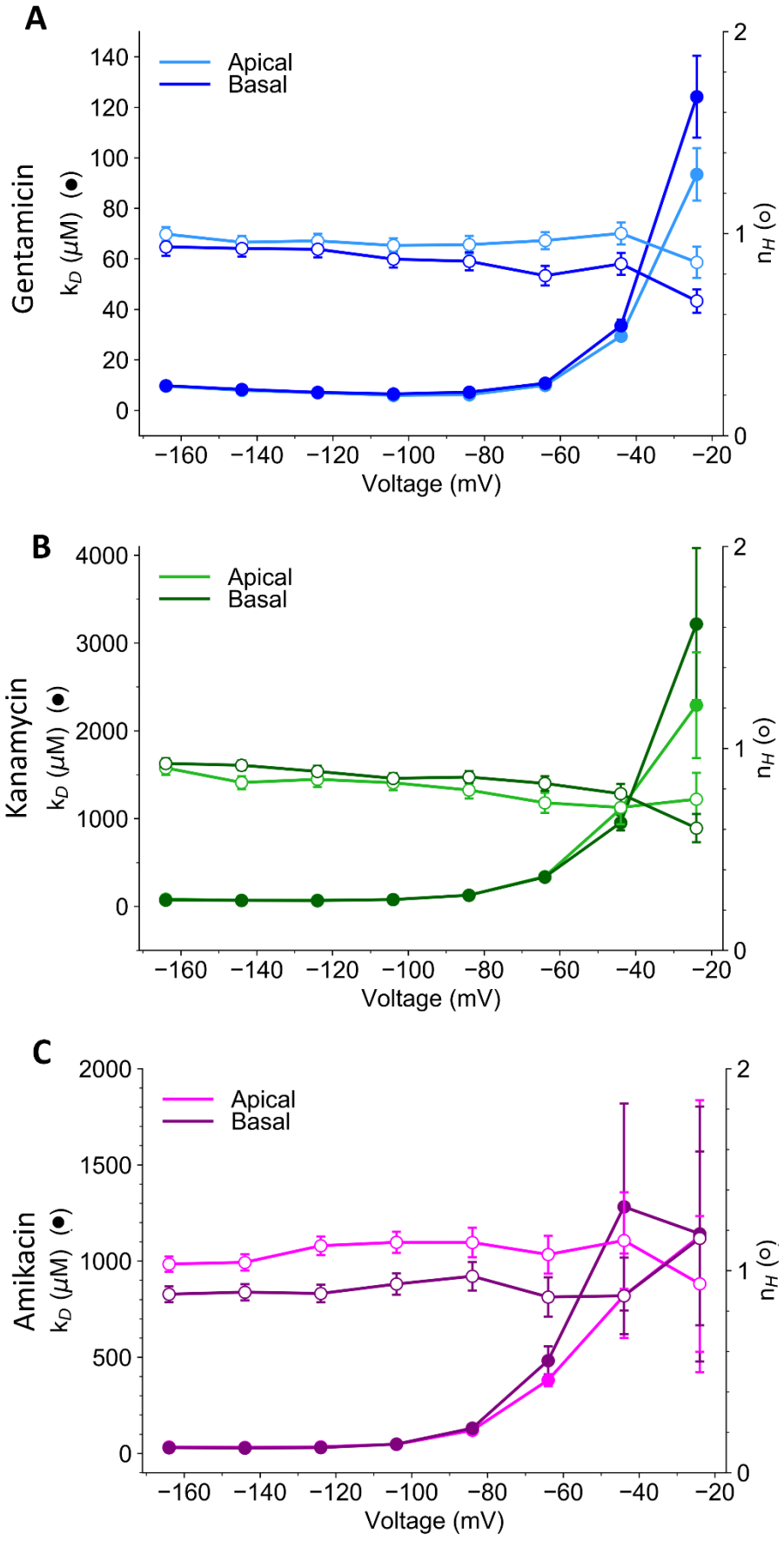

FIGURE 3-6: Voltage dependence of block of MET channel by three aminoglycosides. Calculated by fitting dose response curves with Hill equation.

	GENTAMICIN		KANAMYCIN		AMIKACIN	
	Apical	Basal	Apical	Basal	Apical	Basal
V_{max} (mV)	-104	-104	-124	-124	-144	-144
K_D (μM)	5.92 ± 0.22	6.52 ± 0.32	69.64 ± 3.52	66.57 ± 2.5	31.1 ± 1.19	27.72 ± 1.34

TABLE 3-1: Maximum block measured for three aminoglycosides

3.2.2 Kinetics of aminoglycoside block

The temporal kinetics of the block by all three AGs was assessed in both apical and basal OHCs as described in the section 2.3. These results are shown in **figure 3-7**. The average time constant of full block upon channel opening at 10 μM for gentamicin was 0.50 ± 0.18 ms (n = 6) in basal OHCs, which was similar to that previously described for DHS *(Marcotti et al., 2005)*. Amikacin was faster but still relatively similar, with a time constant of 0.33 ± 0.19 ms (n = 3). The time constant for kanamycin however was much faster than either gentamicin or amikacin, at 0.03 ± 0.01 ms (n = 9). The slope of each dataset was measured, and this equals k_1 in **table 3-2**.

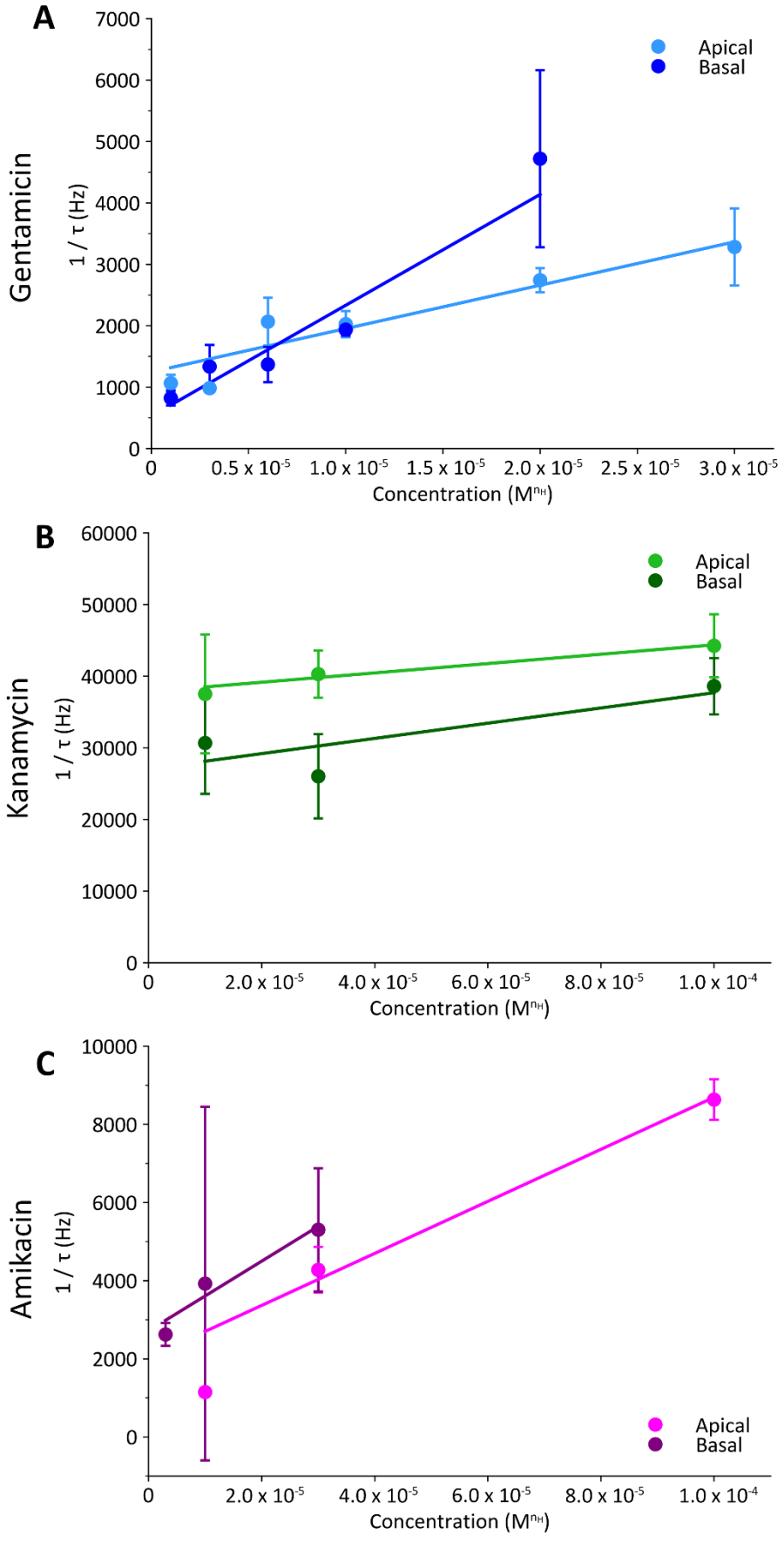
A
Gentamicin
1 / τ (Hz)
Concentration (M^nH)
Apical
Basal
B
Kanamycin
1 / τ (Hz)
Concentration (M^nH)
Apical
Basal
C
Amikacin
1 / τ (Hz)
Concentration (M^nH)
Apical
Basal

FIGURE 3-7: Results of fitted time constants for three aminoglycosides in apical and basal OHCs per concentration. The number of measurements per concentration at each location is: (A) Gentamicin, apical OHCs: 1 µM, n = 3; 3 µM, n = 3; 6 µM, n = 5; 10 µM, n = 6; 20 µM, n = 5; 30 µM, n = 8. Gentamicin, basal OHCs: 1 µM, n = 5; 3 µM, n = 5; 6 µM, n = 3; 10 µM, n = 6; 20 µM, n = 2. (B) Kanamycin, apical OHCs: 10 µM, n = 2; 30 µM, n = 5; 100 µM, n = 7. Kanamycin, basal OHCs: 10 µM, n = 9; 30 µM, n = 7; 100 µM, n = 5. (C) Amikacin, apical OHCs: 10 µM, n = 1; 30 µM, n = 8; 100 µM, n = 8. Amikacin, basal OHCs: 3 µM, n = 2; 10 µM, n = 3; 30 µM, n = 3.

3.2.3 Modelling results

Fitting the fractional block curves with the two-barrier one-binding site model resulted in good fits as shown in **figure 3-4**. These fits, as well as the fits of the time constant data produced values describing the MET channel permeation pathway which are summarised in **table 3-2**. 95% confidence intervals are reported for parameters obtained from fitting the data. The remaining parameters are calculated as described in section 2.4.2. Data for the highest concentrations was more variable due to difficulties in acquiring stable recordings from such small currents. But excluding these points from the modelling only slightly affected the results so they were included. The apparent charge of the molecule with respect to the channel was approximately 1.5-1.6 for gentamicin and kanamycin and was slightly higher for amikacin at 1.7 in the apex and 1.8 in the base. The confidence intervals on these charges dictate that these differences are not significantly different from each other. The relative position and strength of the binding site within the pore are given by δ_b and E_b, and the values for the energy barriers at the entrance and exit are given by E_1 and E_2 which are calculated from k_1 and ΔE. Using these values, energy profiles can be constructed that describe the relative position and strength of interaction of sites within the permeation pathway. These are shown comparing apex and base in **figure 3-8** and comparing drugs in **figure 3-11**.

3.2.4 Energy profiles and entry rates vary as a function of position along the cochlea

The energy profiles show similar patterns between apex and base. For gentamicin and kanamycin, the apex had higher energy barriers at both the entrance and exit. For gentamicin and amikacin, the binding site position was shifted slightly towards the extracellular side in the apex. These parameters are closely linked to each other in the fitting process. Both the higher energy barriers and the shift in binding site will contribute to differences in entry rate, and it seems that in the model, each drug has its signature profile of how this difference is achieved. The entry rates for all three drugs saturated about 1.5-3 times lower in the apex than in the base. Interestingly, the entry rate for kanamycin in both the apex and base ultimately saturated at a much higher level than the other two drugs, which is likely due to its higher half-blocking concentration and faster time constants. This can be conceptualised as the drug interacting less with the channel as it passes through, thus both reducing its affinity at lower concentrations and then at higher concentrations making it more susceptible to the chemical driving force pushing it into the cell.

	GENTAMICIN		KANAMYCIN		AMIKACIN	
	Apical	Basal	Apical	Basal	Apical	Basal
n_H	1	1	1	1	1	1
k_1 (s^{-1} $(M^{nH})^{-1}$	7.06e7 ± 3.76e3	1.81e8 ± 5.26e2	6.53e7 ± 3.75e4	1.06e8 ± 2.7e4	6.66e7 ± 2.03e3	8.91e7 ± 2.72e3
δb	0.74 ± 0.07	0.78 ± 0.08	0.74 ± 0.15	0.77 ± 0.12	0.74 ± 0.18	0.76 ± 0.17
E_b (kT)	-8.50 ± 0.60	-8.34 ± 0.64	-5.12 ± 0.56	-5.29 ± 0.41	-5.08 ± 0.73	-4.57 ± 0.72
Apparent charge	1.58 ± 0.12	1.55 ± 0.12	1.59 ± 0.22	1.50 ± 0.15	1.69 ± 0.28	1.79 ± 0.25
ΔE (kT)	5.39 ± 0.75	5.177 ± 0.76	6.77 ±1.59	6.34 ± 1.1	8.17 ± 2.08	8.54 ± 1.88
E1 (kT)	11.38	10.44	11.46	10.97	11.44	11.15
E2 (kT)	16.77	15.62	18.23	17.32	19.61	19.69
V_0 (mV)	-105.6	-106.65	-126.87	-129.81	-139.32	-139.22
Entry at 1 uM (molecules/s)	7.85	23.32	2.16	4.36	0.70	0.79
Entry at 100 uM (molecules/s)	130.04	416.49	179.75	358.38	57.23	67.34
Half entry rate (molecules/s)	77.13	250.94	530.17	985.6	150.62	228.36
Half entry concentration (μM)	18.61	20.51	488.01	448.41	425.01	575.51

TABLE 3-2: Model results for three aminoglycosides in apical and basal OHCs.

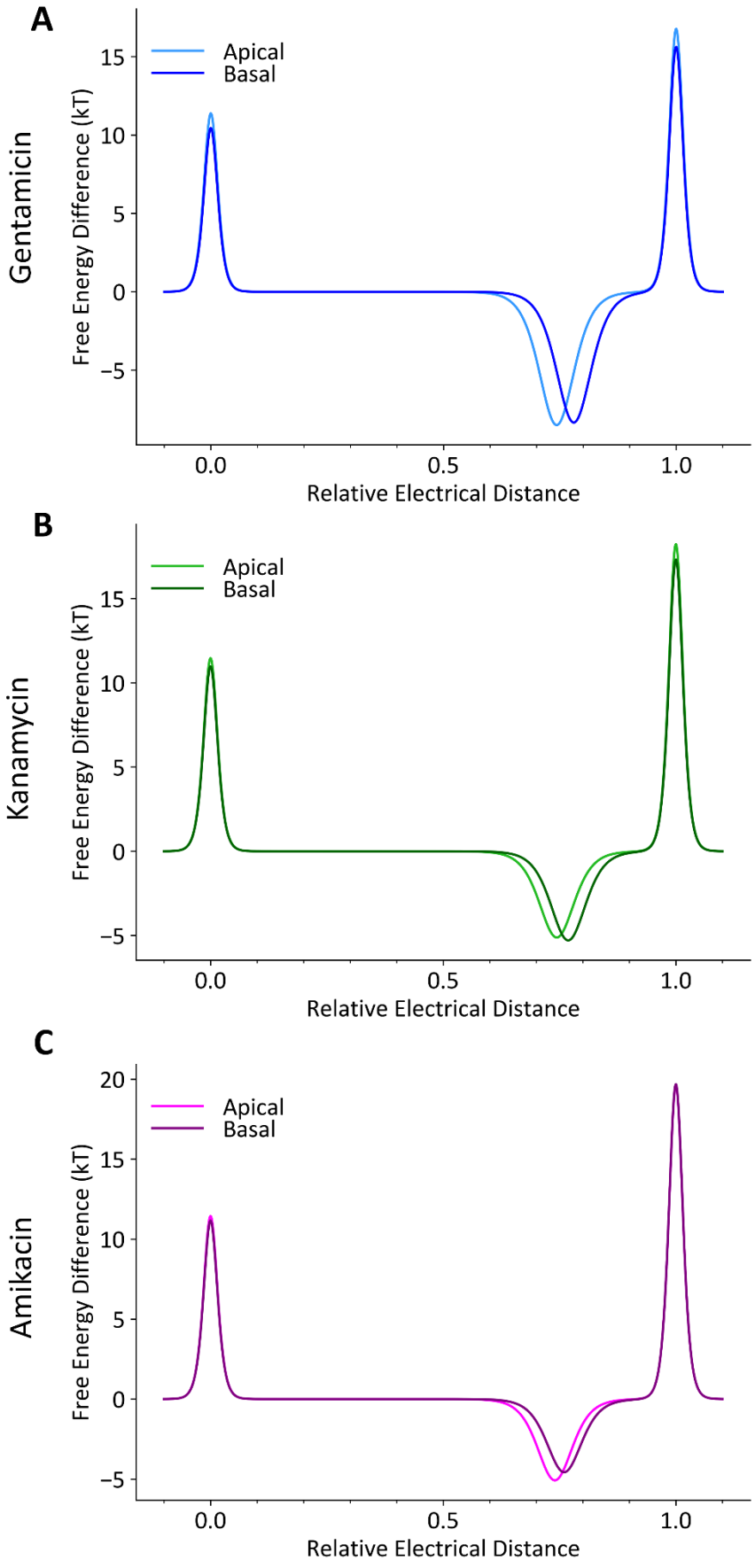

FIGURE 3-8: Energy profiles of interaction between three aminoglycosides and the MET channel in apical and basal OHCs.

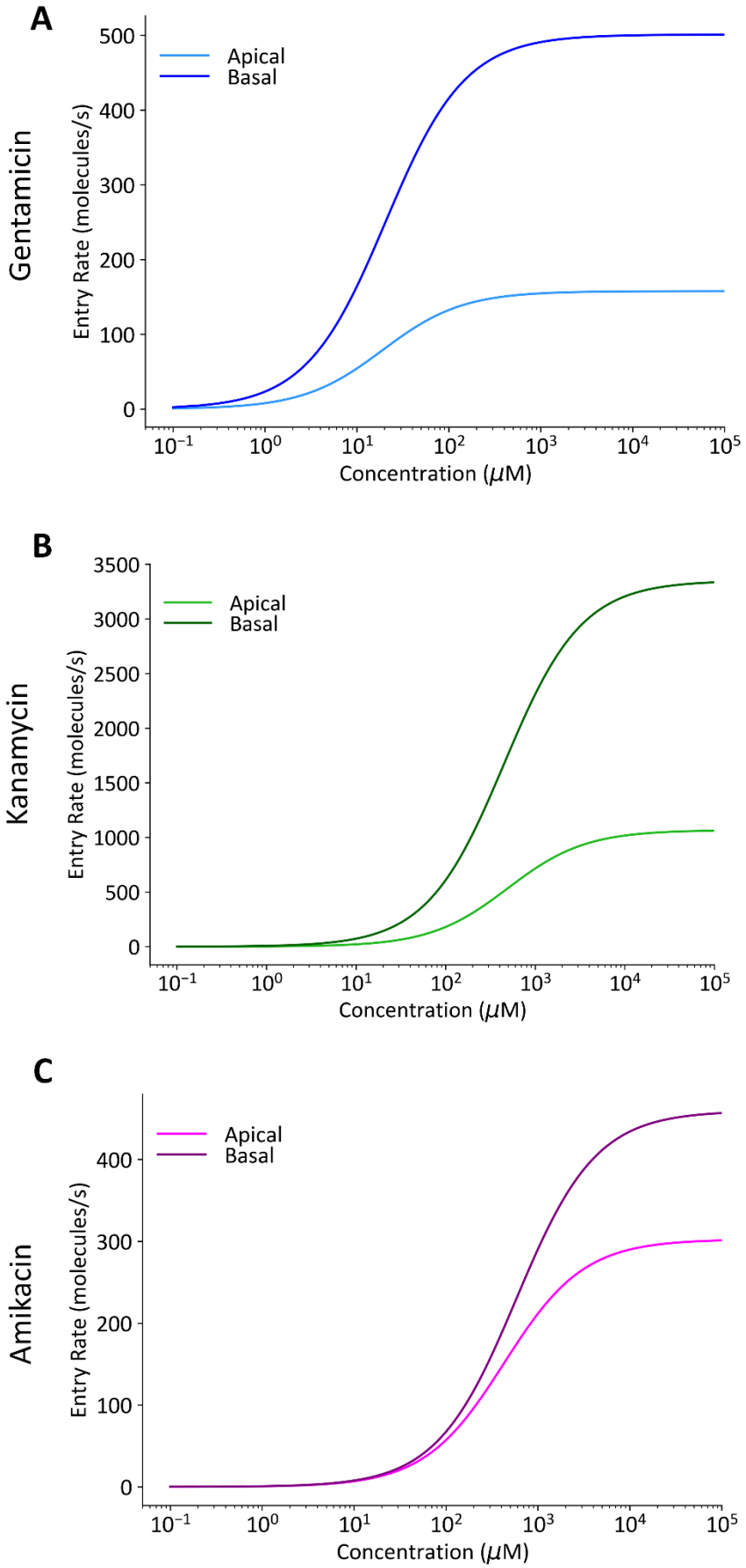

FIGURE 3-9: Predicted entry rates of three aminoglycosides through individual open MET channels in apical and basal OHCs at -55mV.

3.2.5 Entry rates of the three aminoglycosides match their toxicity

The comparative toxicity of gentamicin, kanamycin and amikacin in the basal turn of the neonatal cochlea was assessed. These experiments were performed by Ms. Cynthia Smith, and the relevant results shown in **figure 3-10** were compiled by Dr. Richard Osgood. P2 cochlear cultures were incubated with varying concentrations of each AG for 48 hours, then fixed in 3.7% formaldehyde, permeabilised in 0.1% Triton X-100 and stained with Texas Red phalloidin and Rabbit α-myosin VIIa, with a secondary stain of Alexa Fluor 488 Goat α Rabbit. Panels A-F of **figure 3-10** show examples of basal OHCs at 30 μM of each AG. The remaining hair cells in fixed basal regions of interest (ROIs) were counted. These results are quantified in panel G of **figure 3-10**. The LD_{50} (determined by counting the number of OHCs that had both a cell body and a hair bundle) for gentamicin was 2 μM, 36.1 μM for kanamycin, and 167.1 μM for amikacin.

The entry rates (shown in panel B of **figure 3-11**) of all three drugs matched their relative toxicity in basal OHCs, with gentamicin being the most readily permeable, and amikacin the least. The LD_{50} concentrations and their matching entry rate are indicated as lines on panel B. This pattern is also reflected in the energy profiles (**figure 3-11**, panel A), which showed a similar staggering of strength at both the binding site and at the second energy barrier. Interestingly, the height of the first energy barrier was very similar for all three drugs.

As mentioned, at high concentrations the relatively weaker affinity of kanamycin for the MET channel forces much higher concentrations of it through the pore and into the cell. However, over the concentrations that are relevant for the toxicity assays, its entry rate sits in between gentamicin and amikacin (**figure 3-11**). Additionally, the concentration at which the entry rate for kanamycin overtakes gentamicin (~5.5 μM) is almost three times above the LD_{50} of gentamicin, so OHCs exposed to this concentration of gentamicin would certainly be dead and a difference in toxicity would not be evident.

Entry rate in basal OHCs of gentamicin saturated at 500 molecules per second per channel, 1900 for kanamycin, and 430 for amikacin.

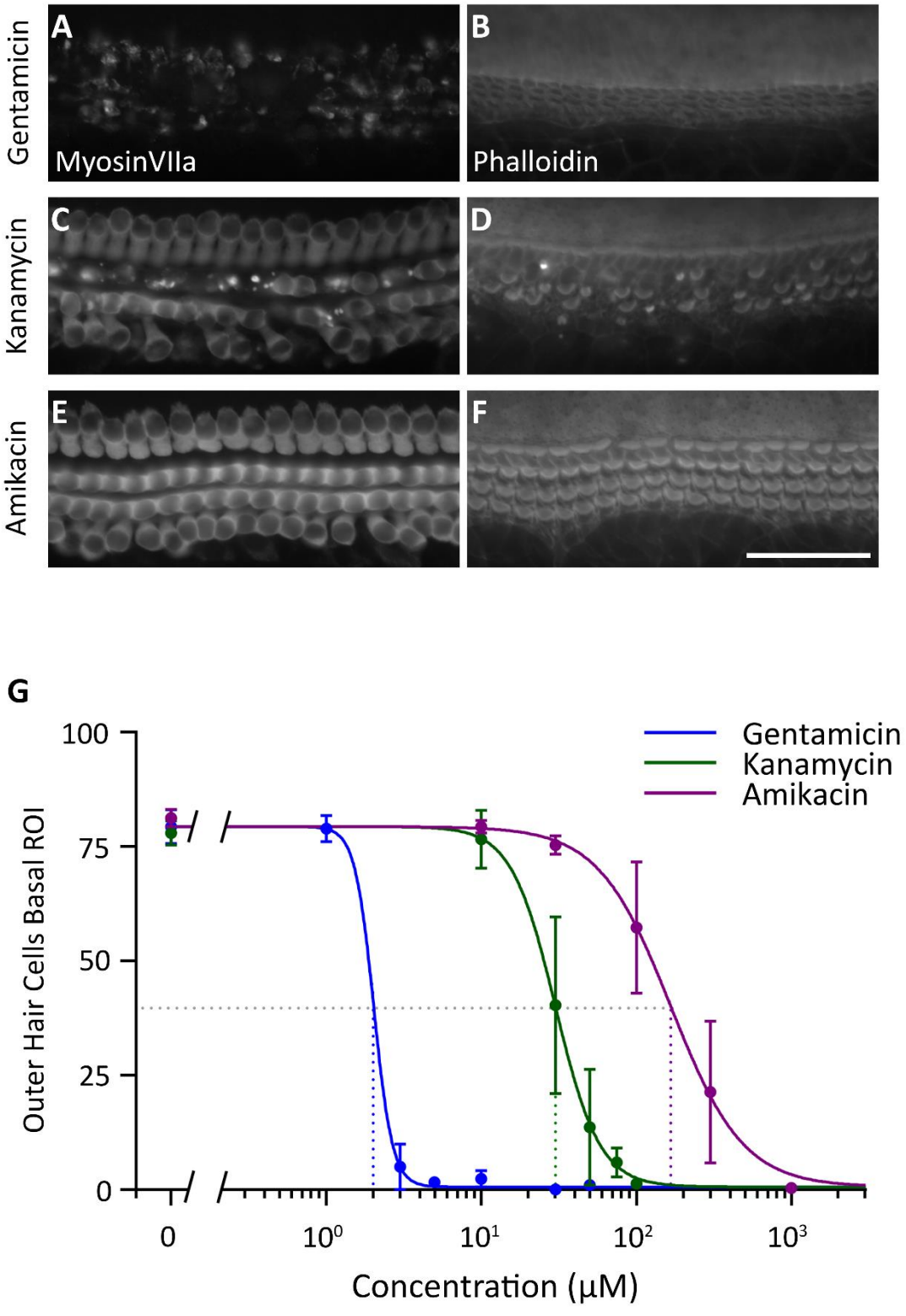

FIGURE 3-10: Toxicity of three aminoglycosides in basal OHCs. (A-F) 24 h incudbation with 30 μM of each AG leads to widely different levels of ototoxicity. (G) Quanitifcation of hair cell death in basal OHCs for gentamicin, kanamycin and amikacin. Dotted lines indicate the LD_{50}s, which were: gentamicin, 2 μM; kanamycin, 36.1 μM; amikacin, 167.1 μM. Data obtained by Ms. Cynthia Smith, and figures compiled by Dr. Richard Osgood.

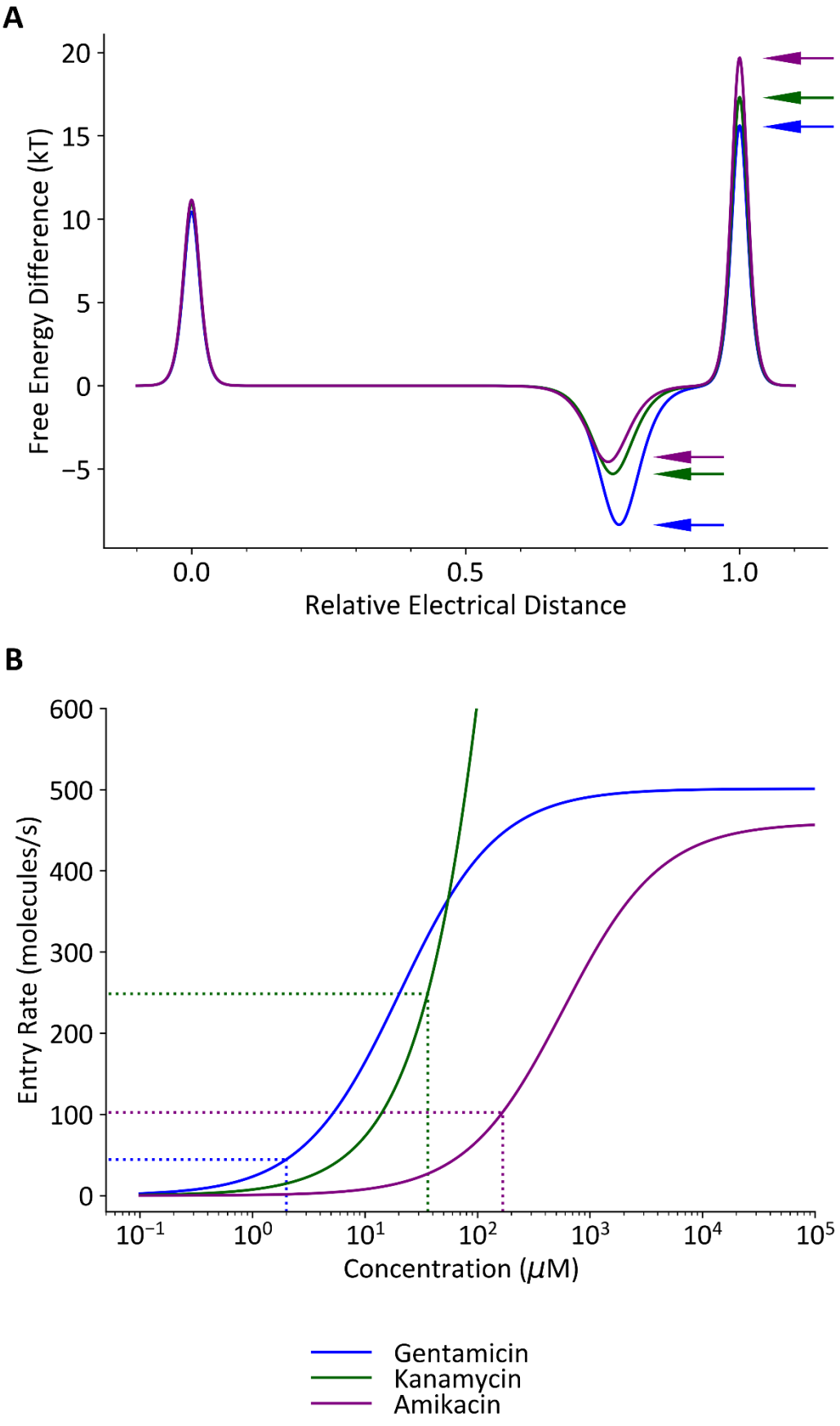

FIGURE 3-11: Comparison of energy profiles and entry rates of three aminoglycosides in basal OHCs. Arrows in (A) indicate the ranking of permeation parameters for the three AGs. Dotted lines in (B) indicate the LD_{50}s of each drug shown in **figure 3-10**.

3.3 Discussion

3.3.1 What leads to the differences in permeation between apex and base?

As discussed in section 1.2.5, there are many differences in the properties of the MET channel between neonatal apical and basal OHCs, the main ones being its number per cell, conductance, and genetic composition. The results presented in this study were modelled for entry through an individual open MET channel, thus controlling for a difference in channel number. *In vitro* and *in vivo*, an excess of channels in basal OHCs would further increase the differences in permeation between the two locations. But the relationship between channel conductance and drug permeation in these data is not immediately obvious.

Because this experiment was not designed to address questions of TMC1 versus TMC2 but to relate AG entry to ototoxicity in cochlear cultures at the same stage of development, these results were obtained in wild type mice with uncontrolled levels of TMC1 and TMC2 in each coil. Thus, the present study can make no conclusions on the roles of TMC1 and TMC2 in the differences found in channel topology and permeation of aminoglycosides in the apex and base. However, it is worth noting that a previous study found that apical cells of *Tmc2*$^{-/-}$ (thus expressing TMC1 only) had a reduced permeation of DHS compared to wild types *(Corns et al., 2016)*. Another study found a higher calcium permeability for TMC2 versus TMC1 *(Goldring et al., 2019)*, which is likely to be a closely related mechanism to the permeation of the polycationic AGs. According to previously published results, it is expected that at this stage the apex will express almost entirely TMC2 and the base will express mostly TMC1 *(Beurg et all., 2018)*. Thus, a difference in permeation between TMC1 and TMC2 alone is not sufficient to explain the differences in permeation between apex and base for each drug presented here.

Perhaps these results are indicative of two simultaneous gradients: as TMC1 has a higher conductance in the base than the apex *(Beurg et al., 2018)*, TMC1 that is present in the base at this age must already have a higher permeability than TMC2 that is present in the apex. This suggests that the machinery setting up the gradient in single-channel conductance in OHCs along the cochlea is already present in the base in the early stages of TMC1 expression. Furthermore, though the energy profile is not a physical map of the channel, it describes its electrical topology and could be related to its shape and size. In this case, the differences noted in the height of the energy barriers and position and strength of the binding site could be indicative of differences between the pore topology of TMC1 and TMC2. This subject will be revisited in chapter 8 following the presentation of further data.

3.3.2 What leads to the differences in permeation between the three drugs?

It is at present unclear what causes these large differences in permeation between AGs. The Hill coefficient for each AG was close to 1 in both apex and base, so it can be safely concluded that gentamicin, kanamycin, and amikacin all bind non-cooperatively to a single binding site within the MET channel pore as was reported for DHS *(Marcotti et al, 2005, Corns et al., 2016)*. Therefore, understanding the differences in permeation rates for each drug requires examining the factors that contribute to them and how they differ.

As it is likely that the positive charges on the AGs are what allow them to permeate through the channel, a difference in charge interacting with the channel pore could explain differences in permeation rate. At a pH of 7.4, the electrical charges of gentamicin, kanamycin, and amikacin were measured by NMR spectroscopy to be 3.3, 2.4 and 2.8 respectively *(Al Khzem, 2019)*. These do not appear to match the charges fit from the MET channel data here reported (approximately 1.5 for gentamicin and kanamycin, and 1.75 for amikacin, though confidence intervals suggest these differences are non-significant), suggesting that the MET channel is only interacting with certain charges (perhaps even the equivalent charge point on each of the molecules), and not in a pattern consistent with either their entry rate or their measured charges. Furthermore, the charge of the molecules alone is not enough to account for the differences in permeation as fixing the charges to either 1.5 or 2 for all drugs did not drastically impact the entry rates.

Perhaps a size restriction of the width of the molecules fitting through pore could explain the differential permeation. As previously discussed, the diameter of the narrowest part of the channel pore was determined to be ~12.5-15 Å *(Farris et al., 2004; Alharazneh et al., 2011)*, but has recently been found to be potentially much larger *(Desmonds, 2015; Ballesteros et al., 2018)*. Gentamicin, kanamycin, and amikacin are predicted to have maximum widths of approximately 9.6 Å, 5.0 Å, and 8.0 Å, respectively. The size of the channel pore is therefore comfortably wider than even the largest AG studied, gentamicin, so it is unintuitive that differences in permeation are due only to a physical constraint. Furthermore, the difference in toxicity does not seem to correlate with the maximum width of each molecule, especially given the relatively small width of kanamycin. This small width does however possibly reflect the ability of kanamycin to pass through the pore with reduced resistance as evidenced by its higher saturation point than the other two AGs. The toxicity of the three AGs and their entry rates does match their ranking of molecular weights (see section 3.1), so it is therefore likely to be a combination of physical and biochemical factors that leads to differential permeation.

The energy profiles give an interesting perspective on how the drugs are interacting with the channel as they permeate. The k_1 (rate over the first energy barrier) and E_b (binding energy) decrease and the ΔE increases in accordance with toxicity for the three drugs. The relatively small differences in k_1 are counterintuitive because of the large differences in temporal kinetics between the three AGs (especially for kanamycin, which had much faster kinetics than either gentamicin or amikacin as shown in **figure 2-6** and **figure 3-7**). But despite this, k_1 varies only minimally between the three drugs, thus producing similar values for the first energy barrier (E_1). While the height of the E_1 only changes minimally, the second energy barrier (E_2) varies in height according to toxicity. E_2 is calculated from E_1 and ΔE, and it appears that its height is reversely proportional to toxicity, perhaps providing more resistance to drugs entering the cell. This indicates that the restriction point leading to differential permeation is at the narrowest part of the pore, the exit. These findings further support the notion that the intracellular side of the pore is the narrowest (**figure 1-9**) *(van Netten and Kros, 2007; Corns et al., 2016)* and that differences in permeation of AGs could be related to their size and shape.

3.3.3 Implications of variation in permeation for ototoxicity and otoprotection

As the entry rates matched the toxicity differences both between drugs and between the apex and base, this indicates that the MET channel serves both as the primary entry route, and in a sense as the rate-limiting factor on ototoxicity. This strongly supports the effort to find otoprotectants that are reversible, ideally non-permeant, MET channel blockers.

Of course, these results do not exclude the possibility that once inside the cell the AGs still enact varying intracellular pathways to cell death. The fact that the LD_{50} lines in panel B of **figure 3-11** do not match consistently with entry rate suggests that indeed there could be other additional factors contributing to differences in toxicity. It is perfectly reasonable to think that if these drugs are permeating differently through the MET channel, they may also for example permeate at different rates through mitochondrial membrane channels. Nevertheless, it is only logical that such large differences in permeation between AGs will lead to differences in intracellular AG concentration and therefore contribute to differences in ototoxicity.

3.3.4 Suggestions for future studies

There are many experiments that could further elucidate the relationship between channel permeation and toxicity, and the differences between drug permeation in the apex and the base of the cochlea. These include:

- Using TMC1 and TMC2 knockout mice to tease apart the contributions of each of these to AG permeation in apical and basal OHCs.
- Investigating if the different isoforms of gentamicin, which have varying degrees of ototoxicity *(O'Sullivan et al., 2020)*, also permeate differently through the MET channel.
- As the channel number, temperature, and time in the permeation model can all be controlled, this allows the possibility of predicting the entry rate of AGs *in vitro* over time. Future experiments could use pulses of AGs over cultures for specified times to produce similar amounts of AG entry and check for their ototoxic effects.
- Comparing permeation modelling data with newly available structural models of TMC1 *(Pan et al., 2018; Ballesteros et al., 2018)* could give insight into the molecular correlates of the interaction sites within the channel pore (see chapter 6 for more detail).

Chapter 4

Permeation of Gentamicin-Texas Red through the MET Channel

4.1 Introduction

GTTR is a fluorescently tagged conjugate of gentamicin and Texas Red that is used to visualise uptake of gentamicin into hair cells. Its uptake via the MET channel competes with native gentamicin, thus reducing ototoxicity *in vitro* and *in vivo (Dai and Steyger, 2008; Wang and Steyger, 2009; Wang et al., 2010; Hailey et al., 2017)*. It is the use of GTTR that proved that hair cells required mechanotransduction for ototoxicity *(Alharezneh et al., 2011)*. It has even been used to follow intracellular trafficking routes of gentamicin in hair cells *(Hailey et al., 2017)*. Furthermore, the application of GTTR leads to a visible tonotopic gradient in fluorescent labelling like that found for several other compounds (**figure 4-1**) *(Gale et al., 2001, Desmonds, 2015)*, and similar to the toxicity gradient of native AGs *(Kotecha and Richardson, 1994; Alharezneh et al., 2010; O'Reilly, 2019)*. Much care has been taken to demonstrate the functional use of GTTR as an indicator for gentamicin uptake in hair cells.

Whilst GTTR certainly does seem to permeate through the MET channel, the question remains of how its permeation compares to native gentamicin. The addition of the Texas Red side chain makes it a much larger compound than gentamicin, with a maximum width of approximately 14.7 Å *(Alharazneh et al., 2011)*. According to early estimates of the MET channel pore width it would have been too narrow for GTTR to fit *(Farris et al., 2004)*, but recent studies have shown compounds up to 23 Å to permeate now making GTTR permeation through the channel perfectly feasible *(Ballesteros et al., 2018)*. However, during synthesis the Texas Red molecule binds onto and neutralises one of the potential regions of positive charge on gentamicin (**figure 4-2**). Because these positive charges are thought to contribute to binding of AGs to the channel binding site, this may impact permeation. Furthermore, it is now believed that the permeation pathway is in fact in the shape of a groove that contacts the cell membrane down one side *(Ballesteros et al., 2018)*. This exposure to the hydrophobic tails of membrane phospholipids could interact with the lipophilic portion of the Texas Red molecule attached to gentamicin and affect the permeation profile and entry rate.

To date only preliminary data have been acquired with regards to the electrophysiological interaction of GTTR with the MET channel and its behaviour as a channel blocker. I have therefore done a full permeation characterisation of GTTR in both apical and basal neonatal OHCs to compare it with gentamicin and to see whether the addition of the large, lipophilic Texas Red side chain affects it permeation through the MET channel. GTTR was obtained from Professor Peter Steyger (Creighton University) in dehydrated powder form (synthesised from a mixture of gentamicin isoforms) and made up into individual aliquots as needed.

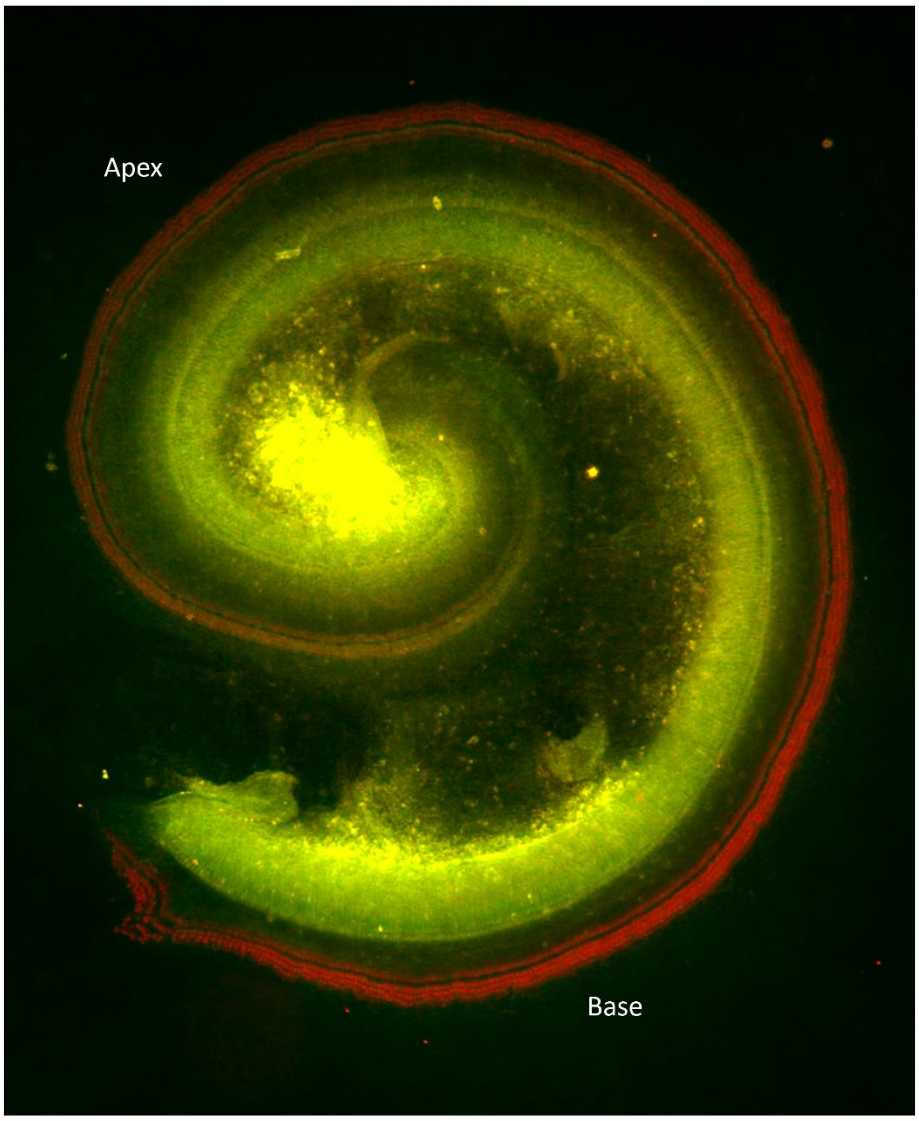

FIGURE 4-1: Tonotopic gradient in uptake of GTTR. Hair cells of the base show stronger fluorescent labelling than hair cells of the apex. Photo provided by Professor Guy Richardson.

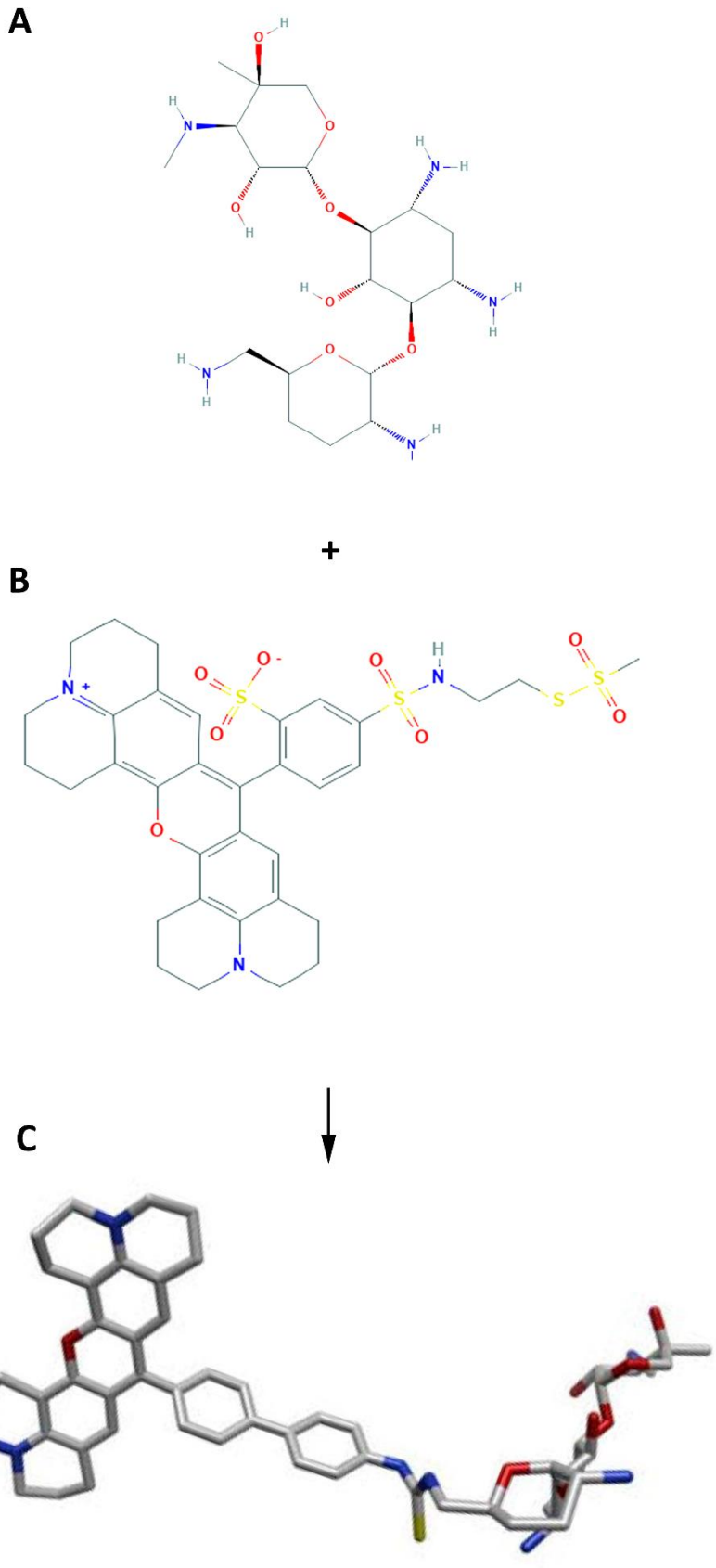

FIGURE 4-2: Molecular structure of GTTR. (A) gentamicin C1, (B) Texas Red, and (C) GTTR. Structures (A) and (B) from PubChem. (C) from *Escobedo et al., 2012*.

4.2 Results

This chapter includes data from 16 apical OHCs and 14 basal OHCs of P2+1 and P2+2 cultured CD-1 wild type mouse cochlea. The average MET current size at -164 mV was -1.32 ± 0.005 nA in the apex, and -1.77 ± 0.007 nA in the base. The average resting MET current at -164 mV was approximately 3% of the maximum in both the apex and base. The largest MET current recorded was -1.93 nA in the apex, and -2.44 nA in the base. Average cell capacitance was 6.14 ± 0.02 pF in the apex, and 5.76 ± 0.02 pF in the base, and average access resistance was 4.69 ± 0.03 MΩ. The data in this chapter were acquired and processed as described in chapters 2 and 3 with key differences where indicated. For instance, due to the slower kinetics of GTTR square waves of 22 Hz (half the usual frequency) were used as a main protocol (**figure 4-3**). Sine waves were used in conjunction to check that stimuli were saturating. As in chapter 3, modelling was done at -55 mV to match the approximate driving force on cells in experimental conditions, and all results are presented for a single open channel, thus with a channel open probability of 1.

4.2.1 Block of MET current by GTTR

GTTR is a much more potent blocker than gentamicin, with approximately 10 times stronger block of MET currents. Its block is also reversible, like the AGs, but it can take longer to wash out and recover full current size. Fractional block curves for apical and basal OHCs are shown in **figure 4-5**, and corresponding dose response curves are shown in **figure 4-6**. As before, voltage-dependence of the K_D and Hill coefficient were calculated for GTTR and results are shown in **figure 4-7**, and are summarised in **table 4-1**. Similar to gentamicin, GTTR also had a clear relief of block at strongly hyperpolarised voltages and is therefore certainly permeating through the MET channel. However, at depolarised potentials the block was relieved more gradually than any of the native AGs, indicating a much higher affinity for the channel and a reduced voltage-dependence of the interaction between the drug and the channel.

Most intriguingly, the Hill coefficient for GTTR had an average of ~2.5 at negative potentials, increasing slightly as voltage increases towards zero and then sharply dropping towards 1 at positive potentials. Because the modelling was done at -55 mV, the Hill coefficient was set to 2.5. No apical to basal difference in K_D or in Hill coefficient is apparent for GTTR, as was found for the three native AGs presented in chapter 3.

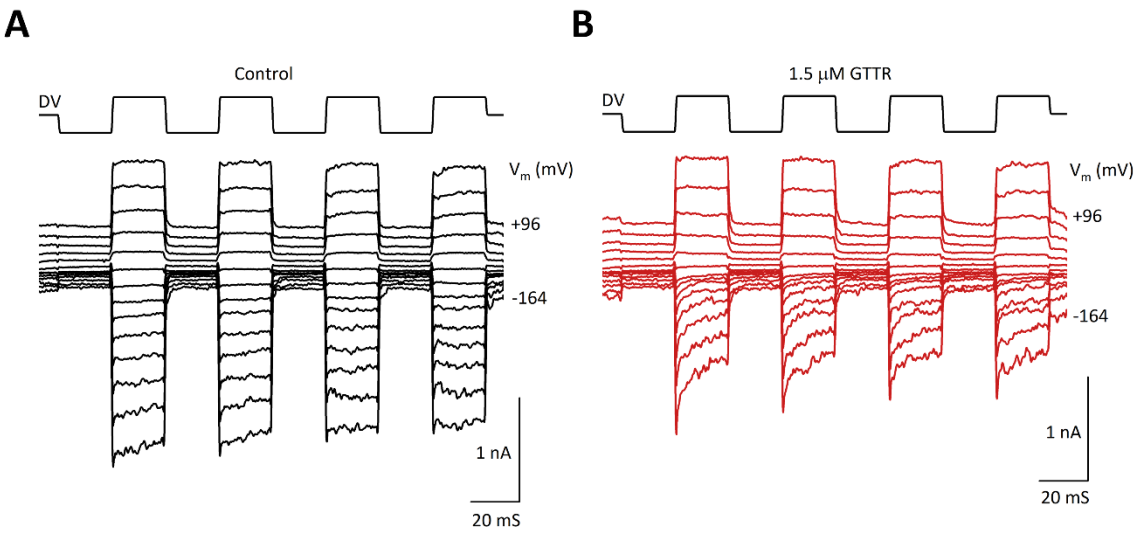

FIGURE 4-3: Examples of MET currents in a basal OHCs stimulated with a square wave before and during superfusion of GTTR. (A) Control, (B) 1.5 µM GTTR.

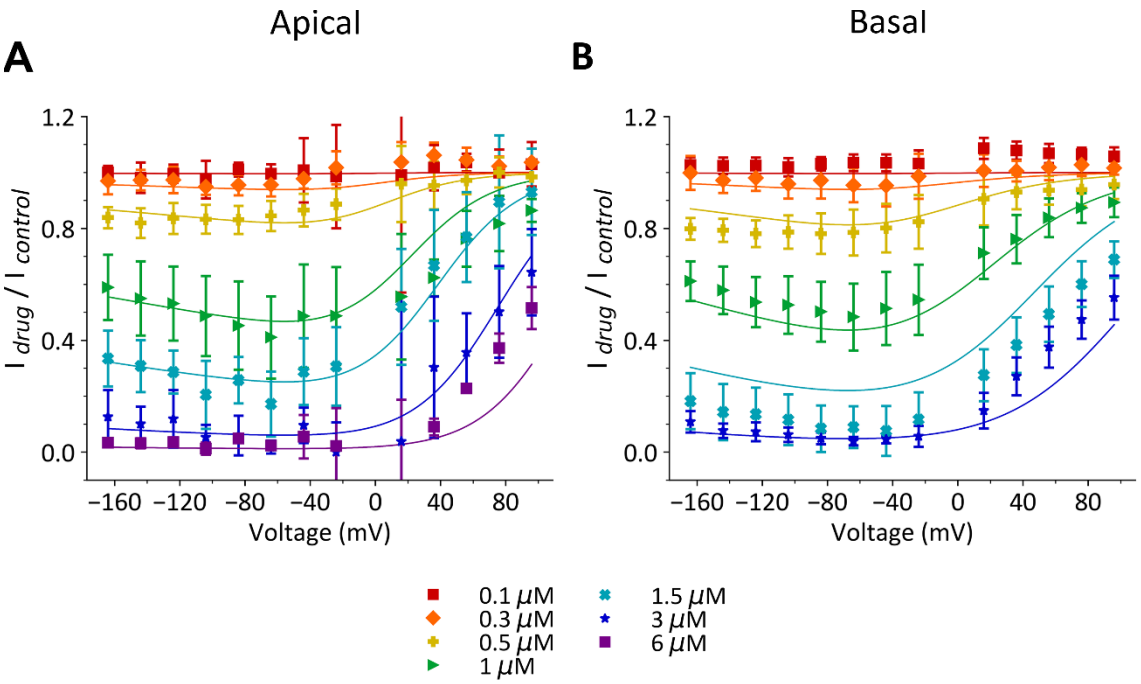

FIGURE 4-4: Fractional block curves for GTTR in apical and basal OHCs. The number of cells per location at each concentration is: (A) GTTR, apical OHCs: 0.1 µM, n = 3; 0.3 µM, n = 7; 0.5 µM, n = 10; 1 µM, n = 7; 1.5 µM, n = 5; 3 µM, n = 4; 6 µM, n = 2. (B) GTTR, basal OHCs: 0.1 µM, n = 5; 0.3 µM, n = 9; 0.5 µM, n = 8; 1 µM, n = 12; 1.5 µM, n = 6; 3 µM, n = 6.

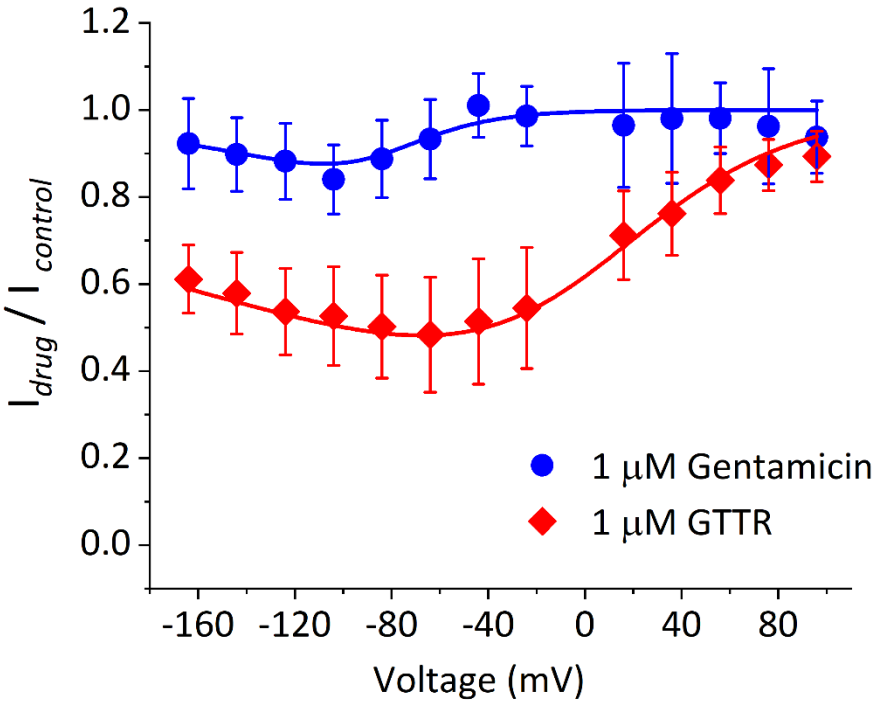

FIGURE 4-5: Comparison of fractional block by 1 µM of gentamicin and GTTR in basal OHCs.
Number of cells per drug: gentamicin, n = 5; GTTR, n = 12.

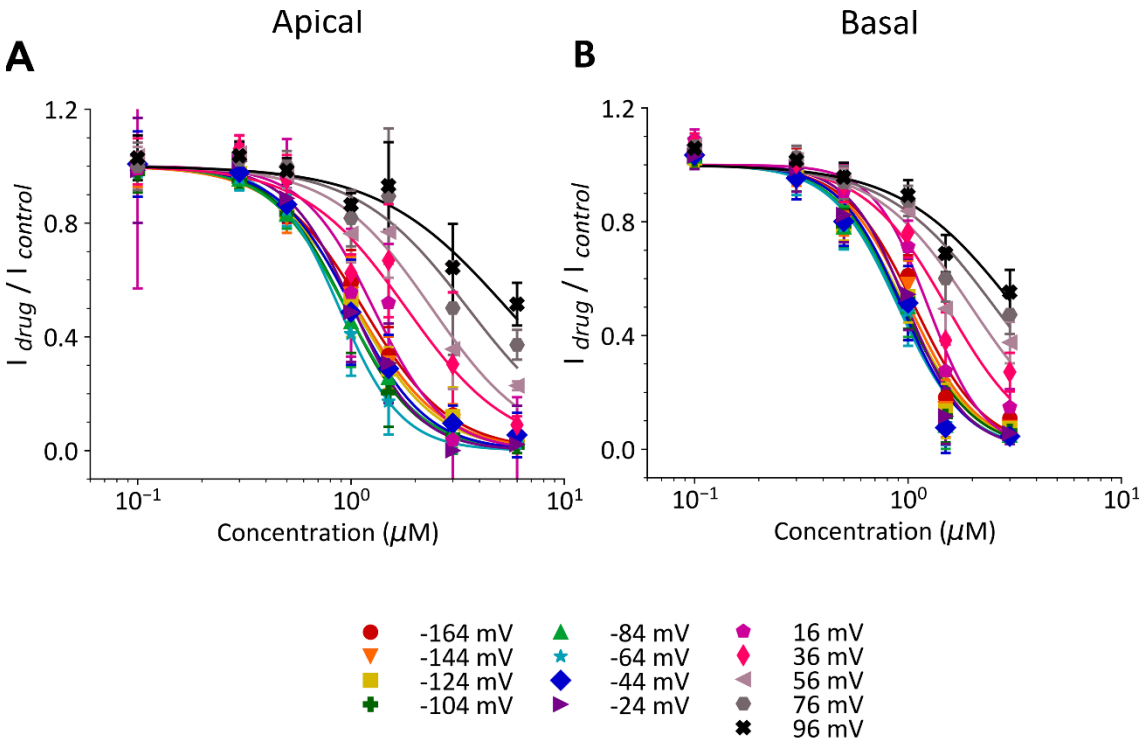

FIGURE 4-6: Dose response curves for GTTR in apical and basal OHCs. Number of cells as in **figure 4-4**.

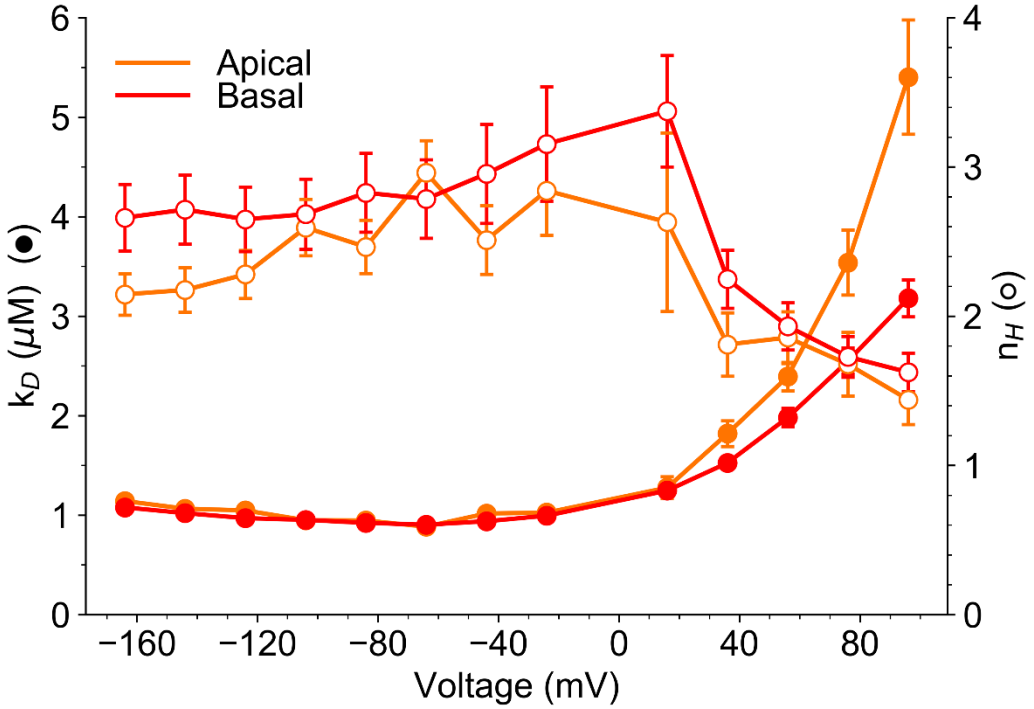

FIGURE 4-7: Voltage dependence of MET channel block by GTTR in apical and basal OHCs.

	GENTAMICIN		GTTR	
	Apical	Basal	Apical	Basal
V_{max} (mV)	-104	-104	-64	-64
K_D (μM)	5.92 ± 0.22	6.52 ± 0.32	0.88 ± 0.02	0.90 ± 0.03

TABLE 4-1: Maximum block measured for GTTR. Results for gentamicin reproduced from Chapter 3 for comparison.

4.2.2 Kinetics of GTTR block

The time constant of the decay in current is significantly different between gentamicin and GTTR, with block by GTTR developing at a much slower rate as shown in **figure 4-8.** A longer force step of 20 ms and occasionally 40 ms for low concentrations was therefore used to ensure that the entire decay curve could be accurately fit. The average time constant of full block upon channel opening by 1 μM GTTR in basal OHCs was 4.89 ms ± 1.01 ms (n = 12), approximately 10 times slower than the 0.5 ms time constant of gentamicin reported in section 3.2.2. The slope of time constants in both apical and basal OHCs was measured and its value k_1 is reported in **table 4-2**.

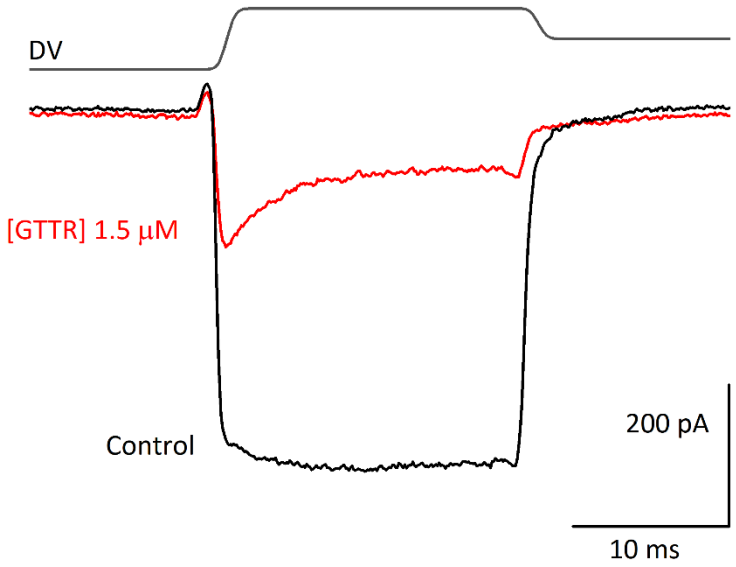

FIGURE 4-8: Example of force steps with and without GTTR. Note the difference in time scale than for native AGs. τ = 5.4 ms.

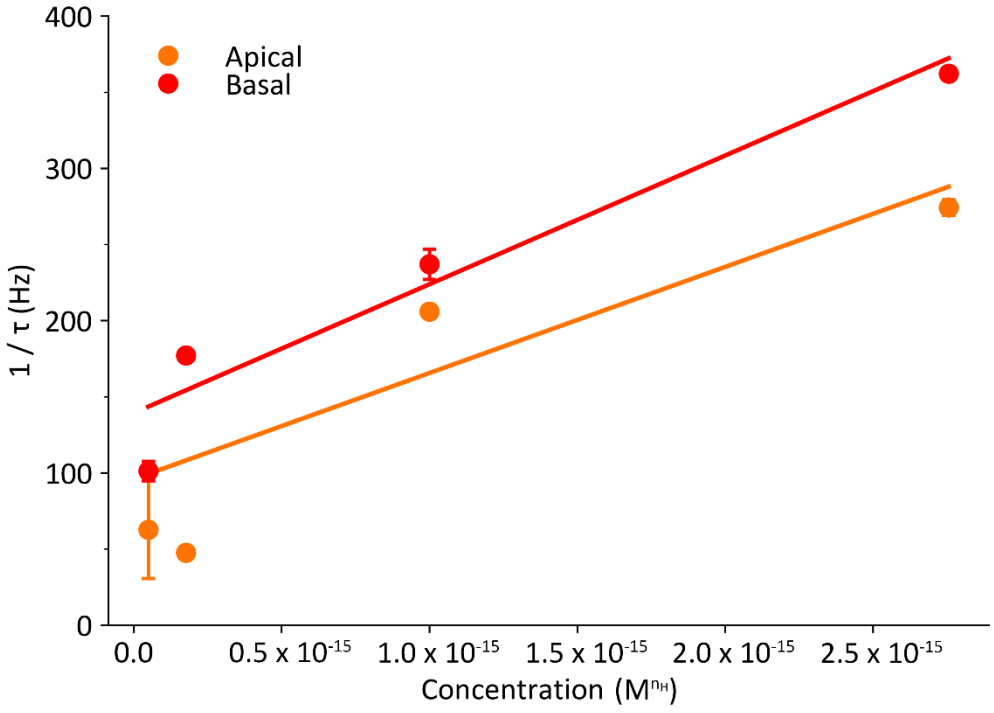

FIGURE 4-9: Results of fitted time constants per concentration for GTTR in apical and basal OHCs. The number of measurements per location at each concentration is: (A) GTTR, apical OHCs: 0.3 µM, n = 2; 0.5 µM, n = 1; 1 µM, n = 5; 1.5 µM, n = 5. (B) GTTR, basal OHCs: 0.3 µM, n = 5; 0.5 µM, n = 5; 1 µM, n = 12; 1.5 µM, n = 6.

4.2.3 Modelling results

Fitting of the fractional block curves with the two-barrier one binding-site model matched the data well. The results of this fit and the subsequent calculations are summarised in **table 4-2**. As expected, the apparent charge of the molecule was lower than for native gentamicin likely due to the Texas-Red side chain taking up one of the charge sites. Unlike any of the native AGs, the apparent charge was different in the apex and base at approximately 1.16 and 0.87, respectively. According to the confidence intervals on these values these differences in charge are statistically significant, but the reason for this is unknown.

The striking differences in the behaviour of GTTR are evidenced by the energy profiles, shown in **figure 4-7** (panel A). First, the binding energy for GTTR at the binding site is far stronger than it is for native gentamicin, at -34.4 kT compared to approximately -8.4 kT for gentamicin. Intriguingly, the binding site is also shifted towards the right in the apex whereas for native gentamicin it was shifted to the left. Most interestingly, the energy barriers in both the apex and base have negative values. This has never been reported before for any drug that has been tested with the MET channel. Mathematically, this result is related to the slow kinetics of block: E_1 is negative because it is calculated from the log of k_1, which is further exaggerated by the high Hill coefficient (see **figure 4-8**). This is interesting to compare with gentamicin and kanamycin, in that although kanamycin had about 10 times faster time constants than gentamicin, the slope of its time constants (and therefore k_1) was still similar.

The ΔE is also much smaller than native gentamicin in both apex and base, and as for the binding site its apical to basal relationship is reversed compared to the native AGs. The significance of this is also unclear, but the fact the trend is reversed for several parameters suggests that this could be indicative of an altered mechanism of binding between GTTR and the MET channel compared to that for native AGs.

Perhaps unsurprisingly, these differences in kinetics contribute to large differences in entry rate (**table 4-2** and **figure 4-7**, panel B). As for the AGs, the apical channel permeates less GTTR compared to the basal channel. But unlike native gentamicin, GTTR appears to quickly saturate the channel at relatively low concentrations of about 3 μM, probably due to its larger size.

	GENTAMICIN		GTTR	
	Apical	Basal	Apical	Basal
n_H	1	1	2.5	2.5
k_1 (s^{-1} (M^{n_H}))$^{-1}$	7.06e7 ± 1.25e3	1.81e8 ± 5.26e2	1.25e16 ± 2.30e2	6.98e16 ± 1.57e2
δb	0.74 ± 0.07	0.78 ± 0.07	0.90 ± 0.07	0.80 ± 0.11
E_b (kT)	-8.50 ± 0.60	-8.34 ± 0.64	-34.47 ± 2.89	-34.41 ± 2.44
Apparent charge	1.58 ± 0.12	1.55 ± 0.12	1.16 ± 0.18	0.87 ± 0.10
ΔE (kT)	5.39 ± 0.75	4.96 ± 0.74	0.19 ± 0.81	0.87 ± 0.82
E1 (kT)	12.01	10.82	-7.61	-9.33
E2 (kT)	17.40	15.99	-7.41	-8.46
V_0 (mV)	-105.6	-106.65	-54.37	-66.73
Entry at 1 uM (molecules/s)	7.85	23.38	6.25	24.77
Entry at 100 uM (molecules/s)	129.97	417.59	13.9	48.18
Half entry rate (molecules/s)	77.09	251.6	6.95	24.09
Half entry concentration (μM)	19.01	21.01	1.08	0.98

TABLE 4-2: Model results for GTTR. Gentamicin results reproduced from Chapter 3 for comparison.

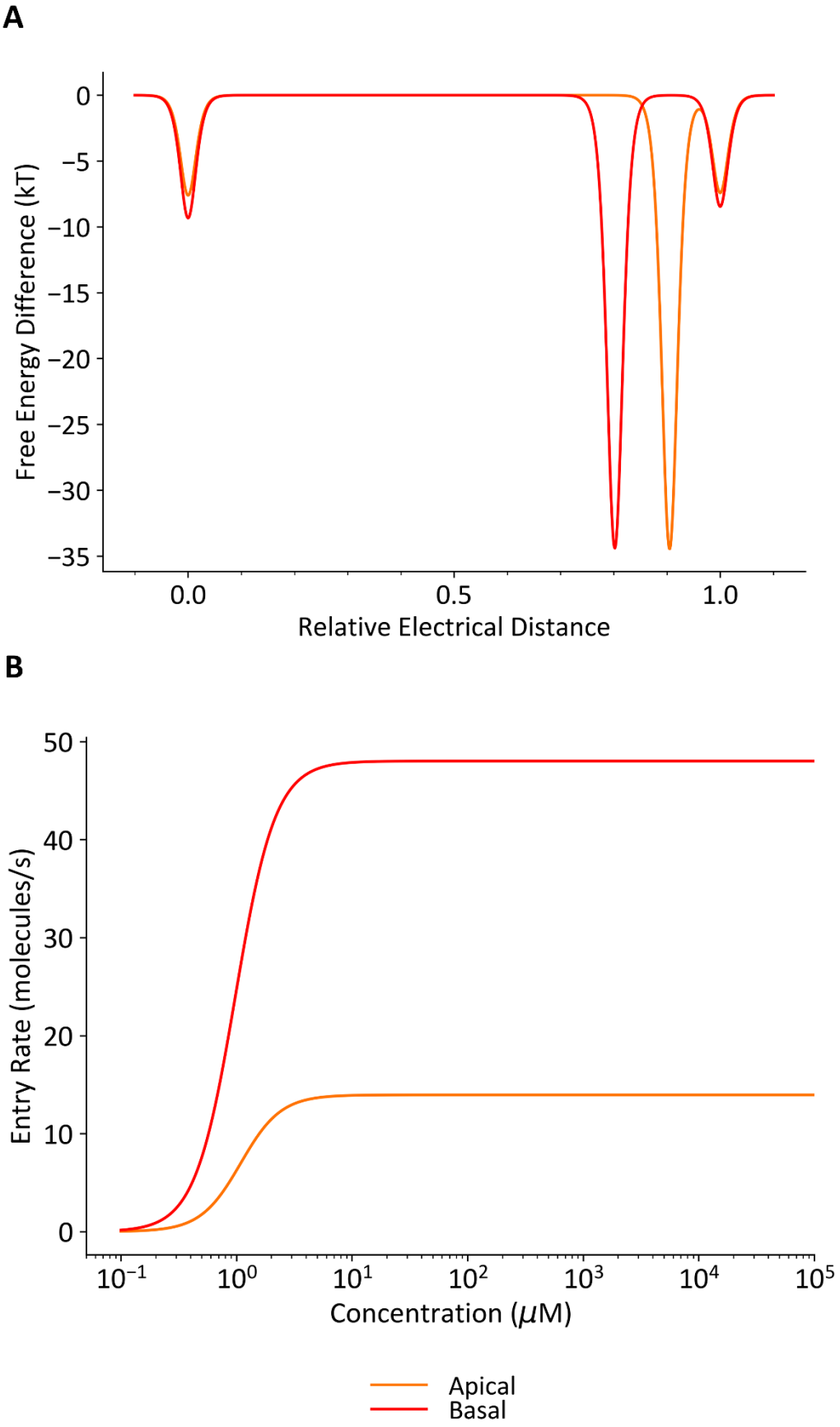

FIGURE 4-10: Energy profiles and entry rates for GTTR in apical and basal OHCs.

4.2.3 Entry rate and ototoxicity

Whilst GTTR has a well-known tonotopic gradient in fluorescence (as shown in **figure 4-1**) and it has been extensively used as an indicator for gentamicin entry intro hair cells, little data has thus far been published on the ototoxic effects of GTTR itself. A dose-response curve for the toxicity of GTTR compared with gentamicin in basal OHCs was presented by Dr. Richard Osgood in his 2019 thesis, which has been reproduced here with permission (**figure 4-11**). The methods for this experiment were as described in section 3.2.4, with exception that the quantification of hair cell survival was done from a phalloidin stain alone. The experiment was performed by Professor Guy Richardson and Ms. Jodi Parslow, and Dr. Richard Osgood quantified the data and created the graph.

Although at first glance GTTR appears to permeate the channel far less than native gentamicin (as it certainly does at high concentrations!), at 1 μM GTTR was modelled to have a slightly higher entry rate of 24.77 molecules per open channel per second, which was 23.38 for gentamicin. By 2 μM, GTTR entry was 41.29 and gentamicin over-took with 44.68. GTTR entry then saturated at about 50 molecules per second around 3 μM whilst gentamicin entry continued to climb and saturated at about 500 molecules around 100 μM. This range of crossover between the entry rates of gentamicin and GTTR at low concentrations is shown in **figure 4-11**.

In fact, in the dose response curve for basal OHCs GTTR was found to be slightly more ototoxic with an LD_{50} of 0.9 μM, compared to 2 μM for native gentamicin. Given that a margin of error is expected in these models of entry rate, and that the GTTR used in these two experiments came from different batches that could vary in purity, it is conceivable that at these low concentrations GTTR could indeed permeate more readily into the cell than native gentamicin, leading it to be more ototoxic in the same way as the native AGs presented in chapter 3. This higher permeation could be explained by its greater binding affinity for the MET channel, but further increasing of entry rate at higher concentrations is prevented by its large size.

Once again, if a difference in permeation between gentamicin and GTTR does occur at these low concentrations, it is unlikely to fully account for their differences in ototoxicity. As before, if the interaction of GTTR with the MET channel is so different from native gentamicin then it is likely that its interactions with other intracellular targets will be different as well. For example, GTTR was found to induce formation of membranous blebs on the apical surface of cochlear hair cells whereas gentamicin did not *(Osgood, 2019)*.

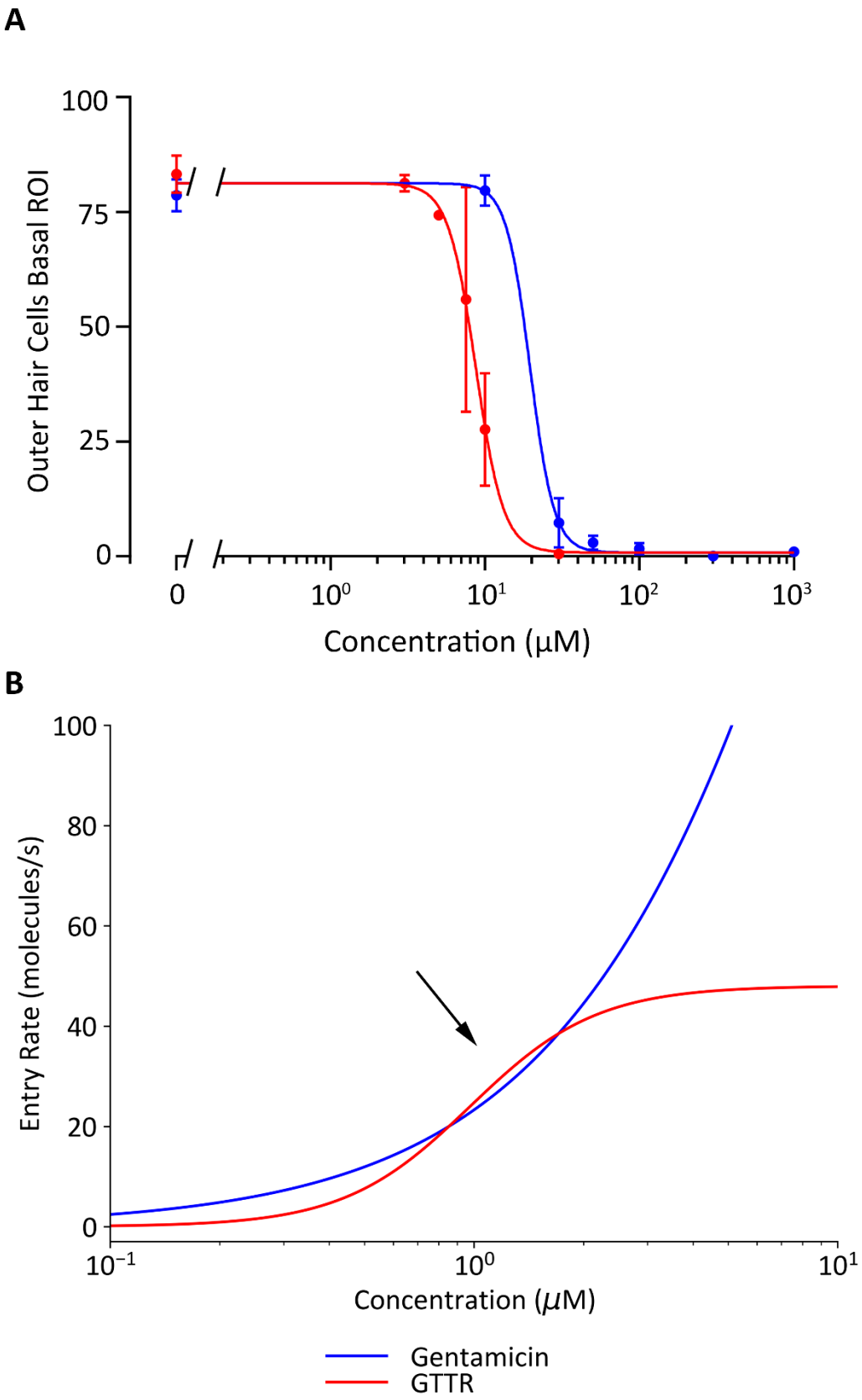

FIGURE 4-11: Comparison of toxicity data and modelled entry rates for gentamicin and GTTR. (A) Dose-response curves for ototoxicity of gentamicin and GTTR in basal OHCs. Data obtained by Professor Guy Richardson and Ms. Jodi Parslow, and figure compiled and published by Dr. Richard Osgood *(2019)*, modified with permission. (B) Modelled entry rates for gentamicin and GTTR. Crossover range around 1 µM is highlighted by the arrow.

4.3 Discussion

Several things stand out from modelling GTTR permeation. First and foremost is the Hill coefficient which increases between 2 and 3 at low potentials, and then drops off sharply at high potentials. This Hill coefficient above 1 indicates that the drug may be able to bind to more than one site within the channel and that binding of multiple molecules to the channel may be cooperative. This cooperative binding appears to be voltage-dependent, as its effect reduces at higher potentials. This could be due either to a reduced affinity of the molecule for the channel, or perhaps even a voltage-dependent conformational change of the channel itself. A similar pattern was described by Gale et al. *(2001)* for the fluorescent dye FM1-43. The key difference is that FM1-43 was found to have an unusual ability to reside inside the closed MET channel, which was evidenced in the force steps as a slow development of current upon channel opening and slow inactivation of current upon channel closure (this also made it impossible to model FM1-43 permeation rate, which is expected to be very high). The observation that the MET currents in the presences of GTTR decline exponentially in response to force steps imply that GTTR is clearly an open-channel blocker and cannot reside in the closed channel. Additionally, FM1-43 was also found to be able to block both inward and outward currents. Extracellular GTTR does block some outward currents, but to a lesser degree than inward currents and generally its pattern of kinetics is more in line with the AGs than with FM1-43.

The other striking observation is that the binding energy is approximately three-fold stronger for GTTR than for native gentamicin, and the energy barriers are both negative. This result is counterintuitive as an energy barrier should by definition be positive. There are several possible interpretations of this phenomenon, three of which I will outline here:

1.) One caveat to the energy profile model is that there is no way to measure the width of the electrical field of the interaction sites, meaning that areas of charge within the channel pore could overlap. The energy barriers could appear negative in the model of GTTR because they are overshadowed by the intense negativity of the binding site. This would explain why the apical energy barriers appear “higher”–less negative–than the basal energy barriers, as they do for native gentamicin.
2.) Another explanation is that according to our model, we believe that these energy barriers correspond to regions of positive charge at the entrance and exit of the pore. It is possible that the Texas Red portion of the molecule has negatively charged residues that bind to these two barriers, producing 3 distinct binding sites which are reflected in the Hill coefficient. Alternatively, new evidence suggests that there could also be areas

of negative charge at these points as well, which GTTR may be interacting with *(Ballesteros et al., 2018)*.

3.) Lastly, it is now believed that the channel pore is shaped like a groove down the side of the TMC1 protein, and that one side is in contact with the cell membrane *(Ballesteros et al., 2018)*. It could be that the gentamicin portion of the molecule is going head-first into the channel pore and binding to the usual AG binding site before permeating into the cell, while the Texas Red portion is attracted to the lipophilic regions of cell membrane within the pore, effectively being "dragged" through the channel by gentamicin. This would cause it to block the channel more strongly than native gentamicin and could result in the higher binding energy and negative energy barriers.

The dynamics of the interaction between GTTR and the MET channel could in fact be a combination of these three scenarios or could be due to a currently unknown property of the channel. It is at present unclear and warrants further study. Comparison of these modelling results with structural models of the TMC1 pore could help to elucidate the intriguing properties of the permeation of GTTR through the MET channel (see chapter 6 for more detail).

The differences between apex and base for GTTR are interesting as well. Unlike the native AGs in which parameters were shifted in the apex to indicate a "narrower" pore, the trend is reversed in several of the parameters for GTTR. For instance, the apical binding site is further down the channel than the basal binding site, and the ΔE is lower. And yet despite these differences the permeation is still predicted to be lower, likely due to the k_1 which is lower in the apex than in the base. The reason why these trends are reversed is uncertain. Considering the three potential explanations outlined above, it is possible that a different mode of binding of GTTR to the channel pore—in some ways opposite—leads to an opposite trend between apex and base. The observation that the apparent charge is higher in the apex than in the base, unlike the native AGs, could also be indicative of a different mode of binding, perhaps between TMC1 and TMC2. (though as before the contributions of TMC1 and TMC2 to this effect cannot be conclusively commented on because wild-type mice were used in this experiment)

What is most fascinating about these results is that despite the differences in kinetics, at low concentrations (1 - 3 μM) the entry rates of gentamicin and GTTR are expected to be similar. As these are the concentrations that are regularly used in fluorescence uptake experiments and over which ototoxicity in culture can be assessed, this indicates that GTTR is a good marker of gentamicin entry into hair cells through the MET channel. Nevertheless, GTTR has kinetics different to gentamicin and pushing it experimentally beyond its limits may be unadvised.

Chapter 5

Effects of Calcium, Maturation, and Driving Force on Aminoglycoside Permeation through the MET Channel

5.1 Introduction

The permeation profiles for native AGs presented in chapter 3 provide insight into how differences in permeation of these drugs may be related to their inherent ototoxicity, but these results are difficult to extrapolate to an *in vivo* situation for several reasons. The aim of this chapter is to explore some of the factors that affect AG permeation and how conditions *in vivo* may vary from experimental conditions, with the goal of providing an estimate of permeation rate for gentamicin through the MET channel in real adult hair cells.

First and foremost, the calcium concentration in the endolymph is far lower than the perilymph, but for experiments that involve incubating hair cells for long periods of time we use a perilymph-like medium to keep cells alive. Thus, the experiments in chapter 3 and 4 were done in a "high" (1.3 mM) calcium medium to match the experimental conditions in toxicity assays. Calcium itself is a permeant blocker of the MET channel, thus lowering the calcium concentration in the superfusion medium produces several interesting effects. 1.) The MET currents increase in size, especially in the inward direction. 2.) The resting current as a percentage of total MET current increases as adaptation is reduced *(Corns et al., 2014)*. 3.) As a blocker, calcium competes with AGs for the pore binding site. Lowering the calcium concentration increases the affinity of AGs for the channel, producing more block *(Marcotti et al., 2005)* (**figure 5-1**). Presumably this would increase the entry rate of gentamicin through the channel, as it was found to for DHS. To test this, I characterised the permeation profile for gentamicin in 100 μM Ca^{2+} medium, the lowest possible without risking damage to tip links.

Second, little is known about how AG permeation may change as hair cells mature, and the kinetics of the MET channel over the course of development are heavily debated. As previously discussed, there is a change in the profiles of TMC1 and TMC2 expression during the first postnatal week. In the apex at P2 it is expected that the MET channel is composed entirely of TMC2, and by P10 it should be entirely TMC1. A previous study by Corns et al. *(2017)* found that *Tmc2*$^{-/-}$ mice had a lower permeation of DHS through apical OHC MET channels compared to wild type. Furthermore, TMC1 is capable of faster calcium adaptation than TMC2 *(Goldring et al., 2019)*, and TMC2 has a larger calcium permeability than TMC1 *(Pan et al., 2013; Beurg et al., 2015)*. Given that these properties are closely related, it would be interesting to see how maturation, which should produce a similar shift in expression profile from TMC2 to TMC1, might affect permeation of drugs through the channel. This could, moreover, elucidate differences in permeation between TMC2 and TMC1 and how these may impact the results presented in chapters 3 and 4.

However, recording MET currents is challenging to begin with and ordinarily recording MET currents from OHCs beyond the first postnatal week is almost impossible. In the neonates the OHCs stick together well and the flexibility of the organ of Corti allows it to maintain its shape during dissection. But as the mice mature, the organ of Corti becomes more rigid and less well-adhered and is therefore more easily breakable during dissection. The hair bundles especially become increasingly delicate as they anchor to the cuticular plate and the tectorial membrane. Removal of the tectorial membrane in older preparations is almost guaranteed to destroy the hair bundles.

In order to study the effect of maturation on MET channel permeation, I used *Tecta/Tectb*$^{-/-}$ mutant mice to record from P9-P10 OHCs. These mutants completely lack a tectorial membrane, making recording MET currents possible at later ages. Even so, only apical OHCs could be recorded from as the basal part of the coil was too brittle to withstand dissection. I also recorded a new dataset for gentamicin in apical OHCs from P2 mice of the same strain to control for any inherent differences in permeation due to the *Tecta/Tectb*$^{-/-}$ mutation. Further adaptations to the experimental process were also made and will be described in section 5.3.1.

Third, the permeation rate of molecules through the MET channel is dependent both on the extracellular concentration of drug and the voltage of the cell, which is different in culture than it is *in vivo* due to the endocochlear potential. In culture, the resting potential of OHCs is thought to range from -55 to -60 mV *(Marcotti and Kros, 1999, Kirkwood et al. 2017)*, so the entry rates I have presented thus far were all modelled at -55 mV to allow for comparison with *in vitro* toxicity assays. *In vivo*, the resting potential of the OHCs is likely to be closer to -150 mV compared to the endolymph with the addition of the endocochlear potential *(Mammano and Ashmore, 1996; Marcotti and Kros, 1999; Johnson et al., 2011)*. This large voltage difference will increase driving force on positively charged ions and molecules flowing into the cell and may also affect the binding properties of drugs with any voltage-dependent kinetics. Therefore, in section 5.4 of this chapter I will show each of the permeation datasets presented thus far in this thesis, but now modelled as a function of both concentration and voltage. This will demonstrate the cooperative effects of voltage and concentration on permeation through the MET channel and how the topology of permeation changes with driving force for each drug and condition.

Finally, I will discuss the interplaying effects of the results of these experiments, and what these results may indicate for permeation in an *in vivo* adult OHC. It should be noted that the completion of these experiments was cut short by the COVID-19 crisis, and therefore some data are missing where indicated and errors may be larger than usual.

5.2 Effect of calcium on gentamicin permeation

This section includes data from 12 basal OHCs of P2+1 and P2+2 cultured CD-1 wild type mouse cochleae. The data in this section were acquired and processed as described in chapters 2 and 3, with the exception that recordings were made in superfusion medium containing 100 μM Ca^{2+} instead of the regular 1.3 mM Ca^{2+}. Because of this, some differences are apparent in MET current characteristics as previously discussed. The average MET current size at -164 mV was -1.71 ± 0.007 nA, and the average resting MET current at -164 mV was 15 ± 0.2% of the maximum in both apex and base. The largest MET current recorded was -2.05 nA. The average cell capacitance was 5.5 ± 0.02 pF, and average access resistance was 8 ± 0.10 MΩ. As in chapter 3, entry rate modelling was done at -55 mV to match the approximate driving force on cells in experimental conditions, and all results are presented for a single open channel, thus with a channel open probability of 1. The solution in the fluid jet was set to low calcium to further avoid mixing of low and high calcium in the immediate extracellular environment.

5.2.1 Block of MET currents by gentamicin in low calcium medium

As expected, lowering the calcium concentration of the superfusion medium increased the size of the MET currents, increased the fraction of the MET current activated at rest, and increased the strength of gentamicin block on the MET currents. These properties are all illustrated in **figure 5-1**.

Quantification of the block (shown in **figure 5-2** and summarised in **table 5-1**) by fitting dose response curves showed that the Hill coefficient remained the same as in regular calcium, at about 1 across voltages. A large shift in K_D was apparent so that gentamicin blocked MET currents by half at a much lower concentration when less calcium was present (**table 5-1**). Voltage-dependent relief of the block upon depolarisation was more acute in low calcium medium, so that by -24 mV there was almost no block of MET current (for this reason this voltage is not plotted in **figure 5-3**).

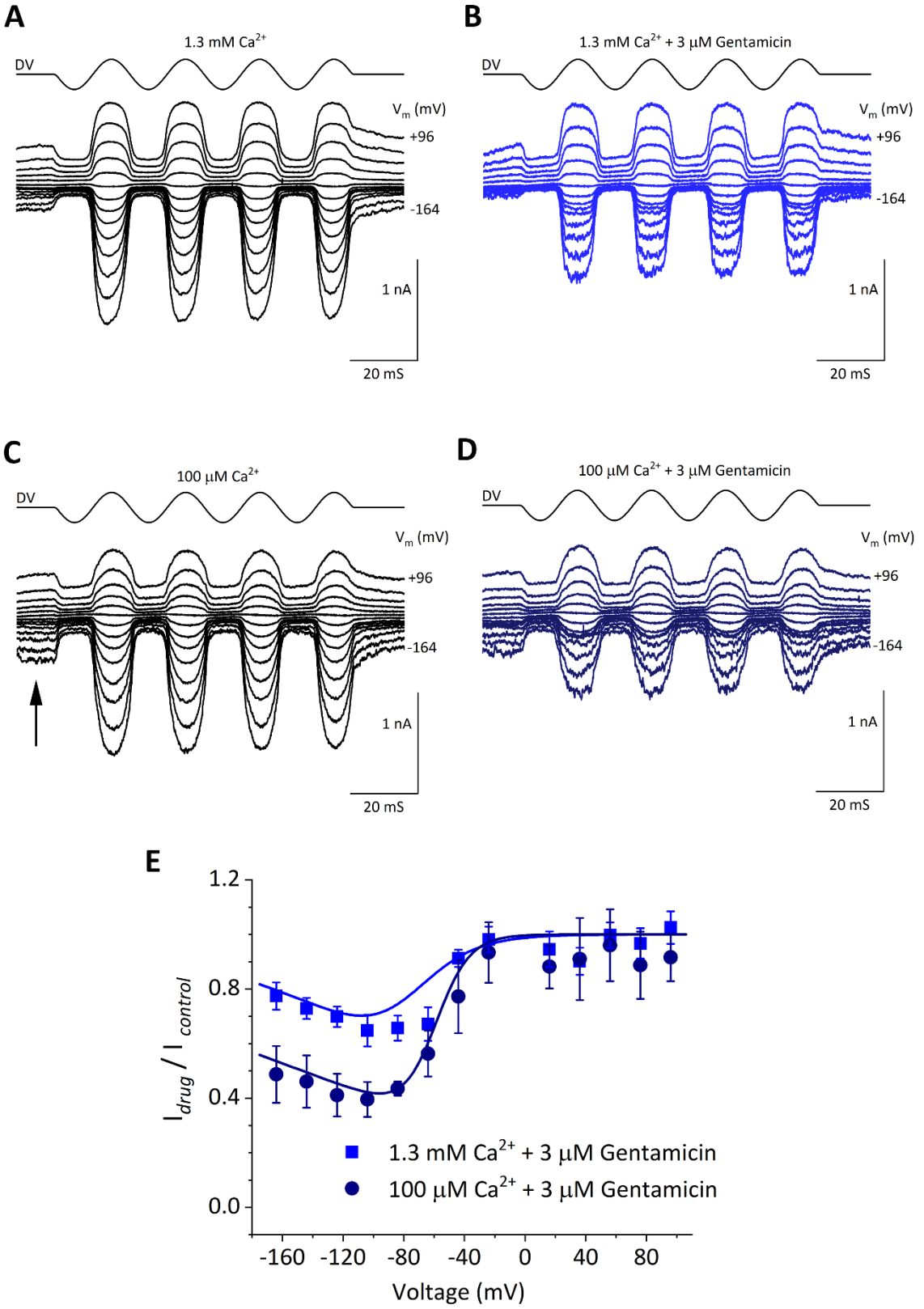

FIGURE 5-1: Examples of MET currents in basal OHCs before and during superfusion of gentamicin in 1.3 mM and 100 µM Ca^{2+} medium (A-B) Regular medium. (C-D) Low calcium medium. The arrow highlights the increased resting current. (E) Mean fractional block curves for all cells at 3 µM gentamicin, fit with two-barrier one-binding site model. The number of cells for each condition is: 1.3 mM Ca^{2+}, n = 5; 100 µM Ca^{2+}, n = 4. Results for 1.3 mM Ca^{2+} reproduced from chapter 3.

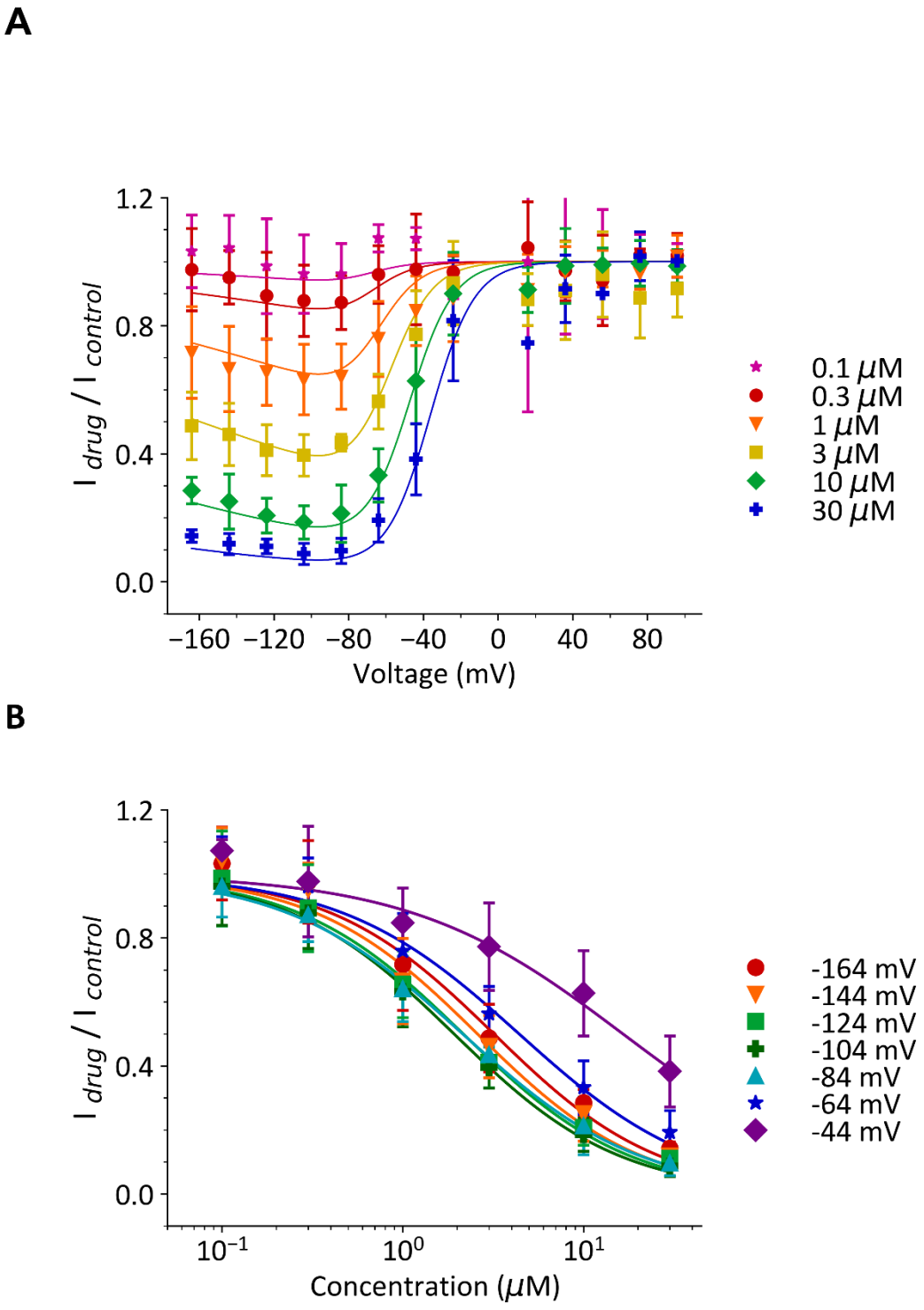

FIGURE 5-2: Fractional block curves and dose response curves for gentamicin in 100 µM Ca^{2+} medium in basal OHCs. The number of cells at each concentration is: 0.1 µM, n = 4; 0.3 µM, n = 5; 1 µM, n = 7; 3 µM, n = 4; 10 µM, n = 3; 30 µM, n = 4.

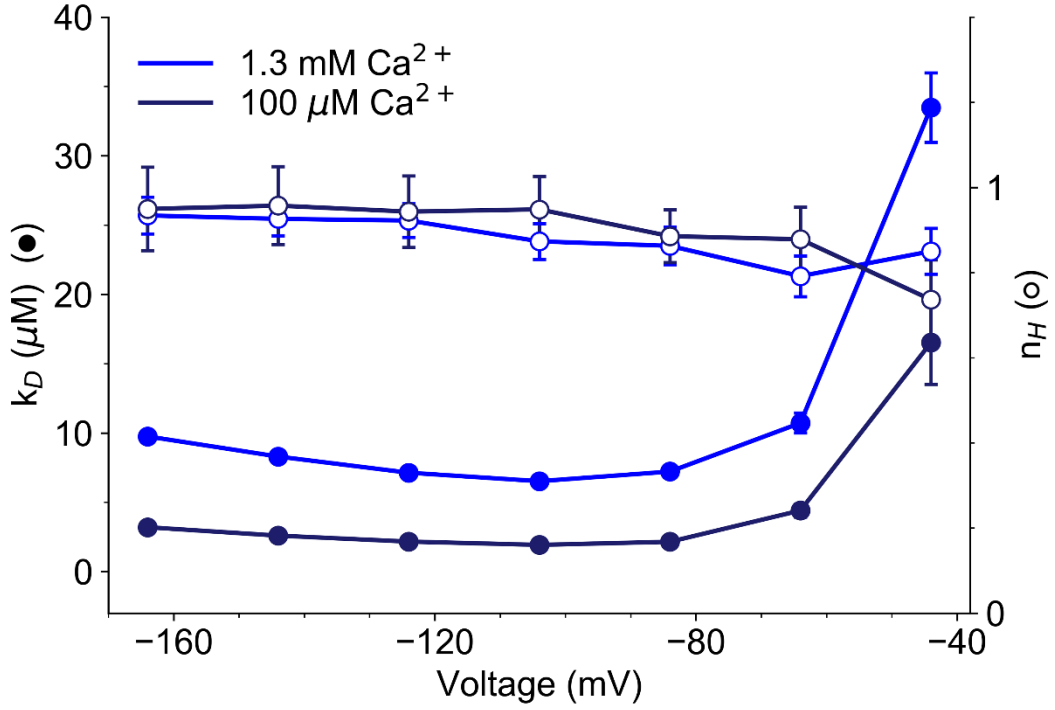

FIGURE 5-3: Voltage dependence of MET channel block by gentamicin in basal OHCs in 1.3 mM Ca^{2+} and in 100 µM Ca^{2+} medium. 1.3 mM Ca^{2+} results reproduced from chapter 3 for comparison.

	1.3 mM Ca^{2+}	100 µM Ca2+
	Basal	Basal
V_{max} (mV)	-104	-104
K_D (µM)	6.52 ± 0.32	1.92 ± 0.17

TABLE 5-1: Maximum block of MET currents by gentamicin measured in 100 µM Ca^{2+} medium. Results for gentamicin block in regular 1.3 mM Ca^{2+} medium reproduced from chapter 3 for comparison.

5.2.2 Kinetics of gentamicin block in low calcium medium

The temporal kinetics of the block by gentamicin in 100 µM Ca^{2+} medium closely resembled those in 1.3 mM Ca^{2+} medium but were slightly faster, and the slope (equal to the rate constant k_1), was steeper as well. These results are shown in **figure 5-4**.

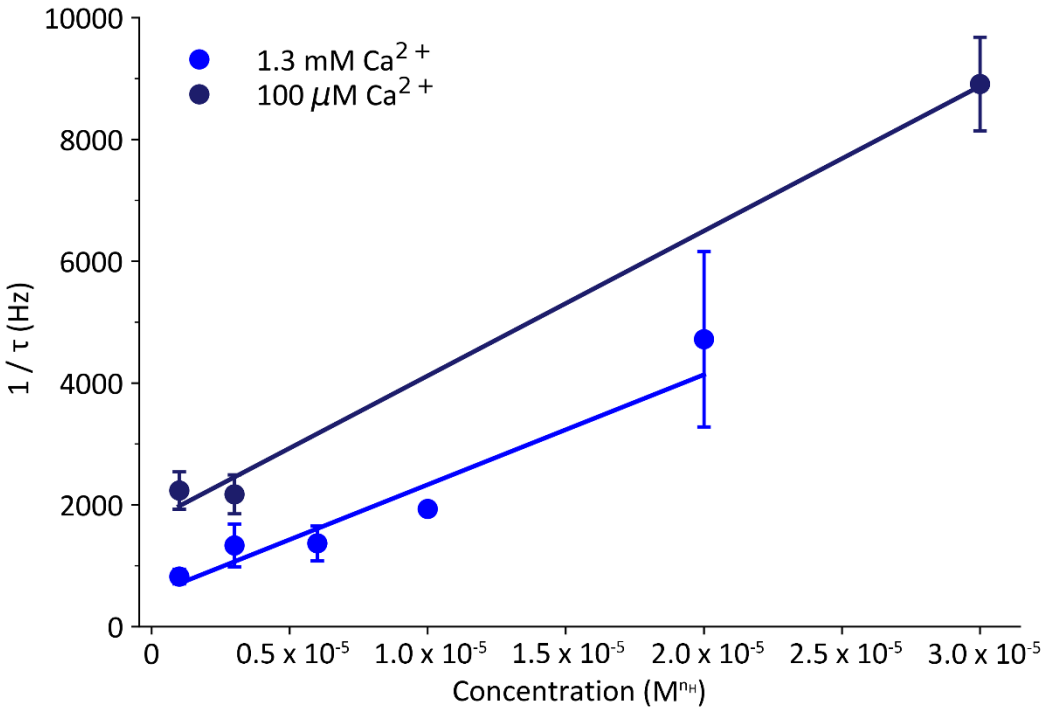

FIGURE 5-4: Time constant results for gentamicin in 100 µM Ca^{2+}. The number of measurements at each concentration is: 1 µM, n = 4; 3 µM, n = 4; 30 µM, n = 2. Results for 1.3 mM Ca^{2+} reproduced from chapter 3 for comparison.

5.2.3 Modelling results

The differences in K_D and k_1 between gentamicin in regular medium and in low calcium medium led to differences in the energy profile and permeation rate through the channel (shown in **table 5-2**, **figure 5-5**). As was found for DHS, the first energy barrier was lower in low calcium medium, but the second energy barrier was unaffected due to a complementary lower ΔE *(Marcotti et al., 2005)*. This makes sense as the extracellular calcium concentration would affect the rate over the first energy barrier but would not affect the second energy barrier which is closer to the intracellular side of the pore.

Intriguingly, the apparent charge was higher for gentamicin in low calcium medium. The binding site was also shifted towards the intracellular side of the pore compared to in regular calcium medium, which is unlike previous results found for DHS. This is likely because in the 2005 study the authors fixed the charge of DHS to 2 for all conditions, whereas I left it as a free parameter in the two-barrier one-binding site fit. Fixing the charge to 2 for gentamicin in both conditions produced a similar shift so that the binding site in regular calcium became 0.86 ± 0.07, and it became 0.88 ± 0.1 in low calcium. The apparent charge therefore has a strong impact on the position of the binding site in the energy profile, which is why I left it free for all of my energy profile comparisons.

According to my modelling results, the entry rate through the MET channel for gentamicin in low calcium medium was over twice as high as it was in regular calcium, saturating at almost 1200 molecules per second per channel compared to 500 in regular calcium (**figure 5-5**, panel B).

	1.3 mM Ca^{2+}	100 µM Ca^{2+}
	Basal	Basal
n_H	1	1
k_1 (s^{-1} (M^{n_H}))$^{-1}$	1.81e8 ± 5.26e2	2.38e8 ± 1.74e3
δb	0.78 ± 0.07	0.91 ± 0.07
E_b (kT)	-8.34 ± 0.64	-6.33 ± 1.20
Apparent charge	1.55 ± 0.12	2.33 ± 0.43
ΔE (kT)	4.96 ± 0.74	6.348 ± 0.92
E1 (kT)	10.82	10.17
E2 (kT)	15.99	16.51
V_0 (mV)	-106.65	-98.54
Entry at 1 uM (molecules/s)	23.38	171.23
Entry at 100 uM (molecules/s)	417.59	1066.48
Half entry rate (molecules/s)	251.6	582.91
Half entry concentration (µM)	21.01	7.11

TABLE 5-2: Model results for gentamicin in 100 µM Ca^{2+} medium. Gentamicin results in 1.3 mM Ca^{2+} medium reproduced from chapter 3 for comparison.

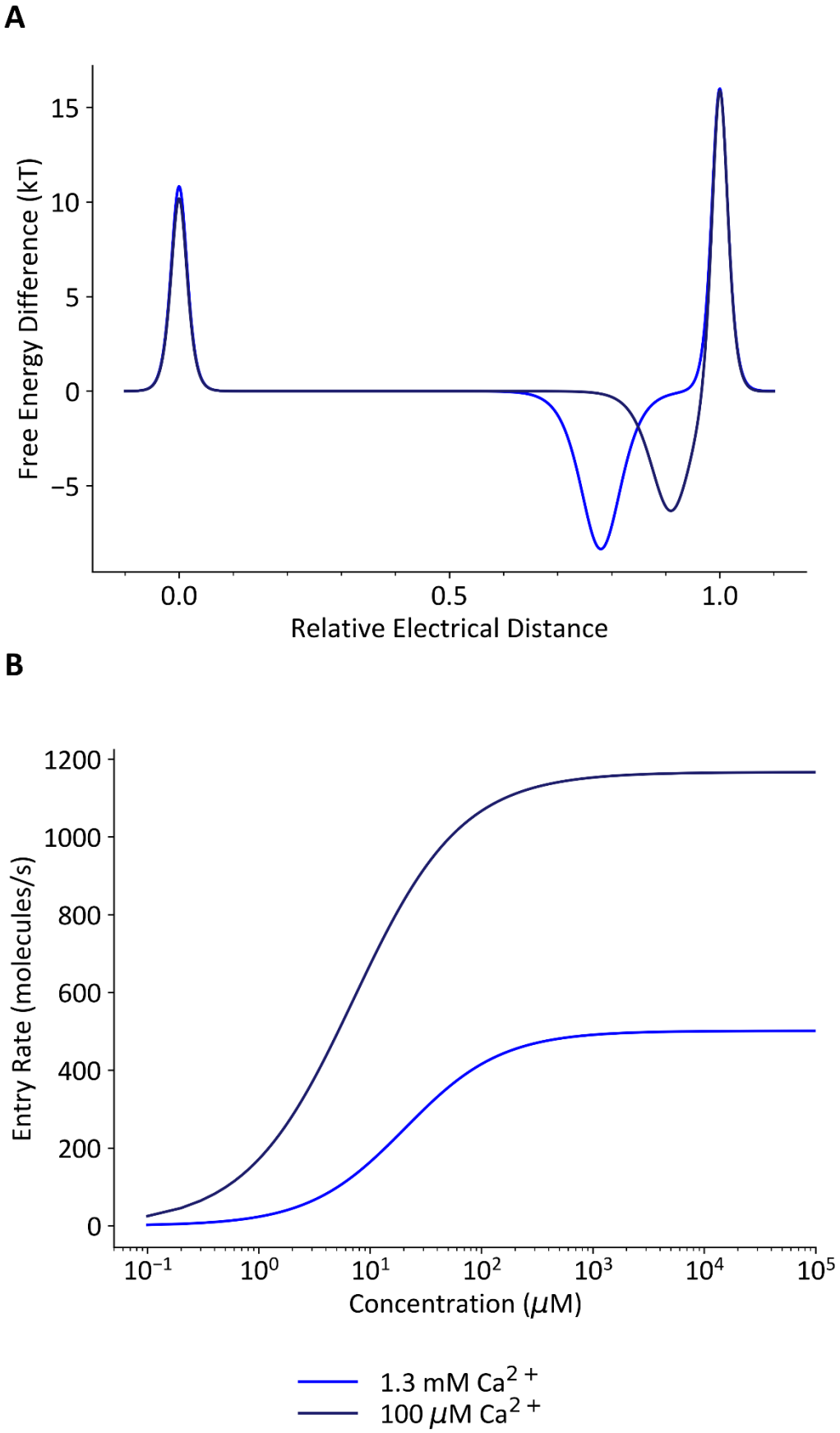

FIGURE 5-5: Energy profiles and entry rates of gentamicin through the MET channel of basal OHCs in 1.3 mM and 100 µM Ca^{2+} medium. (A) Energy profiles. (B) Entry rates. Results for 1.3 mM Ca^{2+} reproduced from chapter 3 for comparison.

5.3 Effect of maturation on gentamicin permeation

This section includes data from 10 apical OHCs of P2 and 12 apical OHCs of P9-P10 acutely dissected *Tecta/Tectb*$^{-/-}$ mutant mouse cochleae. The average MET current size at -164 mV in P2 OHCs was -0.98 ± 0.01 nA and was -1.90 ± 0.006 nA in P9-P10 OHCs. The average resting MET current at -164 mV was 2.6 ± 0.03% in P2 and was larger at 9.4 ± 0.001% in P9-P10 OHCs. The largest MET current recorded was -1.72 nA in P2 OHCs and -2.49 nA in P9-10 OHCs. The average cell capacitance was 6 ± 0.02 pF in P2 OHCs and increased to 6.73 ± 0.01 pF in P9-P10 OHCs, and average access resistance was 5.32 ± 0.04 MΩ. Aside from the specific adaptations mentioned in the following section, the data in this section were acquired and processed as described in chapters 2 and 3. As in chapter 3, modelling was done at -55 mV to match the approximate driving force on cells in experimental conditions, and all results are presented for a single open channel, thus with a channel open probability of 1.

5.3.1 Adaptations to methods for P9-P10 recordings

Adaptations to the dissection and recording procedure were made in order to record from P9-P10 OHCs. Only the very most apical part of the apical coil (~5-8 kHz) could be recorded from due to instability of the basal turn. Great care was taken during dissection to avoid stretching of the coil as this would distort and break the organ of Corti (which was far more rigid and delicate than in the neonates). The superfusion flow pressure was reduced by lowering the level of the syringes by about 1 cm, which was necessary as the cells were less adherent to one another and risked being blown away or disrupting the patch pipette seal while changing superfusion lines. The amplitude of the fluid jet stimulus was reduced by half, as the hair bundles were more delicate and needed far less stimulation to produce saturating MET currents—in fact, the usual fluid jet amplitude tended to immediately destroy the hair bundles. No surface cleaning of the cells was necessary as the basolateral membranes of the OHCs were already exposed immediately after dissection.

Data collection for this experiment was cut short due to the COVID-19 crisis. As such data for the lowest and highest concentrations of the dose response curve for the P9-P10 dataset could not be collected in time for submission of this thesis (**figure 5-8**, panel B). Whilst not ideal, this should not drastically affect the fit of the curve as the upper and lower bounds of the Hill equation fit are routinely fixed to 1 and 0 respectively, and the Hill coefficient is fixed to 1 for all native AG datasets.

5.3.2 Block of MET current by gentamicin in P9-P10 OHCs

Following adaptations to the dissection and recording procedure as described, large MET currents could be elicited from P9-P10 apical OHCs of *Tecta/Tectb*$^{-/-}$ mutants with relative ease. An example of these is shown in **figure 5-6** (panels C and D). Membrane seals on OHCs were easy to form and stable, though MET currents tended to deteriorate relatively quickly during experiments probably due to the increased fragility of the hair bundles compared to neonatal OHCs.

The block of MET currents was quantified by fitting the dose response curves (**figure 5-8**) as before and was found to be different in the P9-P10 OHCs compared to P2 (**figure 5-9**). The Hill coefficient for gentamicin was again close to 1 across voltages at both ages, but unlike in any of the previous datasets the K_D was higher in P9-P10 OHCs. This is also unlike the difference in results found previously for immature *Tmc2*$^{-/-}$ OHCs, which showed an increased block by DHS *(Corns et al., 2017)*. Interestingly, voltage-dependence of the block was again much steeper in P9-P10 OHCs compared to P2 OHCs, this time no longer blocking by -44 mV.

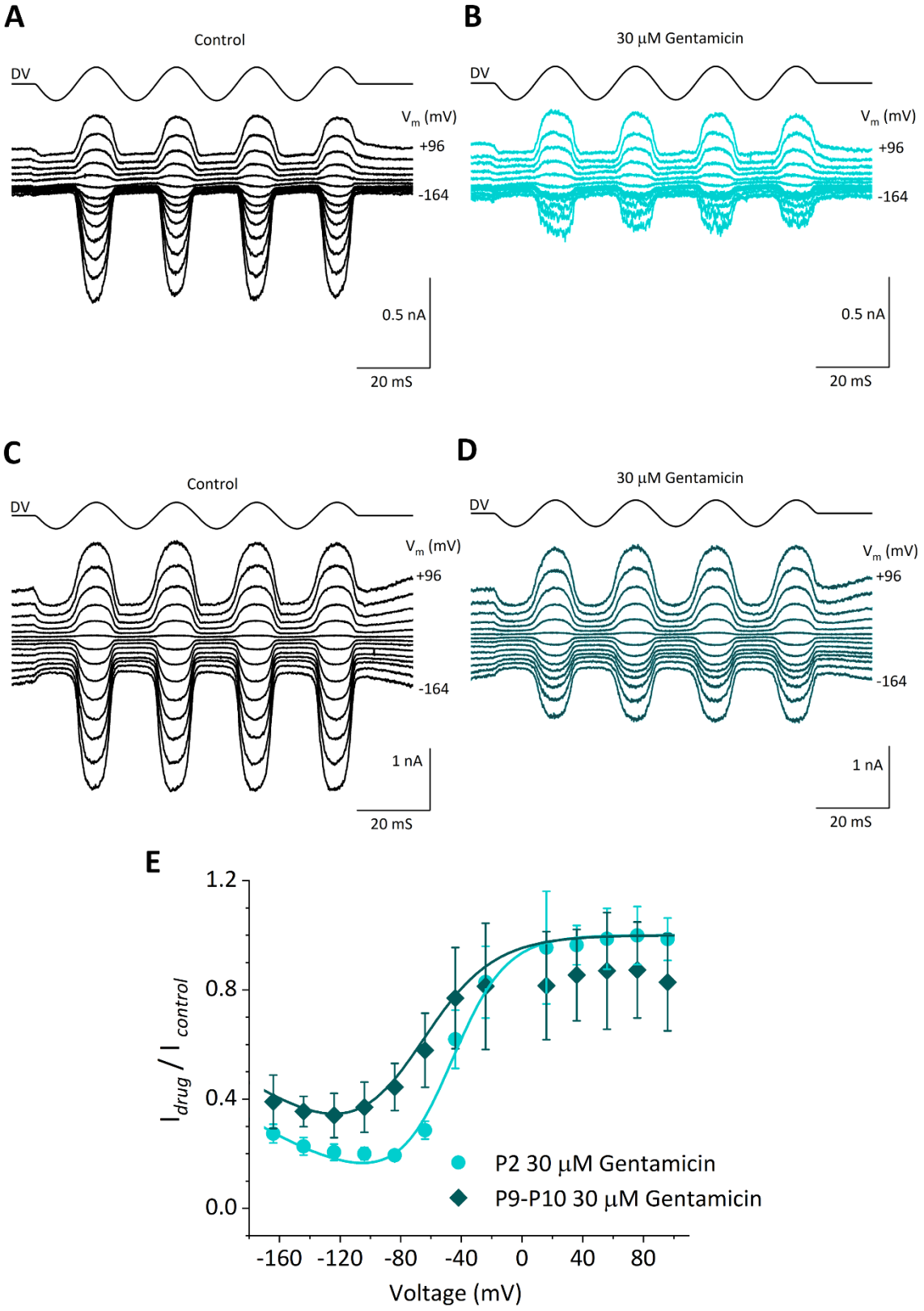

FIGURE 5-6: Examples of MET currents in P2 and P9-P10 OHCs of Tecta/Tectb$^{-/-}$ mutants before and during superfusion of 30 µM gentamicin. (A-B) P2 OHC. (C-D) P10 OHC. (E) Mean fractional block curves for all cells at 30 µM gentamicin, fit with two-barrier one-binding site model. Number of cells at each age: P2, n = 7; P9-P10, n = 5.

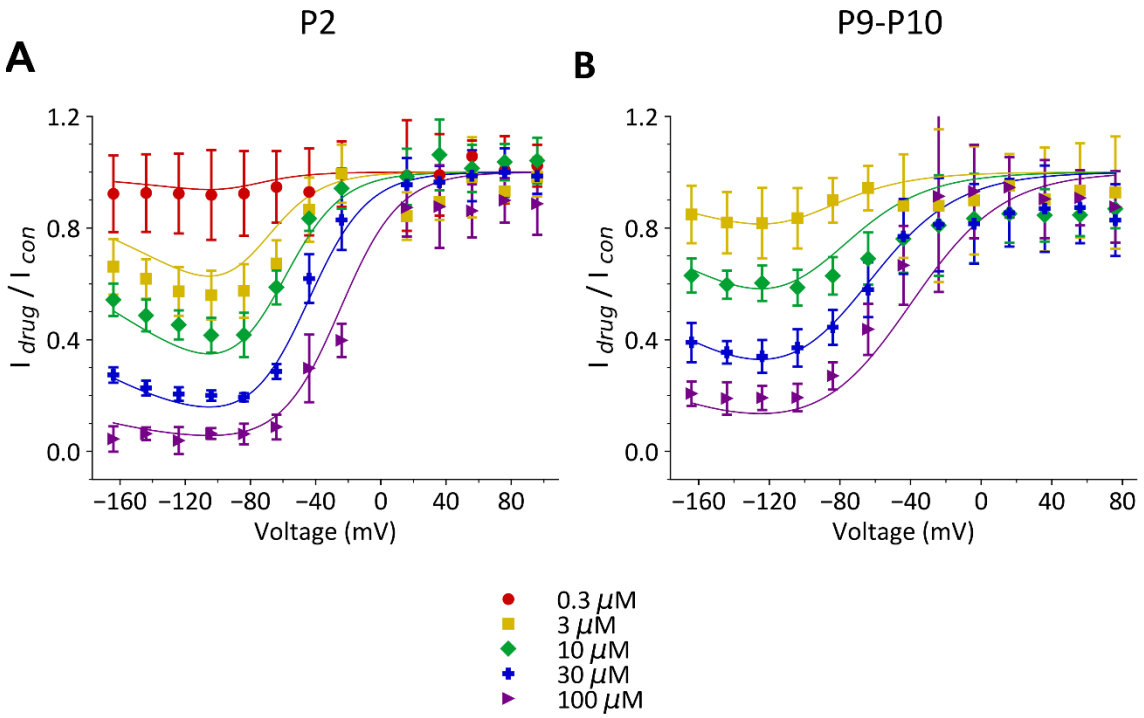

FIGURE 5-7: Fractional block curves for gentamicin in P2 and P9-P10 apical OHCs of *Tecta/Tectb*$^{-/-}$ mutants. The number of cells at each age and concentration is: (A) Gentamicin in P2 apical OHCs: 0.3 μM, n = 3; 3 μM, n = 4; 10 μM, n = 5; 30 μM, n = 7; 100 μM, n = 4. (B) Gentamicin in P9-P10 apical OHCs: 3 μM, n = 6; 10 μM, n = 8; 30 μM, n = 5; 100 μM, n = 4.

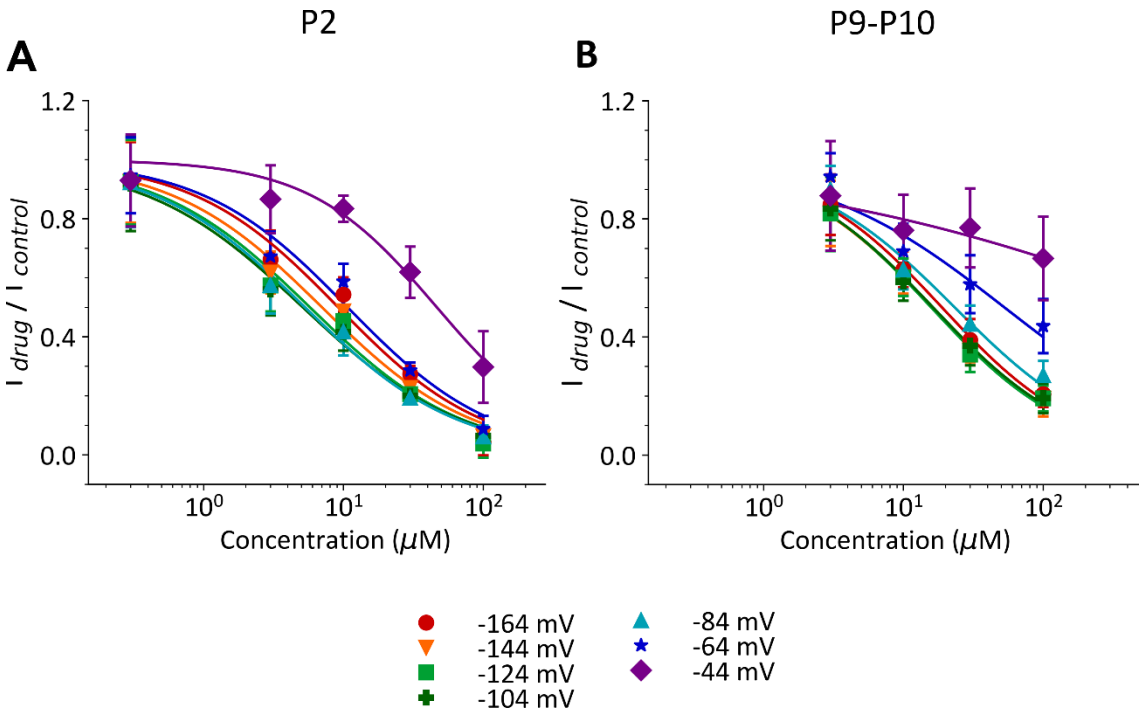

FIGURE 5-8: Dose response curves for gentamicin in P2 and P9-P10 apical OHCs of *Tecta/Tectb*$^{-/-}$ mutants. Number of cells as in **figure 5-7**.

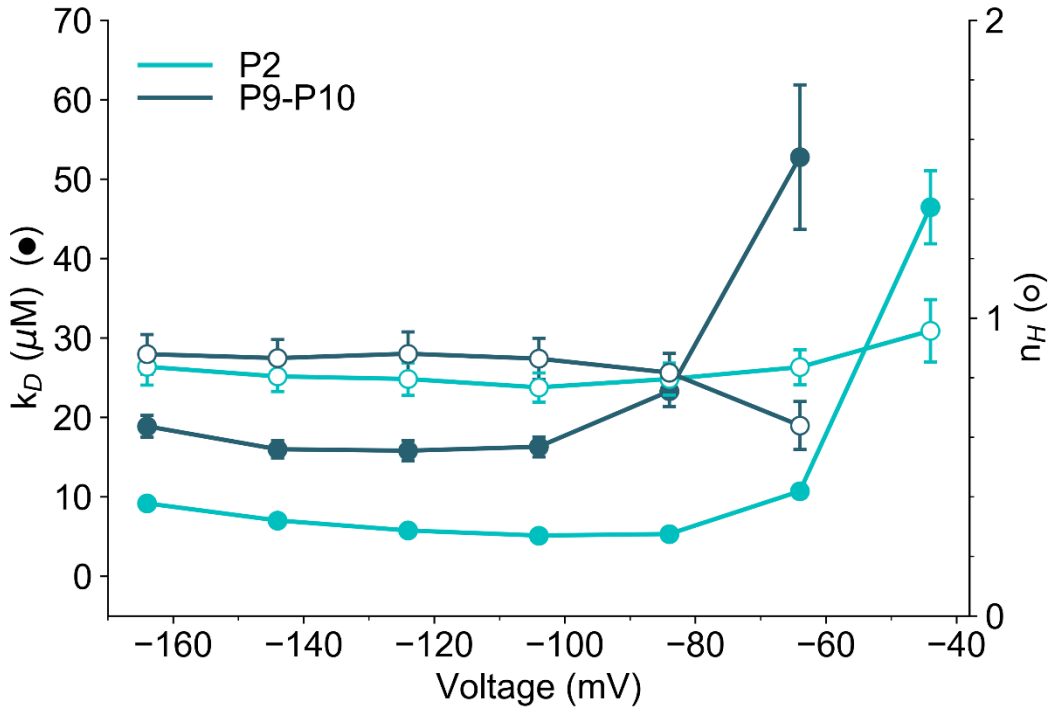

FIGURE 5-9: Voltage dependence of MET channel block by gentamicin in P2 and P9-P10 apical OHCs of *Tecta/Tectb*$^{-/-}$ mutants.

	P2	P9-P10
	Apical	Apical
V_{max} (mV)	-104	-124
K_D (μM)	5.92 ± 0.22	15.79 ± 1.26

TABLE 5-3: Maximum block of MET currents measured by gentamicin in P2 and P9-P10 apical OHCs of *Tecta/Tectb*$^{-/-}$ mutants.

5.3.4 Kinetics of gentamicin block in P9-P10 OHCs

The time constants for gentamicin in P9-P10 OHCs were much faster (as is often observed for weaker blockers) than the ones for P2 OHCs (**figure 5-10**) and the forward rate k_1 had a lower value.

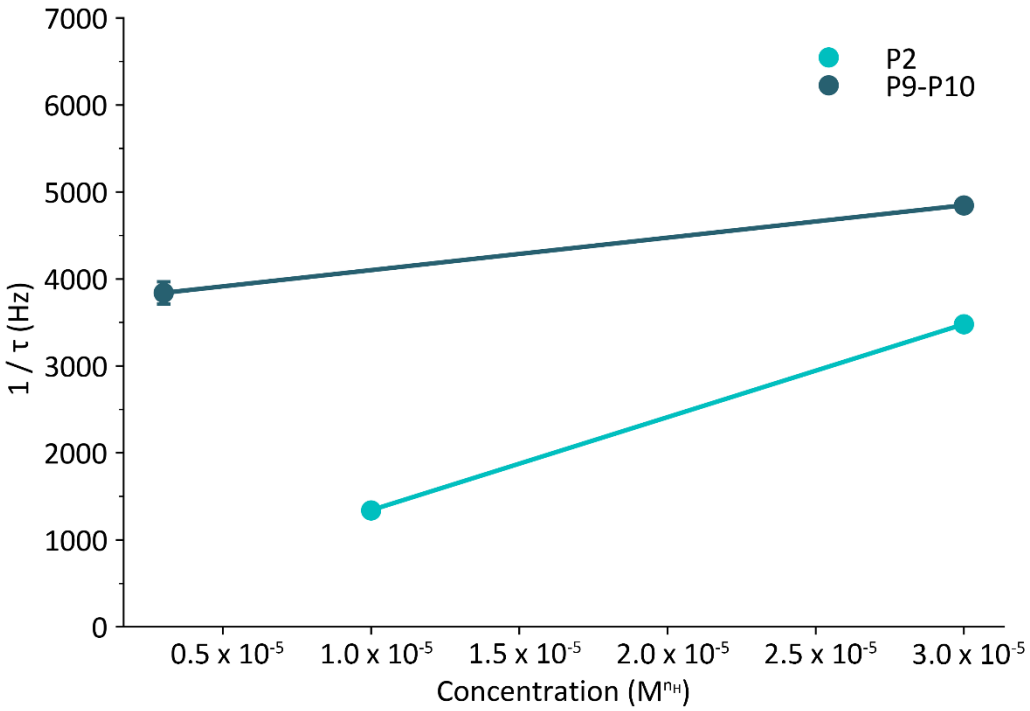

FIGURE 5-10: Time constants for gentamicin in P2 and P9-P10 apical OHCs of *Tecta/Tectb*$^{-/-}$ mutants. Number of cells at each age: P2, 10 µM, n = 3; 30 µM n = 5. P9-P10, 3 µM, n = 4; 30 µM, n = 4.

5.3.4 Modelling results

Comparing the acute apical P2 dataset in *Tecta/Tectb*$^{-/-}$ mutants to previous results for acute apical OHCs in wild type CD1 mice shows that the *Tecta/Tectb*$^{-/-}$ mutation does not drastically impact the permeation rate of gentamicin through the MET channel. Minor differences can be accounted for by smaller N numbers due to cut-off of the experiment by COVID-19. As such these datasets can be safely compared.

The energy profile of the MET channel had some interesting differences between P2 and P9-P10 OHCs, as shown in **table 5-4** and **figure 5-11** (panel A). The first energy barrier was higher in P9-P10 OHCs due to the lower k_1, but the second energy barrier was almost identical at both ages due to a difference in ΔE. In P9-P10 OHCs the apparent charge was lower, and the binding site was shifted to the left. This shift is in the opposite direction to what would be expected if the results in permeation between apex and base presented in chapter 3 were representative purely of a difference in permeation between TMC1 and TMC2.

The entry rate for gentamicin in P9-P10 OHCs was lower than it was for P2 OHCs (**figure 5-11**, panel B). This agrees with previous results found in *Tmc2*$^{-/-}$ OHCs in which a lower entry rate per channel was found than in wild type OHCs *(Corns et al., 2017)*. This difference in permeation is likely to be due to TMC2 having a slightly larger N-terminal domain which could affect the entrance energy barrier and calcium selectivity *(Goldring et al., 2019)*. Furthermore, this again supports the results from chapter 3 for which I suggested that a difference in TMC2 and TMC1 alone was not enough to account for the difference in permeation found between apex and base in neonates. There must therefore be an additional gradient in permeation of TMC1 of apical and basal MET channels, in accordance with its gradient in single channel conductance *(Ricci et al., 2003; Beurg et al., 2006; Fettiplace and Kim, 2014; Beurg et al., 2015; Beurg et al., 2018)*. Given that TMC2 is thought to have little to no gradient in conductance along the neonatal cochlea *(Beurg et al., 2018)*, it is therefore likely that TMC2 would have a similar lack of a gradient in permeation. This hypothesis remains to be tested.

	P2	P9-P10
	Apical	Apical
n_H	1	1
$k_1 (s^{-1} (M^{n_H}))^{-1}$	1.07e8 ± 2.70e2	5.82e7 ± 4.01e7
δb	0.78 ± 0.09	0.75 ± 0.29
E_b (kT)	-7.75 ± 0.95	-7.41 ± 1.57
Apparent charge	1.83 ± 0.19	1.41 ± 0.33
ΔE (kT)	6.121 ± 0.95	5.60 ± 2.57
E1 (kT)	10.97	11.57
E2 (kT)	17.09	17.17
V_0 (mV)	-104.06	-122.56
Entry at 1 uM (molecules/s)	10.15	3.99
Entry at 100 uM (molecules/s)	192.52	164.47
Half entry rate (molecules/s)	117.57	138.2
Half entry concentration (μM)	22.21	68.11

TABLE 5-4: Model results for gentamicin in P2 and P9-P10 apical OHCs of *Tecta/Tectb*$^{-/-}$ mutants.

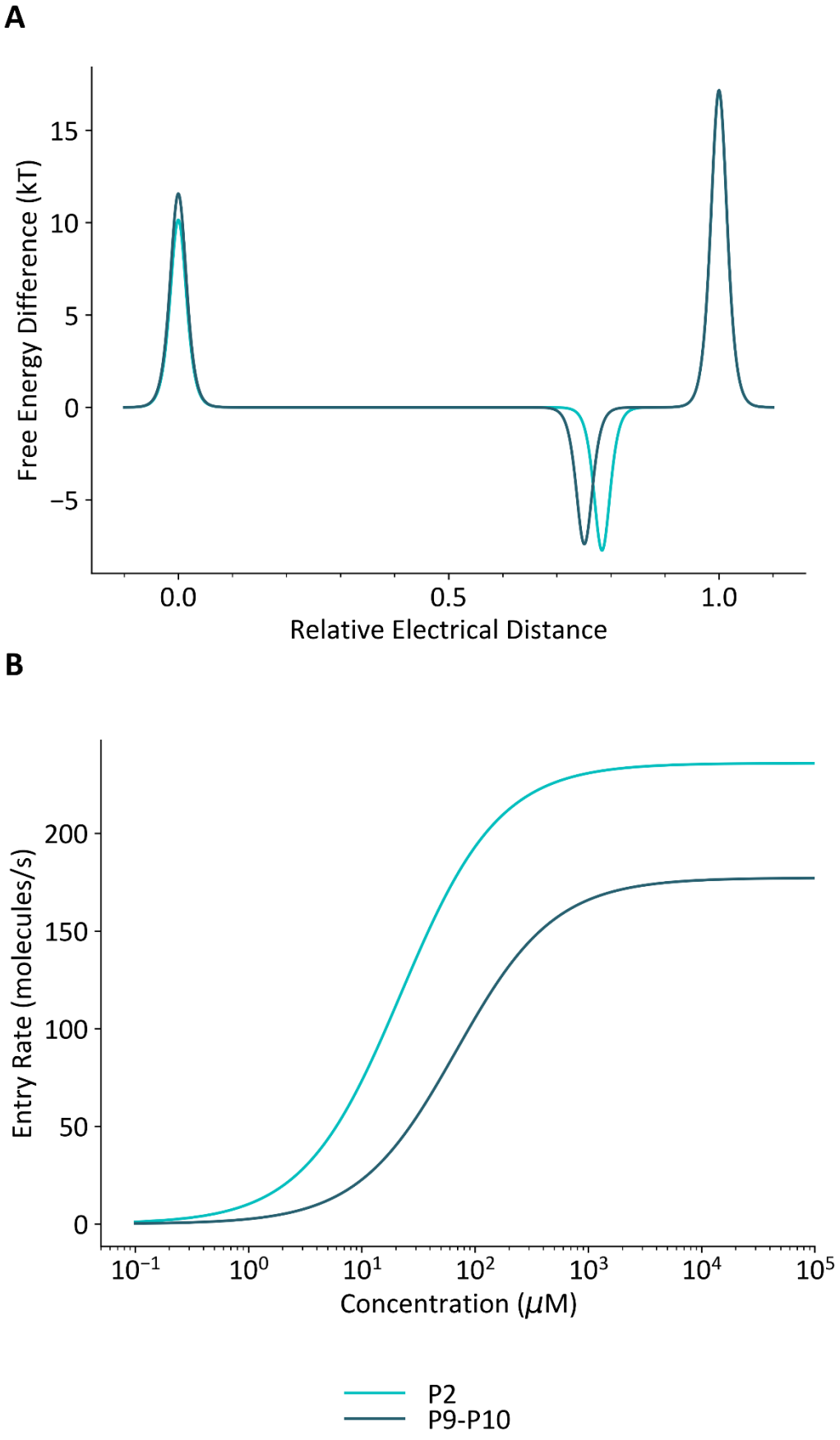

FIGURE 5-11: Energy profiles and entry rates of gentamicin in P2 and P9-P10 apical OHCs of *Tecta/Tectb*$^{-/-}$ mutants

5.4 3-dimensional entry rate modelling

For simplicity, the models of permeation rate shown thus far have all been represented as a function of concentration at a fixed voltage of -55 mV. This allows for comparison with toxicity assays in which the cells rest in culture at approximately -55 mV and the concentration of drug they are incubated in is experimentally varied. It is important to bear in mind that in a hair cell *in situ* in the cochlea, the cooperative effects of both voltage and concentration on driving force will affect permeation of drugs through the MET channel. The addition of the endocochlear potential will increase the driving force at rest to approximately -150 mV, and as the cells are active their electrical potential will constantly change. Therefore, in order to gain a broader understanding of permeation as it may occur *in vivo*, **figures 5-12** through **5-17** show each dataset thus far presented in this thesis modelled as a function of both voltage and concentration. These reveal similarities and differences between the permeation profiles of different drugs and conditions.

For example, the 3 native AGs look similar except for differences in the scale of the Y axis. Kanamycin (**figure 5-13**) is "pointier", so even though it can reach entry rates much greater than gentamicin (**figure 5-12**), it is more susceptible to driving force and only does so at the lowest voltages and highest concentrations. Kanamycin and amikacin (**figure 5-14**) look particularly alike except that the scale of the Y axis is much larger for kanamycin. Comparing these molecules this way highlights that the modification made to kanamycin to produce amikacin makes it less permeant through the MET channel. This could guide the future redesign of AGs that permeate less and are therefore less ototoxic.

As expected, the topology of GTTR permeation is very different to that of the native AGs (**figure 5-15**). In fact, in this figure the voltage is represented on a different scale, from -200 to 200 mV. The saturation of the block is clear at relatively low concentrations but lowering the voltage can continue to increase permeation.

The permeation profile of gentamicin in low calcium medium (**figure 5-16**) is uneven at high voltages and low concentrations, reflecting the sharper voltage-dependent relief in block. Permeation is consistently higher than in regular medium, but interestingly at the lowest voltage and highest concentration modelled (-200 mV and 1000 μM), the entry rate is very similar. The reason for this is unknown. The permeation profile of gentamicin in P9-P10 OHCs (**figure 5-17**) looks almost identical to that of P2 OHCs but a little lower, indicating that permeation of TMC1 and TMC2 is likely to be very similar just reduced in TMC1 compared to TMC2.

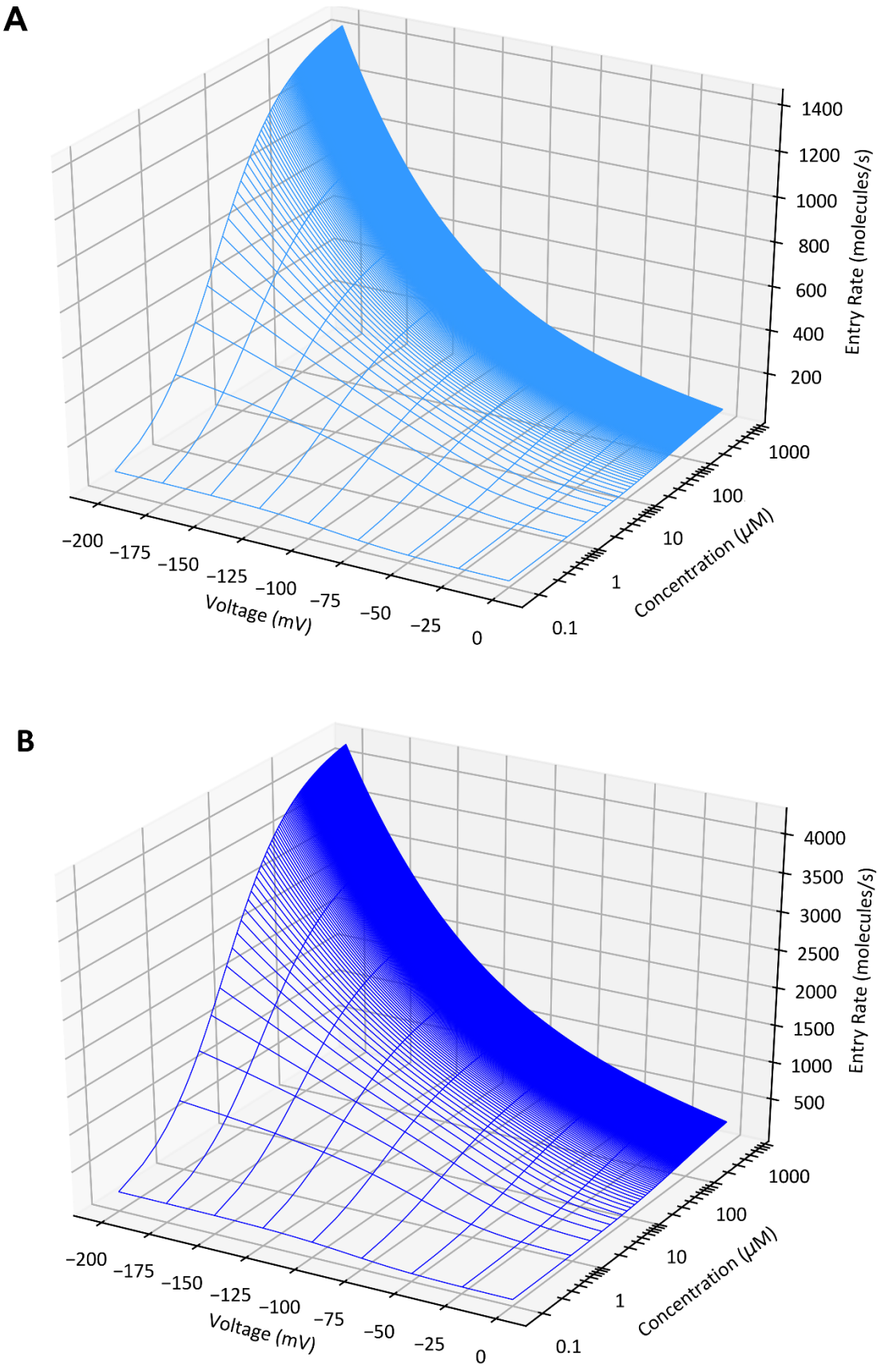

FIGURE 5-12: Entry rate of gentamicin through the MET channel of neonatal apical and basal OHCs as a function of both concentration and voltage. (A) Apical OHCs. (B) Basal OHCs.

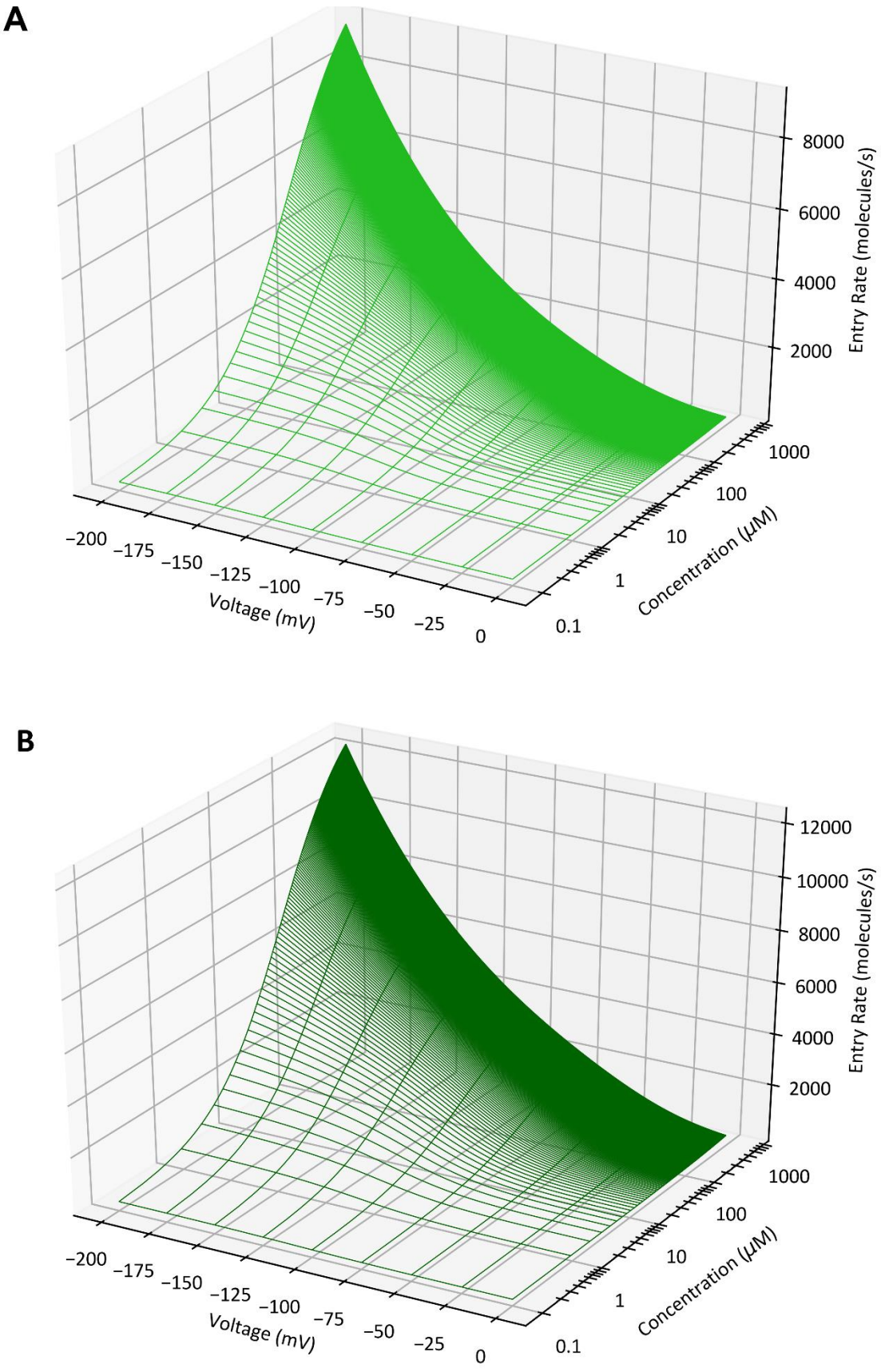

FIGURE 5-13: Entry rate of kanamycin through the MET channel of neonatal apical and basal OHCs as a function of both concentration and voltage. (A) Apical OHCs. (B) Basal OHCs.

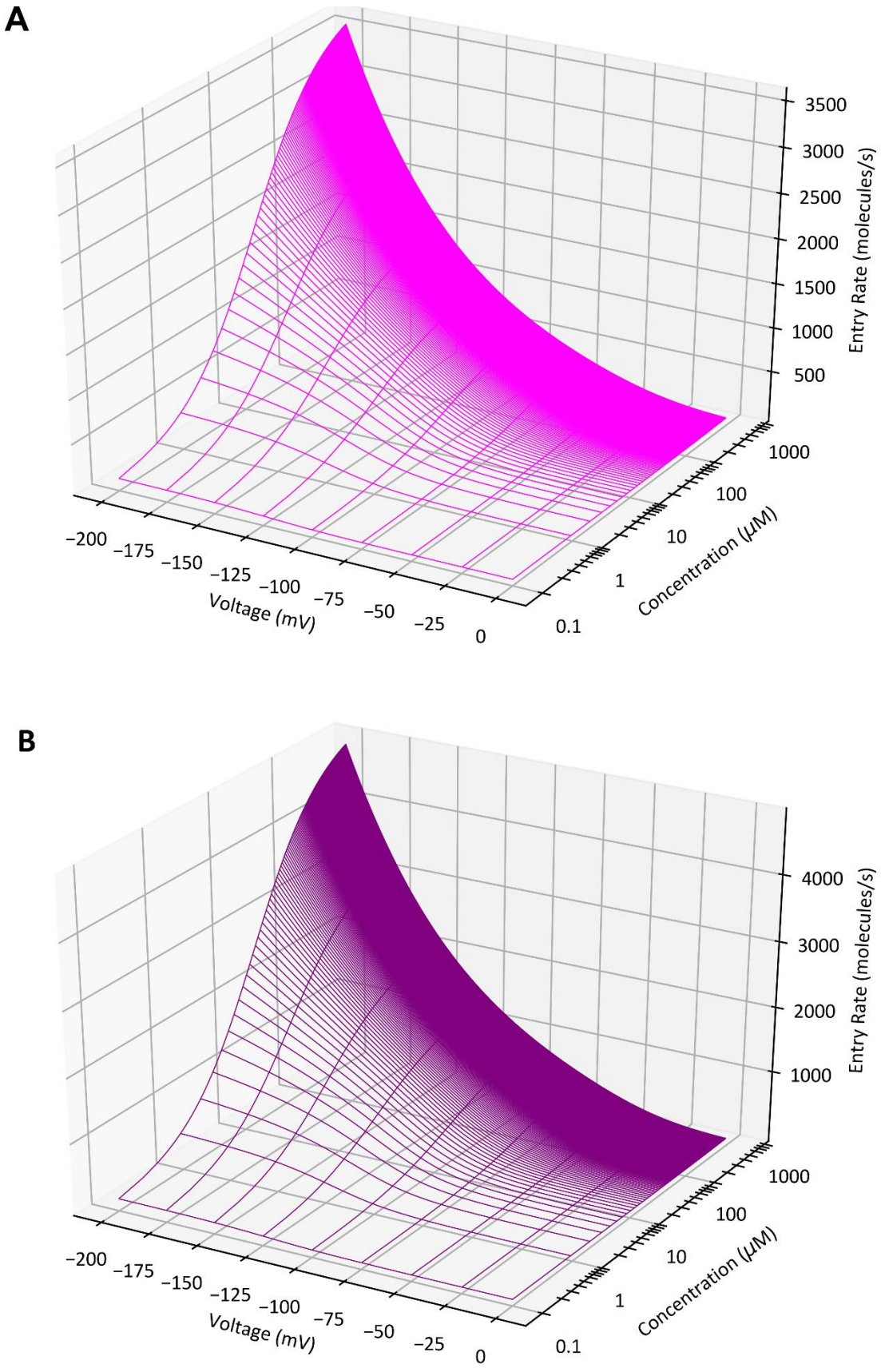

FIGURE 5-14: Entry rate of amikacin through the MET channel of neonatal apical and basal OHCs as a function of both concentration and voltage. (A) Apical OHCs. (B) Basal OHCs.

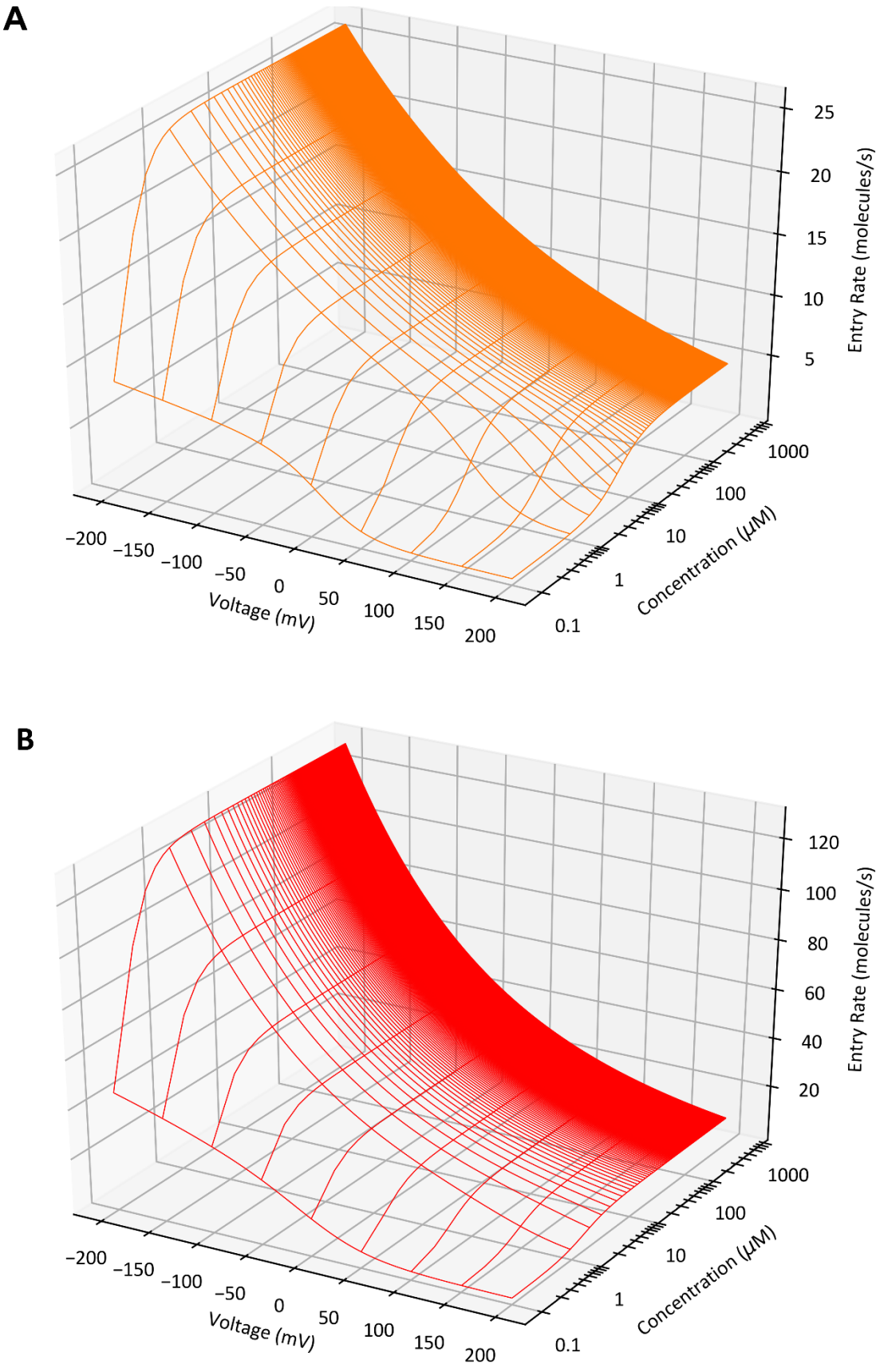

FIGURE 5-15: Entry rate of GTTR through the MET channel of neonatal apical and basal OHCs as a function of both concentration and voltage. (A) Apical OHCs. (B) Basal OHCs. Note the difference in scale of the voltage compared to native gentamicin.

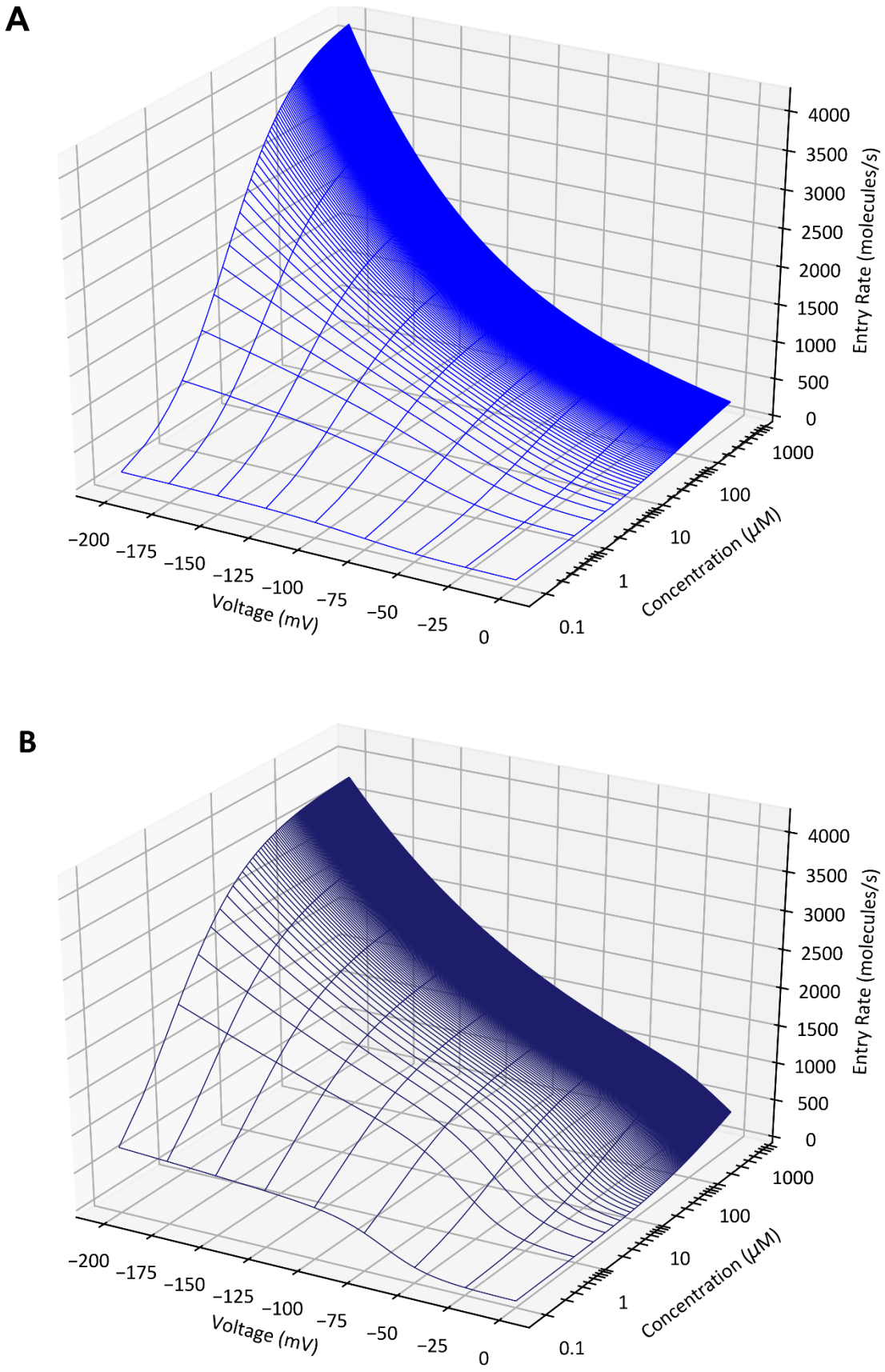

FIGURE 5-16: Entry rate of gentamicin through the MET channel of basal OHCs in regular and low calcium medium as a function of both concentration and voltage. (A) 1.3 mM Ca^{2+} (reproduced for comparison). (B) 100 µM Ca^{2+}.

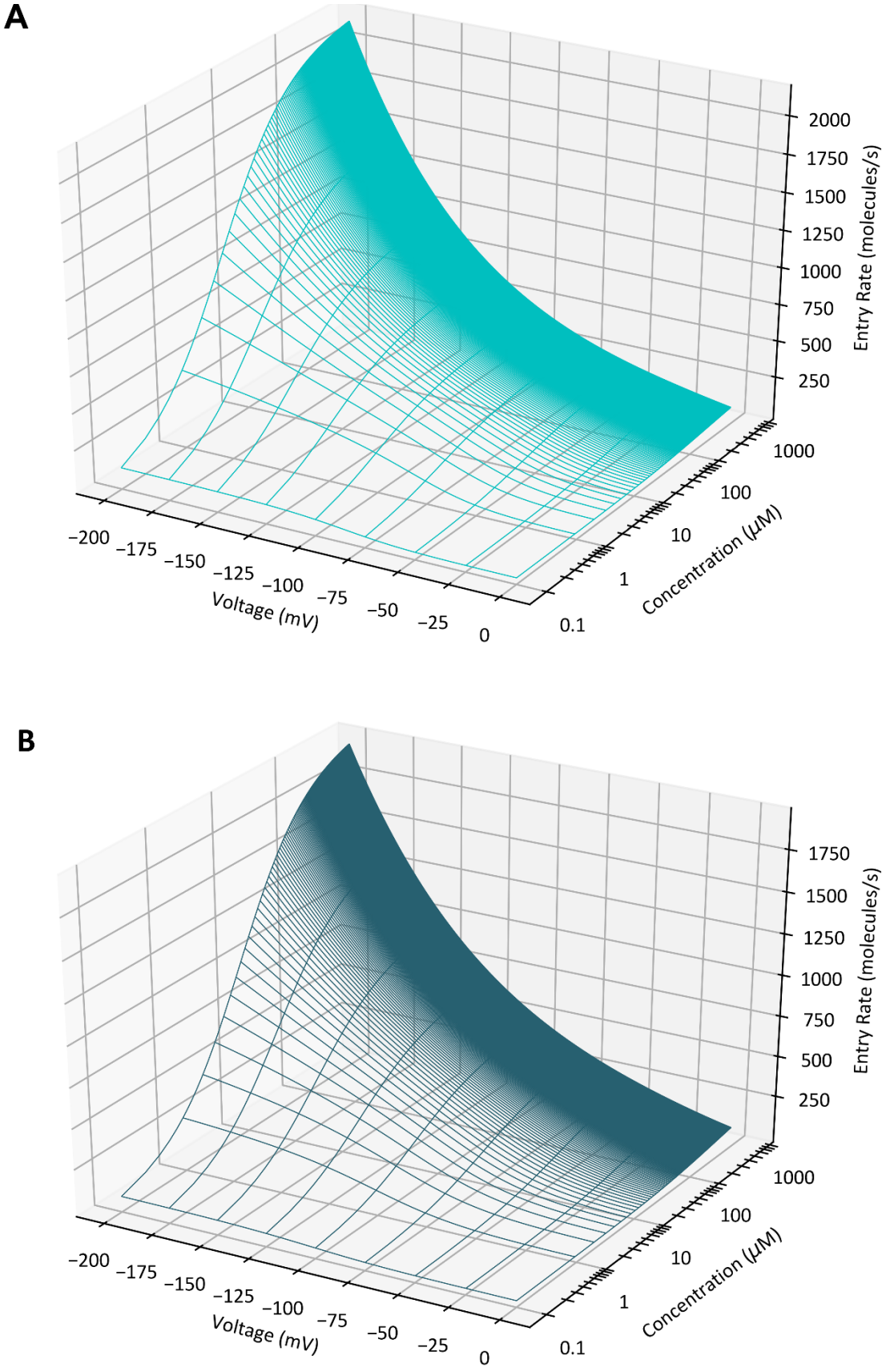

FIGURE 5-17: Entry rate of gentamicin through the MET channel of apical OHCs of P2 and P9-P10 *Tecta/Tectb*$^{-/-}$ mice as a function of both concentration and voltage. (A) P2 OHCs. (B) P9-P10 OHCs.

5.5 Discussion

With the results of these and my previous experiments I can make a prediction for the entry rate of gentamicin in apical and basal cells of a mature mouse cochlea. To summarise, the main factors that will influence entry rate of drugs into hair cells through the MET channels are: the concentration of drug, the membrane potential, the temperature, the resting open probability, the number of channels per cell, the location along the coil (as evidenced by the results in chapters 3 and 4), and the concentration of calcium. These first five parameters can be taken from the literature and the final two conditions can be extrapolated from my data.

The best estimate of a physiologically relevant concentration for AGs in the endolymphatic space that will cause ototoxicity is approximately 1 μM *(Tran Ba Huy et al., 1981; Marcotti et al., 2005)*. Furthermore, according to toxicity dose response data this is slightly below the LD_{50} in the basal turn, so should cause a low level of toxicity to basal OHCs probably similar to that seen in patients. In a mature animal, the endocochlear potential is expected to produce a driving force of approximately -150 mV into the hair cells *(Mammano and Ashmore, 1996; Marcotti and Kros, 1999; Johnson et al., 2011)*, and the body temperature of a mouse would be approximately 36°C. Given that my measurement of resting open probability of 0.15 in low calcium may be slightly low due to the negative pressure of the fluid jet, I will set it to 0.3, at the point of maximum sensitivity of the MET channel and to allow for comparison with results for DHS from Marcotti et al., 2005.

The number of channels per hair cell is a question fraught with controversy. The main issue lies with the definition of a single channel, as recent evidence suggests that each MET channel complex may contain a variable number of TMC1 dimers, each with their own permeation pore *(Beurg et al., 2018)*. Given that these multiples of TMC1 (if they do exist) are likely to be closely cooperatively gated, disentangling what is a single channel from a single pore becomes complicated. Additionally, it has long been thought that there are two MET channels per tip link (each anchored to the two bottom strands of PCDH15) *(Beurg et al., 2006)*. If, for simplicity, in our model we consider a single channel to be equivalent to a channel complex including its potential multiple TMC1 pores, we can estimate the number of channels as twice the number of tip links per hair cell, which is different between the apex and base. There are about 50 tip links per apical cell and 60 tip links per basal cell, meaning that there are likely to be approximately 100 channel complexes per apical cell and 120 per basal cell *(Beurg et al., 2006)*.

The controversy surrounding single MET channels and how this relates to our model will be discussed again in chapter 8.

Using these factors, I can extrapolate an entry rate *in vivo* from my mature and low calcium datasets. As the *Tecta/Tectb*$^{-/-}$ mutation does not appear to change MET channel permeation and the drop in permeability of gentamicin at P9-P10 agrees with what was previously found for DHS in *Tmc2*$^{-/-}$ mutants *(Corns et al., 2017)*, I can use the P9-P10 dataset as an indication of permeation in mature apical wild type OHCs. The basal OHCs are expected to have fully matured by the age in which my basal experiments were conducted *(Lelli et al., 2009)*, so I can therefore use the low calcium dataset as an indicator of entry rate in mature basal OHCs in the presence of the endolymph. I can calculate a scaling factor of how low calcium will affect permeation by dividing the entry rate in low calcium by that in regular calcium of basal OHCs and apply this factor to the P9-P10 dataset to predict the entry rate in endolymph. Finally, I can multiply these predicted entry rates by the number of channels to get an estimate of entry rate per cell per second in both mature apical and basal OHCs *in vivo*.

First, I calculated an entry rate for gentamicin in low calcium at 1 μM, -150 mV, and 36°C, with a resting open probability of 0.3. This produced an entry rate of 210.2 molecules per second per channel. Comparing this with entry rate for the same parameters in the regular calcium dataset (47.7) shows that the low calcium medium scales the entry rate at 1 μM by a factor of 4.40. Multiplying the entry rate for the P9-P10 dataset, which is 9.6 molecules per second, by this scaling factor gives 42.4. Multiplying each of these two values by the number of channels in each location (100 and 120, respectively) gives 4245 molecules per second in an apical cell and 25227 in a basal cell.

This entry rate of 4245 in mature apical hair cells is a little lower than the 9000 molecules that were predicted for DHS in neonatal apical cells *(Marcotti et al., 2005)*. For direct comparison, the same prediction for gentamicin in my neonatal apical wild type OHC dataset produces an entry rate of 8140 molecules per second, almost identical to DHS.

To conclude, these calculations predict that over 6 times more gentamicin will permeate into high frequency cells than low frequency cells of the adult cochlea. This shows that basal cells will be flooded with gentamicin compared to apical cells and leaves little room for doubt that it is primarily permeation through the MET channel that makes the hair cells more susceptible to ototoxic drugs than any other route of uptake. This also explains why patients who experience drug-induced ototoxicity selectively lose their high frequency hearing.

Chapter 6

Effects of Genetic Mutations on Calcium and Aminoglycoside Permeation through the MET Channel

6.1 Introduction

Despite extensive characterisation of the kinetics of the MET channel and its permeation profile, we still are unsure of the molecular correlates for the interaction sites of drugs permeating through the channel. In fact, at the start of this thesis the identity of the MET channel was still unknown, and only very recently has its main pore-forming subunit been identified as TMC1 *(Ballesteros et al., 2018; Pan et al., 2018)*. This identification presents new opportunities to further probe the permeation pathway and to potentially pinpoint residues within the protein that correspond to the interaction sites predicted by our model. Furthermore, the MET channel is a large complex with multiple subunits, others of which might interact with TMC1 and affect its permeation kinetics. The goal of this chapter is therefore to address how certain genetic aspects of the channel may affect our permeation model. Sections 6.2 and 6.3 of this chapter include data from collaboration with the two groups responsible for proving the MET channel pore identity. Section 6.2 will discuss how structural modelling of the channel can inform and complement biophysical modelling, and section 6.3 will describe a project designed to probe the role of the residues lining the pore in channel permeation, including one which could potentially be our predicted binding site—D569. Section 6.4 will present the results of an experiment assessing the influence of ASIC1b, a potential MET channel complex candidate, on the calcium permeability of the pore.

6.2 Structural modelling of the TMC1 pore

In 2018, Ballesteros et al. produced a model of the structure of TMC1 based on homology modelling with TMEM16, which revealed the presence of a large anionic cavity built by transmembrane helices 4-7 that could serve as a permeation pore. Following a discussion at the Association for Research in Otolaryngology MidWinter meeting in January 2020, I contacted Dr. Ballesteros to ask if she could provide insight into how her structural data might correspond with our experimental permeation data. She responded by very kindly offering to produce a series of customised figures that would highlight the areas within the TMC1 protein of particular interest to our model. These are shown in **figure 6-1**.

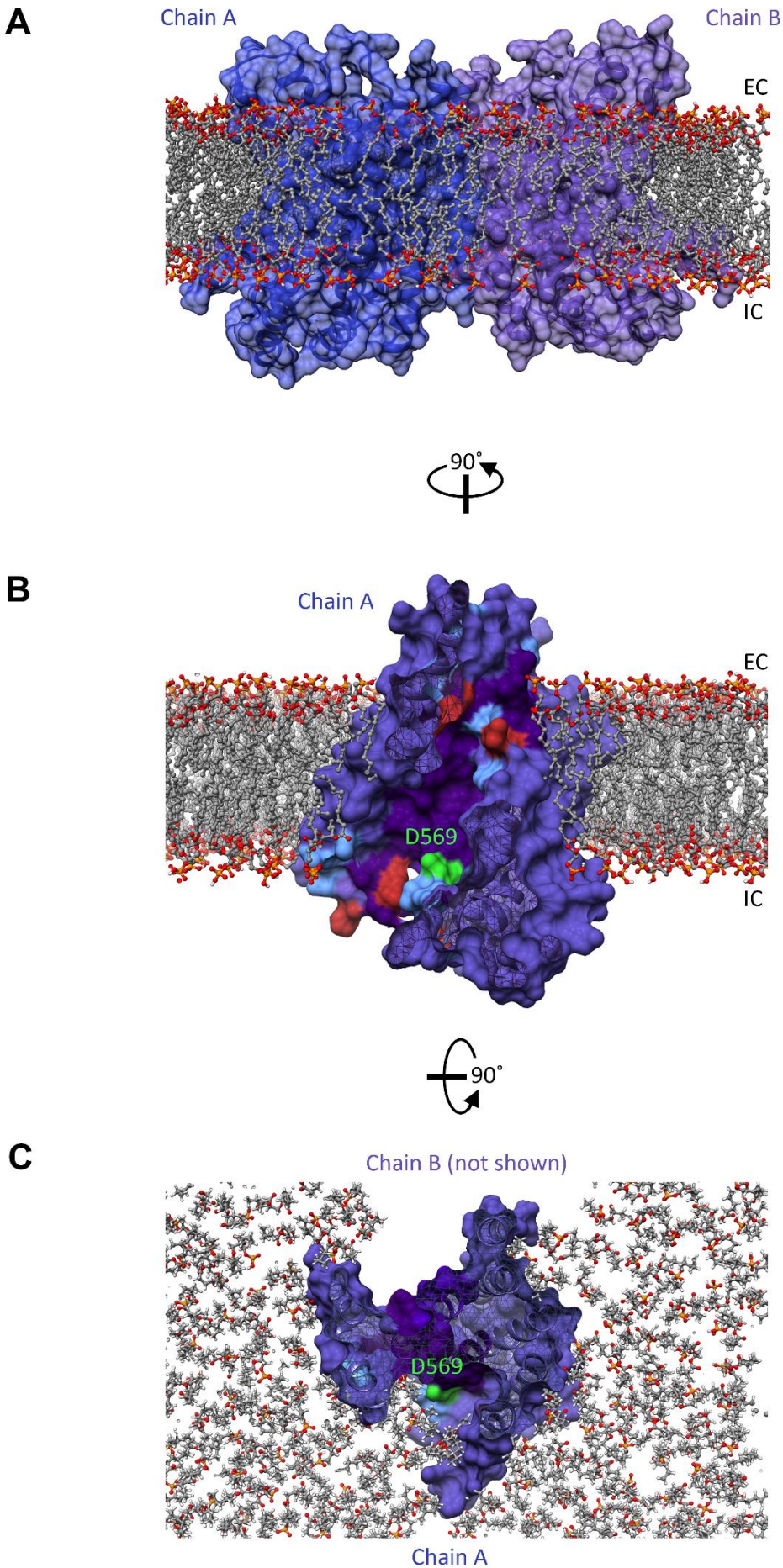
A
Chain A
Chain B
EC
IC
90°
B
Chain A
EC
D569
IC
90°
C
Chain B (not shown)
D569
Chain A

FIGURE 6-1: Structural model of TMC1 and locations of potential interaction sites. (A) Surface representation of a mTMC1 dimer in a lipid membrane. TMC1 model was built using the structure of nhTMEM16 (PDB ID: 4WIS) as a template and was placed in a lipid membrane using the OPM server and CHARMM-GUI. Each TMC1 monomer is indicated as Chain A and Chain B, and colored in blue and purple, respectively. (B) Surface representation of the cavity built by the transmembrane segments 4-7 revealing the localization of the amino acid D569 (green) and other negatively (blue) and positively (red) charged residues. (C) Top-down cross-sectional view of TMC1 at the level of the D569 residue, showing groove-like shape of the permeation pore in contact with cell membrane. The intracellular (IC) and extracellular (EC) sides are indicated in (A) and (B). The lipid molecules in all panels are shown in ball and stick representation with the carbon atoms in grey, phosphates in orange and oxygens in red. Figure graciously produced for this thesis by Dr. Angela Ballesteros (National Institute of Neurological Disorders and Stroke).

6.2.1 Discussion

This structural model reveals some fascinating aspects of the MET channel permeation pathway. Panel A shows the TMC1 dimer as it is thought to assemble, with the two TMC1 chains coloured in purple and blue, respectively. Panel B focuses on chain A looking through the side of the molecule and into the pore. This shows the areas of negative and positive charge lining the channel pore, with negatively charged residues coloured in light blue and positively charged residues in red. This pore structure can be compared with panel B of **figure 1-9** showing our schematic model based on the energy profile of the interaction with DHS *(Corns et al. 2016)*, which my results in chapters 3 and 5 further corroborate. Comparison of these models reveals that the area of negative charge near the bottom end of the pore corresponds to the predicted location of our AG binding site (though this prediction was made from the energy profiles of AG interaction which represent electrical distance and may not map directly onto physical distance). The negative residue D569 is highlighted in green and will be discussed in further detail in section 6.3. There are also areas of positive charge near the entrance and exit of the pore which correlate well with our two predicted energy barriers. The shape of the pore fits with our expectation, i.e. a narrow entrance with a large cavity in the bottom region, and an even narrower exit. This demonstrates how differential permeation of AGs may be due to size restriction at the exit—our second energy barrier—of the pore.

Most intriguingly, there are additional areas of negative charge around the entrance and exit. In fact, this results in 3 distinct areas of negative charge, which could be related to the Hill coefficient of almost 3 calculated for GTTR permeating through the channel. This raises the possibility that if GTTR could in fact bind to these areas, then potentially so could other molecules. So, although our model appears to neatly describe the method of binding of the native AGs, it could be incomplete and other molecules could have modes of binding that we are not yet aware of. For example, this could explain the mechanism by which FM1-43 permeates *(Gale et al., 2001)*, which is clearly very different to the AGs. Given the shape of the pore it is evident how FM1-43 might be able to reside inside the closed channel: the cavity is quite large, and FM1-43 is a long and thin molecule.

Finally, panel C shows a cross-sectional view of the channel at the level of the D569 residue, revealing a C-shape of the pore with cell membrane contacting one side (as described in *Ballesteros et al., 2018*). This suggests further possibilities for why GTTR may saturate the channel so readily and exhibit an unusual binding profile, as the Texas Red side chain may be "dragging" through the side of the membrane.

6.3 TMC1 pore mutation D569C

6.3.1 Introduction

The Holt group, jointly based at Boston Children's Hospital and Harvard Medical School, have developed a series of viral vectors that contain point mutations of 17 residues of TMC1 to cysteine. These vectors can be injected into *Tmc1*$^{-/-}$/*Tmc2*$^{-/-}$ early neonatal mice, leading to expression of selectively mutated TMC1 within the first few days of development. It was by using this method that the Holt lab was able to prove that TMC1 is the pore-forming subunit of the MET channel, and the results were published Cell in 2018 *(Pan et al., 2018)*. As these TMC1 point mutations would be ideal for teasing out the contributions of charged residues to the biochemical interaction between the channel and the ototoxic drugs that permeate it, we contacted the Holt lab to ask if they would be interested in a collaboration, to which they agreed.

I went to visit the Holt lab in Boston for two weeks in March 2019 to acquire preliminary data towards developing the project. For the scope of the trip we decided to focus on just one pore mutation, D569C. There were several reasons for this choice, primarily that aspartic acid (D) is negatively charged making it a candidate for the AG binding site in our model. According to the electrophysiology data in Pan et al. *(2018)*, full-sized MET currents can still be elicited from D569C mutants in IHCs, but the currents are reduced by application of MTSET (which binds irreversibly to cysteine) indicating that the residue faces the interior of the pore. In the supplementary data, they found that D569C in the utricular MET channels reduced the potency of the block by DHS. Furthermore, recent evidence by the Fettiplace group shows that D569N mouse mutants have a reduced calcium permeability compared to wild type *(Beurg et al., 2019)*. At the time the exact location of the residue within the pore was uncertain, but it was thought to be at the lower end of the cavity, further supporting it as a prime candidate for the AG binding site.

I originally aimed to do both electrophysiology in IHCs (as the uptake of the viral vectors is better than in OHCs) and immunolabelling experiments. I wanted to probe the affinity of gentamicin for the D569C MET channel in IHCs (and ideally calculate an entry rate!), but two weeks proved too little time to acquire enough viable physiology data on an unfamiliar setup. The other experiment aimed to see whether the D569C mutation would protect hair cells from ototoxicity of gentamicin over a 48 h period. This did yield some results, though at present the results are inconclusive due to a lack of confirmation of mutated TMC1 expression.

6.3.2 Methods

In preparation for the trip, we determined that a concentration of 30 μM gentamicin for 48 h would be the minimum required to produce full ototoxicity of IHCs (which are less sensitive than OHCs), making any protection conferred to IHCs by reduced uptake of gentamicin evident. Prior to my arrival, a litter of *Tmc1*$^{-/-}$*/Tmc2*$^{-/-}$ mouse pups were injected at P1 with the AAV2/1-CMV-Tmc1ex1-D569C viral vector via the round window membrane (left side only) *(Askew et al., 2015; Pan et al., 2018)*. Three *Tmc1*^{D569C}-injected pups and two wild type pups were dissected at P5 and the apical and basal turns of the cochleae were cultured separately for 24 hours through a similar process to that described in chapter 2 (fully described in *Pan et al., 2018*). 3 wild type and 3 *Tmc1*^{D569C} cultures were incubated in 30 μM gentamicin for 48 h. FM1-43FX, a fixable analogue of the fluorescent dye FM1-43 was briefly applied (~10 sec) to the cultures and washed out. FM1-43 rapidly enters the hair cells through the MET channel *(Gale et al. 2001)* and is often used as an indicator of functional mechanotransduction. The cultures were then fixed in 3.7% formaldehyde for 1 h, permeabilised in 0.1% Triton X-100, and stained with Rabbit α myosin VIIA overnight. A secondary stain of phalloidin 647 and Goat α Rabbit 555 was applied for 1 h, and the cultures were then mounted and imaged by confocal microscopy.

6.3.3 Results

The results of this experiment are shown in **figure 6-2**. It is clear that 30 μM gentamicin is sufficient for destroying the majority of hair cells in the wild type culture (panel B). It appeared that the *Tmc1*^{D569C} cultures incubated with gentamicin suffered no hair cell lost at all, in any of the 3 cultures tested and in either the apical or basal turn. However, though great care was taken (and the same batch had been successfully tested by a lab member earlier in the week), the FM1-43FX did not produce any signal under confocal microscopy. Without this signal it was not possible to conclusively determine whether the *Tmc1*$^{-/-}$*/Tmc2*$^{-/-}$ cultures were expressing the injected *Tmc1*^{D569C}, thus the protection observed could be due to a lack of functioning mechanotransduction and not protection conferred by the D569C mutation. However, to follow up on this an acute dissection of a mouse from the same litter (now P11) that had also been injected with *Tmc1*^{D569C} was made and native FM1-43 was applied to test whether this littermate had functional MET channels. FM1-43 labelling after 30 seconds could be strongly viewed under upright dissection microscope, indicating that the MET channels were in fact functional in this littermate and were likely to also be functional in the cultures presented in **figure 6-2**. Unfortunately, no images were taken of this.

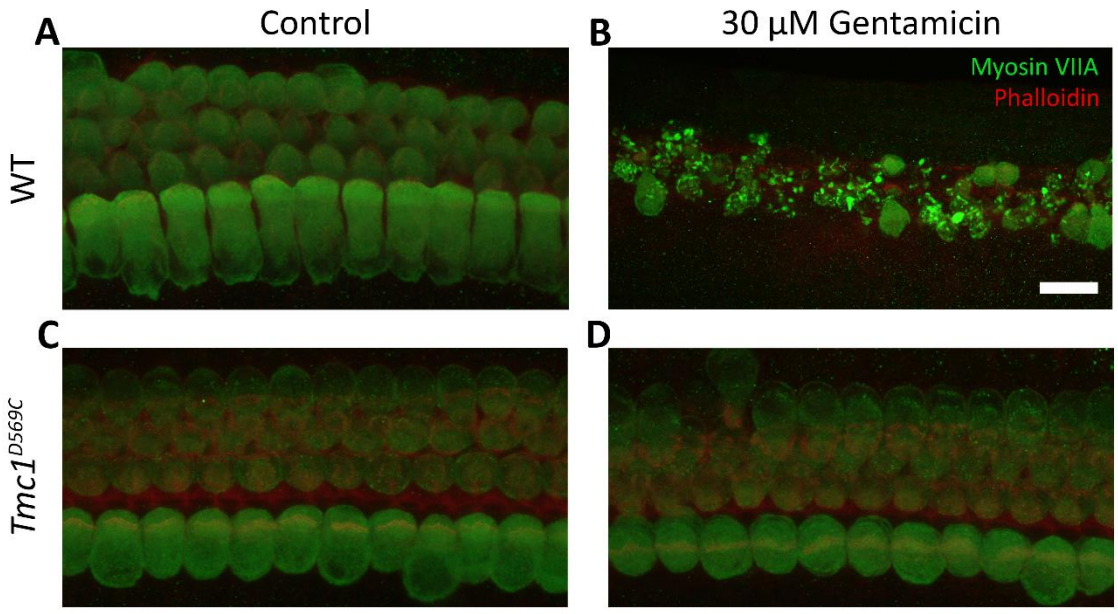

FIGURE 6-2: MET channel pore mutation D569C may confer protection against gentamicin toxicity. Cultured cochlea from wild type mice (A and B) and *Tmc1*$^{-/-}$/*Tmc2*$^{-/-}$ mice injected with *Tmc1*^{D569C} (C and D) were incubated in 30 µM gentamicin for 48 hrs (B and D). D569C mutation appears to confer protection against gentamicin toxicity (D), but *Tmc1*^{D569C} expression could not be confirmed so it is possible that protection was due to lack of functional MET. channels. Scale bar is 10 µm. These images show cells from the basal turn, but results were the same in apical and basal cells.

6.3.4 Discussion

Based on the reduced sensitivity to DHS of utricular MET currents (*Pan et al., 2018*, supplementary figure S13), we estimated that the D569C mutation should halve the toxicity of 30 μM gentamicin applied for 48 hrs in IHCs. In fact, the protection observed was stronger than anticipated, so that no gentamicin damage was seen in any *Tmc1*^{D569C} cultures. Thus, without the FM1-43 signal to prove expression of *Tmc1*^{D569C} it is difficult to say whether the cells were protected by the mutation or whether they were protected due to their lack of functional MET channels. Subsequent application of native FM1-43 to an acute cochlea taken from a co-injected littermate provided anecdotal indication that the results were genuine.

The preliminary data acquired during my trip to Boston are promising, but they are only a scratch on the surface of the experiments that would be made possible by this project. Repetition of this experiment as well as electrophysiological characterisations of *Tmc*^{D569C} cells could reveal the exact role of the D569 residue in AG binding and permeation through the MET channel. Furthermore, in their study, Pan et al., *(2018)* describe several other residue mutations that were found to have profound impacts on transduction and were likely to line the pore of the MET channel, and many of these are charged. For example, another aspartic acid-to-cysteine mutation, D528C, had a massive reduction in steady-state MET currents even before the addition of MTSET. The structural model in panel B of **figure 1-9** suggests that the D528 residue is located near the entrance of the pore and could be part of the region of negative charge seen in this region in **figure 6-1**. The reason for its drastic effect on MET currents upon mutation would be very interesting to investigate, especially given that our model does not predict a negative charge at this location. It could be playing a crucial role of balancing charge in that region, without which the first energy barrier could be too strong to let anything through, even cations.

Other mutations with a strong impact on channel currents include G411C, T532C, N447C, and M412C *(Pan et al., 2018)*. This final mutation is on the same residue as the Beethoven mutation, which was also previously found to have a reduced sensitivity to DHS when mutated to lysine *(Corns et al., 2016)*. The contribution of each of these pore-lining residues could be assessed for their impact on the permeation profile of AGs, and by this method we could determine exactly how drugs are moving through the channel and what biokinetic property of the channel makes gentamicin more permeant than amikacin, for example. Furthermore, we could assess whether the channel might have voltage-dependent changes in configuration suggested by drugs with a changing Hill coefficient such as GTTR and FM1-43.

6.4 The role of ASIC1b in calcium permeability

6.4.1 Introduction

Expression of the acid-sensing ion channel 1b (ASIC1b) has been discovered in hair cells *(Ugawa et al., 2006; Ugawa et al., 2008)* but its function is uncertain. A previous lab member discovered the presence of a current in the IHC membrane that could be elicited by drops in extracellular pH *(Roberts, 2013)*. As their name implies, ASICs conduct cations in response to increases in proton concentration. ASIC1b was therefore considered to potentially be responsible for this acid-sensitive current, but the same current could be elicited in *Asic1b*$^{-/-}$ IHCs *(Roberts, 2013)*. It is possible that other ASIC variants may also be expressed in hair cells and could be functionally redundant, thereby compensating for lack of ASIC1b. However, so far there has been no evidence for this.

Furthermore, ASIC1b has been localised to several parts of the hair cell body, and in the stereocilia. Its presence near the ankle links led to a hypothesis that it could be part of the unconventional MET channel (responsible for reverse-polarity currents observed during mechanical stimulation of the OHC membrane following deterioration of the tip links) *(Ugawa et al., 2006)*, but the identification of PIEZO2 as responsible for these currents renders this unlikely *(Beurg and Fettiplace, 2017)*. More recently it was found at the tips of the stereocilia, suggesting involvement in mechanotransduction *(Ugawa et al., 2008)*. If it is a part of the MET channel complex, its role remains unknown. Like the MET channel, it forms a potentially mechanosensitive pore that is permeable to K^+ and blocked by amiloride *(Rüsch et al., 1994; Ugawa et al., 2008)*. It was therefore considered a potential candidate for the pore of the MET channel, but subsequent confirmation of this role by the TMCs renders this hypothesis doubtful.

To determine whether ASIC1b is involved in MET channel permeation and to further our understanding of its role in hair cells, I investigated whether the *Asic1b*$^{-/-}$ mutation affects the instantaneous calcium permeability of the MET channel. This experiment involved recording MET currents under superfusion of a high calcium solution with no other free cations present either extra- or intra-cellularly and determining the membrane potential at which the flow of current carried by calcium reverses. If the permeability of calcium has been affected by the removal of ASIC1b, then the reversal potential should be shifted as was found for the *Tmc*$^{Bth/Bth}$ mutation *(Corns et al., 2016)*. A negative result for this experiment would almost definitely exclude ASIC1b from having a direct influence on the MET channel permeation pathway.

6.4.2 Methods

The data in this section were acquired and processed as described in chapter 2, with some slight differences. In this experiment, a modified superfusion solution was used containing (in mM): 100 $CaCl_2$, 20 N-methylglucamine, 6 Tris, 10 D-glucose (adjusted to pH 7.4 with HCl, osmolality ~300 mOsmol kg^{-1}). A modified intracellular solution was also used, containing (in mM): 135 CsCl, 3 MgATP, 10 Tris phosphocreatine, 1 EGTA-CsOH, 10 HEPES-CsOH (adjusted to pH 7.2 with CsOH, osmolality ~295 mOsmol kg^{-1}). These solutions were designed to restrict the passage of cations through the MET channel to calcium only (as in *Corns et al., 2016*). Voltage-step protocols from both -164 mV to +96 mV in 20 mV steps, and from -84 to +76 mV in 10 mV steps were used, with a sine wave stimulation of 45 Hz in both. The first protocol was used to allow comparison with other experiments and to show maximal current sizes (as in **figure 6-3**). The latter protocol was used to obtain a more precise resolution of the currents around the point of reversal.

6.4.3 Results

This section includes data from apical OHCs of P4-P7 C57b mouse cochleae, 7 of which were wild type and 9 were *Asic1b*$^{-/-}$. Because of the higher calcium medium, some differences are apparent in MET current characteristics opposite to the differences found in low calcium medium in chapter 5. The average MET current size was smaller than usual: at -84 mV it was -0.309 ± 0.004 nA in wild type and -0.307 ± 0.002 nA in *Asic1b*$^{-/-}$, and the average resting MET current at -84 mV was 9.19 ± 0.04% of the maximum in wild type and 9.06 ± 0.11% in *Asic1b*$^{-/-}$. These values of resting current are counterintuitively higher than in regular medium due to the smaller MET currents overall, but the smaller absolute resting current is evident in **figure 6-3**. The largest MET current recorded at -84 mV was -0.459 nA in wild type and -0.556 nA in *Asic1b*$^{-/-}$. Average cell capacitance and access resistance data are only available for a select few recordings in *Asic1b*$^{-/-}$. These values were 4.75 ± 0.047 pF capacitance (n = 2), and 4.75 ± 0.03 MΩ access resistance (n = 2), well within the range of other values reported in this thesis. The solution in the fluid jet was set to high calcium to further avoid mixing of low and high calcium in the immediate extracellular environment.

MET currents under superfusion of 100 mM Ca^{2+} solution from a total of 7 cells were recorded for the wild type mice, and 9 for the *Asic1b*$^{-/-}$ mice. An example MET current trace from each is shown in **figure 6-3**. MET current traces were averaged for each cell, and IV curves and their corresponding reversal potentials were calculated from the averaged traces (shown in **figure 6-4**). IV curves were analysed three ways to look for any sign of voltage-dependent effect: averaged, normalised to most depolarised current, and normalised to most hyperpolarised current. In each case no obvious difference can be seen. The reversal potential under control solution is normally about -5 to +5 mV and is shifted upwards by about +20 mV in high calcium medium. Reversal potentials under high calcium in wild-type and knockout were statistically tested with an independent-samples t-test and were found to have $p < 0.94$, indicating that it is highly unlikely that there is a significant difference between the two samples. Genotyping was confirmed for all cells included in the data by Professor Shinya Ugawa. From these results it does not seem that ASIC1b directly influences the calcium kinetics of the channel.

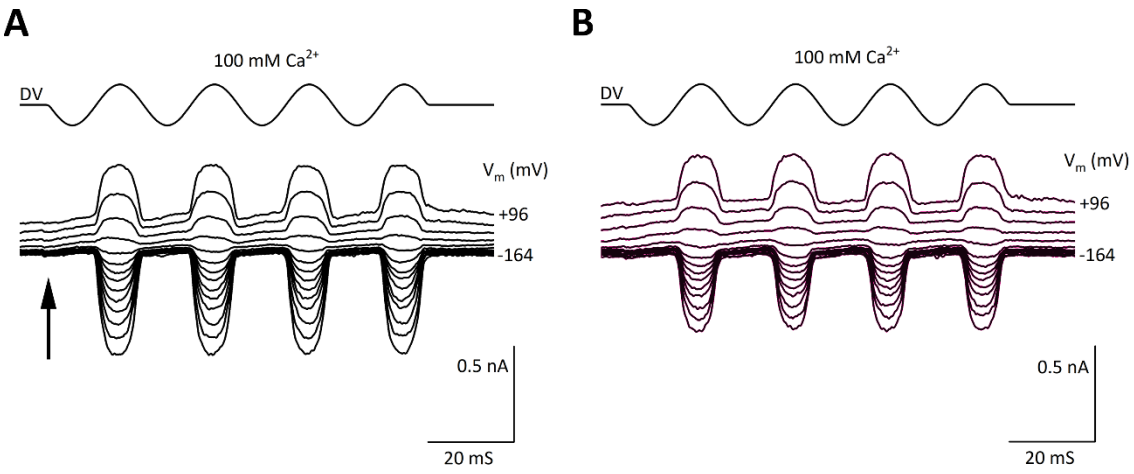

FIGURE 6-3: Examples of MET currents in 100 mM calcium medium in wild type and *Asic1b*$^{-/-}$ mice. (A) Wild type. (B) *Asic1b*$^{-/-}$. The arrow highlights the decreased resting current compared to experiments in 1.3 mM Ca^{2+} such as in Chapters 3,4, and 5.

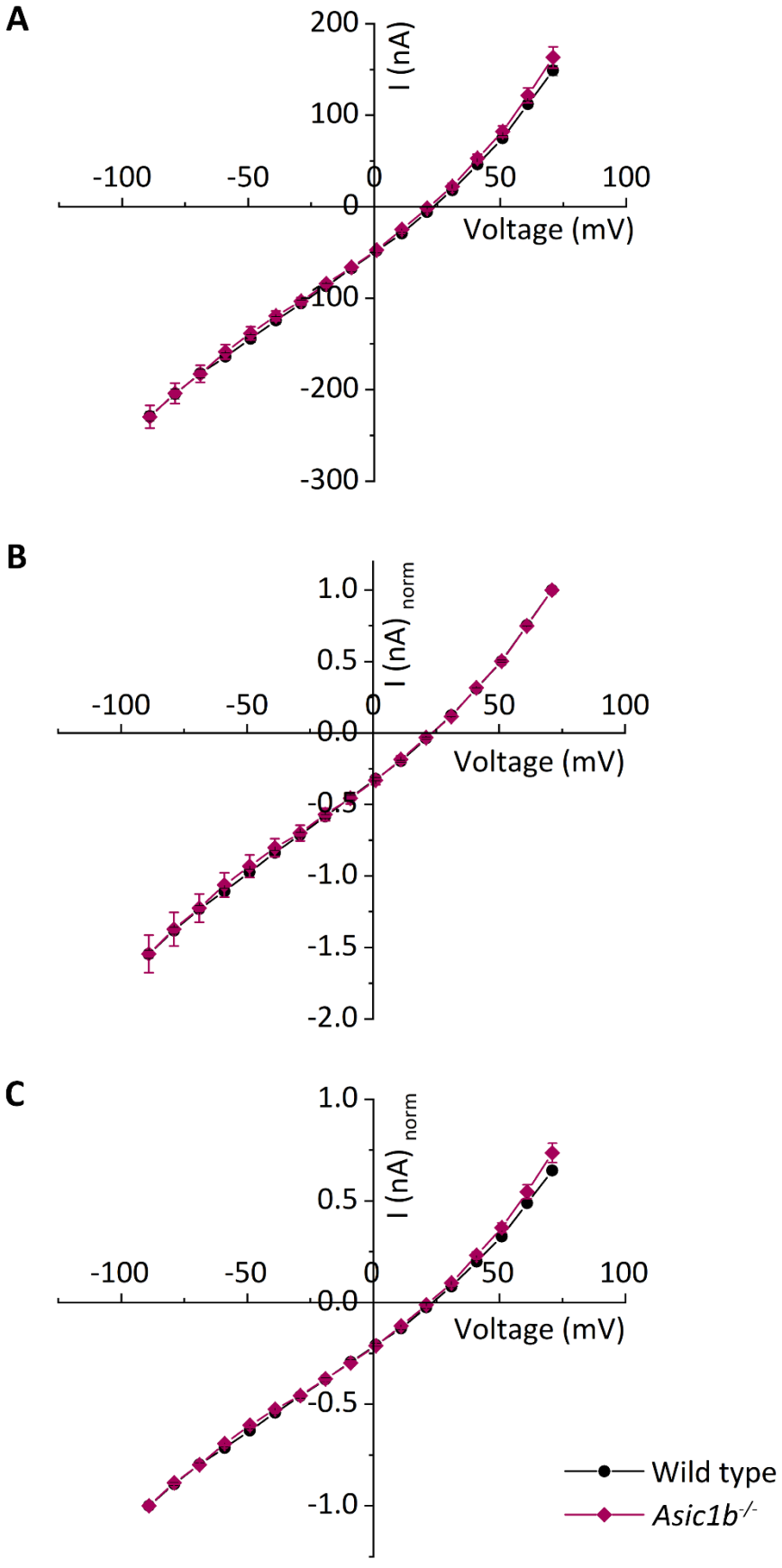

FIGURE 6-4: IV curves for wild type and *Asic1b*$^{-/-}$ OHCs. (A) All IV curves averaged together. (B) IV curves normalised to the most positive potential. (C) IV curves normalised to the most negative potential. Number of cells in each condition: wild type, n = 7; *Asic1b*$^{-/-}$, n = 9 .

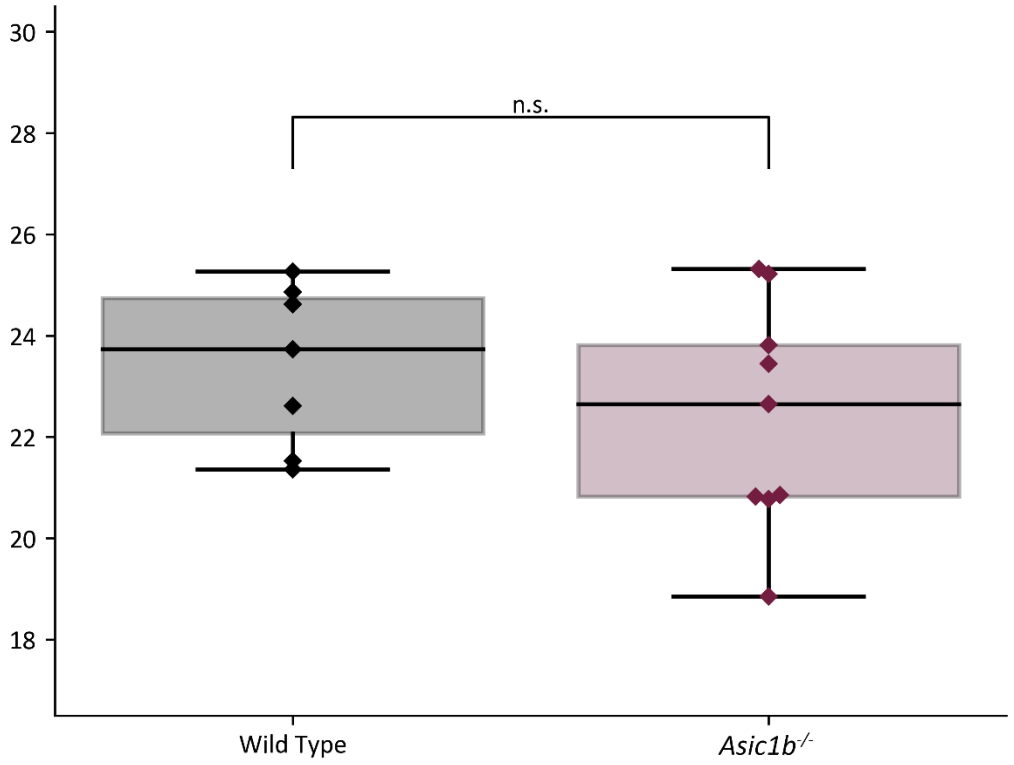

FIGURE 6-5: Reversal potentials for wild type and *Asic1b*$^{-/-}$ OHCs in 100 mM Ca^{2+} medium. Number of cells for each condition: wild type, n = 7; *Asic1b*$^{-/-}$, n = 9 .

6.4.4 Discussion

These results indicate that ASIC1b does not modulate calcium sensitivity of the MET channel, and therefore further support the role of the TMCs as the pore-forming subunit. Nevertheless, even though ASIC1b does not appear to directly impact permeation, its location at the tips of the stereocilia suggests that it could still have some other role in the MET channel complex. Furthermore, as with the acid-sensitive currents, if other ASIC subunits are indeed present in hair cells then we cannot exclude that they could be functionally redundant and compensating for the lack of ASIC1b.

Chapter 7

Volume Regulated Anion Channels: an Alternative Route of Ototoxic Drug Permeation in Hair Cells?

7.1 Introduction

Volume-regulated anion channels (VRACs) allow cells to respond to osmotic changes in their environment. They play an essential role in several fundamental cellular functions *(König and Stauber, 2019)*, and are seemingly ubiquitous in mammalian cells *(Stauber, 2015)*. VRACs are activated in response to swelling of the cell and allow efflux/influx of ions followed by water to produce a phenomenon called regulatory volume decrease (RVD) *(Stauber, 2015)*. Like the MET channel, their unitary conductance is large (10-20 pS inward and 40-80 pS outward) *(Hoffman et al., 2015; König and Stauber, 2019)*, and they can be permeated and blocked by a variety of molecules *(Friard et al., 2017)*. Though intuitively they should be mechanically gated, it is presently unclear how VRACs are activated. Reports of VRAC-mediated RVD current through stimulation by cellular injection without changes in osmotic pressure are mixed *(König and Stauber, 2019)*, and there are multiple reports of activation through various intracellular signalling pathways *(Best and Brown, 2009; König and Stauber, 2019)*. Their molecular identity was proven just 6 six years ago and was found to be a complex of multiple subunits of the LRRC8 family, most prominently LRRC8A *(Voss et al., 2014)*.

The role (or even existence!) of VRACs in hair cells has, to my knowledge, never been investigated. According to RNA-sequencing data made available through the gEAR portal (https://umgear.org/), both of the main VRAC subunits, LRRC8A and LRRC8D, are expressed throughout the organ of Corti, including by the hair cells. If VRACs are indeed active in OHCs, their non-selective permeability raises the possibility of VRAC-mediated ototoxin entry and may be relevant for some compounds that demonstrate behaviours in hair cells that are currently unexplained, like cisplatin.

A potential avenue of interest in hair cells is that VRACs could be interacting with AGs. When AGs are first applied to OHCs numerous large membranous blebs appear on the apical surface of the cells *(Goodyear et al., 2008; Osgood, 2020)*. These blebs can be fully endocytosed by the cell so long as AGs are soon washed out. This process can be blocked by the co-application of niflumic acid, which inhibits VRACs *(Osgood, 2020)*. This suggests that VRACs are involved with cellular membrane repair following insult, and that AGs block this repair process leading to increased damage of the cells. Furthermore, AG loading is potentiated by inflammation *(Koo et al., 2015)* and osmotic stress *(Osgood, 2020)*, further suggesting the possibility of AG permeation through activated VRAC channels.

Cisplatin is a platinum-based anticancer drug that is also, unfortunately, ototoxic. At low doses it causes selective OHC death in a tonotopic gradient like that of the AGs. Abolishing mechanotransduction protects from cisplatin toxicity *(Thomas et al., 2013)*, and several compounds that protect against AG-induced ototoxicity also protect against cisplatin, including ORC-13661, berbamine and d-turbocurarine *(Kitcher, 2019)*. But the similarities between cisplatin and the AGs end here. In high doses, cisplatin produces damage to other cells of the organ of Corti, and its tonotopic gradient in ototoxicity is less pronounced than it is for gentamicin *(Kitcher, 2019)*. The entry mechanism of cisplatin into hair cells has not yet been proven as it does not seem to block the MET channel, even in low calcium medium (**figure 7-1**). VRAC downregulation is connected to halting of apoptosis and is thought to be a mechanism for cisplatin resistance in tumour cells *(Planells-Cases et al., 2015)*, indicating that cisplatin may enter cells through VRACs. Additionally, one study found that about 50% of cisplatin uptake in HEK cells depended on expression of the main LRRC8 subunits, and that uptake was increased by activation of VRACs *(Planells-Cases et al., 2015)*. A later study found that overnight incubation with cisplatin profoundly potentiated the RVD current in HEK cells expressing VRACs, and this did not happen in cells without VRACs *(Gradogna et al., 2017)*.

There are other channels present in hair cell membranes that are permeable to AGs and possibly to cisplatin. For example, TRPA1 channels are permeable to GTTR when activated with an agonist that is present in the cochlea during oxidative stress *(Stepanyan et al., 2011)*. Mechanically activated Piezo2 channels in the membrane have also been shown to interact with DHS, but with a lesser affinity than with the MET channel suggesting less permeation of AGs *(Marcotti et al., 2014; Beurg and Fettiplace, 2017)*. But research into the contributions of these channels to AG toxicity in hair cells has been relatively quiet recently due to the discovery that permeation through the MET channel was the primary route of AG entry *(Marcotti et al., 2005)*.

The recent observation regarding the effect of neomycin on membrane bleb endocytosis during hair cell repair *(Osgood, 2020)* brings VRACs into focus as a new avenue of research to potentially prevent ototoxicity. VRACs, if they are indeed present in OHCs, could be an alternative route of entry into hair cells for ototoxic drugs and could present a novel therapeutic target for otoprotection. To test whether VRACs are active in hair cells, I measured the macroscopic voltage-dependent current and resting current before and during osmotic stress on cultured OHCs via whole-cell patch-clamp. As a preliminary experiment, I then co-applied three compounds of potential interest (niflumic acid, neomycin, cisplatin) during osmotic stress to determine if these interact with the VRAC current and potentially permeate through the channel.

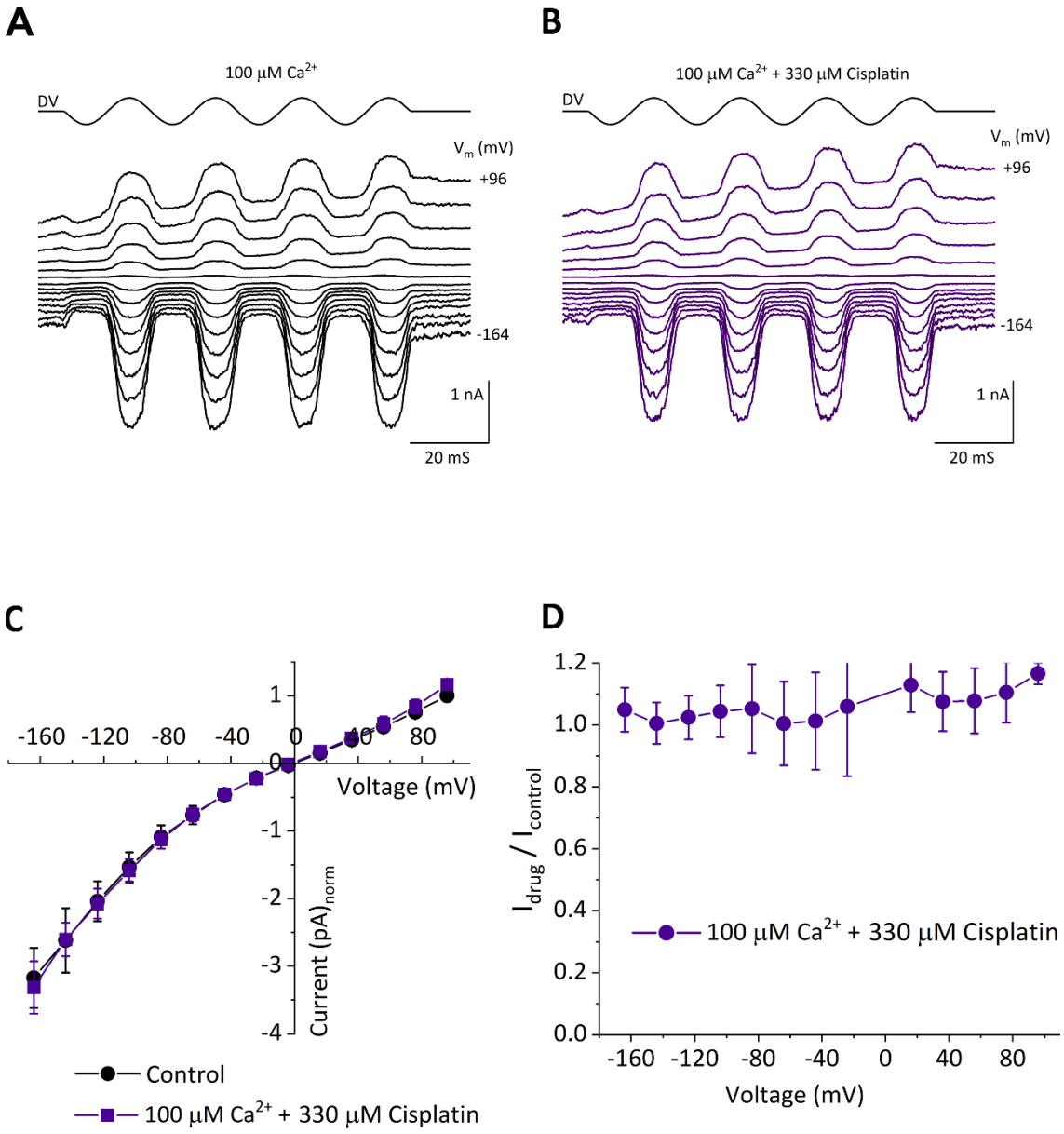

FIGURE 7-1: Cisplatin does not block the MET channel. (A-B) Example MET currents before and during application of 330 µM cisplatin in 100 µM Ca^{2+} medium (Note: linear leak of ~ 0.1 µS subtracted from both examples). (C) IV curves normalised to current at most depolarised potential. (D) Fractional block curve obtained by dividing IV curves. No evidence of block is visible. Number of cells in (C-D): 3.

7.2 Methods and results

The data in this section were acquired as described in chapter 2 except for a few differences that will be described here. No fluid jet was used as no MET currents were elicited. Two modified superfusion solutions were used. The base low osmolality solution contained (in mM): 88 NaCl, 5.33 KCl, 5.55 Glucose, 0.33 NaH_2PO_4, 0.44 KH_2PO_4, 4.17 $NaHCO_3$, 0.41 $MgSO_4$, 0.49 $MgCl_2$, 10 HEPES, 1.2 $CaCl_2$, and had an osmolality of 204 mOsmol kg^{-1}. Into this was added 100 mM mannitol to bring the osmolality to 312 mOsmol kg^{-1}. The first solution was used in the hypotonic condition and the second was used in the isotonic condition. The intracellular solution was the standard caesium-based solution described in chapter 2 to block most of the voltage-dependent basolateral K^+ current of the OHCs. The recording protocol consisted of ten repeats of a 500 ms voltage ramp from -104 mV to +96 mV followed by a rest period of a further 500 ms at -84 mV. Recordings were digitally time-stamped, and repeats were averaged post-hoc. The resting current was calculated as the average of the final 250 ms of each averaged recording.

Patched OHCs were locally perfused with control isotonic 100 mM mannitol solution for 1 to 5 minutes. Voltage ramps were applied every 10-30 seconds for the duration of the experiment. During this time no changes in cell morphology, resting current, or voltage-dependent current were observed. The solution was then switched to the hypotonic solution of 0 mM mannitol. All cells in the field of view visibly swelled in size within approximately 1 minute (**figure 7-2**). The resting membrane current dropped significantly, and a rectifying current with a reversal potential of approximately -5 to -10 mV was observed during voltage ramps (examples shown in **figure 7-3, figure 7-4**). These changes were usually followed shortly by cell death; all but one patched cell exploded after less than 2 minutes in hypotonic solution. This cell was recovered by switching back to isotonic solution. The resting membrane current following recovery returned halfway to the level of the control current, and the currents during voltage ramps decreased back to control. The currents from this cell are shown in **figure 7-4**. Due to the close match of the behaviour of these currents with the descriptions in published literature, we concluded that these were indeed VRAC-mediated RVD currents in OHCs.

VRAC currents were elicited from a total of 5 apical OHCs of P2+1 and P2+2 cultured CD-1 mouse cochleae. The average peak VRAC current size (with current at rest subtracted) at -104 mV was –158.15 ± 88.08 pA and at +96 mv was 149.79 ± 88.98 pA. The average resting current before osmotic stress was -25.09 ± 9.85 mV and during osmotic stress the resting current peaked on average at -133.15 ± 62.34 mV. The largest VRAC current recorded at -104 mV was -285.16 pA and at +96 mV was 267.64 pA. The average cell capacitance was 5.6 ± 0.03 pF and access

resistance was 5.6 ± 0.09 MΩ. Currents from an additional 2 cells were recorded but these were likely patched too quickly after return to superfusion of isotonic solution from the previous cells as on analysis they appeared to already have large rectifying VRAC currents that did not further increase when changing to hypotonic solution. A comparison with isotonic currents could therefore not be made and these cells were excluded from analysis. Some of this effect to a lesser extreme is visible in panel A of **figure 7-4**.

Further to this, three compounds were each co-applied to wild type cells during osmotic stress: niflumic acid, neomycin, and cisplatin. The results are shown in **figure 7-5**. Each graph includes the same five control cells as previously described, and three cells with drugs applied. Though the results are preliminary, all three compounds exhibited some degree of block of the VRAC current. The strongest block was seen by neomycin, bearing mind that a relatively high concentration was used. Intriguingly, some degree of block by cisplatin can be seen in panel C, though only one cell lasted for long enough to be able to see this effect and it was not as strong as either niflumic acid or neomycin. This delay in activation of VRAC currents measured at -100 mV indicates that all three compounds may block inward VRAC currents. No block or delay in activation was seen in currents at +100 mV measured over the same time period (data not shown), so it is possible that these compounds act as extracellular pore blockers of inward currents.

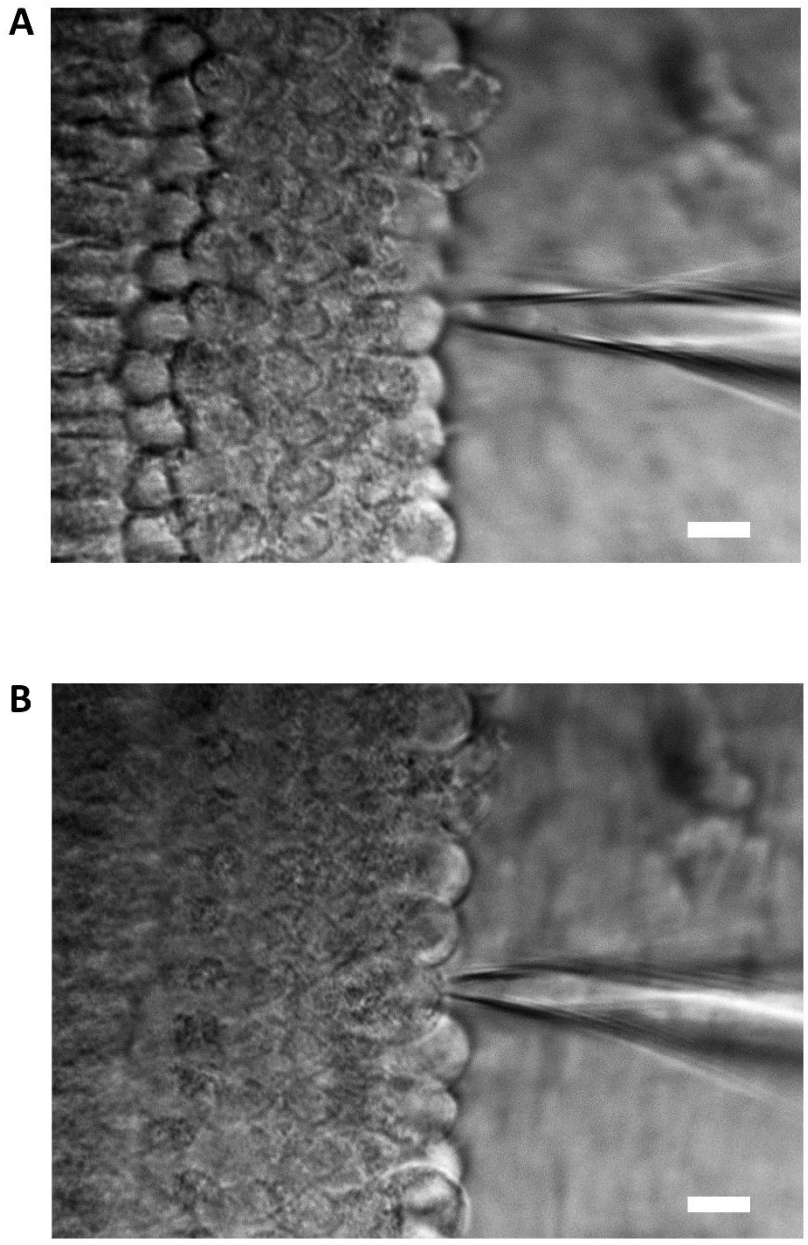

FIGURE 7-2: OHCs before and during osmotic stress. (A) Superfusion of 100 mM mannitol solution. (B) Superfusion of 0 mM mannitol solution. Osmotic stress causes swelling of cells and rounding of hair bundles. Scale bars are 10 μm.

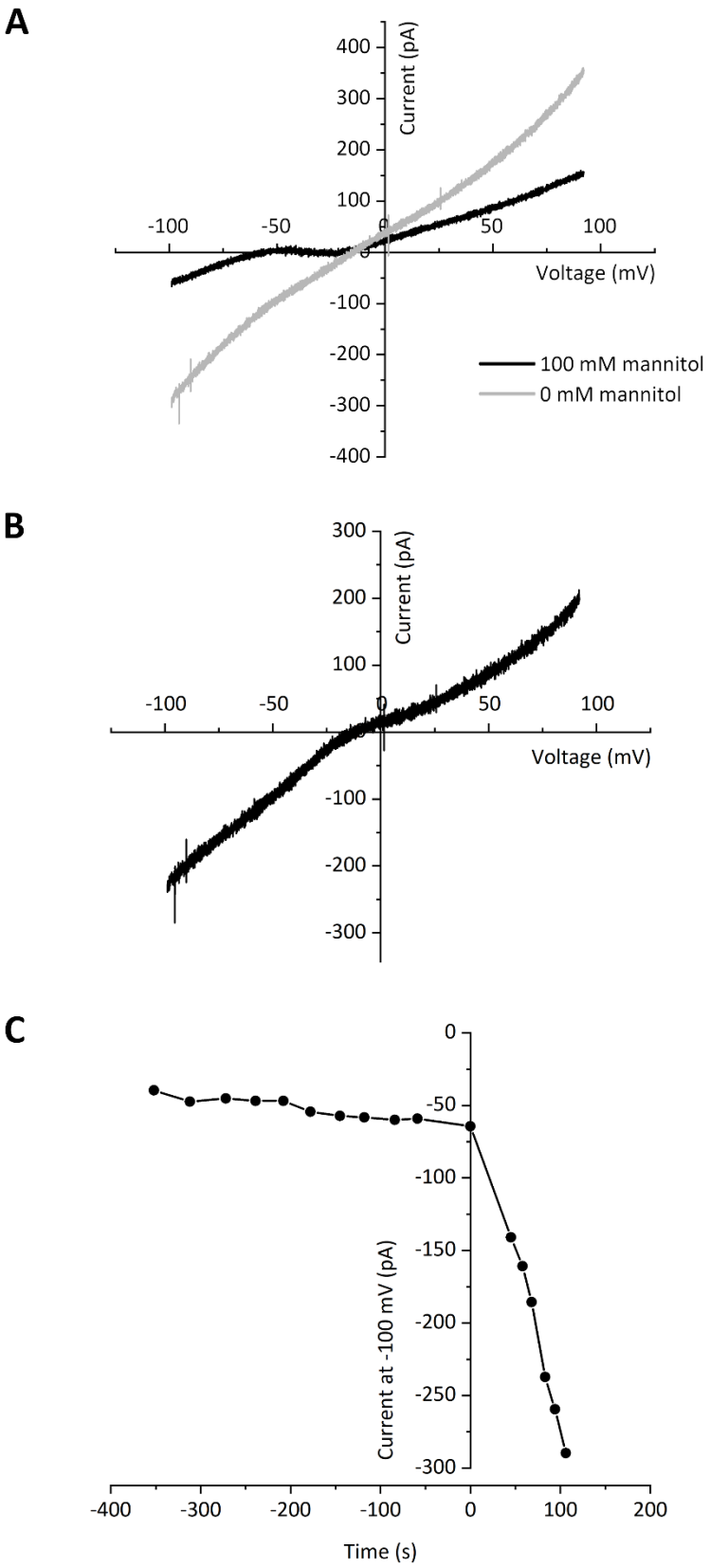

FIGURE 7-3: Example of VRAC currents in OHCs. (A) Whole cell current before and during osmotic stress induced by superfusion with hypotonic solution (0 mM mannitol). (B) Resting current subtracted from current during osmotic stress, giving current due to activation of VRAC. (C) Resting current at -84 mV over time, with change to hypotonic solution at time 0.

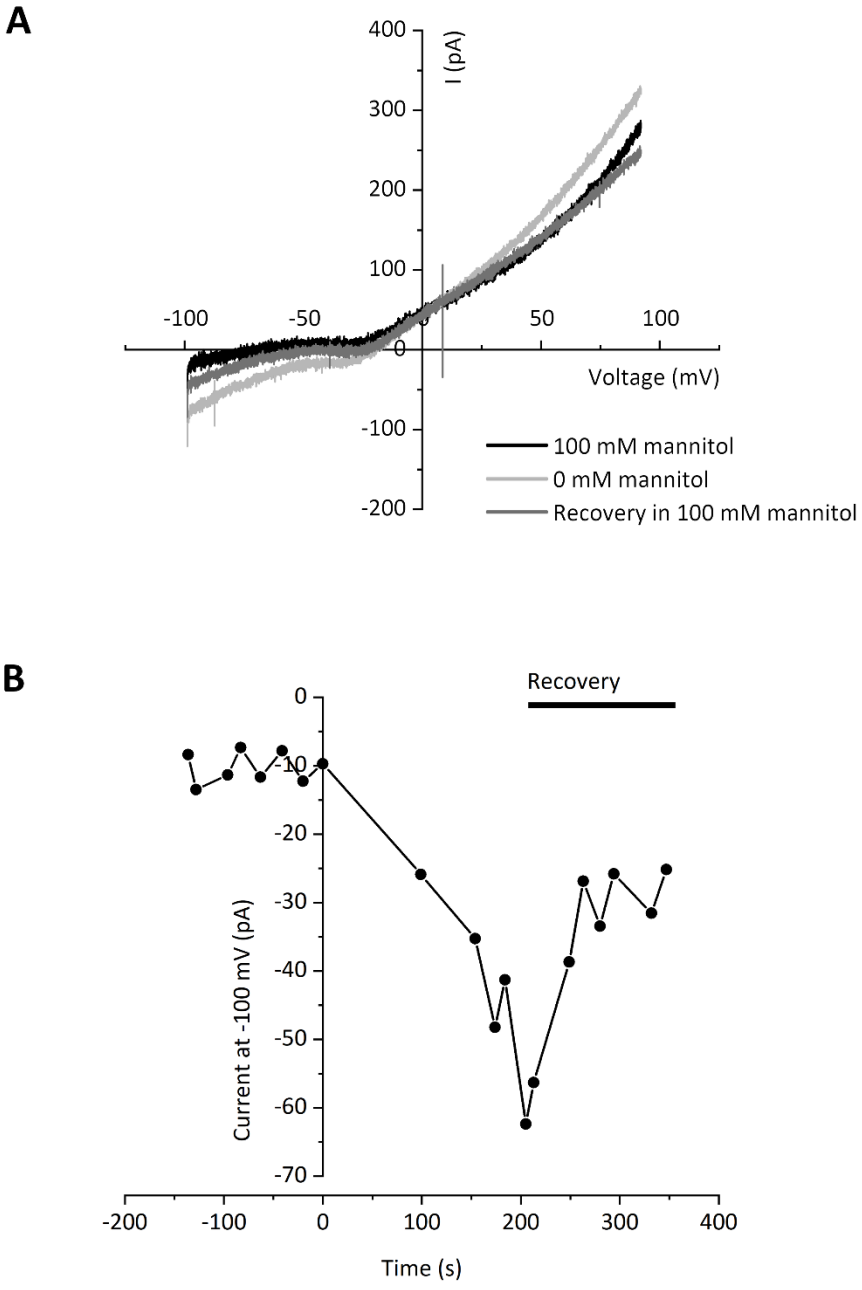

FIGURE 7-4: Cell with recovery from osmotic stress. (A) Whole cell current before, during and after superfusion with low osmotic pressure solution (0 mM mannitol). (B) Resting current at -84 mV returned halfway to normal before patch was lost.

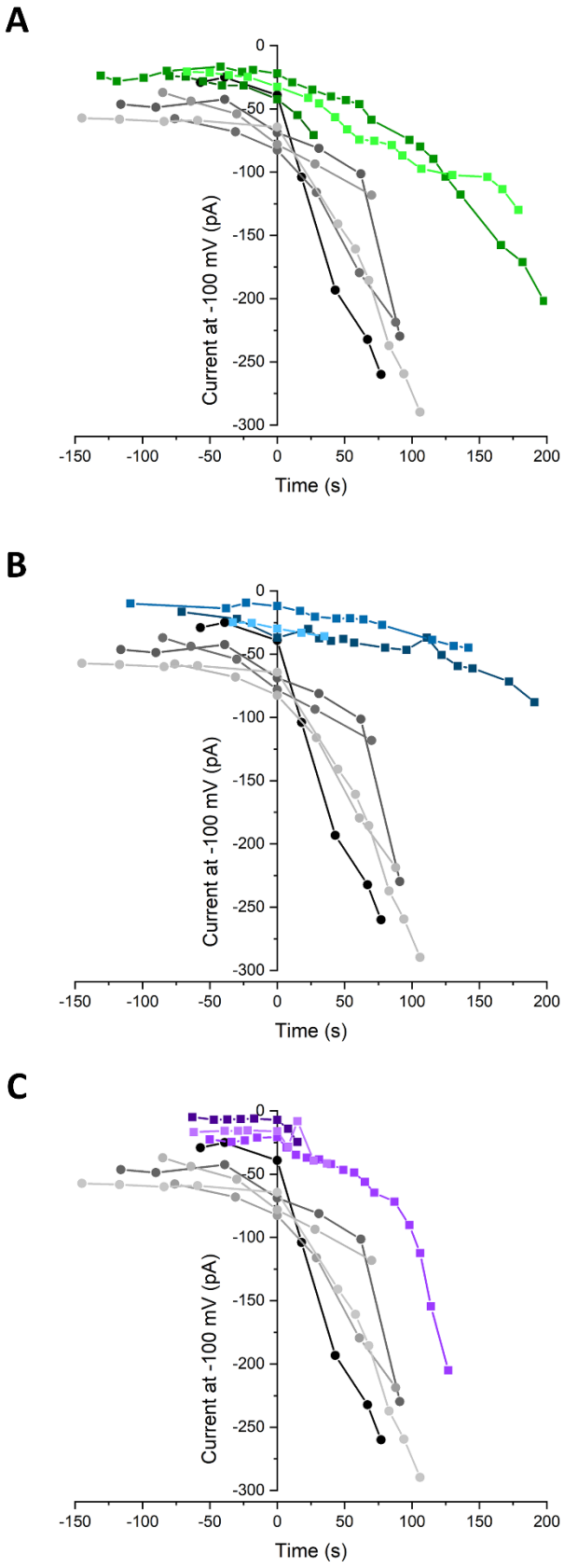

FIGURE 7-5: Block of VRAC current by three extracellular compounds. Greyscale circles indicate control cells with application of hypotonic solution at time 0. Coloured squares indicate cells with application of hypotonic solution + test drug at time 0: (A) 100 µM niflumic acid (green), (B) 1 mM neomycin (blue), (C) 330 µM cisplatin (purple).

7.3 Discussion

These data show that VRAC currents do indeed exist in OHCs as they match every published description of the VRAC-mediated RVD current, including the characteristic outward rectification at positive potentials evident in panel B of **figure 7-3** and more prominently in panel A of **figure 7-4** *(Planells-Cases et al., 2015; Hoffman et al., 2015; Friard et al., 2017)*. Additionally, my results with neomycin and cisplatin presented in **figure 7-5** show that these compounds may interact with VRACs and may permeate through them.

It should be noted that in these experiments I did not control for the potential contribution of other mechanically sensitive channels in the hair cell membrane such as Piezo2 *(Marcotti et al., 2014; Beurg and Fettiplace, 2017)*. Though the effect of Piezo2 activity on these currents cannot be excluded, the block of the VRAC current by niflumic acid (a Cl^- channel blocker which should not interact with Piezo2) shown in panel A of **figure 7-5** indicates that these currents are mostly due to VRAC activity. Future experiments could determine whether application of a Piezo channel blocker such as GsMTx4 affects the characteristics of the VRAC currents I have presented, and therefore whether Piezo2 is activated by osmotic membrane stretch in OHCs.

The block by neomycin evident in panel B of **figure 7-5** is strongly indicative of an interaction between neomycin and the VRACs. The biophysical mechanism of this block is yet to be determined: whether it is like the MET channel block by AGs (pore block of the permeation path), or whether it is intracellularly blocking activation of the VRACs. Either way, relieving this block could prevent the disruption of the RVD process and therefore protect hair cells from some of the ototoxic effects of neomycin. This presents a novel potential therapeutic target for research in otoprotection.

Cisplatin has long been a mysterious compound due its unusual behaviour in hair cells which at times mimics that of the behaviour of AGs and at times does not *(Thomas et al., 2013; Kitcher, 2019)*. Given the lack of block of the MET current by cisplatin (**figure 7-1**), my preliminary data showing block of the VRAC current by cisplatin (**figure 7-5**, panel C) raises the possibility that cisplatin may interact with the MET channel through a different mechanism than with the VRACs. If cisplatin were to permeate through both the MET channels and the VRACs, this would account for many aspects of its behaviour: the reduced gradient in ototoxicity, the protection by MET channel blockers *(Kitcher, 2019)* and loss of mechanotransduction *(Thomas et al., 2013)*, and the potentiation of uptake following VRAC activation *(Planells-Cases et al., 2015)*. Further experiments to conclusively determine whether cisplatin does indeed block VRAC currents in OHCs may offer insight into the kinetics of this elusive compound.

Chapter 8

Conclusions

8.1 Differential permeation of ototoxic drugs

In this thesis, I investigated the permeation characteristics of five ototoxic compounds in several different conditions through the MET channel of mouse OHCs. These included: gentamicin, kanamycin, amikacin, GTTR, and cisplatin. In chapter 3, I found that in conditions relevant to ototoxicity *in vitro*, the entry rate of the native AGs correlated with their respective degree of toxicity. In chapter 4, I found that GTTR, though it saturates the channel at a far lower rate than native gentamicin, permeates at a similar rate at low concentrations commonly used for *in vitro* uptake experiments, and is therefore a suitable indicator of gentamicin entry into hair cells. In chapter 5, I investigated the effects of driving force on gentamicin permeation and found that the differences set up by the endolymphatic medium and the endocochlear potential will summate to an increased permeation rate *in vivo* compared to *in vitro*. I also predicted that mature basal cells would have a 6-fold higher rate of gentamicin permeation than mature apical cells in a live cochlea, likely contributing to the frequently reported loss of high frequency hearing by patients receiving AG treatment. Additionally, I found that the entry rates of all drugs were lower in apical cells than in basal cells, which corresponds to their gradient in sensitivity and further supports the idea of the degree of toxicity being related to entry rate through the MET channel. Finally, in chapter 7 I found that cisplatin does not block the MET channel even with the removal of calcium competition for the binding site, and I discussed alternative methods by which it (and potentially the AGs) may be entering into hair cells, for example through VRACs.

These results demonstrate the relationship between permeation rate and ototoxicity of AGs and strongly support the notion of targeting entry of drugs into hair cells through the MET channel as a main priority for preventing ototoxicity in patients receiving acute and chronic AG treatment. A deeper understanding of the factors that lead to differential permeation of AGs through the MET channel, perhaps through dynamic molecular simulations using recent structural data of the permeation pore, could lead to design of novel AGs that are less permeant and therefore less ototoxic. Alternatively, understanding what makes molecules permeant or not could guide the search for selective non-permeant competitive channel blockers that will have no other deleterious effects on hair cells.

8.1.1 Observation on half-block and entry rate

An interesting observation throughout these experiments is that the relationship between permeation rate and half blocking concentration (K_D) was not always straightforward. For gentamicin, generally conditions that caused stronger block of the channel corresponded to a higher entry rate and vice versa. For example, the K_D of gentamicin in low calcium medium was lower than in regular medium and its entry rate higher, whereas the K_D in mature cells was higher than in neonatal cells and the entry rate lower. This trend did not hold across different drugs however, as the K_D of amikacin was in between that of gentamicin and kanamycin, and yet at certain concentrations the entry rate of kanamycin was between that of gentamicin and amikacin. Furthermore, the K_D of GTTR was far lower than native gentamicin, but its entry rate at high concentrations was much lower due to saturation of the channel by the large size of the molecule. Finally, for every drug tested no difference was evident in between the K_D of apical and basal channels and yet large differences in permeation were found in every case. Though the K_D is not always a predictor of the entry rate, the span of the lower and upper bounds of the dose response curves does seem to relate to the spread of the entry rates over voltage and concentration, in other words the steepness of the saturation of permeation.

8.2 Tonotopic gradient in permeation of neonatal OHCs

All together the data for the three AGs and GTTR suggest that the cause of the well-reported tonotopic gradients in ototoxicity and in fluorescence uptake observed in neonatal cochlear cultures is rooted in differences in permeation of the drugs through the apical and basal MET channels. The reason for this differential permeation is not straightforward and is related to significant controversy in the literature of the last few years surrounding the expression profile of the MET channel and its single channel conductance. It may be tempting to simply take the larger total current size and channel number of basal cells compared to apical cells as an indication of higher permeation, but all results are normalised for current size and presented for a single open channel. Furthermore, the larger size of currents in mature OHCs and their lower entry rate show this not to be the case. There are currently two main models by which graded permeation might be achieved by the channel. Simply put, the first is a gradient in pore diameter, and the second is a gradient in pore number per cell.

The situation is further complicated by a gradient in the expression of TMC1 and TMC2 in the neonatal cochlea. Because my results were obtained in wild type mice with uncontrolled expression of the two TMC isoforms, I cannot directly comment on the role of these two proteins in permeation. However, I can provide some speculative insight based on evidence in the literature and the resulting predictions for what the behaviour of these two isoforms would be and compare this with my results. Furthermore, the question of single channel conductance in our model of permeation becomes complicated by the implications of recent evidence showing that TMC1 assembles as a dimer *(Pan et al., 2018; Ballesteros et al., 2018)*, and that the MET channel complex may contain multiple TMC dimers per complex *(Beurg et al., 2018)*. I will address both questions as they relate to my results and our model of MET channel permeation.

8.2.1 Permeation of TMC1 versus TMC2

At the age in which my cultures are made (P2) it is thought that the basal cells will express mostly TMC1 while the apical cells will only express TMC2 *(Kurima et al., 2015)*. However, viewing my results in the context of previous experiments comparing the permeation of DHS through the MET channel in *Tmc2*$^{-/-}$ mice suggests that my results are not indicative of a shift simply in the expression levels of the TMCs. These previous results found a lower entry rate in apical OHCs of *Tmc2*$^{-/-}$ (TMC1 only) mice *(Corns et al., 2017)* whereas according to my results the basal OHCs (which express more TMC1) had a higher entry rate. Furthermore, this previous study found a difference in the K_D between *Tmc2*$^{-/-}$ and wild type cells, but I did not observe this between apical and basal cells of neonatal cultures for any drug. I did however see a difference in K_D between neonatal apical cells and mature apical cells which should reflect the same shift in TMC expression as the *Tmc2*$^{-/-}$ mice, though the shift I saw was in the opposite direction—the reason for this is unclear. The reason for the lack of a shift in K_D between apical and basal neonatal cells is also unclear. Taken together, these results indicate that the differences in permeation I have presented probably reflect a gradient in the permeation of TMC1 which corresponds to its gradient in single channel conductance, and not simply to a difference in between TMC1 and TMC2. In other words, the mechanism setting up the gradient in TMC1 conductance is already present at the early stages of TMC1 expression in the neonatal cochlea. In fact, the observation that apical and basal MET channels of the neonatal cochlea had the same K_D for all drugs tested suggests an intentional developmental balance in between TMC1 and TMC2, though evidence for this is currently lacking as *Tmc2*$^{-/-}$ mutants show no deleterious effects during development *(Kawashima et al., 2011; Corns et al., 2017)*.

8.2.2 The definition of a single MET channel

Understanding the difference in permeation between apical and basal cells in my results requires probing the definition of a single channel in our model, which has become fraught with controversy. Ordinarily a single channel would be taken as a single pore through which ions flow. However, the unique properties of the MET channel, specifically its tight mechanical gating, render the story more complicated. It has long been thought that multiple channels may be cooperatively gated by the tip link *(Beurg et al., 2006; Gianoli et al., 2017)*, making recording true single channel activity difficult. Furthermore, recent evidence by the Fettiplace group suggests that the MET channel complex may comprise multiple TMC1 inserts with what they term variable conductance states, which they observe in discrete multiples of approximately 50 pS *(Beurg et al., 2018)*. This is based on measures of single channel conductance using BAPTA to break tip links and recording rare instances in which they observe discrete single channel-like currents. While interesting, these methods are questionable, and there could be alternative explanations such as residual cooperative gating of channels that are intricately linked together. They also further suggest that the number of TMC1 pore insertions varies from apex to base with ~20 per basal channel and 8 per apical channel, citing observation of multiple fluorescently tagged TMC molecules per tip link insertion *(Beurg et al., 2018)*.

Our two-barrier one-binding site model suggests that the differences in permeation between the apex and the base are due to differences in the height of the energy barriers and position of the binding site within the channel pore. The simplest interpretation of these results is that basal channels have a larger pore diameter than apical channels. This variation in shape could be due to posttranslational phosphorylation *(Pan et al., 2018; Corey et al., 2019)* or perhaps variable tip link tensioning deforming the membrane or channel itself *(Powers et al., 2012; Reichenbach and Hudsepth, 2014; Tobin et al., 2019)*. However, given the recent evidence from the Fettiplace group our pore diameter hypothesis must be called into question. While discrete levels of single-channel conductance could perfectly agree with our model, the idea that the number of TMC1 insertion sites changes per single channel complex does not. Though our model is certainly capable of detecting differences in permeation, how it would account for multiple cooperatively gated pores is uncertain. The model has a finite number of parameters and varies these to fit the data that it is given. It is possible that in our model multiple distinct permeation pores per “single channel complex” could appear as an individual channel which the model interprets as having a larger conductance. However, I would not exclude the possibility that a variable number of TMC1 molecules around a central attachment point could also alter their conformation. There could be multiple factors influencing the gradient in conductance.

8.3 MET channel pore modelling and its future

The future of this field is without doubt in combining multiple modelling approaches, including structural homology modelling of the pore-forming subunit with experimental modelling of molecule permeation, particularly using genetically modified TMCs. Together these approaches can further elucidate the biokinetics of the MET channel, which in turn can help us to understand how to prevent ototoxicity.

Specifically, it would be interesting to determine the exact roles of each of the charged pore-lining residues in the permeation of the channel. By selectively modifying each of these residues we could determine the identity of the interaction sites and build a dynamic molecular simulation of how drugs permeate through the MET channel pore. This approach could aid in preventing drug permeation either by refining the search for non-permeant channel blockers, or by redesigning AGs so they are still as bactericidal but less permeant through the MET channel. It could also help elucidate whether the TMC1 pore can distort in shape between the apex and base either through differences in gating, in assembly around a central unit, or in phosphorylation. Conversely, it could determine whether the differences in single channel conductance are in fact due to cooperatively-gated multiples of the same pore with no additional conformational changes. Furthermore, it would be interesting to discover the exact roles of the other potential members of the MET channel complex: CIB2, ASIC1b, LHFPL5, and TMIE.

These could clarify how the MET channel complex is assembled, whether it is indeed comprised of multiple discrete pores beyond the dimer that is expected, and how it is gated so precisely. A new structural model that includes each of these accessories to the MET channel complex could very well be essential to understanding the graded permeation of the TMC1 pore.

8.5 Final remarks

In this thesis I hope to have contributed to the understanding of the complicated but beautiful permeation path of the MET channel, how it is related to ototoxicity, and what future experiments could be done to further address these questions. I hope to have provided a roadmap for approaches to preventing the permeation of essential life-saving drugs into auditory hair cells in the interest of protecting patients from hearing loss.

References

Al Khzem, A.H., 2019. Medicinal chemistry of aminoglycosides (Masters Thesis). University of Bath.

Alharazneh, A., Luk, L., Huth, M., Monfared, A., Steyger, P.S., Cheng, A.G., Ricci, A.J., 2011. Functional hair cell mechanotransducer channels are required for aminoglycoside ototoxicity. PLoS ONE 6, e22347. https://doi.org/10.1371/journal.pone.0022347

Allen, P.D., Eddins, D.A., 2010. Presbycusis phenotypes form a heterogeneous continuum when ordered by degree and configuration of hearing loss. Hear. Res. 264, 10–20. https://doi.org/10.1016/j.heares.2010.02.001

Al-Malky, G., Suri, R., Dawson, S.J., Sirimanna, T., Kemp, D., 2011. Aminoglycoside antibiotics cochleotoxicity in paediatric cystic fibrosis (CF) patients: A study using extended high-frequency audiometry and distortion product otoacoustic emissions. Int J Audiol 50, 112–122. https://doi.org/10.3109/14992027.2010.524253

Ashmore, J., 2008. Cochlear outer hair cell motility. Physiol. Rev. 88, 173–210. https://doi.org/10.1152/physrev.00044.2006

Askew, C., Rochat, C., Pan, B., Asai, Y., Ahmed, H., Child, E., Schneider, B.L., Aebischer, P., Holt, J.R., 2015. Tmc gene therapy restores auditory function in deaf mice. Sci Transl Med 7, 295ra108. https://doi.org/10.1126/scitranslmed.aab1996

Assad, J.A., Shepherd, G.M., Corey, D.P., 1991. Tip-link integrity and mechanical transduction in vertebrate hair cells. Neuron 7, 985–994. https://doi.org/10.1016/0896-6273(91)90343-x

Ballesteros, A., Fenollar-Ferrer, C., Swartz, K.J., 2018. Structural relationship between the putative hair cell mechanotransduction channel TMC1 and TMEM16 proteins. eLife 7, e38433. https://doi.org/10.7554/eLife.38433

Bartsch, T.F., Hudspeth, A.J., 2018. A New Twist on Tip Links. Neuron 99, 423–425. https://doi.org/10.1016/j.neuron.2018.07.041

Batts, S.A., Shoemaker, C.R., Raphael, Y., 2009. Notch signaling and Hes labeling in the normal and drug-damaged organ of Corti. Hear. Res. 249, 15–22. https://doi.org/10.1016/j.heares.2008.12.008

Best, L., Brown, P.D., 2009. Studies of the Mechanism of Activation of the Volume-Regulated Anion Channel in Rat Pancreatic β-Cells. J Membrane Biol 230, 83–91. https://doi.org/10.1007/s00232-009-9189-x

Beurg, M., Barlow, A., Furness, D.N., Fettiplace, R., 2019. A Tmc1 mutation reduces calcium permeability and expression of mechanoelectrical transduction channels in cochlear hair cells. PNAS 116, 20743–20749. https://doi.org/10.1073/pnas.1908058116

Beurg, M., Cui, R., Goldring, A.C., Ebrahim, S., Fettiplace, R., Kachar, B., 2018. Variable number of TMC1-dependent mechanotransducer channels underlie tonotopic conductance gradients in the cochlea. Nature Communications 9, 1–15. https://doi.org/10.1038/s41467-018-04589-8

Beurg, M., Evans, M.G., Hackney, C.M., Fettiplace, R., 2006. A Large-Conductance Calcium-Selective Mechanotransducer Channel in Mammalian Cochlear Hair Cells. J. Neurosci. 26, 10992–11000. https://doi.org/10.1523/JNEUROSCI.2188-06.2006

Beurg, M., Fettiplace, R., 2017. PIEZO2 as the anomalous mechanotransducer channel in auditory hair cells. J Physiol 595, 7039–7048. https://doi.org/10.1113/JP274996

Beurg, M., Fettiplace, R., Nam, J.-H., Ricci, A.J., 2009. Localization of inner hair cell mechanotransducer channels using high-speed calcium imaging. Nat. Neurosci. 12, 553–558. https://doi.org/10.1038/nn.2295

Beurg, M., Goldring, A.C., Fettiplace, R., 2015. The effects of Tmc1 Beethoven mutation on mechanotransducer channel function in cochlear hair cells. J Gen Physiol 146, 233–243. https://doi.org/10.1085/jgp.201511458

Beurg, M., Nam, J.-H., Chen, Q., Fettiplace, R., 2010. Calcium Balance and Mechanotransduction in Rat Cochlear Hair Cells. Journal of Neurophysiology 104, 18–34. https://doi.org/10.1152/jn.00019.2010

Bok, J., Chang, W., Wu, D.K., 2007. Patterning and morphogenesis of the vertebrate inner ear. Int. J. Dev. Biol. 51, 521–533. https://doi.org/10.1387/ijdb.072381jb

Bok, J., Raft, S., Kong, K.-A., Koo, S.K., Dräger, U.C., Wu, D.K., 2011. Transient retinoic acid signaling confers anterior-posterior polarity to the inner ear. Proc. Natl. Acad. Sci. U.S.A. 108, 161–166. https://doi.org/10.1073/pnas.1010547108

Cabañas, M.J., Vázquez, D., Modolell, J., 1978. Inhibition of ribosomal translocation by aminoglycoside antibiotics. Biochem. Biophys. Res. Commun. 83, 991–997. https://doi.org/10.1016/0006-291x(78)91493-6

Cais, O., Herguedas, B., Krol, K., Cull-Candy, S.G., Farrant, M., Greger, I.H., 2014. Mapping the Interaction Sites between AMPA Receptors and TARPs Reveals a Role for the Receptor N-Terminal Domain in Channel Gating. Cell Reports 9, 728–740. https://doi.org/10.1016/j.celrep.2014.09.029

Chatzigeorgiou, M., Bang, S., Hwang, S.W., Schafer, W.R., 2013. tmc-1 encodes a sodium-sensitive channel required for salt chemosensation in C. elegans. Nature 494, 95–99. https://doi.org/10.1038/nature11845

Chen, P., Johnson, J.E., Zoghbi, H.Y., Segil, N., 2002. The role of Math1 in inner ear development: Uncoupling the establishment of the sensory primordium from hair cell fate determination. Development 129, 2495–2505.

Choi, J.J., Wang, S., Tung, Y.-S., Morrison, B., Konofagou, E.E., 2010. Molecules of various pharmacologically-relevant sizes can cross the ultrasound-induced blood-brain barrier opening in vivo. Ultrasound Med Biol 36, 58–67. https://doi.org/10.1016/j.ultrasmedbio.2009.08.006

Corey, D.P., Akyuz, N., Holt, J.R., 2019. Function and Dysfunction of TMC Channels in Inner Ear Hair Cells. Cold Spring Harb Perspect Med 9. https://doi.org/10.1101/cshperspect.a033506

Corey, D.P., Holt, J.R., 2016. Are TMCs the Mechanotransduction Channels of Vertebrate Hair Cells? J. Neurosci. 36, 10921–10926. https://doi.org/10.1523/JNEUROSCI.1148-16.2016

Corey, D.P., Hudspeth, A.J., 1983. Kinetics of the receptor current in bullfrog saccular hair cells. J. Neurosci. 3, 962–976. https://doi.org/10.1523/JNEUROSCI.03-05-00962.1983

Corey, D.P., Hudspeth, A.J., 1979. Ionic basis of the receptor potential in a vertebrate hair cell. Nature 281, 281675a0. https://doi.org/10.1038/281675a0

Corns, L.F., Jeng, J.-Y., Richardson, G.P., Kros, C.J., Marcotti, W., 2017. TMC2 Modifies Permeation Properties of the Mechanoelectrical Transducer Channel in Early Postnatal Mouse Cochlear Outer Hair Cells. Front Mol Neurosci 10. https://doi.org/10.3389/fnmol.2017.00326

Corns, L.F., Johnson, S.L., Kros, C.J., Marcotti, W., 2016. Tmc1 Point Mutation Affects Ca2+ Sensitivity and Block by Dihydrostreptomycin of the Mechanoelectrical Transducer Current of Mouse Outer Hair Cells. J Neurosci 36, 336–349. https://doi.org/10.1523/JNEUROSCI.2439-15.2016

Corns, L.F., Johnson, S.L., Kros, C.J., Marcotti, W., 2014. Calcium entry into stereocilia drives adaptation of the mechanoelectrical transducer current of mammalian cochlear hair cells. Proc Natl Acad Sci U S A 111, 14918–14923. https://doi.org/10.1073/pnas.1409920111

Cunningham, L.L., Tucci, D.L., 2017. Hearing Loss in Adults. N Engl J Med 377, 2465–2473. https://doi.org/10.1056/NEJMra1616601

Dai, C.-F., Mangiardi, D., Cotanche, D., Steyger, P., 2006. Uptake of fluorescent gentamicin by vertebrate sensory cells in vivo. Hearing Research 213, 64–78. https://doi.org/10.1016/j.heares.2005.11.011

Dai, C.F., Steyger, P.S., 2008. A systemic gentamicin pathway across the stria vascularis. Hear Res 235, 114–124. https://doi.org/10.1016/j.heares.2007.10.010

Dallos, P., 2008. Cochlear amplification, outer hair cells and prestin. Curr Opin Neurobiol 18, 370–376. https://doi.org/10.1016/j.conb.2008.08.016

Davies, J., Davis, B.D., 1968. Misreading of ribonucleic acid code words induced by aminoglycoside antibiotics. The effect of drug concentration. J. Biol. Chem. 243, 3312–3316.

Desmonds, T., 2015. Mechano-electrical transduction in cochlear hair cells: channel blockers, an anomalous mechano-sensitive current and TRPC knockout mice (Ph.D.). University of Sussex, Brighton, UK.

Doll, J.C., Peng, A.W., Ricci, A.J., Pruitt, B.L., 2012. Faster than the Speed of Hearing: Nanomechanical Force Probes Enable the Electromechanical Observation of Cochlear Hair Cells. Nano Lett. 12, 6107–6111. https://doi.org/10.1021/nl3036349

Duggal, P., Sarkar, M., 2007. Audiologic monitoring of multi-drug resistant tuberculosis patients on aminoglycoside treatment with long term follow-up. BMC Ear Nose Throat Disord 7, 5. https://doi.org/10.1186/1472-6815-7-5

Edelstein, A.D., Tsuchida, M.A., Amodaj, N., Pinkard, H., Vale, R.D., Stuurman, N., 2014. Advanced methods of microscope control using μManager software. Journal of Biological Methods 1, e10. https://doi.org/10.14440/jbm.2014.36

Engström, H., Engström, B., 1978. Structure of the hairs on cochlear sensory cells. Hearing Research 1, 49–66. https://doi.org/10.1016/0378-5955(78)90009-6

Escobedo, J.O., Chu, Y.-H., Wang, Q., Steyger, P.S., Strongin, R.M., 2012. Live Cell Imaging of a Fluorescent Gentamicin Conjugate. Nat Prod Commun 7, 317–320.

Farris, H.E., LeBlanc, C.L., Goswami, J., Ricci, A.J., 2004. Probing the pore of the auditory hair cell mechanotransducer channel in turtle. J Physiol 558, 769–792. https://doi.org/10.1113/jphysiol.2004.061267

Farris, H.E., Wells, G.B., Ricci, A.J., 2006. Steady-State Adaptation of Mechanotransduction Modulates the Resting Potential of Auditory Hair Cells, Providing an Assay for Endolymph [Ca2+]. J Neurosci 26, 12526–12536. https://doi.org/10.1523/JNEUROSCI.3569-06.2006

Fettiplace, R., 2017. Hair cell transduction, tuning and synaptic transmission in the mammalian cochlea. Compr Physiol 7, 1197–1227. https://doi.org/10.1002/cphy.c160049

Fettiplace, R., 2016. Is TMC1 the Hair Cell Mechanotransducer Channel? 111, 3–9.

Fettiplace, R., 2009. Defining features of the hair cell mechanoelectrical transducer channel. Pflugers Arch 458, 1115–1123. https://doi.org/10.1007/s00424-009-0683-x

Fettiplace, R., Kim, K.X., 2014. The Physiology of Mechanoelectrical Transduction Channels in Hearing. Physiol Rev 94, 951–986. https://doi.org/10.1152/physrev.00038.2013

Friard, J., Tauc, M., Cougnon, M., Compan, V., Duranton, C., Rubera, I., 2017. Comparative Effects of Chloride Channel Inhibitors on LRRC8/VRAC-Mediated Chloride Conductance. Front. Pharmacol. 8. https://doi.org/10.3389/fphar.2017.00328

Gale, J.E., Marcotti, W., Kennedy, H.J., Kros, C.J., Richardson, G.P., 2001. FM1-43 Dye Behaves as a Permeant Blocker of the Hair-Cell Mechanotransducer Channel. J. Neurosci. 21, 7013–7025. https://doi.org/10.1523/JNEUROSCI.21-18-07013.2001

Garinis, A.C., Cross, C.P., Srikanth, P., Carroll, K., Feeney, M.P., Keefe, D.H., Hunter, L.L., Putterman, D.B., Cohen, D.M., Gold, J.A., Steyger, P.S., 2017. The cumulative effects of intravenous antibiotic treatments on hearing in patients with cystic fibrosis. J. Cyst. Fibros. 16, 401–409. https://doi.org/10.1016/j.jcf.2017.01.006

Gianoli, F., Risler, T., Kozlov, A.S., 2017. Lipid bilayer mediates ion-channel cooperativity in a model of hair-cell mechanotransduction. PNAS 114, E11010–E11019. https://doi.org/10.1073/pnas.1713135114

Giese, A.P.J., Tang, Y.-Q., Sinha, G.P., Bowl, M.R., Goldring, A.C., Parker, A., Freeman, M.J., Brown, S.D.M., Riazuddin, S., Fettiplace, R., Schafer, W.R., Frolenkov, G.I., Ahmed, Z.M., 2017. CIB2 interacts with TMC1 and TMC2 and is essential for mechanotransduction in auditory hair cells. Nature Communications 8, 43. https://doi.org/10.1038/s41467-017-00061-1

Gillespie, P.G., 2004. Myosin I and adaptation of mechanical transduction by the inner ear. Philos. Trans. R. Soc. Lond., B, Biol. Sci. 359, 1945–1951. https://doi.org/10.1098/rstb.2004.1564

Gleason, M., Nagiel, A., Jamet, S., Vologodskaia, M., Lopez-Schier, H., Hudspeth, A.J., 2009. The transmembrane inner ear (Tmie) protein is essential for normal hearing and balance in the zebrafish. PNAS 106, 21347–21352.

Goldring, A.C., Beurg, M., Fettiplace, R., 2019. The contribution of TMC1 to adaptation of mechanoelectrical transduction channels in cochlear outer hair cells. The Journal of Physiology 597, 5949–5961. https://doi.org/10.1113/JP278799

Goodyear, R.J., Forge, A., Legan, P.K., Richardson, G.P., 2010. Asymmetric Distribution of Cadherin 23 and Protocadherin 15 in the Kinocilial Links of Avian Sensory Hair Cells. J Comp Neurol 518, 4288–4297. https://doi.org/10.1002/cne.22456

Goodyear, R.J., Gale, J.E., Ranatunga, K.M., Kros, C.J., Richardson, G.P., 2008. Aminoglycoside-Induced Phosphatidylserine Externalization in Sensory Hair Cells Is Regionally Restricted, Rapid, and Reversible. J Neurosci 28, 9939–9952. https://doi.org/10.1523/JNEUROSCI.1124-08.2008

Gradogna, A., Gaitán-Peñas, H., Boccaccio, A., Estévez, R., Pusch, M., 2017. Cisplatin activates volume sensitive LRRC8 channel mediated currents in Xenopus oocytes. Channels (Austin) 11, 254–260. https://doi.org/10.1080/19336950.2017.1284717

Grati, M., Kachar, B., 2011. Myosin VIIa and sans localization at stereocilia upper tip-link density implicates these Usher syndrome proteins in mechanotransduction. Proc. Natl. Acad. Sci. U.S.A. 108, 11476–11481. https://doi.org/10.1073/pnas.1104161108

Groves, A.K., Fekete, D.M., 2012. Shaping sound in space: the regulation of inner ear patterning. Development 139, 245–257. https://doi.org/10.1242/dev.067074

Groves, A.K., Zhang, K.D., Fekete, D.M., 2013. The Genetics of Hair Cell Development and Regeneration. Annu Rev Neurosci 36, 361–381. https://doi.org/10.1146/annurev-neuro-062012-170309

Guo, W., Lei, C., Dengke, L., Wei, S., Shiming, Y., 2012. Endocochlear Potential and Potassium Concentration Recording in Minipig Cochlea. Journal of Otology 7, 103–105. https://doi.org/10.1016/S1672-2930(12)50024-3

Hertzano, R., Orvis, J., n.d. gEAR Portal [WWW Document]. URL https://umgear.org/ (accessed 7.30.20).

Hailey, D.W., Esterberg, R., Linbo, T.H., Rubel, E.W., Raible, D.W., 2017. Fluorescent aminoglycosides reveal intracellular trafficking routes in mechanosensory hair cells. J Clin Invest 127, 472–486. https://doi.org/10.1172/JCI85052

He, D.Z., 1997. Relationship between the development of outer hair cell electromotility and efferent innervation: a study in cultured organ of corti of neonatal gerbils. J. Neurosci. 17, 3634–3643.

Hille, B., 2001. Ion Channels of Excitable Membranes, Ion Channels of Excitable Membranes.

Hoffmann, E.K., Sørensen, B.H., Sauter, D.P.R., Lambert, I.H., 2015. Role of volume-regulated and calcium-activated anion channels in cell volume homeostasis, cancer and drug resistance. Channels (Austin) 9, 380–396. https://doi.org/10.1080/19336950.2015.1089007

Howard, J., Hudspeth, A.J., 1988. Compliance of the hair bundle associated with gating of mechanoelectrical transduction channels in the bullfrog's saccular hair cell. Neuron 1, 189–199.

Hudspeth, A., 1982. Extracellular current flow and the site of transduction by vertebrate hair cells. J Neurosci 2, 1–10. https://doi.org/10.1523/JNEUROSCI.02-01-00001.1982

Hudspeth, A.J., Corey, D.P., 1977. Sensitivity, polarity, and conductance change in the response of vertebrate hair cells to controlled mechanical stimuli. PNAS 74, 2407–2411. https://doi.org/10.1073/pnas.74.6.2407

Humes, L.E., Dubno, J.R., Gordon-Salant, S., Lister, J.J., Cacace, A.T., Cruickshanks, K.J., Gates, G.A., Wilson, R.H., Wingfield, A., 2012. Central Presbycusis: A Review and Evaluation of the Evidence. J Am Acad Audiol 23, 635–666. https://doi.org/10.3766/jaaa.23.8.5

Indzhykulian, A.A., Stepanyan, R., Nelina, A., Spinelli, K.J., Ahmed, Z.M., Belyantseva, I.A., Friedman, T.B., Barr-Gillespie, P.G., Frolenkov, G.I., 2013. Molecular Remodeling of Tip Links Underlies Mechanosensory Regeneration in Auditory Hair Cells. PLOS Biology 11, e1001583. https://doi.org/10.1371/journal.pbio.1001583

Jia, Y., Zhao, Y., Kusakizako, T., Wang, Y., Pan, C., Zhang, Y., Nureki, O., Hattori, M., Yan, Z., 2020. TMC1 and TMC2 Proteins Are Pore-Forming Subunits of Mechanosensitive Ion Channels. Neuron 105, 310-321.e3. https://doi.org/10.1016/j.neuron.2019.10.017

Johnson, S.L., Beurg, M., Marcotti, W., Fettiplace, R., 2011. Prestin-Driven Cochlear Amplification Is Not Limited by the Outer Hair Cell Membrane Time Constant. Neuron 70, 1143–1154. https://doi.org/10.1016/j.neuron.2011.04.024

Kachar, B., Parakkal, M., Kurc, M., Zhao, Y., Gillespie, P.G., 2000. High-resolution structure of hair-cell tip links. Proceedings of the National Academy of Sciences of the United States of America 97, 13336–41.

Kawashima, Y., Géléoc, G.S.G., Kurima, K., Labay, V., Lelli, A., Asai, Y., Makishima, T., Wu, D.K., Della Santina, C.C., Holt, J.R., Griffith, A.J., 2011. Mechanotransduction in mouse inner ear hair cells requires transmembrane channel-like genes. J. Clin. Invest. 121, 4796–4809. https://doi.org/10.1172/JCI60405

Kazmierczak, P., Sakaguchi, H., Tokita, J., Wilson-Kubalek, E.M., Milligan, R.A., Müller, U., Kachar, B., 2007. Cadherin 23 and protocadherin 15 interact to form tip-link filaments in sensory hair cells. Nature 449, 87–91. https://doi.org/10.1038/nature06091

Kenyon, E.J., Kirkwood, N.K., Kitcher, S.R., O'Reilly, M., Derudas, M., Cantillon, D.M., Goodyear, R.J., Secker, A., Baxendale, S., Bull, J.C., Waddell, S.J., Whitfield, T.T., Ward, S.E., Kros, C.J., Richardson, G.P., 2017. Identification of ion-channel modulators that protect against aminoglycoside-induced hair cell death. JCI Insight 2. https://doi.org/10.1172/jci.insight.96773

Kim, K.X., Beurg, M., Hackney, C.M., Furness, D.N., Mahendrasingam, S., Fettiplace, R., 2013. The role of transmembrane channel-like proteins in the operation of hair cell mechanotransducer channels. J. Gen. Physiol. 142, 493–505. https://doi.org/10.1085/jgp.201311068

Kirkwood, N.K., O'Reilly, M., Derudas, M., Kenyon, E.J., Huckvale, R., van Netten, S.M., Ward, S.E., Richardson, G.P., Kros, C.J., 2017. d-Tubocurarine and Berbamine: Alkaloids That Are Permeant Blockers of the Hair Cell's Mechano-Electrical Transducer Channel and Protect from Aminoglycoside Toxicity. Front Cell Neurosci 11, 262. https://doi.org/10.3389/fncel.2017.00262

Kitcher, S.R., 2019. Cisplatin and gentamicin ototoxicity: a search for protectants and comparison of entry routes into sensory hair cells (Doctoral Thesis). University of Sussex.

Kitcher, S.R., Kirkwood, N.K., Camci, E.D., Wu, P., Gibson, R.M., Redila, V.A., Ogelman, R., Simon, J.A., Rubel, E.W., Raible, D.W., Richardson, G.P., Kros, C.J., 2019. ORC-13661 protects sensory hair cells from aminoglycoside and cisplatin ototoxicity. JCI Insight 4. https://doi.org/10.1172/jci.insight.126764

König, B., Stauber, T., 2019. Biophysics and Structure-Function Relationships of LRRC8-Formed Volume-Regulated Anion Channels. Biophysical Journal 116, 1185–1193. https://doi.org/10.1016/j.bpj.2019.02.014

Konishi, T., Mendelsohn, M., 1970. Effect of ouabain on cochlear potentials and endolymph composition in guinea pigs. Acta Otolaryngol. 69, 192–199. https://doi.org/10.3109/00016487009123353

Koo, J.-W., Quintanilla-Dieck, L., Jiang, M., Liu, J., Urdang, Z.D., Allensworth, J.J., Cross, C.P., Li, H., Steyger, P.S., 2015. Endotoxemia-mediated inflammation potentiates aminoglycoside-induced ototoxicity. Sci Transl Med 7, 298ra118. https://doi.org/10.1126/scitranslmed.aac5546

Kotecha, B., Richardson, G.P., 1994. Ototoxicity in vitro: effects of neomycin, gentamicin, dihydrostreptomycin, amikacin, spectinomycin, neamine, spermine and poly-l-lysine. Hearing Research 73, 173–184. https://doi.org/10.1016/0378-5955(94)90232-1

Krause, K.M., Serio, A.W., Kane, T.R., Connolly, L.E., 2016. Aminoglycosides: An Overview. Cold Spring Harb Perspect Med 6. https://doi.org/10.1101/cshperspect.a027029

Kros, C.J., Marcotti, W., van Netten, S.M., Self, T.J., Libby, R.T., Brown, S.D.M., Richardson, G.P., Steel, K.P., 2002. Reduced climbing and increased slipping adaptation in cochlear hair cells of mice with Myo7a mutations. Nat. Neurosci. 5, 41–47. https://doi.org/10.1038/nn784

Kros, C.J., Rusch, A., Richardson, G.P., 1992. Mechano-Electrical Transducer Currents in Hair Cells of the Cultured Neonatal Mouse Cochlea. Proceedings of the Royal Society of London B: Biological Sciences 249, 185–193. https://doi.org/10.1098/rspb.1992.0102

Kros, C.J., Steyger, P.S., 2019. Aminoglycoside- and Cisplatin-Induced Ototoxicity: Mechanisms and Otoprotective Strategies. Cold Spring Harb Perspect Med 9. https://doi.org/10.1101/cshperspect.a033548

Kujawa, S.G., Liberman, M.C., 2009. Adding Insult to Injury: Cochlear Nerve Degeneration after "Temporary" Noise-Induced Hearing Loss. J Neurosci 29, 14077–14085. https://doi.org/10.1523/JNEUROSCI.2845-09.2009

Kurima, K., Ebrahim, S., Pan, B., Sedlacek, M., Sengupta, P., Millis, B.A., Cui, R., Nakanishi, H., Fujikawa, T., Kawashima, Y., Choi, B.Y., Monahan, K., Holt, J.R., Griffith, A.J., Kachar, B., 2015. TMC1 and TMC2 Localize at the Site of Mechanotransduction in Mammalian Inner Ear Hair Cell Stereocilia. Cell Rep 12, 1606–1617. https://doi.org/10.1016/j.celrep.2015.07.058

Kurima, K., Peters, L.M., Yang, Y., Riazuddin, Saima, Ahmed, Z.M., Naz, S., Arnaud, D., Drury, S., Mo, J., Makishima, T., Ghosh, M., Menon, P.S.N., Deshmukh, D., Oddoux, C., Ostrer, H., Khan, S., Riazuddin, Sheikh, Deininger, P.L., Hampton, L.L., Sullivan, S.L., Jr, J.F.B., Keats, B.J.B., Wilcox, E.R., Friedman, T.B., Griffith, A.J., 2002. Dominant and recessive deafness caused by mutations of a novel gene, *TMC1*, required for cochlear hair-cell function. Nature Genetics 30, 277–284. https://doi.org/10.1038/ng842

Kushner, B., Allen, P.D., Crane, B.T., 2016. Frequency and Demographics of Gentamicin Use. Otol Neurotol 37, 190–195. https://doi.org/10.1097/MAO.0000000000000937

Lelli, A., Asai, Y., Forge, A., Holt, J.R., Géléoc, G.S.G., 2009. Tonotopic gradient in the developmental acquisition of sensory transduction in outer hair cells of the mouse cochlea. J. Neurophysiol. 101, 2961–2973. https://doi.org/10.1152/jn.00136.2009

Li, H., Steyger, P.S., 2011. Systemic aminoglycosides are trafficked via endolymph into cochlear hair cells. Scientific Reports 1, 159. https://doi.org/10.1038/srep00159

Lin, F.R., Albert, M., 2014. Hearing Loss and Dementia – Who's Listening? Aging Ment Health 18, 671–673. https://doi.org/10.1080/13607863.2014.915924

Lopez-Novoa, J.M., Quiros, Y., Vicente, L., Morales, A.I., Lopez-Hernandez, F.J., 2011. New insights into the mechanism of aminoglycoside nephrotoxicity: an integrative point of view. Kidney International 79, 33–45. https://doi.org/10.1038/ki.2010.337

Maeda, R., Kindt, K.S., Mo, W., Morgan, C.P., Erickson, T., Zhao, H., Clemens-Grisham, R., Barr-Gillespie, P.G., Nicolson, T., 2014. Tip-link protein protocadherin 15 interacts with transmembrane channel-like proteins TMC1 and TMC2. Proc. Natl. Acad. Sci. U.S.A. 111, 12907–12912. https://doi.org/10.1073/pnas.1402152111

Mammano, F., Ashmore, J.F., 1996. Differential expression of outer hair cell potassium currents in the isolated cochlea of the guinea-pig. J Physiol 496, 639–646.

Marcotti, W., Corns, L.F., Desmonds, T., Kirkwood, N.K., Richardson, G.P., Kros, C.J., 2014. Transduction without Tip Links in Cochlear Hair Cells Is Mediated by Ion Channels with Permeation Properties Distinct from Those of the Mechano-Electrical Transducer Channel. J Neurosci 34, 5505–5514. https://doi.org/10.1523/JNEUROSCI.4086-13.2014

Marcotti, W., Erven, A., Johnson, S.L., Steel, K.P., Kros, C.J., 2006. Tmc1 is necessary for normal functional maturation and survival of inner and outer hair cells in the mouse cochlea. J Physiol 574, 677–698. https://doi.org/10.1113/jphysiol.2005.095661

Marcotti, W., Kros, C.J., 1999. Developmental expression of the potassium current IK,n contributes to maturation of mouse outer hair cells. J. Physiol. (Lond.) 520 Pt 3, 653–660. https://doi.org/10.1111/j.1469-7793.1999.00653.x

Marcotti, W., Netten, S.M.V., Kros, C.J., 2005. The aminoglycoside antibiotic dihydrostreptomycin rapidly enters mouse outer hair cells through the mechano -electrical transducer channels. The Journal of Physiology 567, 505–521. https://doi.org/10.1113/jphysiol.2005.085951

Michel, V., Booth, K.T., Patni, P., Cortese, M., Azaiez, H., Bahloul, A., Kahrizi, K., Labbé, M., Emptoz, A., Lelli, A., Dégardin, J., Dupont, T., Aghaie, A., Oficjalska-Pham, D., Picaud, S., Najmabadi, H., Smith, R.J., Bowl, M.R., Brown, S.D., Avan, P., Petit, C., El-Amraoui, A., 2017. CIB2, defective in isolated deafness, is key for auditory hair cell mechanotransduction and survival. EMBO Molecular Medicine 9, 1711–1731. https://doi.org/10.15252/emmm.201708087

Müller, M., von Hünerbein, K., Hoidis, S., Smolders, J.W.T., 2005. A physiological place-frequency map of the cochlea in the CBA/J mouse. Hear. Res. 202, 63–73. https://doi.org/10.1016/j.heares.2004.08.011

Nist-Lund, C.A., Pan, B., Patterson, A., Asai, Y., Chen, T., Zhou, W., Zhu, H., Romero, S., Resnik, J., Polley, D.B., Géléoc, G.S., Holt, J.R., 2019. Improved TMC1 gene therapy restores hearing and balance in mice with genetic inner ear disorders. Nature Communications 10, 236. https://doi.org/10.1038/s41467-018-08264-w

O'Reilly, M., 2019. Prevention of aminoglycoside antibiotic-induced ototoxicity of auditory hair cells via block of mechano-electrical transducer channels or intracellular mechanisms (Doctoral Thesis). University of Sussex.

O'Reilly, M., Kirkwood, N.K., Kenyon, E.J., Huckvale, R., Cantillon, D.M., Waddell, S.J., Ward, S.E., Richardson, G.P., Kros, C.J., Derudas, M., 2019. Design, Synthesis, and Biological Evaluation of a New Series of Carvedilol Derivatives That Protect Sensory Hair Cells from Aminoglycoside-Induced Damage by Blocking the Mechanoelectrical Transducer Channel. J. Med. Chem. 62, 5312–5329. https://doi.org/10.1021/acs.jmedchem.8b01325

Osgood, R.T., 2020. Cellular mechanisms of damage and repair in sensory hair cells (Doctoral Thesis). University of Sussex.

O'Sullivan, M., Lin, R., Greenhouse, R., Cheng, A., Ricci, A., 2020. Reformulating Gentamicin to Reduce Ototoxicity and Maintain Antimicrobial Activity. Presented at the Assoc. Res. Otolaryngol. Abs., pp. 692–693.

O'Sullivan, M.E., Perez, A., Lin, R., Sajjadi, A., Ricci, A.J., Cheng, A.G., 2017. Towards the Prevention of Aminoglycoside-Related Hearing Loss. Front Cell Neurosci 11. https://doi.org/10.3389/fncel.2017.00325

Owens, K.N., Coffin, A.B., Hong, L.S., Bennett, K.O., Rubel, E.W., Raible, D.W., 2009. Response of mechanosensory hair cells of the zebrafish lateral line to aminoglycosides reveals distinct cell death pathways. Hear. Res. 253, 32–41. https://doi.org/10.1016/j.heares.2009.03.001

Pan, B., Akyuz, N., Liu, X.-P., Asai, Y., Nist-Lund, C., Kurima, K., Derfler, B.H., György, B., Limapichat, W., Walujkar, S., Wimalasena, L.N., Sotomayor, M., Corey, D.P., Holt, J.R., 2018. TMC1 Forms the Pore of Mechanosensory Transduction Channels in Vertebrate Inner Ear Hair Cells. Neuron 99, 736-753.e6. https://doi.org/10.1016/j.neuron.2018.07.033

Pan, B., Géléoc, G.S., Asai, Y., Horwitz, G.C., Kurima, K., Ishikawa, K., Kawashima, Y., Griffith, A.J., Holt, J.R., 2013. TMC1 and TMC2 are components of the mechanotransduction channel in hair cells of the mammalian inner ear. Neuron 79, 504–515. https://doi.org/10.1016/j.neuron.2013.06.019

Planells-Cases, R., Lutter, D., Guyader, C., Gerhards, N.M., Ullrich, F., Elger, D.A., Kucukosmanoglu, A., Xu, G., Voss, F.K., Reincke, S.M., Stauber, T., Blomen, V.A., Vis, D.J., Wessels, L.F., Brummelkamp, T.R., Borst, P., Rottenberg, S., Jentsch, T.J., 2015. Subunit composition of VRAC channels determines substrate specificity and cellular resistance to Pt-based anti-cancer drugs. EMBO J. 34, 2993–3008. https://doi.org/10.15252/embj.201592409

Powers, R.E., Gaudet, R., Sotomayor, M., 2017. A Partial Calcium-Free Linker Confers Flexibility to Inner-Ear Protocadherin-15. Structure 25, 482–495. https://doi.org/10.1016/j.str.2017.01.014

Powers, R.J., Roy, S., Atilgan, E., Brownell, W.E., Sun, S.X., Gillespie, P.G., Spector, A.A., 2012. Stereocilia Membrane Deformation: Implications for the Gating Spring and Mechanotransduction Channel. Biophys J 102, 201–210. https://doi.org/10.1016/j.bpj.2011.12.022

Purves, D., Augustine, G., Fitzpatrick, D., Hall, W.C., LaMantia, A., Mooney, R., White, L.E., 2018. Neuroscience. Sinauer.

Reichenbach, T., Hudspeth, A.J., 2014. The physics of hearing: fluid mechanics and the active process of the inner ear. Rep. Prog. Phys. 77, 076601. https://doi.org/10.1088/0034-4885/77/7/076601

Ricci, A., 2002. Differences in mechano-transducer channel kinetics underlie tonotopic distribution of fast adaptation in auditory hair cells. Journal of neurophysiology 87, 1738–48. https://doi.org/10.1152/jn.00574.2001

Ricci, A.J., Crawford, A.C., Fettiplace, R., 2003. Tonotopic Variation in the Conductance of the Hair Cell Mechanotransducer Channel. Neuron 40, 983–990. https://doi.org/10.1016/S0896-6273(03)00721-9

Ricci, A.J., Fettiplace, R., 1997. The effects of calcium buffering and cyclic AMP on mechano-electrical transduction in turtle auditory hair cells. J Physiol 501, 111–124.

Ricci, A.J., Gray-Keller, M., Fettiplace, R., 2000. Tonotopic variations of calcium signalling in turtle auditory hair cells. J Physiol 524, 423–436. https://doi.org/10.1111/j.1469-7793.2000.00423.x

Roberts, T.P., 2013. Developmental failure in cochlear hair cells from mouse models of Usher syndrome and the identification of an acid sensitive ionic current in Inner and Outer hair cells (Doctoral Thesis). University of Sussex.

Rusch, A., Kros, C., Richardson, G., 1994. Block by amiloride and its derivatives of mechano-electrical transduction in outer hair cells of mouse cochlear cultures. Journal of Physiology 474, 75–86.

Russell, I.J., Richardson, G.P., 1987. The morphology and physiology of hair cells in organotypic cultures of the mouse cochlea. Hear. Res. 31, 9–24.

Schacht, J., Talaska, A.E., Rybak, L.P., 2012. Cisplatin and Aminoglycoside Antibiotics: Hearing Loss and Its Prevention. The Anatomical Record 295, 1837–1850. https://doi.org/10.1002/ar.22578

Sotomayor, M., Weihofen, W.A., Gaudet, R., Corey, D.P., 2012. Structure of a Force-Conveying Cadherin Bond Essential for Inner-Ear Mechanotransduction. Nature 492, 128–132. https://doi.org/10.1038/nature11590

Sotomayor, M., Weihofen, W.A., Gaudet, R., Corey, D.P., 2010. Structural determinants of cadherin-23 function in hearing and deafness. Neuron 66, 85–100. https://doi.org/10.1016/j.neuron.2010.03.028

Starr, A., Rance, G., 2015. Auditory neuropathy. Handb Clin Neurol 129, 495–508. https://doi.org/10.1016/B978-0-444-62630-1.00028-7

Stauber, T., 2015. The volume-regulated anion channel is formed by LRRC8 heteromers – molecular identification and roles in membrane transport and physiology. Biol. Chem. 396, 975–990. https://doi.org/10.1515/hsz-2015-0127

Stepanyan, R.S., Indzhykulian, A.A., Vélez-Ortega, A.C., Boger, E.T., Steyger, P.S., Friedman, T.B., Frolenkov, G.I., 2011. TRPA1-Mediated Accumulation of Aminoglycosides in Mouse Cochlear Outer Hair Cells. J Assoc Res Otolaryngol 12, 729–740. https://doi.org/10.1007/s10162-011-0288-x

Sul, B., Iwasa, K.H., 2010. Gating of Two Mechanoelectrical Transducer Channels Associated with a Single Tip Link. Biophysical Journal 99, 1027–1033. https://doi.org/10.1016/j.bpj.2010.05.029

Tanaka, N., 1983. Mechanism of action of and resistance to aminoglycoside antibiotics. Arch. Pharm. Res. 6, 93–102. https://doi.org/10.1007/BF02855708

Tasaki, I., Spyropoulos, C.S., 1959. Stria vascularis as source of endocochlear potential. J. Neurophysiol. 22, 149–155. https://doi.org/10.1152/jn.1959.22.2.149

Thomas, A.J., Hailey, D.W., Stawicki, T.M., Wu, P., Coffin, A.B., Rubel, E.W., Raible, D.W., Simon, J.A., Ou, H.C., 2013. Functional Mechanotransduction Is Required for Cisplatin-Induced Hair Cell Death in the Zebrafish Lateral Line. J Neurosci 33, 4405–4414. https://doi.org/10.1523/JNEUROSCI.3940-12.2013

Tobin, M., Chaiyasitdhi, A., Michel, V., Michalski, N., Martin, P., 2019. Stiffness and tension gradients of the hair cell's tip-link complex in the mammalian cochlea. eLife 8. https://doi.org/10.7554/eLife.43473

Tran Ba Huy, P., Meulemans, A., Manuel, C., Sterkers, O., Wassef, M., 1981. Critical appraisal of the experimental studies on the ototoxic interaction between ethacrynic acid and aminoglycoside antibiotics. A pharmacokinetical standpoint. Scand Audiol Suppl 14 Suppl, 225–232.

Ugawa, S., Inagaki, A., Yamamura, H., Ueda, T., Ishida, Y., Kajita, K., Shimizu, H., Shimada, S., 2006. Acid-sensing ion channel-1b in the stereocilia of mammalian cochlear hair cells. Neuroreport 17, 1235–1239. https://doi.org/10.1097/01.wnr.0000233093.67289.66

Ugawa, S., Ishida, Y., Ueda, T., Yu, Y., Shimada, S., 2008. Hypotonic stimuli enhance proton-gated currents of acid-sensing ion channel-1b. Biochem. Biophys. Res. Commun. 367, 530–534. https://doi.org/10.1016/j.bbrc.2007.12.096

Uhlmann, R.F., Larson, E.B., Rees, T.S., Koepsell, T.D., Duckert, L.G., 1989. Relationship of hearing impairment to dementia and cognitive dysfunction in older adults. JAMA 261, 1916–1919.

van Netten, S.M., Kros, C.J., 2007. Insights into the pore of the hair cell transducer channel from experiments with permeant blockers. Curr Top Membr 59, 375–398. https://doi.org/10.1016/S1063-5823(06)59013-1

Virtanen, P., Gommers, R., Oliphant, T.E., Haberland, M., Reddy, T., Cournapeau, D., Burovski, E., Peterson, P., Weckesser, W., Bright, J., van der Walt, S.J., Brett, M., Wilson, J., Millman, K.J., Mayorov, N., Nelson, A.R.J., Jones, E., Kern, R., Larson, E., Carey, C.J., Polat, İ., Feng, Y., Moore, E.W., VanderPlas, J., Laxalde, D., Perktold, J., Cimrman, R., Henriksen, I., Quintero, E.A., Harris, C.R., Archibald, A.M., Ribeiro, A.H., Pedregosa, F., van Mulbregt, P., 2020. SciPy 1.0: fundamental algorithms for scientific computing in Python. Nature Methods 17, 261–272. https://doi.org/10.1038/s41592-019-0686-2

Voss, F.K., Ullrich, F., Münch, J., Lazarow, K., Lutter, D., Mah, N., Andrade-Navarro, M.A., von Kries, J.P., Stauber, T., Jentsch, T.J., 2014. Identification of LRRC8 Heteromers as an Essential Component of the Volume-Regulated Anion Channel VRAC. Science 344, 634–638.

Walters, B.J., Liu, Z., Crabtree, M., Coak, E., Cox, B.C., Zuo, J., 2014. Auditory Hair Cell-Specific Deletion of p27Kip1 in Postnatal Mice Promotes Cell-Autonomous Generation of New Hair Cells and Normal Hearing. J Neurosci 34, 15751–15763. https://doi.org/10.1523/JNEUROSCI.3200-14.2014

Wang, Q., Kachelmeier, A., Steyger, P.S., 2010. Competitive antagonism of fluorescent gentamicin uptake in the cochlea. Hear Res 268, 250–259. https://doi.org/10.1016/j.heares.2010.06.008

Wang, Q., Steyger, P.S., 2009. Trafficking of Systemic Fluorescent Gentamicin into the Cochlea and Hair Cells. J Assoc Res Otolaryngol 10, 205–219. https://doi.org/10.1007/s10162-009-0160-4

Wangemann, P., 2006. Supporting sensory transduction: cochlear fluid homeostasis and the endocochlear potential. J Physiol 576, 11–21. https://doi.org/10.1113/jphysiol.2006.112888

Wersinger, E., Fuchs, P.A., 2011. Modulation of hair cell efferents. Hear Res 279, 1–12. https://doi.org/10.1016/j.heares.2010.12.018

Willcox, T.O., Artz, G.J., 2007. Chapter 26 - Auditory System Disorders, in: Schapira, A.H.V., Byrne, E., DiMauro, S., Frackowiak, R.S.J., Johnson, R.T., Mizuno, Y., Samuels, M.A., Silberstein, S.D., Wszolek, Z.K. (Eds.), Neurology and Clinical Neuroscience. Mosby, Philadelphia, pp. 329–335. https://doi.org/10.1016/B978-0-323-03354-1.50030-4

Woodhull, A.M., 1973. Ionic Blockage of Sodium Channels in Nerve. J Gen Physiol 61, 687–708.

Wu, W.J., Sha, S.H., McLaren, J.D., Kawamoto, K., Raphael, Y., Schacht, J., 2001. Aminoglycoside ototoxicity in adult CBA, C57BL and BALB mice and the Sprague-Dawley rat. Hear. Res. 158, 165–178. https://doi.org/10.1016/s0378-5955(01)00303-3

Wu, Y.C., Ricci, A.J., Fettiplace, R., 1999. Two components of transducer adaptation in auditory hair cells. J. Neurophysiol. 82, 2171–2181.

Wu, Z., Müller, U., 2016. Molecular Identity of the Mechanotransduction Channel in Hair Cells: Not Quiet There Yet. J. Neurosci. 36, 10927–10934. https://doi.org/10.1523/JNEUROSCI.1149-16.2016

Xiong, W., Grillet, N., Elledge, H.M., Wagner, T.F.J., Zhao, B., Johnson, K.R., Kazmierczak, P., Müller, U., 2012. TMHS is an integral component of the mechanotransduction machinery of cochlear hair cells. Cell 151, 1283–1295. https://doi.org/10.1016/j.cell.2012.10.041

Zhao, B., Wu, Z., Grillet, N., Yan, L., Xiong, W., Harkins-Perry, S., Müller, U., 2014. TMIE is an essential component of the mechanotransduction machinery of cochlear hair cells. Neuron 84, 954–967. https://doi.org/10.1016/j.neuron.2014.10.041

Zhao, Y., Yamoah, E.N., Gillespie, P.G., 1996. Regeneration of broken tip links and restoration of mechanical transduction in hair cells. PNAS 93, 15469–15474. https://doi.org/10.1073/pnas.93.26.15469